Multiscale approach to the description of high-harmonics generation in gases

Jan Vábek

To cite this version:

Jan Vábek. Multiscale approach to the description of high-harmonics generation in gases. Physics [physics]. Université de Bordeaux; Université technique tchèque. Faculté de Génie nucléaire et de Sciences de l'ingénieur (Prague), 2022. English. NNT : 2022BORD0338 . tel-04192431

HAL Id: tel-04192431

https://theses.hal.science/tel-04192431

Submitted on 31 Aug 2023

A thesis submitted in fulfilment of the requirement

for the degrees of

Docteur de L'Université de Bordeaux

Doctoral school of Physics and engineering

Lasers, matter and nano-science

and

Doctor

Czech Technical university in Prague

Faculty of Nuclear Sciences and Physical Engineering

presented by: **Jan Vábek**

Multiscale approach to the description of high-harmonic generation in gases

Supervisors: **prof. Eric Mével, Ph.D.** & **prof. Ing. Jiří Limpouch, CSc.**
Co-supervisors: **Ing. Fabrice Catoire, Ph.D.** & **Ondřej Hort, Ph.D.**

Defended on the 6th of December 2022

The members of the jury:

Mme. Amelle ZAÏR	Directrice de Recherche	King's College London	Reviewer
M. Richard TAÏEB	Directeur de Recherche	Sorbonne Universités	Reviewer
M. Ivan RICHTER	Professor	Czech Technical University in Prague	Chairperson
M. Jiří PETRÁČEK	Professor	Brno University of Technology	Examiner
M. Carlos HERNÁNDEZ-GARCÍA	Assistant professor	Universidad de Salamanca	Examiner
Mme. Miroslava VRBOVÁ	Professor	Czech Technical University in Prague	Examiner
M. Vladimir TIKHONCHUK	Professeur	Université de Bordeaux	Examiner
M. Eric MÉVEL	Professeur	Université de Bordeaux	Invited
M. Jiří LIMPOUCH	Professor	Czech Technical University in Prague	Invited

CZECH TECHNICAL UNIVERSITY IN PRAGUE
Faculty of Nuclear Sciences and Physical Engineering

UNIVERSITY OF BORDEAUX
Doctoral school of Physics and engineering

Doctoral thesis

Multiscale approach to the description of high-harmonics generation in gases

Jan Vábek

Supervisors: Jiří Limpouch; Éric Mével (Henri Bachau, emerit.)

Co-supervisors: Fabrice Catoire; Ondřej Hort (Marcelo F. Ciappina, emerit.)

Prague/Bordeaux, October 2022

Bibliographic entry

Title:	**Multiscale approach to the description of high-harmonics generation in gases**
Author:	Jan Vábek Czech Technical University in Prague (CTU), Faculty of Nuclear Sciences and Physical Engineering, Department of Physical Electronics & Centre Lasers Intenses et Applications (CELIA), Université de Bordeaux-CNRS-CEA
Degree programme:	Applications of Natural Sciences
Field of study:	Physical Engineering
Supervisors:	prof. Éric Mével, PhD., CELIA prof. Ing. Jiří Limpouch, CSc., CTU
Supervisor-specialists:	Ing. Fabrice Catoire, Ph.D., CELIA Ondřej Hort, Ph.D. ELI Beamlines Centre, Institute of Physics of the Czech Academy of Sciences
Second edition	
Number of pages:	277
Key words:	High-harmonics generation in gases, Multiscale HHG modelling, Ionisation by optical fields, HHG in thin targets, Phase-matching in HHG, High-performance computing

The typesetting was done with LaTeX.

Bibliografický záznam

Název práce:	**Multiškálový přístup ke generaci vysokých harmonických v plynech**
Autor:	Jan Vábek České vysoké učení technické v Praze (ČVUT), Fakulta jaderná a fyzikálně inženýrská, Katedra fyzikální elektroniky & Centre Lasers Intenses et Applications (CELIA), Université de Bordeaux-CNRS-CEA
Studijní program:	Aplikace přírodních věd
Studijní obor:	Fyzikální inženýrství
Školitelé:	prof. Éric Mével, PhD., CELIA prof. Ing. Jiří Limpouch, CSc., ČVUT
Školitelé-specialisté:	Ing. Fabrice Catoire, Ph.D., CELIA Ondřej Hort, Ph.D. Centrum ELI Beamlines, Fyzikální ústav Akademie věd České republiky
Druhé vydání	
Počet stran:	277
Klíčová slova:	Generace vysokých harmonických frekvencí v plynech, Multiškálové modelování HHG, Ionizace opticým polem, Generace vysokých harmonických v tenkých terčích, Sfázování v generaci vysokých harmonických, Výkonná výpočetní infrastruktura

Práce byla vysázena v systému LaTeX.

Declaration

I declare that I wrote this thesis independently with the use of cited bibliography.

Žďár nad Sázavou, 12 October 2022

ABSTRACT

High-order harmonic generation (HHG) from gas media is now a workhorse tool that is widely used in attosecond science. It provides XUV pulses with unique sub-femtosecond and nanometric resolutions in time and space, respectively. The XUV radiation is produced by the interaction of short (usually below picosecond scale), infrared (IR), and intense laser pulses with atoms or molecules in a gas target. The main goals of today's research and engineering are to control and to optimise the generation process, which comes along with challenges such as the XUV wavefront shaping, the control of XUV angular momentum (e.g. the polarisation, the macroscopic angular distribution of the phase, and their interplay), spectral selectivity, and XUV signal enhancement.

In this work, we develop a theoretical multi-scale model for the description of the whole HHG process, one of the main outcomes is the spatio-spectral characterisation of the XUV beam. We describe the effects emerging from the microscopic description of a single atom up to forming a macroscopic XUV field given by the collective contribution of all the atomic emitters of the generating medium. The single-atom response in the XUV region is treated by non-relativistic quantum physics, and the macroscopic propagation of the IR and XUV fields is described by respectively non-linear and linear optics.

We use this model to address different physical problems. From the microscopic viewpoint, we provide a novel unambiguous approach to describe the ionisation dynamics and, especially, the time-dependent evolution of the electron density. This quantity is further used in the macroscopic approach, where it contributes to the non-linear propagation of the IR field.

At the macroscopic scale, we investigate the spatio-spectral characteristics of the XUV beam from HHG. In particular, we show that the focusing properties of the XUV beam can be controlled by imprinting a specific phase distribution of the driving field. We show that different harmonics are focused at different positions. As a result, we may create a high-, or low-pass filter by spatially selecting the harmonic beams. Last, we use the filter to homogenise the XUV field. This theoretical work is obtained in the frame of thin media approximation and is compared with experiments realised at the CELIA laboratory showing a good qualitative agreement.

The second macroscopically investigated scheme is HHG in a pre-ionised medium. The pre-ionisation is obtained, in our case, by an electrical discharge leading to the formation of a small homogeneous fraction of electron density. We start the model with the propagation of the driving

IR pulse. It reveals that there are two characteristic regions: i) The first region, where is a fast spatial re-shaping of an initial Gaussian profile directly after entering the medium. ii) The second region, where the IR beam is stabilised with only slight changes during the propagation. We demonstrate that an efficient build-up of the XUV field is possible in the second region due to quasi-phase-matching driven by the pre-ionisation. We show that an enhancement of up to a factor of eight is obtained in the harmonic signal generated in krypton, which is in good quantitative agreement with experiments conducted at ELI-Beamlines. Our model suggests that the yield can be optimised even further in some configurations.

ABSTRAKT

Generace vysokých harmonických frekvencí (HHG, z anglického High-order harmonic generation) v plynných médiích je nyní nástrojem se širokým využitím v attosekundové vědě. HHG je sekundárním zdrojem impulzů v XUV oblasti, které poskytují unikátní subfemtosekundové rozlišení v čase a nanometrické rozlišení v prostoru. Tyto impulzy vznikají typicky při interakci krátkých (obvykle subpikosekundových) primárních infračervených (IR) intenzivních laserových impulzů s atomy nebo molekulami v plynných terčích. Hlavními cíli aktuálního výzkumu a návrhu schémat generace jsou kontrola a optimalizace celého procesu, konkrétněji: tvar XUV vlnoploch, kontrola momentu hybnosti XUV (tj. polarizace, makroskopického úhlového rozložení fáze a jejich vzájemného vztahu), spektrální selektivita, či zesílení XUV záření.

V této práci se zaměříme na teoretický a numerický popis s použitím multiškálového přístupu, jedním z hlavních výsledků je prostorová a frekvenční charakterizace XUV záření. Základní jednotkou popisu je odezva jediného atomu média. Makroskopické XUV záření je zformováno z kolektivního příspěvku záření všech atomů média. K popisu atomární odezvy v XUV oblasti použijeme nerelativistickou kvantovou fyziku, makroskopický model budícího IR impulzu vychází z nelineární optiky a vygenerované záření je popsáno pomocí lineární optiky.

Tento model použijeme k vyřešení několika fyzikálních problémů. V mikroskopické části poskytneme inovativní pohled na dynamiku ionizace, kde se zaměříme především na vývoj distribuce energie v čase.

V makroskopické části se nejprve zaměříme na prostorové rozložení (fokusaci) různých frekvenčních komponent vygenerovaného záření z tenkých terčů. Ukážeme, že fokusace může být řízena pomocí vlnoploch řídícího svazku, jejichž fáze se promítne do generovaného záření. Výsledný mechanismus vede k rozdílné fokusaci svazků odpovídajícím různým harmonickým řádům. Tento mechanismus dále využijeme ke zkonstruování spektrálního filtru pomocí prostorové separace jednotlivých svazků. Dále ukážeme, že tato filtrace může vést ke vzniku frekvenčně homogenního svazku. Tato část práce poskytne komplexní analýzu problému ve spolupráci s experimenty realizovanými v laboratoři CELIA.

Druhé analyzované makroskopické schéma je generace vysokých harmonických v dlouhém médiu. Hlavním mechanismem je zde homogenní před-ionizace média. V této části nejprve namodelujeme šíření řídícího IR pulzu. Ukážeme, že v médiu se pulz šíří ve 2 různých režimech. Nejprve dochází k podstatným změnám pulzu po vstupu do média. Dále následuje oblast stabilního šíření s velmi pozvolnou změnou intenzity. V této části je možno předionizací dosáhnout sfázovaní primárního a generovaného záření. Ve výsledku jsme pozorovali až osminásobné zesílení v souladu s experimenty v kryptonu provedenými v ELI-Beamlines. Náš model dále indikuje, že v určitých případech je možno docílit ještě vyššího zesílení.

Résumé

La génération d'harmoniques d'ordre élevé (HHG en abréviation anglaise) à partir de milieux dilués est désormais un outil de travail largement utilisé dans la science des attosecondes. Elle fournit des impulsions XUV ayant des résolutions sub-femtosecondes temporellement et nanométriques spatialement qui sont uniques. Le rayonnement XUV est produit par l'interaction d'impulsions laser brèves (généralement inférieures à la picoseconde), infra-rouge (IR), intenses avec des atomes ou des molécules avec une cible en phase gaz. Les principaux objectifs de la recherche actuelles et de l'ingénierie sont de contrôler et d'optimiser le processus de génération, ce qui s'accompagne de défis tels que le contrôle du front d'onde XUV et de l'état de polarisation, la sélectivité spectrale, la structuration du moment angulaire ou l'augmentation du signal XUV.

Dans ce travail, nous avons développé un modèle théorique multi-échelle décrivant les propriétés spatio-spectrales du faisceau XUV. Les caractéristiques provenant de la description de l'atome unique jusqu'à la formation du champ XUV macroscopique décrit par la contribution collective de tous les émetteurs atomiques du milieu générateur sont complémentent prises en compte dans ce modèle. L'échelle microscopique décrit la réponse de l'atome unique et est basée sur une description quantique non-relativiste. L'échelle macroscopique décrit la propagation des champs et résout les équations de l'optique non-linéaire pour modéliser le champ laser générateur et les équations de l'optique linéaire pour le champ XUV.

Ce modèle a été appliqué pour répondre à différentes situations physiques. Du point de vue microscopique, nous décrivons une nouvelle approche invariante pour décrire la dynamique d'ionisation et en particulier l'évolution dépendante du temps de la densité électronique qui pourra par la suite être utilisée dans l'approche macroscopique et plus particulièrement dans la propagation non-linéaire de l'IR. A partir du modèle macroscopique, nous avons étudié les caractéristiques spatio-spectrales du faisceau XUV issu de la HHG. En particulier, nous montrons que les propriétés de focalisation du faisceau XUV peuvent-être contrôlées en imprimant une distribution de phase spécifique au faisceau générateur. Nous avons utilisé cette propriété pour sélectionné spectralement le peigne de fréquence harmonique créant ainsi un filtre soit passe haut soit passe bas. Nous montrons également que la distribution spatiale en champ lointain peut-être contrôlée de telle sorte qu'un faisceau plus homogène, d'une harmonique à l'autre, peut-être obtenu. Ce travail théorique a été obtenu dans le cadre de l'approximation des milieux fins et a été comparé à des expériences réalisées au laboratoire CELIA et montre un bon accord qualitatif. Nous avons également appliqué notre modèle à un schéma où une pré-ionisation du milieu a été réalisée. Elle a été obtenue par une décharge électrique conduisant à la formation d'une petite fraction de densité électronique homogène. Dans ce schéma, pour lequel le modèle numérique complet a été utilisé pour la propagation de l'IR, nous montrons que la propagation du champ IR se comporte différemment en deux région distinctes : i – une première correspondant à la propagation en entrée de milieu et présente une évolution spatiale du faisceau très rapide ii – une seconde, se situant après la première dans la direction de propagation, où le faisceau se stabilise et peut former des interférences constructives du faisceau XUV de telle sorte qu'un quasi accord de phase est obtenu. Nous avons montré qu'une amplification du signal harmonique jusqu'à un facteur huit peut ainsi être obtenu. Un rendement encore meilleur peut-être atteint dans certaines configurations. Ce travail a été obtenu conjointement à un travail expérimental réalisé à ELI-Beamlines. La comparaison des résultats expérimentaux et théoriques montre un bon accord quantitatif.

To my parents Anna and Jan, who support me
To Martinka
To Ládík and Toník
To all children, our future

Acknowledgements

I would like to thank many people that helped me during my PhD. I would like to mention some of them and apologise to them who I may have forgotten to mention. For me, the people mentioned below have significantly contributed to this work. Moreover, most of them are also my friends and have helped me by being unique humans and have inspired me by giving me their views and opinions about the World.

First, I would like to thank my family, my mum and dad, who have raised me and have been supporting me.

Next, I would to thank *Fabrice Catoire* for his patience in discussing physics with me, stimulating ideas, projects and support during my PhD. Also at this important place, I would like to thank *Stefan Skupin*, who although not officially related with the work, has significantly contributed to the final results. His contribution is similar as being a regular (co-)supervisor. The actual macroscopic model in this work would not be possible without his CUPRAD code and help. Next, I would like to thank all the others supervisors and co-supervisors related to the PhD project: *Henri Bachau* for his knowledge and wisdom in HHG and related modelling; *Éric Mével* for giving the direction of the projects related with experiments and my successful stays at CELIA; *Jiří Limpouch* for interesting discussions and helping me with opportunities at CTU as teaching and administration of the joint-PhD programme; *Ondřej Hort* for the comments from the experimental perspective and link of my work with experiments; *Marcelo Fabián Ciappina* for interesting and stimulating discussions as well as the horizons beyond HHG in gases.

Next, I would like to thank all the institutions and their representatives that have hosted me during my PhD project: ELI-Beamlines, CELIA laboratory (the University of Bordeaux, CNRS, CEA), the Faculty of Nuclear Sciences and Physical Engineering of the Czech Technical University in Prague and CAMPUS France administrating and funding the part of the project in France, there I would like to mention namely *Farid Saadoun*, who helped me with administration and accommodation in Bordeaux. This work was supported by the European Regional Development Fund and by Ministry of Education, Youth and Sports within targeted support of Large infrastructures (project LM2018141). This project was also supported by the project Advanced research using high intensity laser produced photons and particles (CZ.02.1.01/0.0/0.0/16_019/0000789) from European Regional Development Fund (ADONIS); and by Grantová agentura České Republiky (GACR Grant 20-24805J).

I thank also all providers of the computer time during the project: Grand Équipement National De Calcul Intensif (GENCI A0100507594); computing facilities MCIA (Mésocentre de Calcul Intensif Aquitain) of the Université de Bordeaux and of the Université de Pau et des Pays de l'Adour; ECLIPSE computational cluster at ELI-Beamlines and computational workstations at CELIA.

Next, I would like to thank my colleagues and friends from the HHG groups at ELI-Beamlines and CELIA. I would like to mention: *Jaroslav Nejdl*, for leading the HHG group and giving me opportunities in the group; *Eric Constant* for stimulating comments and joint work on the thin-targets problem; *Ondřej Finke* for the work on the experimental counterpart of the pre-ionisation project; *Matej Jurkovič* for the work on the two-colour HHG; *Martin Albrecht* for friendly discussions; *Victoria Nefedova* for joint work in the early PhD stage.

Next, I would like to thank all who helped me with the development of the computer codes: *Rachel Nuter* and *Jiří Vyskočil* for helping me understand and use HDF5 API's; *Nicole Audiffren* from GENCI for the assistance with MPI; *Edwin Chacon-Golcher* for helping me to deploy CUPRAD at ECLIPSE and other advices about its development.

Next, I would like to thank many other people from ELI-Beamlines and CELIA: *Petr Valenta* and *Jan Nikl* for stimulating discussions about physics, computer modelling and its visualisation; *Martin Matys* for chairing the SPIE chapter; *Valeria Istokskaia* for friendly discussions and the time at the PowerLaps summer school; *Michael Vích* and *Hana Strnadová* for their work on the popularisation of science and the opportunity for me to participate.

Next, I would like to thank many other people from the departments of physics and physical electronics at FNSPE: *Petr Novotný* for discussions about classical field theory and physics in general and organising Winter School of Mathematical Physics; *Dagmar Bendová* for discussions about science and sub-atomic physics and sailing on the waves of the Tyrrhenian Sea; *Lenka Motlochová* for discussions about physics and mathematical structures used both in formulation of fundamental physics and also numerics; *Dominika Mašlárová* for co-teaching the class of numerical methods; *Petr Kulhánek* for discussions about physics and running Aldebaran group and its events.

Next, I would like to thank all the teachers of physics and mathematics who raised my interest in science. Because there are too many of them, I would mention only my high-school teacher *Karel Koten* who steered me into physics together with the organisers of the TCN summer camp when I was a teenager. I thank all the others from Czech Technical University in Prague and the University of Bordeaux.

Next, I would like to thank all the students and interns I have met and worked with during my PhD and stay at ELI-Beamlines: *Tadeáš Němec*, a great student working on SFA calculation of HHG and two-colour schemes; *Jakub Jelínek* who implemented a part of the HDF5 library in CUPRAD and brought the view of a computer scientist; *Miłosz Lepak* who started the work on the SQL database system used to list experimental data; *Hryhorii Ovcharenko* who worked on further development of the CUPRAD code and related analyses.

Next, I would like to thank my friends: *Dan Homola* for the insight in the software engineering and the maintenance of software project as well as various programming techniques; *Lenka Moutelíková* for her reason and keeping me updated about the world around us; *Vojtěch Haman* for his views and insight into the world of law; *Quentin Malapert* for helping me to orientate in Bordeaux.

Next, I would like to thank people from King's College London, who I have met during the final stage of my thesis and with whom I have started my first post-PhD projects: *Amelle Zaïr* for organising my visit, welcoming and stimulating scientific project; *Emilio Pisanty* and *Margarita Khokhlova* for warm welcome and fast adaptation in the group and new horizons in HHG; *Anne Weber* for the help with the planning of my arrival.

Finally, I would like to thank *Martinka* for the time when her smiles were the brightest and most beautiful essence in the world. I thank her also for the amazing moments of belief that truth, sincerity, esteem, empathy, trust, home, love, family, forgiveness, understanding, reconciliation and equality of people extend beyond time and make us humans. These infinite qualities make life meaningful. *Martinka*, thank you for all the days you illuminated by your smile in the morning.

CONTENTS

INTRODUCTION

Principles and applications of High-order harmonic generation (HHG)

This work is dedicated to the theoretical study of High-order harmonic generation in gas phase. The interest in this physical phenomenon arises from the fact that it provides one of the sources of attosecond pulses in the XUV domain together with free-electron lasers (FEL) [1] and plasma mirrors [2]. An advantage of HHG in gases is its high coherence, versatility, possible high-repetition rate and accessibility of the source compared to the other sources. The coherence is also linked with the precise timing of the process, which makes HHG ideal for pump-probe schemes [3, 4]. Furthermore, FEL's and plasma mirrors are limited to large facilities since it requires the production of an energetic laser pulse,[1] while an HHG source may be constructed from commercially available equipment and is reachable for standard university laboratories. Such a source is of high practical interest as the resulting XUV radiation may be used to probe matter on ultrashort (attosecond, i.e. 10^{-18} s) time scales – comparable with the characteristic times of electronic motion in atoms and molecules. HHG opens a way to directly access these scales because it produces XUV pulses of comparable duration. A pulse of the duration down to 43 as was actually produced and measured experimentally [6]. This state-of-the-art temporal resolution allows to study atomic processes like electronic and molecular motion in "real-time" [7, 8, 9]. Complementary to the dynamical phenomena studied in time domain, it also provides access to spatial resolution of atomic and molecular orbitals via tomography [10, 11]. See also a comprehensive review of techniques and applications [4].[2] In this sense, attosecond XUV pulses become a unique tool being our sight and touch of the World at atomic scales.

A limiting factor for some applications of HHG is its low conversion efficiency, which is under a high development since the discovery of this source. However, the efficiency is still reaching at most up to $\sim 10^{-6}$–10^{-4} (depending on the XUV region of the interest) [13, 14]. This motivates high interest to study the source and find ways to control and optimise it, which requires a deep understanding of the underlying physics.

---

[1] These limitations are of course a subject of development to make them more accessible, an example is the scheme of a rotating plasma mirror as proposed in [5].

[2] To apply the XUV for precise measurements, its own metrology is necessary. A review of various techniques is provided in [12].

Let us discuss the mechanism of HHG. It is a secondary source of radiation, which means that a primary laser source is needed. This primary source interacts with matter, which is a gaseous medium in our case. Because the physics of HHG is swinging around the ionisation threshold of the atoms of the medium, the intensity of the primary source must be intense enough to induce the ionisation process but not too high to fully ionise the gas instantly. A typical intensity range to produce efficiently harmonics is of the order $I \in \left]10^{13}, 10^{16}\right[$ W/cm^2 (in comparison, the threshold intensity for suppressing the Coulomb potential in argon is $I \approx 2.5 \times 10^{14}$ W/cm^2).

There may be additional requirements on the driving pulse characteristics depending on the usage of the XUV field. For example, a single-cycle pulse may be used to generate a single attosecond pulse, which is required for some applications [15]. Another aspect of the primary-laser profile is that it is macroscopic compared to the atomic scales – the spatial evolution of the driving field is negligible within a single microscopic system. Next, it is shown that in some cases the HHG process is scalable and different geometries may produce the same outputs [16]. For example, the longitudinal dimension, radial dimension, medium density and driving pulse energy (z, ρ, ϱ, E) scale with a dimensionless η as $(\eta^2 z, \eta\rho, \varrho/\eta^2, \eta^2 E)$ in certain conditions. This may provide flexibility in designing efficient schemes for HHG [17]. From the previous discussion, it is obvious that the better control we have over the primary source, the more control we have over the secondary source.

The basic principle suggests that there are two scales of interest: 1) microscopic scale of a single atom of the gas, where the laser-matter interaction induces the HHG process; 2) macroscopic scale describing the propagation of both the driving laser field and the secondary radiation in the medium.

We start with the microscopic part. HHG may be considered as going beyond standard perturbative non-linear optics. Let us explain the reason. The perturbative treatment writes the non-linear response $P_{\text{non-lin}}$ as a power series in the electric field $\mathcal{E}$, namely $\boldsymbol{P}_{\text{non-lin}} = \sum_{i=1}^{+\infty} \chi^{(i)} \mathcal{E}^i$. In the perturbative regime, the electric susceptibilities, $\chi^{(i)}$, are assumed to drop fast with their order i, [18]. However, it did not agree with experiments [19, 20, 21], where an extended plateau in the harmonic orders of the primary laser was observed. Such a mechanism was briefly discussed theoretically in [22]. A quantitative explanation of this surprising result came later [23, 24, 25]. The explanation is the following: the perturbative approach assumes that the electrons remain bound in the electron shell.[3] In HHG, the response does not drop with the harmonic order because the electron is torn out of the atom during the process. The full process is explained in three steps: 1) the atom is ionised by the laser field; 2) the liberated electron is driven by the field and due to its periodicity, it may recombine with the parent ion; 3) the electron emits the excess of energy gained from accelerating in the field in the form of an XUV-photon. This process repeats twice per optical cycle, which results in a train of attosecond pulses [26]. The periodicity in time together

---

[3] The power series then somehow fits a notorious physical model of an anharmonic oscillator.

with the spatial symmetry of the atom is then translated in the spectrum to form odd harmonics.

Macroscopic effects

The main interest of this work goes further towards macroscopic properties of HHG, which fundamentally emerge from the collective contribution of many microscopic systems. (One of the typical targets for HHG contains $\sim 10^9$ atoms.)[4] We focus on two aspects of the macroscopic generation: a) the control of the divergence of XUV beams generated in thin media, b) the phase-matching of the generated field in long media. The studies of the two configurations have been done in close collaborations with experiments conducted at CELIA and ELI-Beamlines.

We specify the classification of the length of the target before we discuss the details of the two geometries. The classification is linked with two characteristic dimensions determining the resulting macroscopic XUV signal. These dimensions are respectively transversal and longitudinal as defined by the optical axis – the direction of the propagation of the driving laser. A thin target means that these two dimensions may be decoupled or even the longitudinal effects may be neglected. As a consequence, all the transversal XUV-signal structures in the thin-target can be attributed to the transversal effects in the generating medium.

Referring the thin-media geometry a). A higher degree of control of the harmonic characteristics can be potentially achieved since the longitudinal aspects are treated independently. Consequently, it allows also a better understanding of physical mechanisms. This brings different questions such as: How does the generated XUV beam look like? More specifically: What are the focusing properties of the beam? What are the sources of interferences in the XUV spectrum? Are these effects spectrally sensitive? Numerous studies [27, 28, 29, 30] recognised the radial interference patterns in the spatially resolved harmonic spectra. A key role was attributed to the interference of different quantum paths [31] leading to the same energy of XUV photons. The mechanism of the *quantum path interference (QPI)* is that more quantum paths [32] contribute to one energy in the spectrum. It was recognised later that another key mechanism there is the radial macroscopic profile of the driving beam [33]. It turns out that the intensity profile is imprinted in the intrinsic phase of the microscopic response, which adds up with the macroscopic phase driven by the curvature of the driving beam.

To summarise the key physical principles: The phase of the XUV beam is dictated by the macroscopic intensity and phase profiles of the driving beams. The role of the quantum paths is also essential because the intrinsic phase of the different paths responds differently to the intensity profile. We exploit these mechanisms in this work. We control the phase by the positioning of

---

[4] This example consider a gas cell with the length $L = 1$ cm filled with a gas at $p = 10$ mbar at standard temperature and a laser focused to the diameter about $\rho = 100$ μm, the number of particles is then $N = L\pi\rho^2(p/p_0)n_L$, where $n_L \approx 2.7 \times 10^{25}$ m^{-3} is the Loschmidt's constant and p_0 the standard pressure.

the thin target which defines the imprinted curvature as of the driving field. We are thus able to control the divergence of the generated XUV beams by this mechanism. Next, we show the spectral selectivity of the process. These results are published in [34, 35].

The second geometry b) is dedicated to the optimisation of the phase-matching (PM) in long media. It is a challenging problem compared to ”usual” non-linear optics in the perturbative regime (Section 2.3, [36]). The reason is that the phase-matching becomes a *dynamical* process in HHG: 1) The medium is being ionised during the passage of the driving pulse, which changes the optical properties of the medium at different parts of the pulse. As a consequence, PM is a time-dependent quantity. 2) Because the intrinsic phase depends on the intensity profile as mentioned above, it gives another time-dependent effect to the phase-matching. The main phase contributions are then: the dispersion, the contribution of the free electrons due to ionisation, the geometrical phase of the driving beam, and the contribution of the intrinsic microscopic phase. Physical insight is based on the study of local dephasing [37]: the phase of any microscopic atomic emitter has to interfere constructively with other emitters in the macroscopic volume. This model is then up-lifted to form a macroscopic response [38]. It enables to infer the range of the constructive interference. This range is the so-called *coherence length* that is defined as the distance along which the generated fields add up constructively. As a result, the model [38] provides the estimate of the total XUV signal.

The phase-matching is instrumental to optimise the XUV signal along the optical axis. Other applications aim to the filtering of the XUV, either in time to produce an isolated attosecond pulse [39] or select only some of the harmonics from the spectrum [40]. PM is therefore of high interests for the HHG community from the beginning and a huge effort has been devoted in this area, for example [41, 42, 38, 37, 43, 44, 45, 46, 47, 48, 49, 50], see also the review in [39].

Moving toward practical realisations, the understanding of phase-matching has been blossoming various ideas and schemes. We mention some of the PM-schemes here. A natural property of intense pulses is the gradual ionisation by the pulse. This creates a window where the PM is possible due to an optimal plasma density produced by the ionisation. It is called the transient phase-matching that has been studied in [51, 48, 52, 53, 54, 55, 56, 39]. The wavelength of the driving laser also changes PM and allows different effects to be at play [57, 58, 50, 59, 14, 60]. The PM can be also assisted by using multicolour driving fields [14]. (The multicolour field contains more dominant spectral components: usually the fundamental frequency together with its 2nd harmonic.) Because the phase is intrinsically linked with the geometry of the beam, controlling its wavefront may drive PM as, for example, a two-foci scheme [61], or a use of a flat-top beam [62], or by two non-collinear beams [63]. Another option is to guide the beams to control their phase, which leads to one of frequent geometries in HHG [64, 52, 65, 66, 67, 68]. Complementary to the geometry of the beam, the geometry of the target may be used for PM as well: A simple geometry is a chain of gas jets [41, 69, 70, 40] resembling the idea of quasi-phase-matching in usual non-linear optics, Section 2.4 of [36]. As mentioned in the thin-media geometry a), the intrinsic microscopic phase is related to the gradient of intensity, which brings another possibility to control PM [71]. In summary, the complexity of the process makes the comprehensive understanding challenging but also brings many possible ways to control it.

The geometry introduced in this work [72] adds the density of the free electrons as a tunable parameter in the phase-matching scheme: the medium is homogeneously pre-ionised before the interaction. It turns out that the pre-ionisation does not lead to the re-shaping of the driving pulse. Basically, we can adjust the phase constantly in the whole medium. The main application is demonstrated in HHG in long media, where the intensity is clamped shortly after the entry of the medium [73, 74, 75]. The clamping also reduces the possibility to design the pulse in this case. Our method implements a way to easily control the phase in this region.

In conclusion, our studies of HHG address two important geometrical effects in HHG: the XUV beam focusing due to the transversal geometry of the target, and the optimisation of the phase-matching due to pre-ionisation in long media. It thus brings novel understandings of these two aspects in HHG.

Numerical modelling: multi-scale approach

An inseparable part of work is its numerical modelling of the physical processes. We discuss some key concepts before we specify our concrete implementation. In some sense, the story of the multi-scale approach contains a repeated motif of coupling and decoupling. We have already seen this motif in the need of coupling the microscopic and macroscopic views, and in the decoupling of the transversal and longitudinal effects in HHG. The same pattern appears to be impressed in the numerics.

To motivate the need of a fully numerical description, we start with a short example: the concept of the refractive index n for ultrashort pulses, i.e. with a broadband spectrum. The refractive index describes the optical properties of a medium and is naturally expressed in the frequency domain as $n(\omega)$. Complementary, we have already discussed the change of the optical properties in time due to the ionisation caused by the passage of an intense pulse. It would naïvely bring the refractive index as a function of both frequency ω and time t. However, such a function is a mathematical nonsense because t and ω are conjugate variables. There is thus a limit in the concept of the refractive index and a way to overcome this problem is to stick to a solution of Maxwell's field equations.[5] To find such a solution, we are left with numerical solvers to include quantitatively the

---

[5] To be rigorous, the use of ω and t may be included using a convolution. However, the inclusion of highly non-linear processes would be complicated anyway.

non-linear effects induced by high intensities involved in HHG.

A consistent multi-scale model of HHG is thus of high interest as it may provide an essential tool a) to understand the interplay of various mechanisms within the process and b) to design the gaseous target and the laser pulse to control the XUV field from HHG. At the moment, we can refer to the thin targets geometry and the two sources of interferences therein – QPI and geometrical effects of the IR-wavefront. The PM in long media is also based on interference, the resulting pattern forms the so-called Maker fringes [76, 77]. The complex interplay of these effects is exactly an example to apply the multi-scale approach. Another important question is the propagation of the driving pulse shaped including non-linearities. Especially, to quantify the plasma defocusing [78] leading to the aforementioned intensity clamping, which may compete with the Kerr-induced self-focusing [79] for some intensities. All these questions may be hard to quantify without a detailed numerical treatment.

Let us introduce our computational strategy and simplifications of the description used in our work. A model from the basic principles would require a feedback loop in the description of the electromagnetic field and atoms of the medium. This loop is computationally demanding when both sides – the field and the atomic responses – are fully numerical themselves. In our approach, we decouple the driving IR-field and the generated XUV-field. The optical response of the medium is then computed by different strategies: the driving pulse is shaped mainly by the effects of standard non-linear optics; the source of the XUV-field needs a particular approach, but the propagation of the XUV-field itself is not strongly affected by non-linearities. The computational modules are then pipelined into three steps: 1) The propagation of the driving laser is computed including the non-linearities described by the means of non-linear optics and a simplified model of ionisation. 2) The numerical field from the previous step is inputted into the microscopic solvers, which provide elementary emitters of XUV radiation at every point of the generating medium. 3) All the microscopic emitters are collected to form the macroscopic XUV field. Another simplification goes towards the reduction of the dimensionality of the problem: We assume cylindrical symmetry in all the configurations in this work.

An inseparable part of the solver is the specification of two components: i) the physical model used for each of the processes 1)–3), and ii) the numerical implementation. The pivoting ideas of the implemented parts summarise as follows: 1) We use the computational kernel developed in [80], the physics is modelled by the non-linear Schrödinger equation implying unidirectional propagation of the field. It includes various linear and non-linear responses of the medium, the implementation uses Fourier transform to describe each of the effects in a suitable domain – time or frequency –; it thus needs to switch the domains frequently during the run of the solver. The propagation of the field in the medium is treated by the Crank-Nicolson propagator [81]. 2) The microscopic response is described by the central equation of quantum mechanics: the time-dependent Schrödinger equation (TDSE). This has to be solved many times for various fields of the medium. Due to the high computational cost, we use a simplified 1D-geometry. The implementation relies on a grid method combined with the Crank-Nicolson propagation. 3) The macroscopic XUV field is retrieved from a diffraction-like integral based on the Hankel transform.

One of the key philosophies within the development is modularity. Each subtask shall be easily replaceable by other models. We thus use a wider range of tools for the microscopic response. Another approach we use is the so-called Strong-Field Approximation (SFA) [25]. This approach avoids the explicit solution of the TDSE by using an ansatz. This is further simplified down to a set of algebraic non-linear equations [82]. A simple model of the microscopic response is of particular interest as its computation by the TDSE is a bottleneck of the calculation.

This gradual palette of models with a various balance of accuracy vs. computational cost is very useful for HHG-schemes, which involve many defining parameters of both the driving field and the target. One of the strategies applied in this work is to use an advanced model to benchmark the validity of a simplified and computationally cheap model on a test example within the range of interest. The simple model is used to recognise promising configurations to optimise the HHG-scheme. Finally, the advanced model is used again to verify and refine the configurations of interest.

To conclude the discussion about numerics, we put our numerical modelling into a broader context and review other approaches. One of the milestones, and possibly the birth of modern computational physics, is the Manhattan project [83], where machine-based computing began to be used extensively. For example, the idea of the Particle-in-cell (PIC) for hydrodynamical problems originated there [84]. Moving to the physics of our interest, numerical tools were already in use in the 1960s for the focusing of an optical beam [85] and the TDSE [86] being exactly the two problems of our interest. The development of these numerical approaches has continued later on, and for example 1D-TDSE is today a standard classroom problem [87]. But it does not mean that novel efficient solvers are not needed. Especially for higher dimensionality as, for example, direct multi-electron solvers are still beyond the numerical power today.

According to the outlined high physical interest of the HHG, several numerical tools covering the multi-scale approach have been already developed:

- A direct coupling of Maxwell's equations with the TDSE is presented in [88]. This calculation is very expensive and only micrometric targets are computable for the 3D-Maxwell-3D-TDSE case with reasonable resources. Such a solver is an ideal tool for fundamental questions as there are only inevitable numerical approximations but no physical approximations (within the framework of non-relativistic quantum physics with classical fields). To downscale the computational cost, some simplifications in this model are introduced: Because the free electrons created by the ionisation may move away from the parent ions, the free electrons are described as plasma after the ionisation [89, 90]. Furthermore, the microscopic model is simplified using the SFA and the number of numerically computed microscopic sources is reduced by their interpolation [91].

- Another approach based on the unidirectional propagation is introduced in [92] and [93]. The microscopic response is treated by the SFA and 1D-TDSE, respectively. This formulation is also used in [94, 49, 95] and further extended in [96], where the SFA is further simplified taking into account only semi-classical quantum paths. A similar approach based on the same formulation is used in [97, 98].
- A multiscale approach is also presented in [99]. This method uses a simplified version of the propagation of the driver; the effects of the medium on the field are linearised and included only by the dispersion and absorption. The microscopic response is then treated with a generalised SFA-approach (referred as SFA+ and introduced in [100]). The XUV field is retrieved by an integral approach based on the so-called Discrete-Dipole Approximation [101, 102] with a randomised sampling [103] of the macroscopic volume.

Unfortunately, these models are not publicly available as open-source packages unlike, for example, some PIC codes [104]. We thus cannot provide a direct comparison of the numerical performance and other details.

The main work done in the multiscale model in this work is thus mainly in the coupling procedure of the originally independent codes. Besides this, we also discuss the development of a 3D-TDSE solver in this work.

Ionisation

Here, we want to clarify one of the crucial terms we have used already several times: *ionisation*. Ionisation is an important interlink of microscopic and macroscopic physics: The process starts with a single atom and leads to the density of free electrons. Once we try to inspect ionisation in detail within the atomic scale during the interaction with an external optical field, we may arrive at some troubles with its proper definition. The reason is that it is non-trivial to choose an invariant reference. Two natural choices seem to rely either on the volume, where the electron is located with a certain probability; or on the projection onto the atomic bound states. The problem with the former is that the volume of an atom is ambiguous. For the latter, the gauge invariance, Chapter 16.4 of [105], comes to play. The presence of the external field affects the states, but their form depends on the choice of the gauge. Although this problem seems subtle at the first sight, it has been a stimulus for further research as there is something non-trivial unclear about this fundamental term in our area.

The idea to use quantum mechanics to treat ionisation using static fields came early with the foundations of quantum mechanics in 1928 [106], where is proposed a correction of the perturbative series for the Stark effect. Practical quantitative calculations became important later with the development of the laser technique generating optical fields strong enough to ionise atoms. Works from that time [107, 108, 109, 110] successfully estimated the ionisation rate; however, they use ad hoc assumptions starting with a fixed gauge. The resulting description provides a rate equation, which lacks the coherence of the process or re-collisions essential for HHG.

To overcome these complications, we develop a novel methodology based on the invariantly calculated energetic distribution of the wavefunction of the electron [111]. We use the formalism of the resolvent operator to find a convenient expression of the energy distribution. This allows us to do a numerical analysis based on numerical implementation of the resolvent formalism [112, 113, 114]. The importance of the work is in a novel insight in the ionisation process. Having this universal tool, we apply it to study the limit pictures of the ionisation explained in the terms of a single-photon [115], multi-photon regime [116], or tunnelling regime [107]. Using our method, we both get insight in the process and obtain a tool to verify the rate equations.

Thesis organisation & units

To ease the orientation in the thesis, there is a signpost. First, we provide a brief phenomenological explanation of the physics involved in all the parts of the multi-scale model in Chapter 1. Then, there are two options for the reading: the work continues talking about physics in more detail from the microscopic, Part I and macroscopic, Part II, viewpoint. The second option is to move directly to Part III of the thesis, for the readers interested only in the implementation of the multi-scale model.

The content of all the remaining chapters is the following: Chapter 2 presents a general quantum-mechanical model and the approximations we use. Based on the quantum-mechanical model, we retrieve the source term of HHG directly from TDSE or further simplified by the SFA. Chapter 3 provides a comprehensive picture of ionisation in optical fields. We introduce there the technique to unambiguously retrieve ionisation from a solution of TDSE. We put this method into the context of usual phenomenological pictures of ionisation. Chapter 4 introduces formulation of the propagation equations, which are shared for both the XUV- and IR-field. Chapter 5 then treats the propagation of the XUV field based on the diffraction-integral formulation. This theory is then applied on the problem of optics-less focusing. Chapter 6 completes the physics of the multiscale model. We provide the details about the model solving the propagation equations of the IR-field. The full model is applied to the problem of the optimisation of the harmonic yield by pre-ionising the target. After this chapter, we move to the details about the numerical implementation in Part III.

Chapter 7 provides the details about the numerical methods to model microscopic physics: the Hamiltonians using 1D- and 3D-geometries; the evolution in time and the methods used to compute the ionisation by the so-called complex rotation. Chapter 8 provides a brief review of the solver we use to model the non-linear propagation of the driving IR-pulse. Chapter 9 introduces the diffraction integral used to model the macroscopic XUV signal. The multi-scale model is assembled in Chapter 10. Finally, Chapter 11 summarises the work and gives perspectives for possible future developments.

The last remark is about the units. According to different suitable units to the physics in microscopic and macroscopic scale, the usage of the units is part-wise in the thesis (if not stated otherwise). Part I uses atomic units (see Appendix A). Part II uses SI units. Part III is indifferent to the units because it discusses only numerical representations for computer modelling. All the factors are then explicitly in the equations, and we assume all the physical constants evaluated in SI units.

1. BASIC CONCEPTS

Although the quantitative multiscale model we will describe in this work relies on large numerical solutions, basic examples and concepts may provide a picture of the involved physics. We overviewed them in the introduction and here we illustrate them by simplified semi-empiric or phenomenological models. The main purpose of this chapter is to build a skeleton that will be encased by more advanced treatments in the rest of this work.

First, we review the picture of the microscopic response of a single atomic system in Section 1.1. Then in Section 1.2, there are discussed the shaping effects of the IR-driving pulse due to the non-linear propagation emphasising the effects in the principal directions: along and transversal to the propagation. Corresponding considerations are done for the generated XUV radiation in Section 1.3. Finally in Section 1.4, there is provided a framework of the coupling used to form the final multi-scale model from all the respective components.

1.1 Physics driven by single-atom response: three-step model, spectra, ionisation

We start with the response of a single atom subjected to an external field with a typical intensity for HHG, which peak value is sufficient to start ionising the atom by few %.

1.1.1 Three-step model

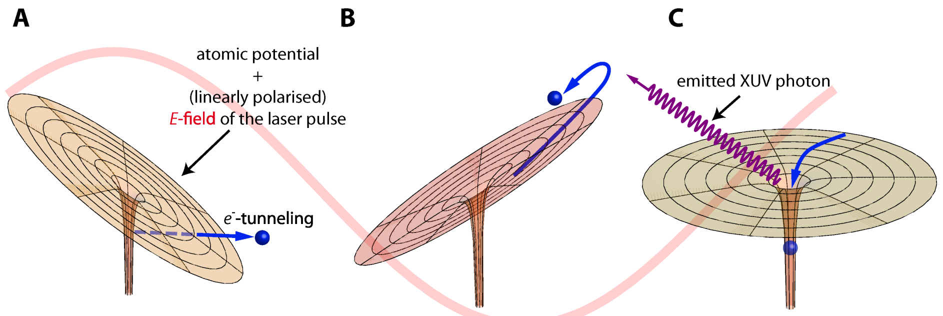

Fig. 1.1: Schematic representation of the three-step model. The electron e^- is ejected near the maximum of the electric field in the first step, **A**. Then it propagates driven by the field and due to its periodicity, its motion is reversed, and it is accelerated towards the parent ion, **B**. Finally, the electron recombines back while emitting the sum of the excess of the kinetic energy and the binding energy in the form of an XUV photon, **C**. Used from [117] under the CC BY-NC-ND 4.0 licence.

The insight into the HHG within a single half-cycle of the driving laser emerges from the aforementioned three-step model. This model is schematically illustrated in Fig. 1.1. Because this process is precisely triggered by the driving laser, it may provide a highly coherent source.

1.1.2 Harmonic spectra

An XUV source is characterised by its spectrum that is the energy distribution of the generated radiation. Figure 1.2(a) shows an example of a numerically computed spectrum of a single atom. To characterise this process, it is convenient to represent the energy E rescaled in harmonic orders of the driving laser, $H = E/(\hbar\omega)$.

The harmonic spectrum can be divided into three regions with two characteristic points separating them. First, there is the perturbative region, where the response is exponentially damped, going towards the ionisation potential I_P. After this point, the physical mechanism is dominated by the freed electrons described by the 3-step model. Classical equations of motion imply the existence of a maximal possible energy E_{cutoff} that may be produced during the recombination [23]. This energy ends a plateau of harmonics between I_P and E_{cutoff} with nearly constant amplitude. The value of the cutoff deduced from the classical equations of motion is

$$E_{\text{cutoff}} \approx I_p + 3.17 U_p \,, \qquad U_p = \frac{2e^2}{c\varepsilon_0 m_e}\frac{I}{4\omega^2} \,, \tag{1.1}$$

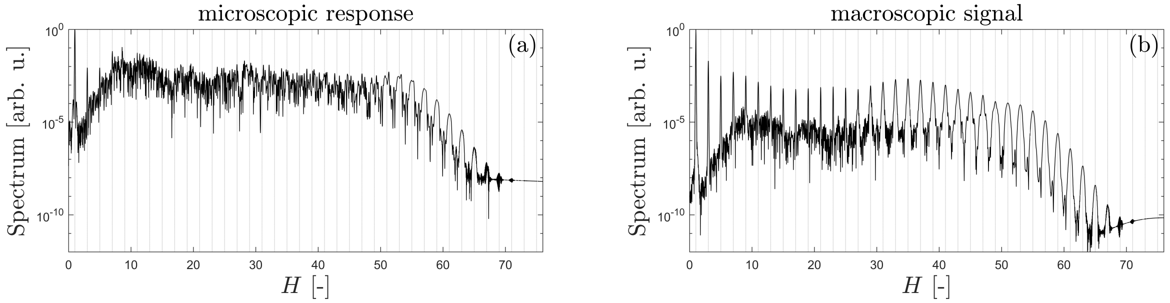

Fig. 1.2: The example of a spectrum retrieved from a numerical simulation of HHG in neon for the intensity corresponding to cutoff starting by the 49th harmonic in this case. The ionisation potential, $I_P \approx 25.5$ eV, which lies between the 13th and 15th harmonic in this case. (a) shows the spectrum from a single atom, while (b) shows a macroscopic spectrum in a far-field region from a radiating plane of the microscopic emitters from a Gaussian beam. (The microscopic response (a) is computed by 1D-TDSE described in Section 7.5 while (b) is a far-field distribution given as a weighted coherent sum of the emitters in a radiating plane. See Section 5.2 for a detailed discussion of the conditions and used methods to compute the spectra.)

U_p is the ponderomotive energy of the field and is proportional to the intensity of the field I and inversely proportional to its squared fundamental frequency ω^2. Note that the numerical value of the pre-factor $2e^2/(c\varepsilon_0 m_e)$ vanishes in the atomic units.

Figure 1.2(b) presents the spectrum of the macroscopic signal. For a basic picture, we may consider it as a coherent sum of many microscopic emitters. A notable feature is that this spectrum is much more regular with well-defined odd-harmonic orders compared to the more ”chaotic” profile in the plateau of the microscopic response. It means that, from the microscopic viewpoint, there are more incoherent processes. Generally, these effects may come from the interferences of multiple cycles that differs from each other in the case of an enveloped laser pulse. Since the macroscopic field is a sum of the elementary emitters, only coherent components prevail leading to more regular spectrum as depicted in Fig. 1.2(b). In this sense, the difference of these spectra is an example of the macroscopic build-up of HHG.[1] For the instant, this provides us the difference between the spectrum of a single microscopic emitter, which corresponds to the local field, and the filtered spectrum in the far-field.

Complementary to frequency, the XUV field is characterised in time. The components of the spectrum are ”mode-locked”, in the sense that the three-step model is repeated every half-cycle. As a consequence, the process leads to well-defined attosecond pulses of XUV radiation. (A detailed

---

[1] To be rigorous, there is a clarification of some terms. The terms microscopic and macroscopic are related to the origin of a phenomenon: originating from the single-atomic response or by the collective contribution of many atoms, respectively. In experiments, XUV is frequently characterised in ”far-field” region defined by the applicability of the Fraunhofer diffraction (see Appendix D). In the sense that ”near-field” is taken as the opposite of ”far-field”, it still contains macroscopic effects. The distinctions of various regions is related to different leading terms contributing to the signal, see Sections 9.1 and 9.2 of [118]. In the limit case being at the position of a single microscopic emitter, the field and the microscopic response are linked, this is discussed more formally in Section 5.1.

study of these effects is the subject of Section 5.2.8.) This typical profile is the so-called attosecond pulse train.

We conclude this section with a remark about the harmonic orders we observe in the spectrum. We use a driving field with a single dominant frequency (single-colour field) for all the examples we study in detail in this work. This together with the spherical symmetry of atomic targets leads to the production of odd harmonics in the spectrum. The spectral properties are changed if some of the symmetries is broken. It leads, for instant, to: i) An XUV supercontinuum is generated if this process is limited to happen only once, see [119] and references therein. ii) Even harmonic orders appears for multi-colour fields, for example [14]. iii) The response differs if there is an asymmetry in space which may be caused by chiral molecules or even by dissociating symmetric molecules in some circumstances [120].

1.1.3 Ionisation

Ionisation within the quantum description of HHG is an important intermediate step forming the 3-step model. There is not much of interest in the electrons that recombine. However, they may contribute significantly to other processes. Namely, they form a low-density plasma, which is important for the propagation of the driving laser. We thus need to estimate the probability of ionisation to obtain the plasma density.

Here, we stick with a pragmatic intuitive picture. Quantum mechanics provide the probability density, $\varrho_e(\boldsymbol{r},t)$, of finding the electron at a given position $\boldsymbol{r}$. We define the ionisation as the probability of finding the electron outside the atom $P_{\text{ion}} = 1 - \int_{V_{\text{atom}}} \varrho_e \, \mathrm{d}^3 x$. To find the evolution in time, a dynamical description is needed. A desired outcome is a rate equation, $\partial_t P_{\text{ion}} = -\Gamma(|\boldsymbol{\mathcal{E}}|) P_{\text{ion}}$, that provides a way to compute the plasma density based only on the time evolution of the electric field $\boldsymbol{\mathcal{E}}(t)$.

1.2 Driving laser: propagation in a non-linear medium

The macroscopic HHG-field is given by the collective contribution of all atoms of the generating medium. As the intensity of the laser must be high enough to induce highly non-linear HHG, other non-linear effects are naturally present as well.[2] These effects significantly reshape the driving pulse. Here, we provide some simple models to get the insight in the principal non-linear effects in our case. We separate two characteristic directions of the problem: along the propagation axis ($\parallel$, *longitudinal*) and transversally to the propagation ($\perp$, *transversal*).

---

[2] Generally, a pulse in time is dispersed already due to the linear effects as estimated in the introductory to the wave propagation in Chapter 7.9 of [118].

1.2.1 Transversal effects

A good insight into the impact of the transversal distribution of radiation comes from geometrical optics and the study of lenses. We will show that the non-linear effects of our interest may be explained using them as an analogy.

Converging lenses are characterised by the optical path being the largest near the beam axis and decreasing with the radius. This profile is reversed for a diverging lens. The optical path is proportional to the real physical path scaled by the refractive index n of the medium. As a result, the phase of the light differs in the transversal dimension. This determines the change of the wavefront of the light. Since the modification of the wavefront is the key physical mechanism, it allows to use equivalently mirrors or other devices instead of the lenses to reach the same effect.

The pivoting ideas of the non-linear propagation can be fairly described using an analogy with the aforementioned lensing properties. The difference is that the lensing properties of the medium are created by the pulse itself due to the non-linear response. There are two effects of our interest: the Kerr effects and plasma defocusing.

We start with the Kerr effect. The related refractive index is $n_{\text{Kerr}} = 1 + n_2 I$, where n_2 is a non-linear refractive index depending on the material (the type of gas in our case) and I the intensity of the field (Chapter 4 of [36] and [121]). Because $I(r)$ decreases with the radius for a usual beam and $n_2 > 0$, it naturally creates a converging lens.

Next, we move to the plasma defocusing. The plasma is characterised by the refractive index $n_{\text{plasma}} = \sqrt{1 - (\omega_p/\omega)^2}$, where the squared electronic plasma frequency, ω_p^2, is proportional to the density of free electrons ϱ_e (Section 7.5.D of [118]). As the free electrons are created by the pulse itself, we see a similar behaviour as for the Kerr effect but with opposite sign of the modification of n: the optical path is shorter close to the optical axis, where the electron density is higher. As a result, a diverging lens is created. Because ionisation evolves in time, we have $n_{\text{plasma}} = n_{\text{plasma}}(t)$; and the associated focal length evolves in time as well.

A mathematical picture may be inferred from the non-linear Schrödinger equation, which can be derived to describe the evolution of the electric field $\mathcal{E}$ in the non-linear medium. Its simplified dimensionless form is

$$\mathbf{i}\partial_z \mathcal{E} = - \triangle_\perp \mathcal{E} - \alpha |\mathcal{E}|^2 \mathcal{E} + \beta \varrho_e \mathcal{E} \, , \tag{1.2}$$

$\triangle_\perp$ is the transverse Laplacian in the dimensions orthogonal to z. α and β are coefficients associated with the competing focusing Kerr effect, $\alpha|\mathcal{E}|^2\mathcal{E}$, and plasma defocusing, $\beta\varrho_e\mathcal{E}$. The plasma electron density ϱ_e is retrieved from a rate equation $\partial_t \varrho_e = \Gamma(|\mathcal{E}|)\varrho_e$, meaning that a complementary model of ionisation is needed as described in the preceding sections. The importance of this equation is that we can clearly see the two competing effects – Kerr effect and plasma generation – related to the beam focusing. By further inspection, these two effects are also non-trivially coupled due to the rate equation governing the factor $\beta\varrho_e$. Although basic roles of these two effects is seen directly from the equation (1.2), a quantitative analysis of the interplay requires a specific solution in given conditions.

1.2.2 Longitudinal effects

Next, we illustrate the longitudinal properties involved in the propagation. We limit this example to modelling the phase as this is substantial to the phase-matching that we will treat in Chapter 6. We initiate the model with a plane wave in vacuum,

$$\mathcal{E}(z,t) \propto \mathrm{e}^{-\mathbf{i}(\omega_0 t - k_0 z)} \,. \tag{1.3}$$

If the vacuum is replaced by a medium that induces a non-linear response, the phase accumulated due to the propagation, $k_0 z$, is modified by the optical path given by the refractive index above. It is convenient to use electric susceptibilities for various contributions to the optical index, as the resulting susceptibility is only their sum. The refractive index containing dispersion, plasma and the Kerr effect would be

$$n = \sqrt{1 + \chi_{\text{dispersion}} + \chi_{\text{plasma}} + \chi_{\text{Kerr}}} \,. \tag{1.4}$$

We recall that n is time-dependent because the Kerr effect follows the intensity profile and the plasma is generated throughout as the pulse propagates. There is still one contribution to the phase missing: the geometrical phase $\phi_G(z)$ related to the profile of the beam, which is a realistic description instead the plane wave. In the case of a Gaussian beam, it corresponds to the Gouy phase. We add this phase within the simplified longitudinal model. The final expression of the field is then

$$\mathcal{E}(z,t) \propto \mathrm{e}^{-\mathbf{i}\left(\omega_0 t - k_0 \int_0^z n(z',t)\,\mathrm{d}z' - \phi_G(z)\right)} \,, \tag{1.5}$$

for $z > 0$. Compared to (1.3), we note that the physical distance z is replaced by the optical path $\int_0^z n(z',t)\,\mathrm{d}z'$. We point out that the *absorption* of the field in the medium may be included in this model via the imaginary part of the refractive index (or, equivalently, imaginary part of electric susceptibilities).[3]

---

[3] An interesting point there is that we need to take into account the direction of the propagation in the integral, $z > 0$, to satisfy causality – only the part of the medium already travelled by the field affects its phase. This constraint allows to link absorption and dispersion in the medium by Kramers–Kronig relations (Section 1.7 of [36]), that are an application of the Sokhotski—Plemelj theorem connecting the real and imaginary parts of analytical electric susceptibilities.

1.2.3 Full picture: couplings

We have described the focusing of the beam leading to spatial shaping of a pulse and also the phase accumulated due to propagation. The goal of this work is to provide a full model accounting for all the effects at once. Although we have the key effects in the transversal and longitudinal directions, a comprehensive picture becomes demanding as they non-trivially couples with each other. Moreover, we have phenomenologically arrived to time-dependent refractive index. A natural variable of the refractive index is ω, the conjugate variable of time. It would be contradictory to have an explicit function of both these variables. In summary, the refractive index is a very useful quantity for having an insight of propagation, but not so useful to quantitative description: Basically, there are possible all mutual couplings of variables $(t, \boldsymbol{r})$ and their conjugates $(\omega, \boldsymbol{k})$. A way to resolve the couplings consistently is to use a direct solution of the Maxwell's field equations.

We show an example of the non-linear propagation in Fig. 1.3. The simulation is performed with a Gaussian profile (both in space and time) shown in (a), which is then propagated through a 15-mm long gas cell filled by Krypton at 50 mbar. The entrance peak intensity is approximately 1.6×10^{14} W/cm^2. (Note that the instantaneous intensity is used in the graphs, see Appendix B.2.) It clearly shows that the Gaussian profile is heavily distorted during the propagation. It also illustrates the formation of the off-axis ”wings” of the pulse. These are caused by the plasma defocusing occurring at the trailing edge of the pulse as mentioned above.

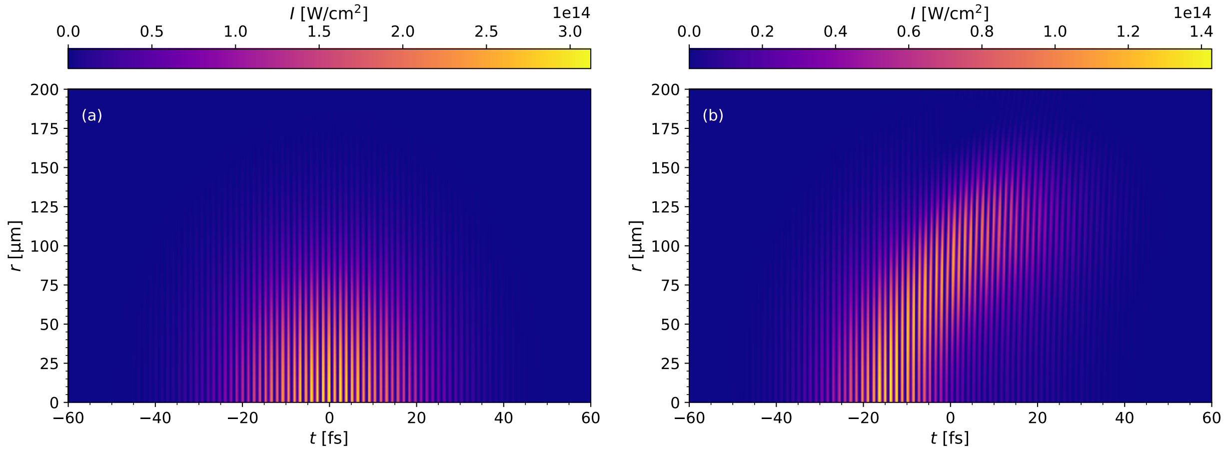

Fig. 1.3: An example of a distorted pulse due to the non-linear numerical propagation. (a) A Gaussian pulse both in time and space at the entry of a 15mm long gas cell filled by krypton at 50 mbar. (b) The pulse after the passage through the cell. (See Section 6.3.6 for a detailed discussion of the conditions.)

1.3 XUV field: Two emitters, Gaussian beams

In the previous sections, we have described the microscopic picture of a single atom in an external field and also of the macroscopic profile of the driving laser. Here, we present the macroscopic model of the XUV field based on simplified phenomenological description.

This study is also separated to the transversal and longitudinal effects similarly to the IR-field. This separation is also aligned to two of the main objectives of this work: the XUV wavefront control in thin targets (where transversal effects prevail), and the control of the phase-matching in long media (the longitudinal effects are dominant).

1.3.1 Longitudinal effects in XUV

We start with the longitudinal effects, our goal is to get a simple insight into phase-matching, which is given by the coherent sum of elementary emitters along the propagation axis. This model lacks the effects due to the intensity profile of the driving field as well as due to the exact propagation of the XUV field from the Maxwell's equations.

Let us start with two on-axis emitters placed in z_1 and z_2 and ordered as $z_1 < z_2$. For the sake of simplicity, the fields generated by both emitters are described by plane waves with the same amplitudes. The XUV field at z_1 is induced by the driving field. Using the propagation in a dispersive medium (1.5), one has

$$\mathcal{E}_{\mathrm{IR}}\big|_{z_1} \propto \mathrm{e}^{-\mathbf{i}\left(\omega_0 t - k_0 \int_0^{z_1} n_{\mathrm{IR}}(\zeta)\,\mathrm{d}\zeta - \phi_G(z_1)\right)}\,, \tag{1.6}$$

$$\mathcal{E}^{(1)}_{\mathrm{XUV}}\Big|_{z_1} \propto \mathrm{e}^{-\mathbf{i}\left(q\omega_0 t - q\left(k_0 \int_0^{z_1} n_{\mathrm{IR}}(\zeta)\,\mathrm{d}\zeta + \phi_G(z_1)\right) - \varphi_{\mathrm{XUV}}(z_1)\right)}\,, \tag{1.7}$$

where $\mathcal{E}_{\mathrm{XUV}}$ describes the XUV field corresponding to the qth harmonic with the carrying frequency $\omega_q = q\omega_0$. The refractive index contains susceptibilities of various processes as given by (1.4).Furthermore, there is an extra *intrinsic* phase of the XUV-generation process, φ_{XUV}, in (1.7). This phase depends on the generation conditions at z_1, and its quantum-mechanical origin of will be explained in Section 2.4.

Now, let us investigate the XUV-field at the point z_2. The IR- and generated XUV-field are given only by changing z_1 to z_2. The XUV-field propagated from the first emitter is $\mathcal{E}^{(1)}_{\mathrm{XUV}}\Big|_{z_2} = \mathcal{E}^{(1)}_{\mathrm{XUV}}\Big|_{z_1} \mathrm{e}^{\mathbf{i}k_q \int_{z_1}^{z_2} n_q(\zeta)\,\mathrm{d}\zeta}$. The complete XUV-field in z_2 is given by the sum of both contributions,[4]

$$\mathcal{E}_{\mathrm{XUV}}\big|_{z_2} = \mathcal{E}^{(1)}_{\mathrm{XUV}}\Big|_{z_2} + \mathcal{E}^{(2)}_{\mathrm{XUV}}\Big|_{z_2} \propto \sqrt{2\left(1 + \cos\left(\Phi\right)\right)}\,, \tag{1.8a}$$

---

[4] The formulae $z = |z|\mathrm{e}^{\mathbf{i}\,\mathrm{Arg}(z)}$ and $\left|\mathrm{e}^{\mathbf{i}a} + \mathrm{e}^{\mathbf{i}b}\right|^2 = 2(1 + \cos(a - b))$ have been applied.

$$\Phi = qk_0 \left(\int_{z_1}^{z_2} (n_{\mathrm{IR}}(\zeta) - n_q(\zeta)) \, \mathrm{d}\zeta \right) + q\Delta\phi_G - \Delta\varphi_{\mathrm{XUV}} \,, \tag{1.8b}$$

where $\Delta f = f(z_2) - f(z_1)$. The phase Φ plays a crucial role as it characterises the constructiveness of the summed signal of the two emitters. The signal is amplified once their phases match. This is the origin of the term *phase-matching*. In an ideal case, the emitters add perfectly, $\Phi = 0$.

We have neglected the absorption included by the imaginary part of n_q, it means that our Φ is real. The absorption gives an inevitable attenuation of the signal proportional to the density of the medium. The absorption thus gives an upper bound of the XUV signal in long media and cannot be controlled compared to phase-matching. The neglect of absorption does not affect the qualitative picture of the phase-matching and we will discuss the quantitative description later (Section 6.3.3).

The signal is maximally amplified in the perfect case $\Phi = 0$. Being less strict, the XUV-yield is increased if $\Phi \in \left]-\frac{\pi}{2}, \frac{\pi}{2}\right[$. Inspecting the constructiveness locally using an infinitesimal Δz, the terms in Φ can be approximated using $\Delta f \approx f'(z)\Delta z$.[5] In this case, we can also assume $f'(z) \approx f'(z_1) \approx f'(z_2)$. Using the expression (1.8b) for Φ, we can assign the phase contribution of various effects:

$$\Phi \approx \Delta k_q \Delta z \,, \qquad \Delta k_q = \Delta k_{\mathrm{medium}} + \Delta k_{\mathrm{geom.}} + \Delta k_{\mathrm{atom}} \,, \tag{1.9}$$

where $\Delta k_{\mathrm{medium}} = qk_0(n_{\mathrm{IR}} - n_q)$ and $\Delta k_{\mathrm{geom.}} = q\partial_z\phi_G(z)$, $\Delta k_{\mathrm{atom}} = -\partial_z\varphi_{\mathrm{XUV}}(z)$.

Although wavenumber mismatch $\Delta k_q = \partial_z\Phi$ is a local quantity, it may give a good estimate of the constructiveness of the contributions in larger volume if it is not fast-changing. The measure is then the *coherence length*:

$$L_{\mathrm{coh}} = \frac{\pi}{|\Delta k_q|} \,. \tag{1.10}$$

It gives the effective length where all emitters add up constructively so that the signal is maximised.

To conclude this part, we use this simple concept to clarify one important aspect of phase-matching. The underlying mechanism is the interference, which means that the total signal is not enhanced or amplified.[6] The signal is only optimised by the constructiveness along the propagation axis. A precise definition is that a phase-matched generation means that the signal is primarily optimised along the optical axis.

---

[5] The range of validity of this approximation always depends on conditions of a given generation scheme. Generally, the stronger non-linear response of the medium is, the smaller is the range the approximation is valid.

[6] The only case for which there may be a quantitative difference in the energy transferred to the XUV field is a non-negligible contribution of the XUV field in the generation process. Because the driving force of HHG is the driving laser, which is stronger by several orders than the generated field, this assumption is satisfied. A possibility to break the assumption is a resonance adjusted to a specific XUV wavelength.

1.3.2 Transversal effects in XUV

We used the example of two emitters to show the longitudinal aspect of HHG phase matching, we use a different picture for the transversal counterpart.

Let us take only a single radiating plane. We model both driving and XUV fields as Gaussian beams. A Gaussian beam is fully defined from its radius $w(z)$ and curvature $1/R(z)$ at any point z along its propagation. The radial intensity profile of the Gaussian beam is then $I(z,\rho) \propto \exp\left(-2\left(\rho/w(z)\right)^2\right)$. As HHG is a highly non-linear process, it emphasises the radial profile and reduces the radius of the generated field. We can see the scaling from

$$I^{q_{\mathrm{eff}}}(z,\rho) \propto \mathrm{e}^{-2\frac{\rho^2}{\left(\frac{w(z)}{\sqrt{q_{\mathrm{eff}}}}\right)^2}},$$

where q_{eff} is an effective non-linear parameter – the response is characterised as q_{eff}-th power of the incident intensity, the quantitative analysis will be done in the section 2.4 –, we recognise $w(z)/\sqrt{q_{\mathrm{eff}}}$ as the radius of the generated beam. Furthermore, the radius of curvature of the driving beam is imprinted in the generated field. However, this is not the only contribution. The phase of an elementary emitter, φ_{XUV}, depends on the local intensity of the driving field. As the intensity varies with the radial profile, we get an additional profile of the radial phase that gives an additional curvature contribution that sums up with the imprinted curvature. The situation is analogical to that we discussed for the non-linear transversal effects of the driving laser – the generation process may be seen as an optical element manipulating the phase.

1.3.3 Full XUV profile

We have seen that both longitudinal and transversal XUV profiles are determined by the phase and intensity given by the discussed models. In this light, the transversal profile is described as off-axis phase-matching, which leads to the interferences in spatially resolved harmonic spectra.

The longitudinal and transversal models already contain the main mechanisms of the two configurations that we will study in detail: the control of the divergence of XUV beams in thin media and the phase matching in long pre-ionised media. The control of the divergence will be obtained by manipulating the wavefront by positioning the target with respect to the driving beam, which drives the curvature inherited from the driving beam. In the second case, the pre-ionisation allows us to externally control the refractive index of the medium via the electric susceptibility χ_{plasma} using (1.4). It allows us to optimise the signal by reaching favourable phase-matching conditions given by (1.8b).

In conclusion, it may enough to consider only one of the mechanisms in the cases it dominates.

Particularly, the longitudinal effects are negligible for thin targets. However, both dimensions are required to resolve fine structures in long media as both aspects are present.

1.4 General framework of the multiscale model

We have introduced the main physical aspects of HHG together with simple examples, the next step to provide a quantitative model of all the processes is the mathematisation and numerical treatment. We continue with the physics and mathematical description in this part, while the details of all the numerical models are a subject of Part III of this thesis.

We start the description with the Maxwell's equations

$$\operatorname{div}\boldsymbol{\mathcal{E}} = \frac{\varrho_Q}{\varepsilon_0}\,, \qquad \operatorname{div}\boldsymbol{B} = 0\,, \tag{1.11a}$$

$$\operatorname{rot}\boldsymbol{\mathcal{E}} = -\frac{\partial \boldsymbol{B}}{\partial t}\,, \qquad \operatorname{rot}\boldsymbol{B} = \mu_0\boldsymbol{j}_Q + \frac{1}{c^2}\frac{\partial \boldsymbol{\mathcal{E}}}{\partial t}\,. \tag{1.11b}$$

These equations are completely general with microscopic charge and current densities ϱ_Q and $\boldsymbol{j}_Q$, respectively. Combining the equations together, one obtains a wave equation[7]

$$\Box\boldsymbol{\mathcal{E}} = -\mu_0\frac{\partial \boldsymbol{j}_Q}{\partial t} - \frac{1}{\varepsilon_0}\operatorname{grad}\varrho_Q\,, \tag{1.12a}$$

We explain later why only the treatment of the electric field is sufficient.

Now, we need to specify a way to compute the densities. Looking at bookshelves of a university library, we look what is on our menu. There are equations of classical or relativistic mechanics coming from the Lorentz force. Continuing the offer, we find the Schrödinger equation for non-relativistic quantum mechanics or Dirac equation for a full quantum and relativistic treatment. For being accurate on the atomic level; we need, for sure, quantum theory. The Dirac equation would do the job well, but once we need to find a numerical solution many times: at every point of the macroscopic interaction region, it will be very expensive and difficult to consume.[8] We pick then the Schrödinger equation, its single-body form reads

$$\mathbf{i}\hbar\partial_t\left|\psi\right\rangle = H(t)\left|\psi\right\rangle\,. \tag{1.12b}$$

The Hamiltonian, $H(t)$, specifies the model of the microscopic target interacting with the external

---

[7] The d'Alambert operator is given by $\Box = \partial_{tt}/c^2 - \bigtriangledown$.

[8] The Dirac equation is mentioned because it would be a natural choice from the theoretical viewpoint: there would be no need to care about some approximations provided by the non-relativistic theory. As we, unfortunately, do not know a computationally cheap way to implement it, we would need to justify that the Schrödinger equation is satisfactory in the next chapter.

field $\boldsymbol{\mathcal{E}}$. However, a vector potential $\boldsymbol{A}$ corresponding to $\boldsymbol{\mathcal{E}}$ is more convenient in quantum mechanics because it is a natural variable of Hamiltonian and Lagrangian formulation [122, 123, 124]. The charge and current densities are, respectively,[9]

$$\varrho_Q(\boldsymbol{x},t) = Q|\psi(\boldsymbol{x},t)|^2\,, \qquad \boldsymbol{j}_Q(\boldsymbol{x},t) = \frac{Q}{m}\,\mathsf{Re}\,\left(\psi^*(\boldsymbol{x},t)(\boldsymbol{p}-Q\boldsymbol{A}(\boldsymbol{x},t))\psi(\boldsymbol{x},t)\right)\,, \tag{1.12c}$$

where Q and m stand for respectively the charge and the mass of the particle described by H. Generally, the introduced microscopic form of the equations (1.11) and (1.12a) is valid on all the scales and they would provide an exact description while considering *every* atom of the medium. However as already mentioned, taking independently all the atoms is computationally impossible; and our final model treats the medium as continuum by averaging over the microscopic volumes [125]. This procedure is detailed in Section 4.1.1; particularly, the current density scales with the gas density (4.3).

The equations enlisted under (1.12) are basically all we need to resolve. There is a clear loop-scheme where field equations drive the motion of charged matter, that creates sources of the field equations. This model is suitable for a numerical implementation; however, an interested reader may argue about the consistency of the model as we link two physical theories obeying different symmetries: Lorentzian for the Maxwell's equations and Galilean for quantum mechanics. We show in Appendix I how they originate from one self-consistent theory as its limit cases.

We keep that motivation in mind and we dive into the world on microscopic scale and investigate single-microscopic target interacting with an external field.

---

[9] See Eq. (11.22) of [124] for the derivation of this invariant source term.

Part I

PHYSICS OF HHG: MICROSCOPIC SCALE

2. DESCRIPTION OF A SINGLE ATOMIC SYSTEM

In this chapter we present how to compute practically the source term of the field at the right-hand side (RHS) of (1.12a) given by (1.12c). Together with this straight advancement to the macroscopic model, this chapter creates the framework for all the other microscopic chapters of this part of the thesis. At the end of this chapter, we also present a simplified model to compute the dipole based on the Strong-field approximation.

This chapter starts with the assumptions leading to the description of a single microscopic system in Section 2.1. This formulation allows to directly find the wavefunction and subsequent current needed for the macroscopic model. This is in principle everything we need for the macroscopic model. However, a more detailed analysis is crucial for understanding emerging physics and related concepts. We discuss the role of the gauges in Section 2.2. The source term and its more suitable form for numerics is derived in Section 2.3. Finally, the *Strong-Field Approximation*, which allows to find a simplified source term in a computationally cheaper way, is presented in Section 2.4; this section was originally published in [126].

2.1 General context and approximations

The first step is to construct the Hamiltonian that will be used in the Schrödinger equation. Complete description of a medium consisting of many atoms, each with several electrons, is practically impossible; we thus use approximations allowing their numerical implementation with keeping the dominant physics. We list the assumptions and approximations here:

1. The density of the gas is low, so we neglect the interaction between different atoms/molecules of the medium. We treat the response from one microscopic system only at each point of the medium (see also Section 4.1.1 describing the construction of the link with the macroscopic scale in more detail). In practice, it means that the neighbouring atoms in the medium are uncorrelated.[1]

---

[1] A basic justification of this assumption may be given by comparing the ideal gas law, $pV_m = RT$, with its first correction given by the Van der Waals equation, $(p + a/V_m^2)(V_m - b) = RT$; where p is the pressure of the gas, V_m the molar volume, $R \approx 8.314$ the universal gas constant, T temperature, and a and b the empiric Van der Weels constants of the given gas. We now infer the validity of the ideal gas law, i.e.when there is no interaction of the atoms. When these laws starts to slightly deviate, we may assume the equality of the molar volumes V_m in the first order of the

2. The intensity typically used for HHG stays within the non-relativistic regime. We thus use quantum-mechanical non-relativistic description.[2]
3. Targets used for HHG are multi-electronic atoms or molecules. A complete solution would require to include all the electrons. Since the dimensionality of the respective space grows with the number of electrons, N, as $3N$, it is not practically computable today by a direct N-body Schrödinger equation.[3] Since most of the physics is governed only by the valence electron, we can work within the Single-active-electron approximation (SAEA). We later discuss in detail even stronger approximation using a one-dimensional atom.
4. We neglect spatial variation of the external field due to the macroscopic beam profile (i.e. due to the radial profile of intensity). The scale of this profile is much larger than the dynamics within a single microscopic system.[4]
5. We also neglect the spatial variation of the field on the scale compared to the wavelength λ of the external field.[5] This together with the previous point gives the so-called *dipole approximation*. It is expressed either as $\boldsymbol{A}(\boldsymbol{x},t) \approx \boldsymbol{A}(\boldsymbol{x}_0,t)$ using the vector potential or $\boldsymbol{\mathcal{E}}(\boldsymbol{x},t) \approx \boldsymbol{\mathcal{E}}(\boldsymbol{x}_0,t)$ and $\boldsymbol{B} \approx 0$ when using the electric and magnetic field (see also the discussion on gauges in the following section). The spatial coordinate $\boldsymbol{x}_0$ denotes the macroscopic position of the microscopic system in the medium and does not act as a variable within the

---

expansion. The difference is then obtained by comparing the universal gas constant with its counterpart from the Van der Waals law. The correction is

$$\tilde{R} = R\left(1 + \frac{ap}{R^2T^2}\right)\left(1 - \frac{pb}{RT}\right) .$$

We use an ambient temperature $T = 300$ K and Van der Waals constants for xenon [127] as an upper bound for rare gases, $a \approx 0.43\ \mathrm{Pa}\cdot\mathrm{m}^6/\mathrm{mol}^2$, $b \approx 56 \times 10^{-6}\ \mathrm{m}^3/\mathrm{mol}$, to find the difference. The correction is below 0.5 % for atmospheric pressure. The corrections for other gases are smaller by orders of magnitude. However, these values probably still overestimate the validity of the approach as the femtosecond scale is short compared to the interatomic processes in gases. Moreover, the collisions due to thermodynamic effects are random. Thus, even if some of the atoms are colliding, it does not contribute coherently and may not affect the macroscopic signal (compare with Fig. 1.2).

[2] Generally, relativistic intensities are characterised by the acceleration of the electrons in along the direction of the laser. This efficiently prevents the recombination in the three-step model. One of the tasks to implement relativistic HHG from gases would be then to compensate this shift [128]. However, another complication of high intensities is the fast depletion of the ground state due to ionisation, which also limits the generation.

[3] See for example [129] discussing the Time-Dependent Density-Functional Theory, which is a theory developed to describe the density of many-electronic system including their quantum-mechanical nature.

[4] The spatial variation of the beam on, typically, the micrometric size is orders of magnitude higher than atomic scales. However, in the physics of free electrons and plasma, this plays a crucial role inducing the ponderomotive force $F = -\operatorname{grad} U_p$.

[5] Considering the harmonic part of the field, it means $\cos(\omega_0 t - k_z z) \approx \cos(\omega_0 t)$ for the values of z from the atomic range. Wavelength of an IR-field is of micrometric scale while atomic sizes are picometric. This approximation thus remains valid even for the nanometric scale of external fields, i.e., to describe the interaction with the XUV field up to extreme short wavelengths. Expressing the wavenumber as $k_z = 2\pi/\lambda = \omega_0/c = 2\pi/(T_0 c)$, the physical insight in the dipole approximation may be then given by fully equivalent pictures of spatial variations or frequency components or characteristics times neglected due to the approximation.

microscopic problem. Neglecting the magnetic field is further related with the non-relativistic treatment as its role becomes also important for relativistic electron velocities.[6]

6. We also neglect all spin effects and possible related spin-orbit couplings. This is consistent with the fact that we neglect the magnetic field as it provides their interaction term.[7]
7. Last, the field is treated classically, and this is usually justified because the typical energy of a driving pulse of the order of 1 mJ corresponds to 10^{11} photons at the wavelength of 800 nm. Proposed corrections due to the quantum nature of the light, for both the IR driver and the generated harmonic field, are in [135].

Summarising these points into mathematical description, we find the Hamiltonian

$$H = \frac{(\boldsymbol{p}+\boldsymbol{A})^2}{2} - \varphi + V\,. \tag{2.1}$$

In all the studied cases, it will be spherically symmetric, $V = V(r)$, and all the other electrons except the valence one would cause only a screening of the ionic core. We can express it (in 3 dimensions) as:

$$V(r) = -\frac{1}{r} + W(r)\,, \tag{2.2}$$

with W being a short-range screening potential.[8] The screening accounts for the effects of the remaining $(N-1)$ electrons included in V within the SAEA.

For this Hamiltonian, we can just put it in a numerical solver of the respective Schrödinger equation (1.12b) and obtain the source terms we need for the coupled model. Before we leave the rest of the work for the numerical solver, we discuss several phenomena laying within the microscopic part of the model in the rest of this chapter and also in the following chapter.

2.2 Length and velocity gauges

Although the Hamiltonian (2.1) governs the dynamics uniquely, there is still a gauge degree of freedom in the four-potentials $A^\mu = (\varphi, \boldsymbol{A})$, keeping the same electric and magnetic fields. We recall that the gauge equivalence says that all the four-potential $(A')^\mu = A^\mu + \partial^\mu \Lambda$ are equivalent

---

[6] This limits also the intensities of the driving field. However, as large intensities lead to fast-ionisation or electron displacements, it efficiently prevent the recombination and the high-harmonic generation process itself.

[7] We see that all the last two points are related to ”magnetic” effects as they enters the Hamiltonian by parts related to either spin or (rot $\boldsymbol{A}$)-effects. We can add also to the discussion the effects related to the coupling of more particles from the point 3. In some circumstances, these effects may be of the cutting edge to be the first correction of the physics we are using. There are some examples of works treating them in detail: two-electron physics [130], spin-orbit coupling [131], non-dipole terms [132, 133, 134].

[8] A precise definition of the short-range potential is that it decreases faster than $1/r$ for $r \to +\infty$.

for Λ being an arbitrary function of x^μ.[9] There are several reasons to discuss the gauges in more detail. First, even if all the gauges are equivalent, they differ in practical implementation and a suitable choice may work better from the numerical viewpoint. Second, the related gauge degree of freedom must be contained in our thinking and interpreting of the physics on the microscopic scale: All the results and interpretations must be gauge invariant.

We start with the *Lorenz gauge* for the laser field. It means $\operatorname{div}\boldsymbol{A} = 0$ and $\varphi = 0$, this gauge is called *velocity gauge* in Atomic and Molecular Physics (AMP). We denote the corresponding vector potential $\boldsymbol{A}^V$. The Hamiltonian under these conditions reads

$$H^V = \frac{\left(\boldsymbol{p} + \boldsymbol{A}^V\right)^2}{2} + V\,. \tag{2.3}$$

A second popular gauge in AMP is the so-called *length gauge.* We proceed generally without considering the dipole approximation yet. We recall the relation with the electric field in the velocity gauge. As there is no charge density related with the external field, we can integrate the vector potential from the field:

$$\boldsymbol{A}^V(\boldsymbol{x},t) = \int_{-\infty}^{t} \boldsymbol{\mathcal{E}}(t',\boldsymbol{x})\,\mathrm{d}t'\,. \tag{2.4}$$

Next, we use a gauge transformation by

$$\Lambda(\boldsymbol{x},t) = \boldsymbol{x}\cdot\boldsymbol{A}^V(\boldsymbol{x},t)\,. \tag{2.5}$$

It directly gives the Hamiltonian in the length gauge:

$$H^L = \frac{\left(\boldsymbol{p} + \boldsymbol{A}^L\right)^2}{2} + V_C - \boldsymbol{x}\cdot\frac{\partial \boldsymbol{A}^V}{\partial t}\,. \tag{2.6}$$

We note there is still a non-vanishing vector potential $\boldsymbol{A}^L$ in this gauge, we can relate this expression to the fields:

$$\varphi^L(\boldsymbol{x},t) = \boldsymbol{x}\cdot\boldsymbol{\mathcal{E}}(\boldsymbol{x},t)\,,\quad \boldsymbol{A}^L(\boldsymbol{x},t) = (\boldsymbol{x}\cdot\triangledown)\int_{-\infty}^{t}\boldsymbol{\mathcal{E}}(t',\boldsymbol{x})\,\mathrm{d}t + \boldsymbol{x}\times\boldsymbol{B}(\boldsymbol{x},t) = (\boldsymbol{x}\times\triangledown)\times\boldsymbol{A}^V\,, \tag{2.7}$$

the ”rotational” ingredients of the last term suggest its relation with the magnetic field that is not described by the scalar potential. An insight from the length gauge is that an important part of the electric field is put out of the vector potential. Indeed, applying the dipole approximation, we

---

[9] Using the words of the group theories, all the equivalent configurations belongs to a single orbit of the group. The different configurations of the field are thus not any particular A^μ, but whole classes of equivalence.

get $\boldsymbol{A}^L \approx 0$, the approximated Hamiltonians in both gauges are

$$H_{\mathrm{A}}^V(t) = \frac{(\boldsymbol{p} + \boldsymbol{A}^V)^2}{2} + V\,, \tag{2.8a}$$

$$H_{\mathrm{A}}^L(t) = \frac{\boldsymbol{p}^2}{2} + V + \boldsymbol{x} \cdot \boldsymbol{\mathcal{E}}\,. \tag{2.8b}$$

where $\boldsymbol{A}^V$ and $\boldsymbol{\mathcal{E}}$ are only time-dependent, but not space-dependent. The advantage of the length gauge is that there is no need of numerical integration – introducing numerical errors – of the field in the case an analytic form is not available, which is exactly the case of the multiscale model in this work since the electric field is obtained by the Maxwell solver. Next, the length gauge is a logical starting point for studies using an adiabatically extended static field as done for the ionisation studies. However, both gauges are important as the velocity form is better suited for some numerical schemes (see Section 7.3.2).

2.3 Source term of HHG

We now focus on the source term needed in the wave equation (1.12a). The source is not the current density, but its time derivative. Because it provides the link with the macroscopic physics, we do not need the result with the atomic resolution: an averaging over the microscopic volume is sufficient. We use a trick to obtain this term directly by a single expected value from the wavefunction.

The starting point is the average value of the current in the dipole approximation[10]

$$\langle \boldsymbol{j} \rangle = \int \psi^* (\boldsymbol{p} - \boldsymbol{A}) \psi \, \mathrm{d}V = \langle \psi | \boldsymbol{p} | \psi \rangle - \boldsymbol{A}(t)\,, \tag{2.9}$$

where we used the Gauss theorem and $\langle \psi | \boldsymbol{A} | \psi \rangle = \boldsymbol{A}$ since $\boldsymbol{A}$ is not a function of $\boldsymbol{x}$. The second step is to apply the Ehrenfest theorem to obtain[11]

$$\frac{\partial \langle \boldsymbol{j} \rangle}{\partial t} = \frac{\partial \langle \boldsymbol{p} \rangle}{\partial t} - \frac{\partial \boldsymbol{A}(t)}{\partial t} = -\langle \psi | \bigtriangledown (V - \varphi) | \psi \rangle - \partial_t \boldsymbol{A} = -\langle \psi | \bigtriangledown V | \psi \rangle + \boldsymbol{\mathcal{E}}\,. \tag{2.10}$$

This is a key expression for implementation: One needs to compute only the average value of $\bigtriangledown V$. Because the gradient is computed analytically, it is a single-step numerical operation. In contrast, if we compute it step-by-step from the wavefunction, we compose numerical errors from 1) the

---

[10] There is no need to specify the gauge, as the current is gauge-invariant, we are not limited to velocity nor length gauge.

[11] We can easily see that this calculation is gauge-invariant obtaining the field $\boldsymbol{\mathcal{E}}$ either from $\boldsymbol{A}$ or from the scalar potential φ. Another interesting point that it also provides insight in the non-dipole corrections that would emerge from $\langle \psi | \boldsymbol{A} | \psi \rangle$, with space-dependent $\boldsymbol{A}$. The vector potential would then weight the spatial distribution given by the wavefunction.

differentiation to get the current, 2) averaging the current, 3) the differentiation of the averaged current with respect to time.

We use this expression also to get further insight in the response of atoms to external fields. We decompose the wavefunction into the bound and continuum part: $|\psi\rangle = |\psi_\mathrm{b}\rangle + |\psi_\mathrm{c}\rangle$, we show an invariant procedure to obtain such a projector in the next chapter. It gives

$$\frac{\partial\langle \boldsymbol{j}\rangle}{\partial t} = \underbrace{\langle\psi_\mathrm{b}| -\nabla V + \mathcal{E}|\psi_\mathrm{b}\rangle}_{\substack{\text{response of bounded electrons,}\\ \text{the index of refraction included}}} + \underbrace{2\,\mathsf{Re}\,\langle\psi_\mathrm{c}| -\nabla V + \mathcal{E}|\psi_\mathrm{b}\rangle}_{\text{HHG + ionisation}} + \underbrace{\langle\psi_\mathrm{c}|\mathcal{E}|\psi_\mathrm{c}\rangle}_{\text{free electrons}} - \underbrace{\langle\psi_\mathrm{c}|\nabla V|\psi_\mathrm{c}\rangle}_{\text{re-scattering}}\,. \tag{2.11}$$

This expression allows us to assign various terms to respective processes: *bound-bound transitions* are responsible for linear and non-linear optics below the ionisation threshold.[12] *bound-continuum transitions* are the essence of HHG physics as explained with the three-step model. *continuum-continuum transitions* contain two parts: 1) $\langle\psi_\mathrm{c}|\mathcal{E}|\psi_\mathrm{c}\rangle$ is the propagation of a free electron in the field. Considering that within the dipole approximation $\langle\psi_\mathrm{c}|\mathcal{E}|\psi_\mathrm{c}\rangle = \mathcal{E}\,\langle\psi_\mathrm{c}|\psi_\mathrm{c}\rangle$ and $\langle\psi_\mathrm{c}|\psi_\mathrm{c}\rangle$ is proportional to the plasma density per single atom, we have incidentally derived the plasma frequency from quantum physics. This treatment is strictly analogical (only by replacing the classical dynamics by its quantum counterpart) to the classical-textbook microscopic solution from Section 7.5.D of [118]. 2) $\langle\psi_\mathrm{c}|\nabla V|\psi_\mathrm{c}\rangle$ is the re-scattering of the electron on the ionic part, its high-frequency components are usually considered as corrections within the HHG process.

2.4 Strong-field approximation (SFA)

To conclude the methods for computing the desired source term, this section provides a computationally simpler alternative compared to the TDSE. Most of the content of this Section is adapted from [126], where more details and comments are provided. The principal idea of this approach is to use an Ansatz of the solution of the TDSE, $|\psi(t)\rangle$. The solution is assumed in the superposition of the ground state, $|\psi_g\rangle$, and plane waves, $|\boldsymbol{k}\rangle$.[13] The Ansatz then reads[14]

$$|\psi(t)\rangle = a(t)\,|\psi_g(t)\rangle + \int \mathrm{d}k^3 b(t,\boldsymbol{k})\,|\boldsymbol{k}\rangle\ , \tag{2.12}$$

where $b(t,\boldsymbol{k})$ is unknown function acting as continuous coefficients of the expansion; $a(t)$ describes the depletion of the ground state with the eigenenergy E_g due to ionisation and if applied, it is

---

[12] We note that the binding forces of the inner electrons are of comparable size. SAEA becomes then questionable for these particular processes.

[13] The plane wave with the momentum $\boldsymbol{k}$ is defined as $\langle \boldsymbol{r}\,|\,\boldsymbol{k}\rangle = (2\pi)^{-3/2}\exp(-\mathbf{i}\boldsymbol{k}\cdot\boldsymbol{r})$.

[14] In fact, this form is not gauge invariant because there is no unambiguous way to choose $|\psi_g\rangle$. We will return to this question in Section 3.1.6 after we have addressed the gauge invariance in detail in the precedent Sections of Chapter 3.

added from an additional model of the ionisation (we will discuss several approaches in Section 3.1). The result is obtained by inserting the ansatz directly into the Schrödinger equation. It turns out to be a differential equation for $b(t, \boldsymbol{k})$, with the solution

$$\begin{aligned} b(\boldsymbol{k}, t) &= -\mathbf{i} \int_{-\infty}^{t} \left(\boldsymbol{\mathcal{E}}(t) \cdot \langle \boldsymbol{q}(\boldsymbol{k}, t, t') \,|\, \boldsymbol{x} \,|\, \psi_g \rangle\right) \mathrm{e}^{-\mathbf{i}\left(\frac{\boldsymbol{q}^2(\boldsymbol{k},t,t'')}{2} - E_g\right) \mathrm{d}t''} \, \mathrm{d}t' \,, \\ \boldsymbol{q}(\boldsymbol{k}, t, t') &= \boldsymbol{k} + \boldsymbol{A}(t') - \boldsymbol{A}(t) \,. \end{aligned} \tag{2.13}$$

The source term of HHG is retrieved from the dipole $\boldsymbol{d}(t) = \langle \psi(t) | \boldsymbol{x} | \psi(t) \rangle$.[15] Using (2.11), we keep only the *bound-continuum* contributions. Expressing the dipole in the spectral domain, we have its final form

$$\tilde{\boldsymbol{d}}(\omega) = -\frac{\mathbf{i}}{\sqrt{2\pi}} \int_{-\infty}^{+\infty} \left(\int_0^t \mathrm{d}t' \int \mathrm{d}^3 k \, \left[\boldsymbol{\mathcal{E}}(t') \cdot \boldsymbol{\tau}(\boldsymbol{k} + \boldsymbol{A}(t')) \mathrm{e}^{\mathbf{i}\left(\omega t - \mathcal{S}(t', t, \boldsymbol{k})\right)} \right] \boldsymbol{\tau}^*(\boldsymbol{k} + \boldsymbol{A}(t)) \right) \mathrm{d}t + \text{c.c.} \,, \tag{2.14}$$

$$\mathcal{S}(t', t, \boldsymbol{k}) = \int_{t'}^{t} \left(\frac{(\boldsymbol{k} + \boldsymbol{A}(t''))^2}{2} - E_g \right) \mathrm{d}t'' \,, \qquad \boldsymbol{\tau}(\boldsymbol{k}) = \langle \boldsymbol{k} | \boldsymbol{x} | \psi_g \rangle \,.$$

This integral form of the dipole is suitable for Saddle point approximation. The transition dipole elements, $\boldsymbol{\tau}(\boldsymbol{k})$, give the transitions between the ground state and continuum states. If the continuum is approximated by the field-free eigenstates of the momentum, it is suitable to compute them from the p-representation:

$$\boldsymbol{\tau}(\boldsymbol{p}) = -\mathbf{i} \frac{\partial \psi_g(\boldsymbol{p})}{\partial \boldsymbol{p}} \,, \tag{2.15}$$

where $\psi_g(\boldsymbol{p})$ is the wavefunction of the ground state in the p-representation.

One possibility is to employ it only in the integration over k-space. This provides a fully quantum model of HHG. Practically, there is needed only one numerical integration over t' to get the dipole in the time domain,

$$\boldsymbol{d}(t) = -2 \,\mathsf{Re}\, \mathbf{i} \int_0^t \left(\boldsymbol{\mathcal{E}}(t') \cdot \boldsymbol{d}(\boldsymbol{k}_{t,t'}^{(\mathrm{sp})} + \boldsymbol{A}(t')) \left(\frac{-2\pi \mathbf{i}}{(t - t')} \right)^{\frac{3}{2}} \mathrm{e}^{-\mathbf{i}\mathcal{S}(t', t, \boldsymbol{k}_{t,t'}^{(\mathrm{sp})})} \right) \boldsymbol{d}^*(\boldsymbol{k}_{t,t'}^{(\mathrm{sp})} + \boldsymbol{A}(t)) \, \mathrm{d}t' \,, \tag{2.16}$$

where $\boldsymbol{k}_{t,t'}^{(\mathrm{sp})} = -\int_{t'}^{t} \boldsymbol{A}(t'') \, \mathrm{d}t'' / (t - t')$ gives the saddle point of the phase. The spectral dipole $\tilde{\boldsymbol{d}}(\omega)$ may be obtained by a fast FFT implementation.

Another possibility is to use Saddle-points in all the integrals, the resulting dipole is then

---

[15] Compared to the TDSE, the source term is there expressed by the dipole form. Its second derivative is needed to match $\partial_t \boldsymbol{j}$.

obtained only from a set of non-linear equations [136, 82],

$$\omega = \frac{(\boldsymbol{k}+\boldsymbol{A}(t_r))^2}{2} - E_g\,, \qquad E_g = \frac{(\boldsymbol{k}+\boldsymbol{A}(t_i))^2}{2}\,, \qquad \boldsymbol{k} = -\frac{\int_{t_i}^{t_r}\boldsymbol{A}(t'')\,\mathrm{d}t''}{(t_r-t_i)}\,, \tag{2.17}$$

for the unknowns t_i and t_r.[16] Substituting the solutions of (2.17) back to the expression of the dipole (2.14), the dipole reads

$$\tilde{\boldsymbol{d}}(\omega) \approx -\frac{\mathbf{i}}{\sqrt{2\pi}}\left(\frac{-2\pi\mathbf{i}}{\sqrt{\det\Phi''_\omega}}\right)^{\frac{5}{2}}\left[\boldsymbol{\mathcal{E}}(t_i)\cdot\boldsymbol{\tau}(\boldsymbol{k}^{(0)}+\boldsymbol{A}(t_i))\mathrm{e}^{\mathbf{i}\Phi_\omega(t_r,t_i,\boldsymbol{k}^{(0)})}\right]\boldsymbol{\tau}^*(\boldsymbol{k}^{(0)}+\boldsymbol{A}(t_r)) + \text{c.c.}\,, \tag{2.18}$$

$$\Phi_\omega(t',t,\boldsymbol{k}) = \omega t - \mathcal{S}(t',t,\boldsymbol{k})\,, \qquad (\Phi''_\omega)_{ij} = \left.\frac{\partial^2\Phi_\omega}{\partial\xi_i\partial\xi_j}\right|_{\xi_i^{(0)},\xi_j^{(0)}}\,,$$

where $\xi_k \in \{t, t', k_x, k_y, k_z\}$ and $\xi_k^{(0)}$ are respective solutions of (2.17). An important consequence is that (2.18) manifestly shows the *intrinsic phase* of the dipole, which principal contribution comes from $\Phi_\omega(t_r, t_i, \boldsymbol{k}^{(0)})$. See also [137] for more details on using this method for describing both ionisation and HHG for advanced configurations of the driving field and microscopic targets. In a simple case, the dipoles may be easily tabulated.[17] It then allows to create a computationally cheap module of the multiscale model, which is reduced into a table-lookup. The numerical approach we used to find (2.18) is explained in Section 7.8.

Finally, it turns out that the form of the dipole as a function of the amplitude of the driving field follows the same pattern for different harmonics in well-defined spectral regions of the plateau and the cutoff (Fig. 1.2). The dipole is then fitted as [138]

$$d(I_{\mathrm{IR}},\omega) \approx |I_{\mathrm{IR}}|^{\frac{q_{\mathrm{eff}}}{2}}\mathrm{e}^{-\mathbf{i}\alpha I_{\mathrm{IR}}}\,. \tag{2.19}$$

This is illustrated in Fig. 2.1. It also reveals the correspondence with the classical picture of long and short trajectories: There are two corresponding solutions in the plateau and they merge into a single solution in the cutoff. This classical picture is illustrated in Section 2.2 of [139]. Further analysis, which also provide methodology to retrieve α more precisely without the Saddle points in t and t' is in [140].

---

[16] A physical meaning is assigned to the equations. They represent, respectively, the recombination process at time t_r, the ionisation process at t_i and the conservation of the momentum, $\boldsymbol{p}$, during the excursion in the continuum [126]. However as $E_g < 0$, only a complex t_i may solve the second equation, it thus requires the extension of the problem into the complex plane.

[17] Formally, the set of equations (2.17) is given for a linearly polarised monochromatic plane wave. However, it can be easily extended to linearly polarised laser pulses with a well-defined central frequency until the envelope of the pulses is slowly varying; see the discussion in 7.8 for more details.

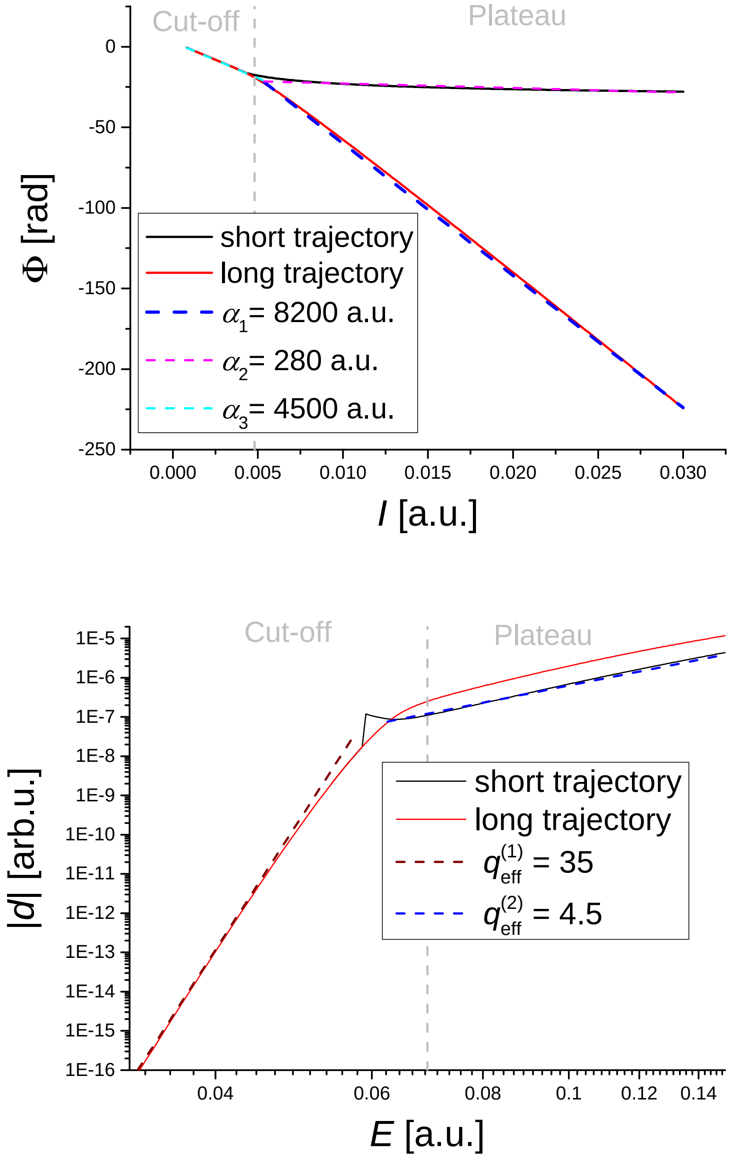

Fig. 2.1: The expression of the generated dipole in dependence on incident field amplitude. The left figure shows the phase Φ and its fits $\Phi \approx -\alpha I$, the right panel shows the the modulus. Estimated values of parameters are $\alpha_1 \approx 8200$ a.u., $\alpha_2 \approx 280$ a.u. and $\alpha_3 \approx 4500$ a.u.. This simulation has been done for H35 in neon ($I_P = 0.792$ a.u. with an incident 800-nm light). The intensity is given by $I = \mathcal{E}^2$ (in atomic units). This figure is reprinted from [126].

3. COMPREHENSIVE PICTURE OF IONISATION

This chapter provides a comprehensive physical analysis of the ionisation process. The main goal of the chapter is to arrive to a consistent definition of the probability of ionisation from the quantum-mechanical viewpoint and apply this definition to get a novel insight into traditional ionisation regimes, which are described in the multi-photon, tunnelling, or over-barrier terms.

One of the reasons why this problem is non-trivial is the gauge invariance. We recall its main ideas: A physical state is a class of equivalence of the corresponding gauge group. A well-defined physical observable cannot depend on the choice of a particular member of the class. It turns out that this makes it difficult to define ionisation during the interaction of the atom with an external electromagnetic field. In this chapter, we arrive to the Lagrangian formulation to find a meaningful energetic distribution of the particle in the field. For the sake of simplicity, we stay within the SAEA and treat only single-ionisation. However, some of the concepts may be generalised without difficulties into multiple-ionisation.

We use a history-based course in this chapter and first review the traditional pictures of ionisation in Section 3.1; it is followed by the unambiguous way to study ionisation in Section 3.2. Alternatively using a theoretical top-down approach, these two sections could be followed in the reversed order starting with the unambiguous definition and arriving to the traditional pictures as specific limit cases. Finally, both pictures are connected by a practical example investigating the traditional regimes in Section 3.3.

3.1 Practical approaches to ionisation

We start with recalling an intuitive picture of the ionisation: the atom is ionised if the active electron is outside of its volume. This gives the probability of ionisation as

$$P(t) = 1 - \int_{V_{\mathrm{atom}}} |\psi(t, \boldsymbol{x})|^2 \,\mathrm{d}^3 x \,. \tag{3.1}$$

This quantity is clearly gauge-invariant, it is then a good definition of an observable quantity.[1] However, the problematic parameter for a rigorous definition is V_{atom} we would like to interpret

---

[1] There is also a way to define this via a projector $P = \int_{\boldsymbol{x} \in V_{\mathrm{atom}}} |\boldsymbol{x}\rangle \langle \boldsymbol{x}|$, using again the Bochner integral.

it as the volume of the atom. But there is no clear definition of such a volume, so there is still ambiguity in the definition. Since quantum mechanics is a probabilistic theory, one may formalise the definition by using, for example, the idea of 68–95–99.7-rule[2] that may help to grasp an intuition about the physics. The intuition comes from the usual interpretation of processes in the x-space. Next, there is also a link with the projection onto the bound states. They are exponentially dumped. If the electron is outside of this region, we can say it is ionised for practical purposes with all the definitions in agreement. The only problematic part is when there is an electronic wavepacket passing through the atomic volume as, e.g., during re-scattering. In this case, the presence of the wavepacket remaining within V_{atom} is not a sufficient criterion to define it as bound.

3.1.1 Adiabatic external field

Using the volumetric definition of the ionisation, we move to practical computational methods. One of the main task is to resolve the time-dependent aspect of the ionisation. We start with a simple model: an atom in a static external field. The static case will be adiabatically extended to a dynamic case; it requires further assumption, namely,the time variations are slow compared to the electronic dynamics. (See the time scales within the ionisation process discussed in Section 3.1.2.) As we build this part of the work using bottom-up path, we discuss generalisations in Section 3.1.6.

The methods we start with share one notorious machinery of quantum mechanics: the perturbation theory. It is natural to use the external field as the perturbation. Usual convention for a 3-D Stark Hamiltonian of the system is

$$H_{\text{static}} = \frac{\boldsymbol{p}^2}{2} - \frac{1}{r} + \mathcal{E} z \,, \tag{3.2}$$

$\mathcal{E}$ is the ”small” parameter for the perturbative series. This result is afterwards extended to time-evolving fields using adiabatic approach. The important quantity is thus the so-called *ionization rate* Γ, it is defined as the probability of ionisation per unit of time. Since the field is static at the first step, the relevant Hamiltonian is the length gauge (2.8b). One then computes $\Gamma(\mathcal{E})$, the adiabatic extension assumes the validity of $\Gamma(t) = \Gamma(|\mathcal{E}(t)|)$. This quantity enables to establish a rate equation for the probability of ionization

$$\frac{\mathrm{d}P(t)}{\mathrm{d}t} = -\Gamma(t)P(t) \,, \quad \text{with } P(t \to -\infty) = 1. \tag{3.3}$$

The rate equation is a fundamental relation to link the microscopic and macroscopic physics. P is the probability of the single scrutinized system being ionised. If P is multiplied by the total number of atoms N, the number of free electrons is then $N_e = PN$. A different normalisation gives

---

[2] This well-known empirical rule is named after the σ–3σ deviations of the standard distribution.

the density of the plasma $\varrho_e = P\varrho$, where ϱ is the atomic density.

The ionisation rate is frequently averaged over the fast oscillations of the external field, $\bar{\Gamma}(t) = \langle\Gamma(t)\rangle_{T_0}$. This is usually done if the slowly varying envelope approximation is applicable, see the details of the propagation in Section 6.1.2. The averaging then reduces the number of required points per optical cycle (fast oscillations being removed).

Now, we present the common historical root of the methods and then we discuss two families of practically used methods related to different physical pictures.

Early historical approach

The idea to use quantum mechanics to treat ionization using static fields came early with the foundations of quantum mechanics at 1928, Oppenheimer [106] proposed to correct the perturbative series for the Stark effect and estimated the dipole transition matrix element from the bound to continuum state.

The need for practical quantitative calculations increased later with the development of laser technique generating optical fields strong enough to ionize atoms. It led then to the development of various quantitative models, which we introduce in the following sections. Due to the high interest for applications, the comparison and calibration with experiments has been exhaustively studied [141, 142, 143, 144].

Probability flux of electron leaving the atom

The first family of methods uses the picture of the volumetric definition of the ionization. The idea is to take (3.1) as the definition of ionisation P, and use the continuity equation in the integral form. One then estimate the probability current flowing through the boundary ∂V_{atom}. An analytic estimation of the current from WKB approximation of bound and continuum state comes from Smirnov and Chibisov [107]. The ionisation rate turns to be the surface integral of the probability current flowing out of the atomic volume: $\Gamma = -\partial_t \int_{V_{\text{atom}}} |\psi(t, \boldsymbol{x})|^2 \, \mathrm{d}^3x = \int_{\partial V_{\text{atom}}} \boldsymbol{j} \, \mathrm{d}\boldsymbol{S}$. There is a large variety of improvements and studies based on this methods until nowadays, we recommend one of recent articles and references therein [145].

The calculations within the WKB approximation are rather technical [107]. There are the forms from, respectively, [146] and [147]:

$$\Gamma_{\text{TI}}(\mathcal{E}) = \frac{C_l^2}{2^{|m|}|m|!} \frac{(2l+1)(l+|m|)!}{2(l-|m|)!} \frac{1}{\kappa^{\frac{2Z_c}{\kappa}-1}} \left(\frac{2\kappa^3}{\mathcal{E}}\right)^{\frac{2Z_c}{\kappa}-|m|-1} \mathrm{e}^{-\frac{2\kappa^3}{3\mathcal{E}}} , \qquad \kappa = \sqrt{2I_P} , \tag{3.4a}$$

$$\Gamma_{\text{TIcorr}}(\mathcal{E}) = \Gamma_{\text{TI}}(\mathcal{E}) \mathrm{e}^{-\tilde{\alpha}\mathcal{E}} . \tag{3.4b}$$

l and m are quantum numbers of the valence orbital. Z_c, I_P, C_l and $\tilde{\alpha}$ are parameters of the model. ”TI” stands for the tunnel ionisation and ”TIcorr” takes into account the exponential correction factor. The idea behind this correction is that once the field is strong enough to fully suppress the barrier, there is no tunnelling necessary for the ionisation. In this regime, the assumed form from the WKB-approximation becomes inaccurate overestimating the rate [147]. From the practical point of view, the result of any of the techniques is a table $(\mathcal{E}, \Gamma(\mathcal{E}))$. Furthermore, $\Gamma(\mathcal{E})$ is usually an analytic function. The table can be used to compute the density of neutrals, ions and free electrons.

Complex-rotation method

The second family of methods relies on the spectral theory of non-Hermitian operators. It was first studied by Aguilar, Balslev and Combes for the decay of autoionised states [148, 149]. Its modification for Stark Hamiltonians was proposed by Ira Herbst [108, 150]. This method is called *complex rotation* because the class of the non-Hermitian operators comes from complex spatial coordinates (rotated in the complex plane). The rotated Hamiltonian is

$$\tilde{H}_\theta(r, \vartheta, \varphi) = H_{\mathrm{static}}(\mathrm{e}^{\mathbf{i}\theta} r, \vartheta, \varphi)\,, \tag{3.5}$$

where the arguments denotes the spherical coordinates, and θ is a free parameter. A curious feature is that the atomic term, $1/r$, is frequently a perturbation in the mathematical research as $\mathcal{E}z$ affects stronger the spectral properties of H_{static}. The key equation of the complex rotation is the eigenvalue problem of $\tilde{H}$. It turns out that the eigenvalues are complex, closely linked with the eigenvalues of H_{static}, and the bound eigenenergies are independent on the choice of θ. The key idea is then to write the evolution of the norm of the corresponding bound state

$$\|\psi_0(t + \Delta t)\| = \mathrm{e}^{2\Delta t\, \mathsf{Im}(E_0)}\, \|\psi_0(t)\|\ . \tag{3.6a}$$

We simply identify the ionization rate as

$$\Gamma = -2\,\mathsf{Im}(E_0)\,. \tag{3.6b}$$

(Note that $\Gamma = 0$ for the field-free case, $\mathcal{E} = 0$, [108, 150]. In the case of a numerical computation, the non-zero imaginary part of E_0 is then related to the numerical precision.)

A practical computation is usually done numerically by solving the eigenvalue of a finite-dimensional representation of the non-Hermitian Hamiltonian relying on the same orbit, in the means of the group of complex rotations, as the Hermitian realisation. Mathematically, there is also one complication of this numerical approach, Cerjan et. al [151] manifested that the fundamental difference between finite-dimensional and infinite-dimensional Hilbert spaces plays an important role in that case. There is involved a residual part of the spectrum that vanishes only in the infinite dimension. Such a property cannot be correctly included in a finite dimension![3] Despite these drawbacks, this method is shown to still estimate the ionisation rates accurately [152, 153]. Further details about mathematics behind the extension of quantum mechanics into the complex plane are discussed in Section 3.1.5.

3.1.2 Ionization regimes in an oscillating field

A rule of thumb [154] to divide the ionization mechanism is to use the so-called *Keldysh parameter* $\gamma = \sqrt{I_p/(2U_p)} = \sqrt{2I_p}/A_0$. There are three physical pictures based on the amplitude of the field together with the energy per photon characterised by the frequency of the field. Using the aforementioned WKB approach, Keldysh parameter is rewritten as $\gamma = 2\pi T_T/T_F$, where $T_T = \sqrt{2I_p}/\mathcal{E}_0$ is the tunnelling time in the words of WKB approach and T_F is the period of the oscillating field. This provides insight that tunnelling dominates, $\gamma < 1$, when the potential is suppressed long enough to allow the electron to escape. Another explanation is needed for $\gamma > 1$. We list three possibilities for usual explanations in Fig. 3.1.[4]

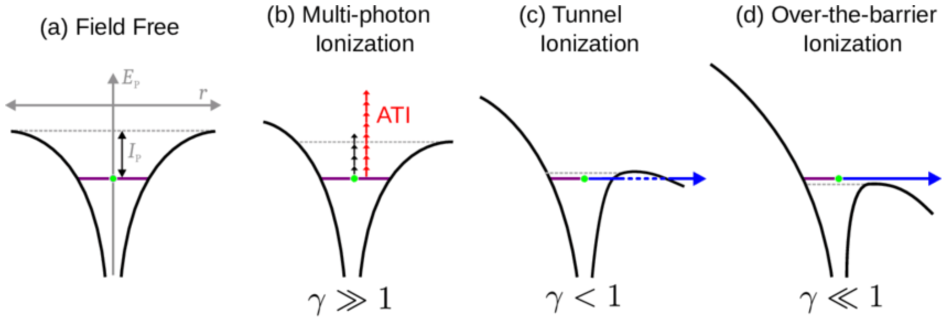

Fig. 3.1: The classical picture of the ionisation regimes by an optical field. (a) A sketch of the potential and its electronic ground states residing I_p below the continuum. (b) The multi-photon regime. The potential is only slightly distorted and the ionisation is explained that the electron gain the necessary energy to leave the potential by absorbing a sufficient number of photons to get in the continuum. (c) The tunnelling regime. The potential is significantly distorted and the electron may escape due to the quantum tunnel effect. (d) The electron may escape even classically. Used from [155] under the CC-BY licence.

---

[3] It is then a fundamental example, when a finite-dimensional Hilbert space can never describe correctly quantum-mechanical nature of infinite dimensional spaces. Another example is the canonical commutation relations.

[4] Note that the purpose of the distinction of the different regimes is to provide a basic picture of the underlying mechanisms. A detailed treatment is more complex, especially for $\gamma \sim 1$, and it will be discussed in detail in the rest of this chapter.

Multi-photon ionization (MPI), $\gamma > 1$

The potential of the atom is not suppressed by the external field enough for leading to tunnelling. The ionization energy for exiting the potential well is gained by absorbing many photons.

Tunnel ionization (TI), $\gamma \lesssim 1$

The Coulombic potential of the atom is significantly suppressed by the external field. The electron still cannot freely exit the atom, however, the classical barrier is weakened enough that the electron may exit atom by the tunnelling effect. This is the framework of the WKB approximation discussed earlier.

Over-barrier ionization (OBI), $\gamma \ll 1$

The Coulombic potential of the atom is fully suppressed by the external field. The electron exits the atom even classically. A simple criterion of this process is obtained by $-1/x_0 - \mathcal{E}x_0 = -E_0$, E_0 is the ground-state energy and x_0 the position of the maximum of the potential. This model represents that the ground-state energy (without considering the Stark shift) lies exactly at the top of the suppressed Coulomb potential in the direction of the field. The critical field of this model is

$$\mathcal{E}_{\text{crit}} = \frac{E_0^2}{4}\,. \tag{3.7}$$

This value is obtained fully in the low-frequency limit.

3.1.3 Low-frequency limit

As we intend to use the results in the adiabatic limit, and Keldysh parameter is a function of the field-frequency; we seek for a case where the oscillations do not play an important role. The key is the ponderomotive energy (1.1): $U_p = I_L/(4\omega_L^2)$, where I_L and ω_L are the intensity and fundamental frequency, respectively, of the oscillating field. The Keldysh parameter can be then scanned varying only I_L with ω_L being fixed. The adiabaticity assumption can be linked with the quantum system following the evolution of the field. Due to the relation of ω_L with the wavelength, it is then linked with the dipole approximation as well.

3.1.4 Comparison of various rates

Here, we provide an example of various ionisation rates computed for argon. There are two methods based on the tunnel ionisation, complex rotation (CR) and a phenomenological fit. The results for

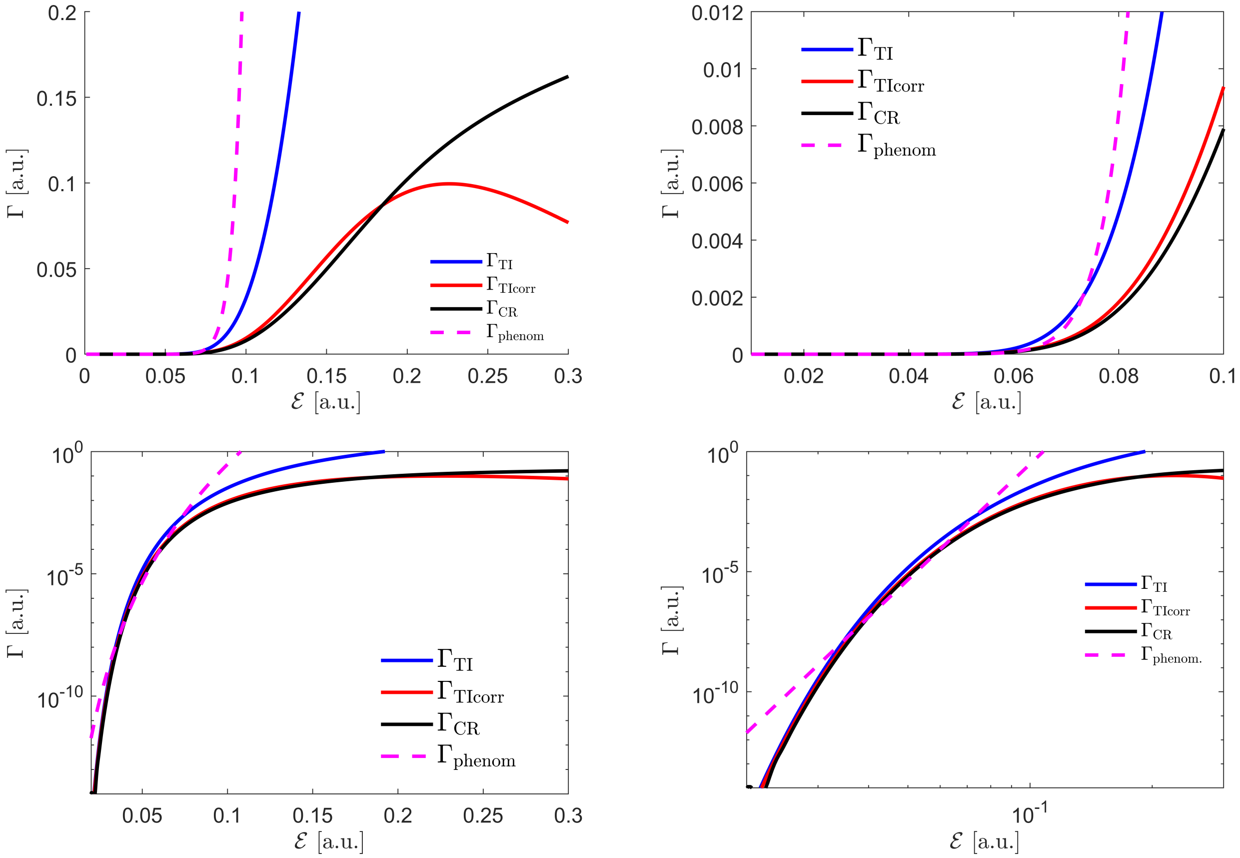

Fig. 3.2: The comparison of the ionisation rates Γ in argon computed by various models in different scales. Upper panels show Γ in linear scale. a) shows that the TIcorr fails for high intensities; however, fields under our consideration are within the range of b); the field strength 0.1 a.u. gives the intensity about 3.5×10^{14} W/cm^2. Lower panels present them in log scale, c), and log-log scale, d). $\Gamma_{\mathrm{phenom}} = a|\mathcal{E}|^k$ is linear in the latter plot because $\log_{10}(\Gamma_{\mathrm{phenom}}) = \log_{10} a + k \log_{10} |\mathcal{E}|$.

the rates are presented in Fig. 3.2. We give also some results in this section in the SI units and explicitly denote it when used.

At the instant, we use CR as a reference since this method is considered as the most accurate from the mentioned works [147, 153], while TI overestimates it. The plot of the rates confirms this statement. TIcorr and CR are similar up to some point before $\mathcal{E} = 0.2$ a.u., TIcorr decreases after this point due to the correctional exponential damping term $\mathrm{e}^{-\tilde{\alpha}\mathcal{E}}$. It shows a limitation of TIcorr since it leads to lower ionisation rate for higher field in this region. It is also worthy to note that the rates are usually depicted in log-scale. It is useful to show the global behaviour of the function, especially for the fast incremental phase in a weak field; however, the amounts of neutrals, $N_n(t)$, and free electrons, $N_i(t) = N_e(t)$, retrieved from the rate equation (3.3) requires a direct integration

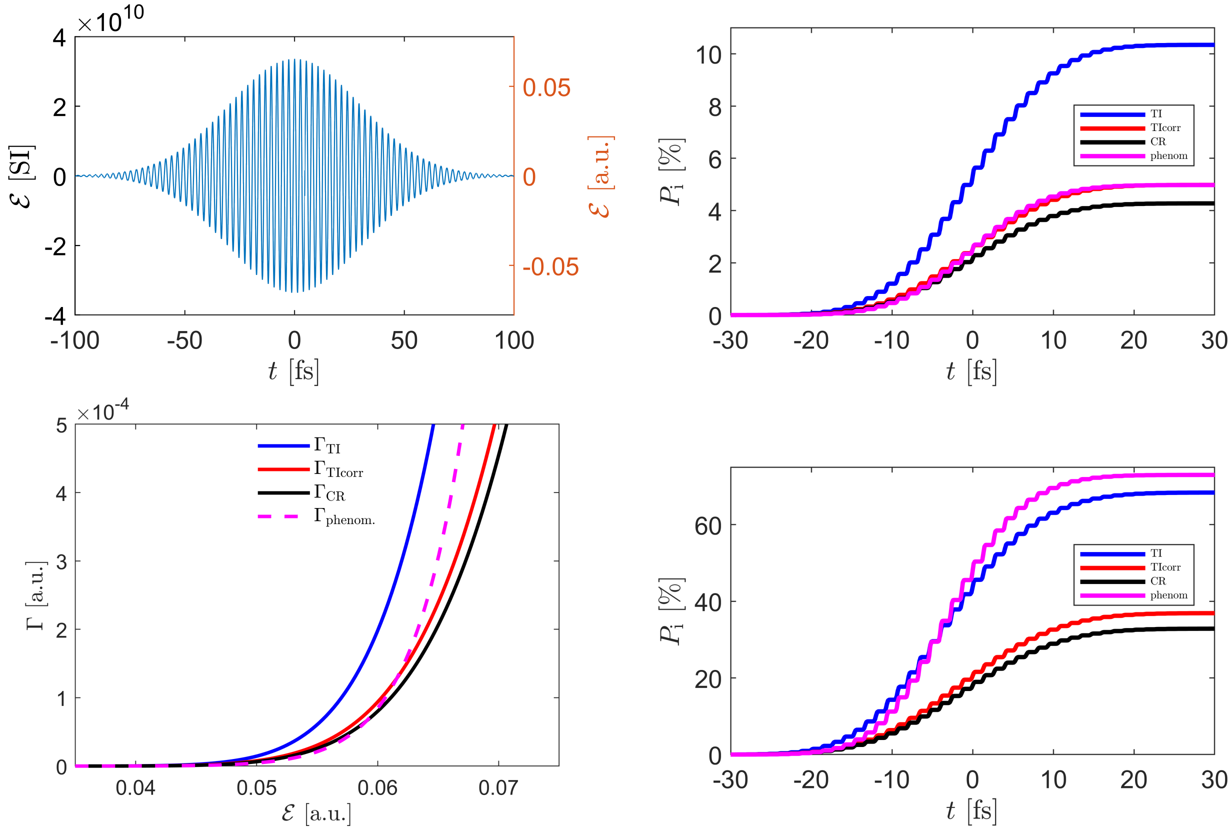

Fig. 3.3: A numerical experiment of the ionisation in argon by a 50-fs (FWHM) Gaussian pulse a). The peak intensity $I_0 = 1.5 \times 10^{14}\mathrm{W/cm}^2$ for this pulse, y-axes show field strength in atomic units and SI (V/m). The ionisation probability P_i during the interaction with this pulse is shown in b). Panel d) shows the probabilities for a pulse with $I_0 = 2.25 \times 10^{14}\mathrm{W/cm}^2$ with all other parameters kept the same. We also present a linear plot of the ionisation rates in the region of field-strengths reached by the pulse a).

of Γ.

Our goal is to investigate the ranges where there is partial ionisation of targets. In other words, the target is not fully ionised nor the ionisation is negligible – a precise ionisation model is not so important in these limit cases. We have chosen two configurations for illustration shown in Fig. 3.3. First $I_0 = 1.5 \times 10^{14}$ W/cm^2, a value giving the ionisation about 10 % that is sometimes referred to be optimal for experiments (see a detailed discussion in the section 6.3). Second, the critical field $\mathcal{E}_\mathrm{crit} = I_p^2/4 \approx 0.08$ a.u. $\approx 2.25 \times 10^{14}$ W/cm^2 is reached at the maximum of the envelope.

The main result is that TI gives significantly different probabilities of ionisation than TIcorr and CR. The relative difference between TIcorr and CR is $\left|P_\mathrm{i}^{(\mathrm{TIcorr})}(t_f) - P_\mathrm{i}^{(\mathrm{CR})}(t_f)\right| / \left|P_\mathrm{i}^{(\mathrm{CR})}(t_f)\right| \approx$ 16 % after the interaction in t_f. Looking at the ionisation rates, the main contribution to ionisation occurs for fields $|\mathcal{E}| > 0.05$ a.u. for all the models. It means that the ionisation is almost negligible for lower field amplitudes.

Since the relevant region of field-strengths is quite narrow, we tried also a phenomenological model of ionisation $\Gamma_{\text{phenom}} = 3 \times 10^{15} |\mathcal{E}|^8$ (in atomic units). The motivation for this model is that it is sometimes used as a simple analytic model of ionisation [156]. This model comes from the multi-photon regime, where the power of $|\mathcal{E}|$ is associated with the number of absorbed photons. However, as these models relies on the extension of a static field, this explanation is not satisfactory for this case. We can rather see it as a fitting parameter characterising the non-linearity of (3.4) in the vicinity of the field $|\mathcal{E}|$ of interest. The numerical parameters of this model are chosen to correspond to TIcorr for the lower peak intensity. The model works well in this narrow region and its use may be then justified in some cases. However, if we go beyond this region (Fig. 3.3d)), there is a significant discrepancy.

3.1.5 Formalization of the static-field methods

We started the practical methods motived by their need for practical applications; we now add some formal remarks that should be kept in mind while using them.

First of all, the presence of a static field strongly changes the nature of the physical system. A field-free atom possesses continuum with only non-negative eigenenergies. This is not the case for the Stark Hamiltonian (3.2). The continuum spans all real numbers and the eigenfuctions are the Airy functions instead of the Coulomb wave. Actually, the studies of the spectral properties of the Hamiltonian then takes the atomic potential as a perturbation ($1/r$ is an integrable singularity in higher dimensions, thus the singularity is not so disturbing). On the other hand, this model is an idealization and the static field can never span the whole space, we conjecture that taking into account a large but finite region with the electric field, i.e. the electric field vanishes at infinity, resolves at least the problem of the lower-unbounded spectrum.

Revising the probabilty-flux-approach, the usual approach glues the state inside the potential well with a free state given by the Airy function outside the well with the same eigenergy. It means that the electron is born at the edge of the classically forbidden region with zero-initial velocity. It was pointed out [157] that TI may overlap MPI. This means the energy may be changed. Further discussion about the quantitative validity of the approach is in [145].

The complex-rotation method is also perturbative [150], one of the motivation for its study is that the perturbation series of the Stark Hamiltonian is classically divergent and only Borel-summable [158]. This summability is necessary for usual perturbative series in quantum mechanics contained in most textbooks. The motivation from the mathematical point of view cannot be expressed better than by Herbst and Simon [158]:

> *Most quantum mechanics texts present three examples of time-independent perturbation*

> *theory as typical and important applications of the method: the x^4 anharmonic oscillator, the Zeeman effect in atoms and the Stark effect in atoms. Ironically, all three perturbation series are divergent!*

A method that can rigorously treat this problem is the so-called *Borel summation.* It may be introduced by

$$A(z) = \sum_{n=0}^{+\infty} a_n z^n = \sum_{n=0}^{+\infty} n! \frac{a_n}{n!} z^n = \sum_{n=0}^{+\infty} \int_0^{+\infty} \mathrm{e}^{-t} \frac{a_n}{n!} (tz)^n \,\mathrm{d}t = \\ = \int_0^{+\infty} \mathrm{e}^{-t} \sum_{n=0}^{+\infty} \frac{a_n}{n!} (tz)^n \,\mathrm{d}t = \int_0^{+\infty} \mathrm{e}^{-t} \mathcal{B}(tz) \,\mathrm{d}t \,. \quad (3.8)$$

If RHS is finite, one can assign its value to $A(z)$ even in the case the sum $\sum_{n=0}^{+\infty} a_n z^n$ is diverging. It can be seen as a regularisation method because the interchange of the sum and the integral is not formally possible for diverging sums. The expression $\mathcal{B}(\zeta) = \sum_{n=0}^{+\infty} \frac{a_n}{n!} \zeta^n$ is the so-called *Borel transform of* a_n. This method is straightforward in the sense that it leads to an analytic function (*Watson's theorem*).[5] The limitation on analytic function is important. Let f be defined as

$$f(x) = \begin{cases} \mathrm{e}^{-\frac{1}{|x|}} \,, & x \neq 0 \,, \\ 0 \,, & x = 0 \,, \end{cases} \quad (3.9)$$

it is easy to infer that $f \in \mathcal{C}^{+\infty}(\mathbb{R})$, but its MacLaurin series is 0 (while f is not).[6] Particularly it means that for any analytic g, the function $g + f$ has exactly the same MacLaurin series as g. The role of an $\mathrm{e}^{-\frac{1}{|x|}}$-term in the Stark effect is exactly the key property recognised in very early studies [106].

As far as we know, a full mathematical correctness of this method remains unproven since it has been discussed together with the range of validity by Herbst [150]. There is still undergoing mathematical research in this domain [159].

This theory may be seen also from a more general viewpoint by considering the time dependence. Possible solutions head towards non-Hermitian quantum mechanics [160, 161] or towards the extension of usual Hilbert spaces into Hardy spaces [162, 163, 164]. The second approach basically formalises analytic continuation of wavefunctions into the complex plane. An important consequence is a formal treatment of causality similarly as in classical physics (see the discussion

---

[5] The analyticity is a unique property that is necessary, e.g., for extending real function into complex plane. Also, there is at most one possible analytic continuation of such a real function.

[6] By symmetry, only right neighbourhood of 0 can be considered. One has $\frac{\mathrm{d}^n}{\mathrm{d}x^n}\Big|_{x\to 0_+} f = \lim_{x\to 0_+} P_n\left(\frac{1}{x}\right) \mathrm{e}^{-\frac{1}{x}} = \lim_{y\to+\infty} \frac{P_n(y)}{\mathrm{e}^y} = 0$, where P_n is an n-th order polynomial.

after (1.5)), which also provides a proper explanation of incoming and outgoing states in the continuum. We favour the mathematical research in this area since it may have important consequences for our subject.

3.1.6 Approximate solutions without adiabaticity

The next step is to use more advanced models overcoming adiabaticity but still below the computational effort required by fully numerical TDSE. A method directly extending the previous results is the so-called PPT model [109, 110, 165, 166]. An analytic expression for the ionization rate is retrieved by approximate methods. One of the great features is that the multi-photon regime for weak intensities is covered. The ionisation rate, Γ, is proportional to I^{N_p}, where I is the intensity and N_p the number of absorbed photons. The main outcome of these results is analytical formulae. These formulae may be used to construct a computationally fast model, which is essential for macroscopic approaches. The rates may be further extended to take into account different ionisation regimes [167].

The complex-rotation method can be also extended to include the external electromagnetic field. See [168], which introduces the complex rotation applied also for quantised photons interacting with the target.

A further analysis is obtained using the SFA (Section 2.4) provides a closer insight. The main goal is to model fully the interaction – it comes from the need to accurately describe also dynamics after the ionization. This is exactly what we have done in the context of HHG, which requires to describe the re-collision. Historically, SFA preceded HHG, and the interest was originally to use it for ionisation. It had started by the generalisation of the Keldysh theory using S-matrix formalism [169], before it celebrated a great success by grounding the quantum-model of HHG [25]. We have introduced SFA in Section 2.4, writing the wavefunction by the ansatz

$$\psi(t,\boldsymbol{x}) = \psi_g(t,\boldsymbol{x}) + \psi_c(t,\boldsymbol{x})\,, \tag{3.10}$$

where $\psi_g(t,\boldsymbol{x})$ is the field-free ground state, and $\psi_c(t,\boldsymbol{x})$ is the perturbation given by continuum states, we leave again technical details to the references. As we already discussed, the bound states can be defined only up-to gauge equivalence: The gauge fixing is then imposed there. It motivated next research of SFA together with the study of various perturbative orders studied [170]. It explains that the perturbative series differ for different gauges; however, the perturbation series are connected together by the gauge transforms of the unperturbed solution. We will clarify the choice of the gauge from energetic viewpoint in the following section, the respective decomposition relies on (3.16). The study [170] also mentions that the high orders of the perturbative series leads to a divergence. This is expected results as already explained in [158].

3.2 Invariant dynamics of ionisation

To infer the ionisation dynamics, it is convenient to do a step back and start with a classical description. The initial point is thus a classical charged particle in an external electromagnetic field emphasising the role of general energy in the Lagrangian formulation; which will help in the construction of the invariant measure of the ionisation. Such an analysis provides also an insight in the dynamical aspect of the ionisation in various regimes. This section is related to one of the outcomes of the thesis [111].

3.2.1 Invariant energy & energy measurements

We have done a review of various methods to compute the ionisation together with some practical calculations. All these calculations have been motivated either by the volumetric definition or the parturbative approach based on the length gauge (the complex rotation). It means that these calculations are not invariant. Our goal now is to find an unambiguous framework. This helps us also to gain further insight in the process.

Let us start with a general classical Lagrangian of an electron interacting with an electromagnetic field

$$L = \frac{m\boldsymbol{v}^2}{2} - q(\varphi - \boldsymbol{v} \cdot \boldsymbol{A})\,. \tag{3.11}$$

The generalised energy of such a system is given by the formula

$$E = \frac{\partial L}{\partial \boldsymbol{v}}\boldsymbol{v} - L = \frac{m\boldsymbol{v}^2}{2} + q\varphi\,. \tag{3.12}$$

From this equation we see that the term $q\varphi$ is not gauge invariant because it can be modified arbitrarily by $\varphi' = \varphi + \partial_t \Lambda$. What is the physical explanation of this term? It is a potential energy, meaning that some part of the energy of the system may be deposed as potential energy in the electromagnetic field. We should emphasise that this is not a choice of global zero of the potential. As gauge theories are by construction local theories, the energy is set locally in the whole spacetime. As gauge theories impose the equations for fields, we should not break it without a good reason by any arbitrary gauge fixing. However, we can use a different freedom in the theory to adjust the energy: any total time derivative of a function may be added to the Lagrangian. If we add $q(\mathrm{d}/\mathrm{d}t)\int_0^t \varphi\,\mathrm{d}t$, the Lagrangian reads

$$L_I = \frac{m\boldsymbol{v}^2}{2} - q\boldsymbol{v} \cdot \left(\boldsymbol{A} + \int_0^t (\triangledown\varphi)\,\mathrm{d}t\right)\,. \tag{3.13}$$

We use the subscript I to denote the invariance, as the generalised energy is only $E_I = m\boldsymbol{v}^2/2$. The physical meaning is that we do not allow any energy to be deposed as a potential energy, and the total energy of the electron is only kinetic.

A further step is the Hamiltonian mechanics. Here, we discuss our system: an electron in a potential and in external field. Although the nature of the potential in the Hamiltonian is also electromagnetic, it is clearly distinct from the external field, we then keep this part as a true potential. The Hamiltonian respecting the invariant construction is

$$H_I = \frac{\left(\boldsymbol{p} - q\left(\boldsymbol{A} + \int_0^t (\triangledown\varphi)\,\mathrm{d}t\right)\right)^2}{2m} + V(r)\,. \tag{3.14}$$

We explicitly denote that there is no gauge fixing at this point, the procedure is that we have first an external field at any gauge and we get this Hamiltonian in the second step by the freedom in the Lagrangian mechanics and not in gauge theories. On the other hand, the Lagrangian is already in the desired form, if the field is in the incomplete Weyl gauge, $\varphi = 0$. The velocity gauge (2.3) is such a gauge. In other words, we can reach the desired invariant form by an appropriate gauge transform. Last, we emphasise that we do not impose this Hamiltonian for the treatment of the dynamics of the system; we need to be sure to transform to this Hamiltonian only once we intend to measure energy.

As we fixed the energies, we stabilised the spectrum. We verify that the spectrum is strictly preserved also in the quantum-mechanical case within the incomplete Weyl gauge. We infer that the only allowed gauge transform to preserve the Weyl gauge are time-independent: $\Lambda = \Lambda(\boldsymbol{x})$. Because the eigenvalue problems

$$\left(\frac{(\boldsymbol{p}+\boldsymbol{A})^2}{2} + V\right)|\psi\rangle = E\,|\psi\rangle\;, \qquad \left(\frac{(\boldsymbol{p}+\boldsymbol{A}+\triangledown\Lambda)^2}{2} + V_C\right)|\tilde{\psi}\rangle = E\,|\tilde{\psi}\rangle\;, \tag{3.15}$$

are equivalent while considering $|\tilde{\psi}\rangle = \mathrm{e}^{\mathbf{i}\Lambda}\,|\psi\rangle$, the spectra are preserved within the Weyl gauge. It proves there are no artificial energy shifts caused by different (sub)gauges within the Weyl gauge.

Having defined the stabilised spectrum, we can invariantly inspect the dynamics of the ionisation by measuring the energy in time. We now recall the method based on the resolvent calculation to construct the projectors onto the spectrum of H. We use the Riesz projector for the operator H onto the energy subspace of the eigenenergy E, it is written as

$$P(H;E) = -\frac{1}{2\pi\mathbf{i}}\oint_{\gamma_E}\frac{\mathrm{d}z}{H-z}\,, \tag{3.16}$$

γ_E is a closed loop in the complex plane circumventing only the eigenvalue E, the integration of the operator is done in the sense of the Bochner integral, see chapter I.2 of [171]. Note the analogy with the Cauchy's residue theorem from complex analysis. The probability distribution in the energy space of a given state is then simply $\mathcal{P}[E = \tilde{E}] = \langle\psi|P(H;\tilde{E})|\psi\rangle$.[7]

This technique is already used to provide great insight of the dynamics. It was empirically introduced by [112], the motivation there was to use a door function in the spectrum to filter the energies. Its extension including normalisation is provided in [172], the projector is there approximated by

$$P(H;E) \approx N_{\epsilon,n} \frac{\epsilon^{2n}}{(E-H)^{2n} + \epsilon^{2n}}\,, \tag{3.17}$$

ϵ can be related to the radius of the chosen curve γ_E and $2n$ with the order of the approximation of the Bochner integral. An advantage is an easy implementation. Finally, there is a normalisation constant $N_{\epsilon,n}$. The normalisation must be treated with care because there is a subtlety in the nature of the spectrum. Projecting onto the eigenstates of the point part of the spectrum is related to the *probability* of finding the system at this state. However, the continuous part of the spectrum correspond to a *probability density*. It thus need to be treated appropriately to keep the correct units. (See also the discussion in Section 7.2.)

Now, we use $P(H;E)$ to measure the energy distribution in time of our system. It is advantageous to start with the velocity gauge as aforementioned. It is written within the dipole approximation as

$$H_V(t) = \frac{(\boldsymbol{p} - q\boldsymbol{A}(t))^2}{2m} + V_C(r)\,. \tag{3.18}$$

There is a further simplification allowing to use the field free-Hamiltonian in the resolvent. We notice that some Hamiltonians with the interaction may be retrieved from the field-free Hamiltonian, $H_0 = \boldsymbol{p}^2/2 + V_C$; we define a unitary operator $U = \mathrm{e}^{\mathrm{i}\chi(\boldsymbol{x},t)}$. We have

$$UH_0U^\dagger = \frac{(\boldsymbol{p} + \triangledown\chi)^2}{2m} + V_C(r)\,. \tag{3.19}$$

We need to emphasise: 1) This is not a gauge transform of the Hamiltonian as the compensating term for the derivative in time is missing. 2) Not every vector field is conservative, i.e. written as $\boldsymbol{A} = \triangledown\chi$ (see the Fundamental theorem of vector calculus). Namely, rot $\triangledown\chi = 0$, $\forall\chi$; so that a magnetic field cannot be described. The field within the dipole approximation may be written

---

[7] For mathematical correctness, E is is defined in the sense of the probabilistic random variable while $\tilde{E}$ is the classical analytical variable used in (3.16). We will not distinguish them in the rest of the work as the meaning is clear from the context.

this way if we choose $\chi(\boldsymbol{x},t) = -q\boldsymbol{x}\cdot\boldsymbol{A}(t)$. We then rewrite the probability of finding the system with the positive energy starting from the velocity gauge:

$$\begin{aligned}\mathcal{P}[E \geq 0] = \langle \psi_V \,|\, P(H_V; E > 0) \,|\, \psi_V \rangle = -\frac{1}{2\pi\mathbf{i}} \left\langle \psi_V \,\middle|\, \oint_{\gamma_E} \frac{\mathrm{d}z}{U H_0 U^\dagger - z} \,\middle|\, \psi_V \right\rangle = \\ = -\frac{1}{2\pi\mathbf{i}} \oint_{\gamma_E} \left\langle \psi_V \,\middle|\, U^\dagger \frac{1}{H_0 - z} U \,\middle|\, \psi_V \right\rangle \mathrm{d}z = -\frac{1}{2\pi\mathbf{i}} \oint_{\gamma_E} \left\langle \psi_L \,\middle|\, \frac{1}{H_0 - z} \,\middle|\, \psi_L \right\rangle \mathrm{d}z = \\ = \langle \psi_L \,|\, P(H_0; E > 0) \,|\, \psi_L \rangle \;, \end{aligned} \tag{3.20}$$

where $|\psi_L\rangle$ is in the length gauge. γ_E is chosen to circumvent all the energies in the discretised positive part of the spectrum.

3.2.2 How to define ionization?

We finally answer the question of how to define the ionisation. We suggest the idea that using $\mathcal{P}[E \geq 0]$ is a good way to define it. Our motivation is the Kepler problem in the classical mechanics. Trajectories for $E < 0$ are closed and always return to the vicinity of the center, in other words, the particle never escapes from the central area. Contrary, trajectories for $E \geq 0$ are non-returning and it is a reasonable to link them with the ionisation. As we stabilised the spectrum, it is well-defined at any time. We may see it as a part of the wavefunction that escapes if the field is turned-off abruptly (we will show that this may be tricky without using the dipole approximation).

This can be seen also in another way. The eigenfunctions corresponding to the continuous spectrum, $\sigma_c(H)$, formally do not belong to the respective Hilbert space $\mathscr{H}$. The Hilbert space must be rigged to include them [173].[8] With a proper extension of the Hilbert space [174, 175], there are defined so-called outgoing $|\varphi^{(+)}(\boldsymbol{p})\rangle$ and incoming $|\varphi^{(-)}(\boldsymbol{p})\rangle$ Coulomb waves, which are assigned to the continuous spectrum of the field-free Hamiltonian H_0 and further specified by their asymptotic behaviour of momentum $\boldsymbol{p}$. The ionisation may be then defined as the projection onto the outgoing states after the interaction of the atom with the pulse. These states then allow to find another form of the projector onto the subspace given by $E > 0$. The projector is then written

$$P(H_0; E > 0) = \int \left|\varphi^{(-)}(\boldsymbol{p})\right\rangle \left\langle \varphi^{(-)}(\boldsymbol{p})\right| \,\mathrm{d}^3 p \,, \tag{3.21}$$

which may be used as well in (3.20).

In conclusion, we recall the main interests in ionisation. The dynamics of the ionisation process

---

[8] The extension is done in the means of the Gel'fand triple. There is defined a set of test functions $\Phi \subset \mathscr{H}$ fulfilling additional constraints (usually continuity going beyond L^2-integrability). The dual space Φ^* in the sense of the scalar product is then larger than $\mathscr{H}$ and include generalised functions, as for example the Dirac distribution δ. The triplet is then formed in the means of inclusion: $\Phi \subset \mathscr{H} \subset \Phi^*$. The generalised states then belong to Φ^*. See also the discussion at the end of Section 3.1.5.

during the interaction is interesting from the microscopic viewpoint. Our method is a tool providing the required insight. Moving to the larger macroscopic scale, the microscopic picture is averaged. The main interest is if the resulting plasma density is quantitatively correct disregarding the details of the underlying processes. The practical use of this method is then to benchmark simplified (and computationally fast) formulae discussed in Section 3.1.

3.2.3 Ionisation in the non-dipole case

Before we show the results of practical computations in the next section, we summarise the findings on the non-dipole case that has been assumed in (3.19). The most important point is that the spectrum of the Hamiltonian is not stabilised any more. Strictly speaking, we have proved that in the dipole case the spectrum is stabilised; but we have not proved that it *is not* stabilised otherwise. This remainder is proved in Appendix C. Next, the consequence of the space dependence of $\boldsymbol{A}$ makes it impossible to abruptly turn off the field keeping the continuity of the vector potential. It also makes impossible to use some fixed states and Hamiltonian as a substitute to compute the projector (3.16) as done in (3.20). Finally, it makes no difficulty to use still the projector with γ_E circumventing the positive real axis. However, the physical picture becomes more complicated. There are some of the subtleties coming either from limiting or not to the dipole case:

- We limit the consideration on the dipole case, and it allows us to use the field-free Hamiltonian H_0 with a fixed spectrum. Moreover, the fixation also preserves the eigenstates in the means of their density distribution $|\psi(\boldsymbol{x}, t)|^2$. It is particularly interesting for the bound states: the distribution in x-space is identical as in the field-free case. The only difference is only in the oscillating part of the wavefunction – given by $\mathrm{e}^{-\mathbf{i}Az}$. $E = 0$ is then a clear threshold between bound and continuum part of the spectrum, which grounds the definition. The most evident drawback of this approach is that the involved approximation is *unphysical*, it violates the solution of the electromagnetic waves by neglecting magnetic components, breaking the invariants of the field and causality [176].
- $E = 0$ may be still defined as a threshold in the non-dipole case because the energy is still invariant. However, the difficulty in this case is that the spectrum is not stabilised and it is not clear that the bound states and continuum states are not mixed. Because the $\boldsymbol{x}$-dependence of the vector potential $\boldsymbol{A}$ creates a true potential term; the situation may be similar as for auto-ionised states (see [177] for the corresponding model potential) encapsulated in the continuum. It makes then a difficulty to interpret the split of the spectrum in the positive and negative parts by the means of bound and continuum states. This discussion is similar to the one presented in [116], where it was argued that the ionisation must be related with the possibility of an electron to escape infinitely from the parent ion as we pointed out in the

classical Kepler problem.

It is not surprising we reach a limit in the precise definition of the ionisation. Being strictly rigorous, the matter and field are coupled, and the true Lagrangian is (I.1), and we sculptured only part of it for studying a subsystem. Next, we mention that these studies were static in the sense that all definitions are done at a fixed time t. In this light, the importance of our study is that we provided an invariant formulation. This formulation is completely clear in the dipole-case, and the non-dipole case needs a special care for phenomena requiring such a description as [178].

3.3 Invariant picture of ionisation: Linear, multi-photon, tunnelling processes

We conclude our discussion of the ionisation by a practical example. The perturbative approaches have brought practical computational methods and also some physical intuition about the process. However, we warned that this intuition had to be very cautious as it was not strictly gauge-invariant. Fortunately, we had also introduced an invariant construction in Section 3.2. We may then combine both paradigms: the perturbative approaches are but a scaffold, which helps us to recognise the key patterns in the universal construction.

We use a 1D-atom with the ground energy $E_g \approx -0.67$ a.u. for our numerical experiments.[9] The atom is subjected to an external field defined by $A(t) = A_0 \sin^2(\pi t/T)\sin(\omega_0 t)$, where $T = 2\pi N_c/\omega_0$ is the total duration of the interaction, and we measure it by the number of cycles N_c in the envelope. There are three cases in the study: A) *linear*, where a single photon can kick-up the electron into the continuum; B) *MPI*, where the single-photon energy lies below the ionisation level; C) *tunnelling*.

The results of energy density distributions are computed from (3.17) by setting $n = 1$,

$$\rho_E(t) = N_{\epsilon,n}\epsilon^2 \left\langle \psi_L(t) \middle| \left((E-H_0)^2+\epsilon^2\right)^{-1} \middle| \psi_L(t) \right\rangle^2 = N_{\epsilon,n}\epsilon^2 \left\| (E-H_0+\mathbf{i}\epsilon)^{-1}\psi_L(t) \right\|^2 ,$$

with removing the bound states from $|\psi_L\rangle$. The results are shown in Fig. 3.4. The corresponding ionisation probabilities, $P_{\text{ion}}(t) = \mathcal{P}[E \geq 0](t) = \int_0^{+\infty} \rho_E(t)\,\mathrm{d}E$. Let us discuss the results:[10]

A) A linear (single-photon) case with $\omega_0 = 1$ a.u., $A_0 = 0.01$, $N_c = 8$; which yields the Keldysh parameter $\gamma \approx 116$. A simple energetic consideration of absorbing a single photon gives an expected energetic peak of the ionised electrons at $E = E_g + \omega_0 \approx 0.33$ a.u. It corresponds to the resulting energetic distribution $\rho_E(t = T_c)$. The width of the energetic distribution is

---

[9] The respective Hamiltonian (7.23) is discussed in the numerical methods. The soft-Coulomb potential in this case is $V(x) = -1/\sqrt{1+x^2}$.

[10] The results were computed by a grid-method in the length gauge with the discretisation Δt and Δx within the box $[-x_{\max}, x_{\max}]$ and energy resolution respectively: A,B) $\Delta t = 0.1$ a.u., $\Delta x = 0.4$ a.u., $x_{\max} = 100$, $\epsilon = 0.03$; C) $\Delta t = 0.05$ a.u., $\Delta x = 0.5$ a.u., $x_{\max} = 500$, $\epsilon = 0.005$.

expected to be inversely proportional to the pulse duration. It agrees with the distribution narrowing for $t \gtrsim 25$ a.u.. This result thus agrees with the analytic expectations in the main features.

Regarding other properties, one striking result is the decrease of $P_{\text{ion}}(t)$ after each minimum of the electric field $\mathcal{E}$. Such a property cannot be obtained from a rate equation such as (3.3) because a positive Γ provides only an increasing $P_{\text{ion}}(t)$ in time. The rate equation, however, lacks two important mechanisms: it does not include the re-absorption and "coherence". The coherence means that the ionisation process at a given time, t, cannot interfere with the ionisation at any precedent time $t' < t$. This can be illustrated by the means of the (first-order) time-dependent perturbation theory (TDPT)

$$P_{\text{ion}}^{(\text{rate eq.})}(t) = 1 - \mathrm{e}^{-\int_0^t \Gamma(|\mathcal{E}(t')|)\,\mathrm{d}t'} \approx \int_0^t \Gamma(|\mathcal{E}(t')|)\,\mathrm{d}t'\,, \tag{3.22a}$$

$$P_{\text{ion}}^{(\text{TDPT})}(t) = \int_0^{+\infty} \left| \int_0^t \mathrm{e}^{\mathbf{i}Et'} \langle E|\mathcal{E}(t')x|g\rangle\, \mathrm{e}^{-\mathbf{i}E_g t'}\,\mathrm{d}t' \right|^2 \mathrm{d}E\,, \tag{3.22b}$$

where $|E\rangle$ is the continuum state with the energy E and $|g\rangle$ is the ground state. The approximation in (3.22a) is valid for small degrees of ionisations. The matrix element $\langle E|\mathcal{E}(t')x|g\rangle$ corresponds to the transition between $|g\rangle$ and $|E\rangle$ induced by the interaction $\mathcal{E}(t')x$. The TDPT provides the coherence in the process by the integration over t', where various contributions sums coherently. Furthermore, it shows that the most probable channel of the ionisation comes via $E - \omega_0 - E_g = 0$ because the oscillating term in the integral vanishes. This agrees with the aforementioned expected energy distribution.

Beside these slight decreases, the shape still contains the "ionisation-ladder" properties, which means that the dominant contributions to the ionisation come at the maxima of the electric field $\mathcal{E}(t)$.

We return to the viewpoint of the re-absorption. Since bound and continuum states form a complete set, a decrement of the population of the continuum states is necessarily an absorption. If this is related to a coherent processes, it is only a wave-particle duality expressed in different words. The "absorption" is related to the consideration of occupied states while the coherence arises from the interference of various paths.

B) The MPI regime uses $\omega_0 = 0.33$ a.u., $A_0 = 0.01$, $N_c = 4$; the Keldysh parameter is the same as in the previous case, $\gamma \approx 116$. The ionisation probability is much smaller, $P_{\text{ion}}(T) \approx 3.5\times10^{-7}$ compared to $P_{\text{ion}}(T) \approx 8.5 \times 10^{-7}$ in A). The reason is that γ, thus A_0, are the same, but the peak electric field is different as it scales as $\omega_0 A_0$.

This evolution of $P_{\text{ion}}(t)$ is considerably different from the ionisation-ladder in this case as its shape follows the field. An explanation goes with the interpretation of ρ_E as the distribution of the energy of the invariant Hamiltonian H_V. We recall the Lagrangian construction; the energy from the field can be deposed only in the kinetic part and the energy of a given bound state cannot be shifted as the spectrum is stabilised. The only way to depose the energy is either to higher energetic bound states (excitations) or in the additional kinetic energy. This stripes in the distribution ρ_E in Fig. 3.4B1) shows the portion of the kinetically deposed energy of the electron, which is dressed by the field. The ratio of the electrons that makes it out of the influence of the Coulomb potential is much smaller. The ionisation per half-cycle may be inferred from $P_{\text{ion}}((1+1/2)T_0) - P_{\text{ion}}(T_0)$, where the times correspond to two consecutive zeros of $\mathcal{E}$.

C) The tunnelling regime is characterised by $\gamma \lesssim 1$. In this case $\gamma \approx 0.57$ by setting $\omega_0 = 0.07$ a.u., $A_0 = 2$ a.u.. Note that the peak electric field $\mathcal{E}_0 = 0.14$ a.u. is then close to the critical field $\mathcal{E}_{\text{crit}} \approx 0.11$ defined by (3.7). The number of cycles is chosen $N_c = 4$.

The structure in Fig. 3.4C1) is much richer than in the previous cases. There is a build-up of the interference pattern leading to the ATI-spectrum [179] with the peaks spaced by ω_0, Fig. 3.4C2), from the repeating interferences/re-collisions of the returning electronic wave-packet with the ionising one. There is also another interference pattern: the ATI-peaks goes in triplets. This interference is due to the shortness of our pulse and the interference within the envelope.

Another feature is the maximal energy of the electrons extending up to 6 a.u. at the maximal oscillations around $t \approx 180$ a.u. and $t \approx 220$ a.u.. This can be inferred from the energy balance. Assuming the electron is primary governed by the external field (the role of V_C can be neglected), the canonical momentum in (3.18) is conserved. The distribution ρ_E shows that the release of the electrons begins before the maximum of the field approximately in the first quarter of the half-cycle ($t \approx 150$ a.u.) with the zero initial velocity. It gives canonical momentum $p_i \approx -\sin(\pi/4)A_0$. Substituting this momentum in the maximum, t_m, of the field into the kinetic term of H_V, one obtains $E_{\text{kin.}}(t_m) = ((1/\sqrt{2}+1)2)^2/2 \approx 5.8$ a.u. $\approx 5U_p$, which corresponds the observed extent. It means that this energetic contribution comes only from the dynamics due to the external field, in contrast with the energy gained by re-collisions [180] producing energies up to $10U_p$. The investigation of these processes is currently out of our scope and would require higher precision in the calculation of (3.16), which can be done, e.g., by the resolvent (3.17) of a higher order.

Finally, the structure of $P_{\text{ion}}(t)$ exhibits the ladder-like structure again with some finer structures than $P_{\text{ion}}^{(\text{rate eq.})}(t)$.

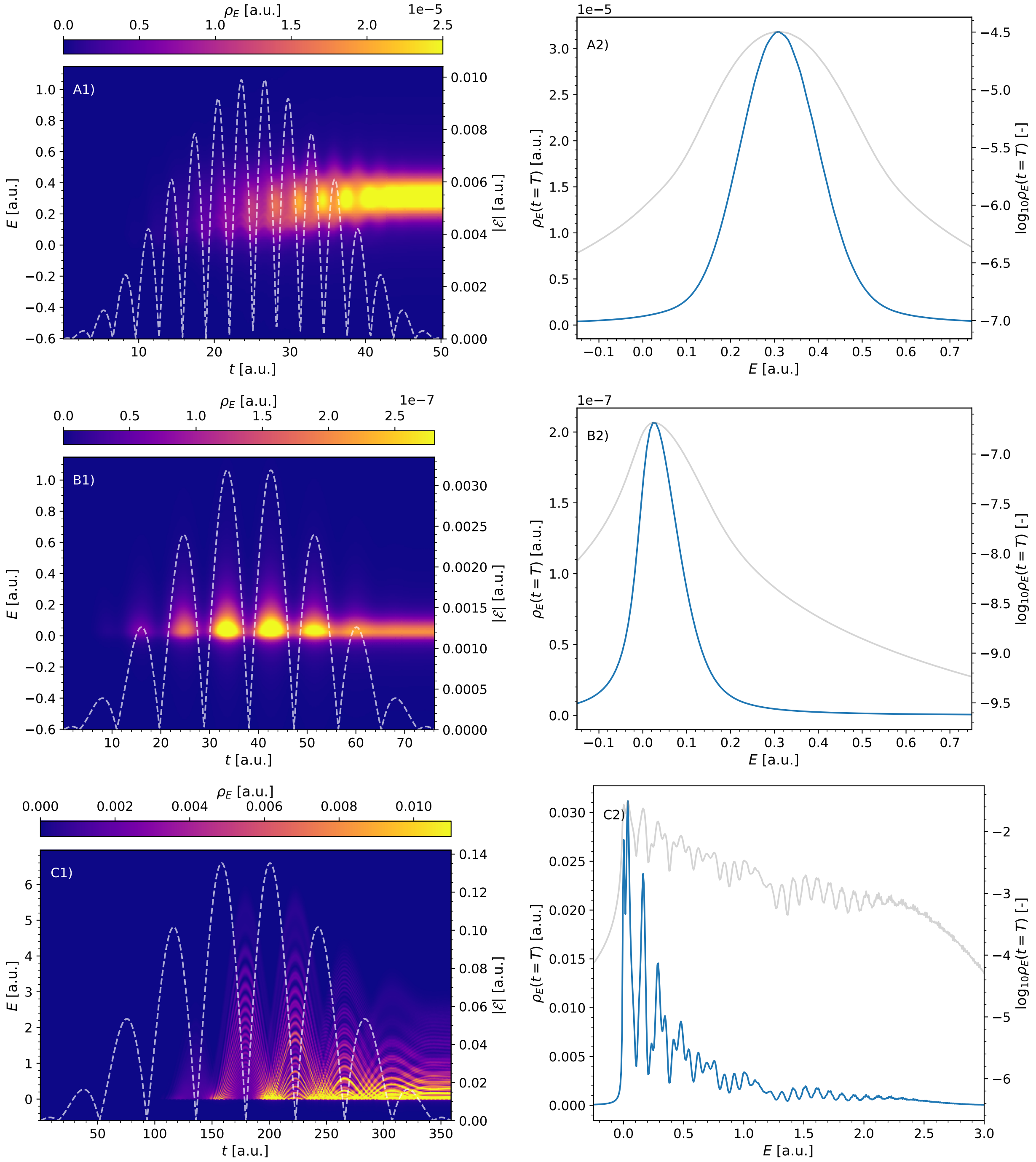

Fig. 3.4: The energy distributions $\rho_E(t)$ of the electron during the interaction with the external field for the three studied cases enlisted correspondingly in Section 3.3. Left panels show the energy spectrum during the interaction $\rho_E(t)$. The dashed lines in A1-C1) represents the magnitude, $|\mathcal{E}|$, of the electric field. Corresponding Keldysh parameters are $\gamma \approx 116$ for A) and B); $\gamma \approx 0.57$ for C). The regime of A) and B) differs due to the different periods of the respective $|\mathcal{E}|$. The bound states of the potential are removed, the extent into the region of $E < 0$ is due to the Lorentzian distribution of the states for $E > 0$ imposed by the approximation of (3.16).

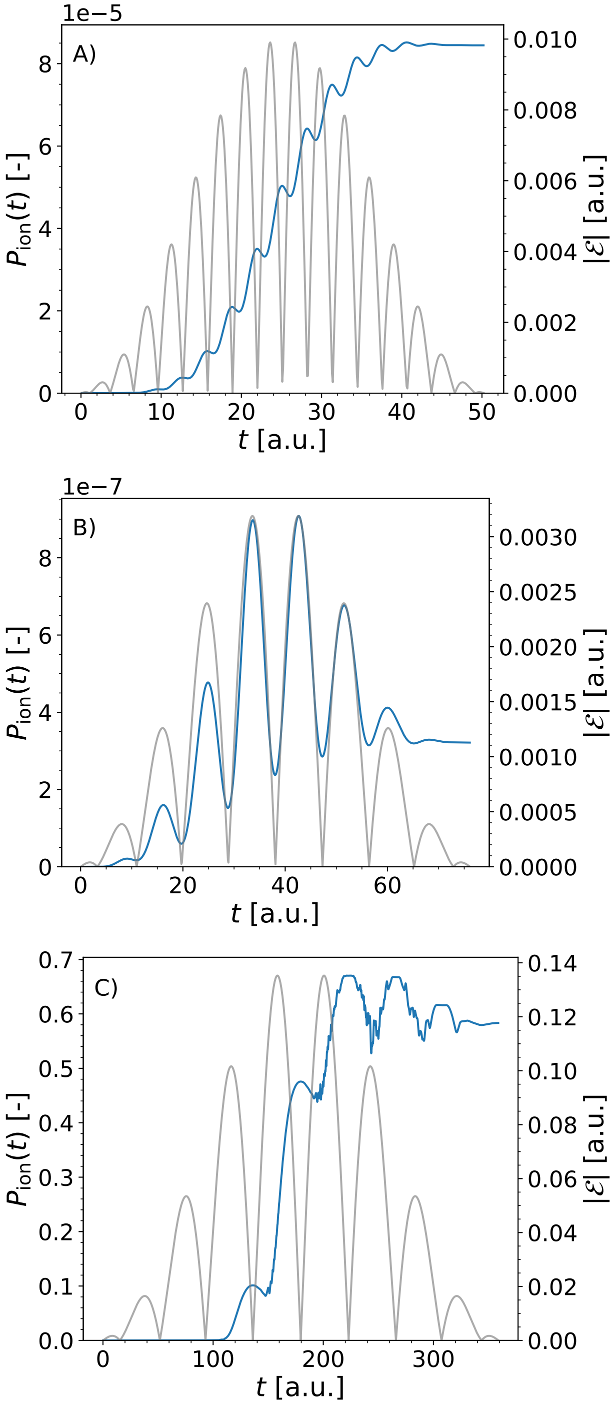

Fig. 3.5: (blue): The ionisation, $P_{\text{ion}}(t)$ in time for the cases A)-C). (grey): The magnitudes of the electric fields $|\mathcal{E}|$.

3.3.1 Conclusion on various ionisation approaches

In conclusion, we have drafted a complex picture of the ionisation. A correct formulation relies on the use of the stabilised spectrum and invariant energy measurements. However, the supplementary perturbative approaches may provide physical intuition and fast computational models. The primary interest of the invariant construction relies in the insight brought by the sub-cycle dynamics. The understanding of the dynamics and appropriate tools are essential to draw an accurate picture of the process and to help in designing new methods to drive the sub-cycle processes. Complementary, the implementation of the simplified methods is important for a fast computing of the plasma density necessary for macroscopic effects.

Part II

PHYSICS OF HHG: MACROSCOPIC SCALE

4. PROPAGATION EQUATIONS

We have described the model to compute the microscopic source term of HHG for an arbitrary electric field in Chapter 2. The tasks are now: 1) compute the electric field at every macroscopic point of the medium, 2) sum all the microscopic responses to form a macroscopic picture of the generation.

In principle, the microscopic source term includes all the effects in both IR and XUV domains. A direct approach would be then to couple the microscopic response directly with the Maxwell's equations (1.11) as done in [88]. We call this approach *the strong coupling*. However, the resulting implementation may be very computationally expensive because of the fine discretisation needed to describe both IR and XUV. Our strategy is then different. First, we note that the XUV spectral range is weakly coupled with the medium because the overall XUV signal is small compared to the IR-field. It means that the XUV propagation may be computed separately from the linearity of the Maxwell's equations. Second, the source term obtained from the TDSE is necessary for the XUV field, but standard non-linear optics describe well the response of the medium for the problems of our interest. In summary, we can decouple several physical processes within the model and treat them independently.

The outlined procedure then leads to our computation strategy, that we call *the weak coupling*. The calculation is then performed in 3 steps: 1) The propagation of the IR-field is computed by means of standard non-linear optics. 2) The fields are used as inputs of the microscopic solver to compute the non-linear response of the medium in the XUV region discussed in Section 2.3. 3) The propagation of the XUV field is computed by means of linear optics.

We can then separate the physical processes and we discuss them in the chapter of this part of thesis as follows: the rest of this chapter provides a unified framework to derive the propagation equations from the Maxwell's equations. Chapter 5 introduces the solution of the propagation of the XUV field using the linear diffraction theory. These tools are already sufficient to treat the physics of the thin targets, and we apply it to find the focusing properties of XUV in this geometry. The multi-scale model is completed in Chapter 6, where the non-linear model of the IR-propagation is introduced. Finally, we use it to the ab-initio study of the optimisation of the phase-matching of HHG in pre-ionised media.

4.1 Macroscopic Maxwell's equations

Because we are moving to the laboratory scale, we use the Macroscopic Maxwell's equations (MaME) to describe the fields,

$$\operatorname{div} \boldsymbol{D} = \varrho_{Q,\text{free}}\,, \qquad \operatorname{div} \boldsymbol{B} = 0\,, \tag{4.1a}$$

$$\operatorname{rot} \boldsymbol{\mathcal{E}} = -\frac{\partial \boldsymbol{B}}{\partial t}\,, \qquad \operatorname{rot} \boldsymbol{H} = \boldsymbol{j}_{Q,\text{free}} + \frac{\partial \boldsymbol{D}}{\partial t}\,. \tag{4.1b}$$

These equations are an averaged version of (1.11).[1] Here we have introduced new quantities $\boldsymbol{H}$ and $\boldsymbol{D}$. The former is straightforwardly, $\boldsymbol{H} = \boldsymbol{B}/\mu_0$; a more complicated relation would be used in the case of magnetic materials (far beyond the scope of gaseous media of our interest). However, the latter is non-trivial $\boldsymbol{D} = \varepsilon_0 \boldsymbol{\mathcal{E}} + \boldsymbol{P}$, where $\boldsymbol{P}$ is the polarisation vector containing both linear and non-linear responses of the medium. To put the MaME in the context, we link them with the microscopic description and then derive the wave equation needed for the propagation of both IR and XUV.

4.1.1 Macroscopic from microscopic

The interlink of these two descriptions is the current density averaged over one microscopic system (2.9), [125] which is further decomposed into the bound and continuum part (which may be done via (C.3)):

$$\langle \boldsymbol{j} \rangle = \langle \psi_\text{b} | \boldsymbol{p} - \boldsymbol{A} | \psi_\text{b} \rangle + 2\,\mathsf{Re}\,\langle \psi_\text{c} | \boldsymbol{p} - \boldsymbol{A} | \psi_\text{b} \rangle + \langle \psi_\text{c} | \boldsymbol{p} - \boldsymbol{A} | \psi_\text{c} \rangle = -\boldsymbol{j}_{Q,\text{free}} - \frac{\partial \boldsymbol{D}}{\partial t}\,. \tag{4.2}$$

The last equality identifies the source term computed from quantum mechanics and from the MaME. Because we consider the current induced by electrons, the relation of the probability current and charge current is simply $\boldsymbol{j}_Q = -\boldsymbol{j}$. Recalling the discussion done after (2.11), various physical phenomena are clearly seen in this equation:[2]

1. The continuum-continuum transition, $\langle \psi_\text{c} | \boldsymbol{p} - \boldsymbol{A} | \psi_\text{c} \rangle$, contains free current, $\boldsymbol{j}_{Q,\text{free}}$. Strictly speaking, there is also scattering of electrons on the microscopic system, discussed as rescattering in HHG.

---

[1] From the fundamental viewpoint, macroscopic does not mean that they include more physics than their microscopic counterpart. In contrary, the macroscopic aspect is an averaging, which may simplify the description.

[2] This schematic form may be modified in the case beyond single active electron for n electron. A j-times ionised state is $\left|\psi_\text{c}^{(1)}, \dots, \psi_\text{c}^{(j)}, \psi_\text{b}^{(j+1)}, \dots, \psi_\text{b}^{(n)}\right\rangle$ with a proper anti-symmetrisation. The collisional ionisation may be included in the model by $\langle \psi_\text{c}, \psi_\text{c}, \psi_\text{b}, \dots, \psi_\text{b} \,|\, \boldsymbol{p} - \boldsymbol{A} \,|\, \psi_\text{c}, \psi_\text{b}, \dots, \psi_\text{b} \rangle$. Generalisations to other multi-electron processes are straightforward.

2. The bound-bound transition, $\langle\psi_\mathrm{b}|\boldsymbol{p}-\boldsymbol{A}|\psi_\mathrm{b}\rangle$, is exactly the averaging procedure [125] giving the principal contribution to $\partial_t\boldsymbol{D}$.
3. The bound-continuum transition, $\langle\psi_\mathrm{c}|\boldsymbol{p}-\boldsymbol{A}|\psi_\mathrm{b}\rangle$, is related to the HHG (that we neglect for the propagation of the driver), but also to optical ionisation, which plays a crucial role. This process violates the formal decomposition $\boldsymbol{j}_{Q,\mathrm{free}}+\partial_t\boldsymbol{D}$, because it contributes to both free, $\boldsymbol{j}_{Q,\mathrm{free}}$ and bound, $\partial_t\boldsymbol{D}$, term. The explanation is clear: the electron contributes to $\partial_t\boldsymbol{D}$ until it is unbound by ionisation, then it is described by $\boldsymbol{j}_{Q,\mathrm{free}}$. The ionisation process then links these two cases.

These effects are accounted in the macroscopic propagation model using approaches of non-linear optics, our concrete implementation for the IR pulse is in Section 6.1.3.

The remaining part is to scale the current density of a single microscopic system into the macroscopic description. Because we do not consider any mutual interactions between the microscopic systems, the appropriate macroscopic current density is retrieved only by multiplying by the number density of particles at a given pressure $N(p)$:

$$\boldsymbol{j}_Q^{(\mathrm{macro})} = N(p)\left\langle \boldsymbol{j}_Q^{(\mathrm{micro})}\right\rangle , \tag{4.3}$$

where $\langle\cdot\rangle$ stands for the average over the microscopic volume [125]. Because the usual gases of interest for HHG satisfy the ideal gas law, the number density of particles at a given temperature T is $N(p)=p/(k_\mathrm{B}T)$.[3] As we will use only the macroscopic current density, we denote it simply $\boldsymbol{j}_Q$ hereafter.

4.1.2 Wave equation

Now, we derive the wave propagation equation for the electric field $\boldsymbol{\mathcal{E}}$ from (4.1). The linear response in $\boldsymbol{D}$ has a simpler expression in the frequency domain: The dispersion and absorption are given just by the multiplication by the complex first-order electric susceptibility $\chi^{(1)}(\omega)$. It means[4]

$$\hat{\boldsymbol{D}} = \varepsilon_0\hat{\boldsymbol{\mathcal{E}}} + \hat{\boldsymbol{P}} = \varepsilon_0\hat{\boldsymbol{\mathcal{E}}} + \hat{\boldsymbol{P}}_\mathrm{lin} + \hat{\boldsymbol{P}}_\text{non-lin} = (\varepsilon_0 + \varepsilon_0\chi^{(1)}(\omega))\hat{\boldsymbol{\mathcal{E}}} + \hat{\boldsymbol{P}}_\text{non-lin} = \varepsilon_0\varepsilon_r(\omega)\hat{\boldsymbol{\mathcal{E}}} + \hat{\boldsymbol{P}}_\text{non-lin} , \tag{4.4}$$

Using this expansion, we have

$$\left(\triangle + k^2(\omega)\right)\hat{\boldsymbol{\mathcal{E}}} = \mu_0\widehat{\partial_t\boldsymbol{j}_{Q,\mathrm{free}}} - \mu_0\omega^2\hat{\boldsymbol{P}}_\text{non-lin} + \frac{1}{\varepsilon_0}\,\mathrm{grad}\left(\varrho_{Q,\mathrm{free}} - \mathrm{div}\,\hat{\boldsymbol{P}}\right) . \tag{4.5}$$

---

[3] Practically, the experiments of our interest are usually done close to the standard temperature and the number density is thus $N(p)=pn_0/p_0$, where p_0 is the standard pressure and n_0 the Loschmidt constant.

[4] Throughout this and the following chapter, we find that some effects are more convenient to be described in the frequency domain while others in the time domain. We thus specify the domain in every equation by denoting the Fourier transform of f by $\hat{f}$ or $\mathscr{F}[f]$ or by the explicit integration.

The linear effects on the left-hand side are indeed encoded in the dispersion relation $k^2(\omega) = \varepsilon_0\mu_0\omega^2\varepsilon_r(\omega) = \omega^2\varepsilon_r(\omega)/c^2$. The last term in (4.5) mixes various vector components. To find a solution, we would need to treat the set of the coupled equations. The problem can then be stated: "Is there a way to approximate the solution to remove the coupling?" First, we need to specify more the geometry of the problem. The solutions of our interest are *beams* with a defined direction of propagation. It decomposes vectors into two subspaces: $\|$ along the propagation direction and $\perp$ its transversal orthogonal complement. Generally, the strength of the coupling of the transversal and longitudinal component is characterised by the parameter $f = \lambda/(2\pi w) \sim k_\perp/k_\|$; where λ is the wavelength of the radiation of interest, w the width of the beam, $k_\perp$ and $k_\|$ the components of the Poynting vector in the respective directions. The last term of (4.5) may be neglected if $f \ll 1$ (see [181, 182, 183]), which is fulfilled in the geometries that we will investigate in this work. The propagation of the field is then described by

$$\left(\triangle + k^2(\omega)\right)\hat{\boldsymbol{\mathcal{E}}} = \mu_0\widehat{\partial_t \boldsymbol{j}_{Q,\text{free}}} - \mu_0\omega^2\hat{\boldsymbol{P}}_{\text{non-lin}}\,. \tag{4.6}$$

The way to solve this equation is split for the XUV and IR beams. This is the subject of the following two chapters.

5. XUV PROPAGATION & THIN TARGETS

We discuss two topics in this chapter. First, we introduce the description of the XUV fields using the diffraction in Section 5.1. This completes the apparatus needed to study the focusing of harmonics on thin targets. The model is then applied to this configuration in Section 5.2. The numerical multi-scale approach is complemented by simpler physical model to recognise the key mechanisms. This chapter is concluded by using a phenomenological model of HHG in long media in Section 5.3.

5.1 Macroscopic model of HHG

Here, we explicitly determine the macroscopic XUV field. Since there are no non-linear effects considered for XUV, only the source $\widehat{\partial_t \boldsymbol{j}_Q}$ remains on the RHS of (4.6).

Before we derive the far-field distribution, we briefly discuss the locally generated electric field under this assumption. If we further neglect the spatial variation in (4.6), we retrieve a simple direct relation between the current and the electric field:

$$\hat{\boldsymbol{\mathcal{E}}} = -\frac{\mathbf{i}\hat{\boldsymbol{j}}_Q}{\varepsilon_0 \omega}\,. \tag{5.1}$$

This equation then complements the intuitive picture that the electric field of a dipole follows directly the moving charge.

Now including the spatial dependence, we need to solve $\left(\triangle + k^2(\omega)\right)\hat{\boldsymbol{\mathcal{E}}} = \mu_0 \widehat{\partial_t \boldsymbol{j}_Q}$. By neglecting the coupling, it may be directly integrated using its Green's function (Chapter 6.4 of [118]):

$$\hat{\boldsymbol{\mathcal{E}}}(\omega, \boldsymbol{r}) = -\frac{\mu_0}{4\pi}\int_{V'} \frac{\mathrm{e}^{\mathbf{i}k(\omega)|\boldsymbol{r}-\boldsymbol{r}'|}}{|\boldsymbol{r}-\boldsymbol{r}'|}\left(\widehat{\frac{\partial \boldsymbol{j}_Q}{\partial t}}\right)\mathrm{d}V'\,. \tag{5.2}$$

The integration is over the whole interaction volume V'.

Next, we use the cylindrical symmetry and simplify the integral in the transversal dimensions

$$\hat{\boldsymbol{\mathcal{E}}}(\omega, \rho, z) \approx -\frac{\mu_0 \mathrm{e}^{\mathbf{i}k(\omega)z}}{4\pi}\int_{z_{\text{entry}}}^{z_{\text{exit}}} \frac{\mathrm{e}^{-\mathbf{i}k(\omega)z'}\,\mathrm{e}^{\mathbf{i}\frac{k(\omega)\rho^2}{2(z-z')}}}{z-z'}\int_{\Delta_T} \mathrm{e}^{\mathbf{i}\frac{k(\omega)(\rho')^2}{2(z-z')}}\left(\widehat{\frac{\partial \boldsymbol{j}_Q}{\partial t}}\right) J_0\left(\frac{k(\omega)\rho\rho'}{z-z'}\right)\rho'\,\mathrm{d}\rho'\,\mathrm{d}z'\,, \tag{5.3}$$

where J_0 is the Bessel function of the first kind. The simplification of the transversal integration is due to the approximation $|z - z'| < \rho'$ and $|z - z'| < \rho$

$$|\boldsymbol{r} - \boldsymbol{r}'| \approx z - z' + \frac{2\rho\rho'\cos\theta}{z - z'} + \frac{\rho^2 + (\rho')^2}{2(z - z')}\,, \tag{5.4}$$

see Appendix D for more detailed discussion of the approximation together with its physical interpretation. Due to this approximation, the integration in (5.3) is simplified for the cylindrical symmetry: The angular integration is analytical by using (the identity 9.1.21 of [184])

$$J_0(z) = \frac{1}{\pi}\int_0^{\pi} \mathrm{e}^{\mathbf{i}z\cos\theta}\,\mathrm{d}\theta\,. \tag{5.5}$$

5.1.1 Metrology of XUV signal

Because the XUV field is our ”final product”, we introduce here some of its shared diagnostics we use in examples. The XUV from HHG has usually a specific shape: it forms a harmonic comb in frequency and a train of pulses in time. A general diagnostic is presented in Appendix B.

The comb naturally separates in various harmonics. We thus define a ”beam” of a given harmonic q as spectral fluence integrated only over the respective harmonic peak:[1]

$$S_q(z,\rho) = \int\limits_{\omega_0\left(q-\frac{1}{2}\right)}^{\omega_0\left(q+\frac{1}{2}\right)} \left|\hat{\mathcal{E}}(z,\rho,\omega)\right|^2\,\mathrm{d}\omega\,. \tag{5.6}$$

A further integration over the radial coordinate gives the energy contained within the disc of radius ρ

$$E_q(\rho,z) = 2\pi\int_0^{\rho} S_q(z,\rho')\rho'\,\mathrm{d}\rho'\,. \tag{5.7}$$

The total energy is given by $E_q^{(\mathrm{tot})} = E_q(\rho\to+\infty, z)$. Because we consider a free-space propagation after the interaction volume, there is no absorption and the energy is then conserved, thus z-independent.

5.2 HHG from thin targets: optics-less focusing

Once we have the source term giving HHG as dipole radiation at any point of the medium, we can sum them up together. Our first study employs a simplified geometry of thin targets. A thin target means that the evolution of the driving laser is negligible along the propagation in the target. The interest of thin targets is that transversal aspects of HHG are decoupled.

---

[1] Because there are no even harmonics generated by a linearly polarised field, the integration may be also extended to $\omega_0\,]q-1, q+1[$.

More rigorously, the reduction to thin targets is possible if:

1. The longitudinal dimension of the target $L = |z_{\text{exit}} - z_{\text{entry}}|$ is much smaller than the Rayleigh range, i.e. $L \ll z_R$.
2. The medium is not dense enough to modify the field significantly along this path.

The integrations over ρ' and z' in (5.3) separate in that case and only the integration over ρ' defines the radial distribution in the far-field. The integration over z' becomes a pre-factor. This pre-factor may accounts for phase-matching in this case, which affects uniformly the whole far-field spectra. An important conclusion is that all the spatially resolved structures within the spectrum are only due to the transversal aspect of the generation.

A practical implementation of our interest is a gas jet. We then use *"jet"* as a synonym of thin target in this work.

5.2.1 Motivation

One of the advantages of the thin targets is that one part of the complexity is removed. It makes easier the macroscopic analysis of the generation process: all the effects are attributed to the transversal aspects of the field. Experimentally, it allows an easier control and manipulation with the XUV beam. Our study continues the work done in [33], which assigned the spatio-frequency interference patterns [185, 186, 187] to spatio-temporal profile of the driving pulse. The next step is to study the profile of the resulting XUV field as a function of the respective position of the thin target and the driving IR-beam. Together with experimentalists, we studied and proved that the focusing properties of the XUV are controlled by this mechanism. The main findings on this topic are summarised in the papers [34, 35], these papers link theory with experimental results. The first paper study the XUV beams in the far-field region. The second paper exploits this study further by placing a pinhole in the XUV beam: The transmittance through the pinhole gives a direct measurement of the focusing properties. We explain more details in this manuscript from the theoretical part. The experiment is treated in more details in the references and in [188].

According to these goals, the main questions to answer are: 1) How are the focusing properties affected by the driving field? In other words, is the process spectrally selective? 2) How do the field change from one harmonic order to the other? 3) How to control this mechanism to engineer the XUV field? This section is organised as follows: We start with a simple model using Gaussian optics in Section 5.2.2, then we move to the fully numerical approach mimicking the experiment in Section 5.2.5.

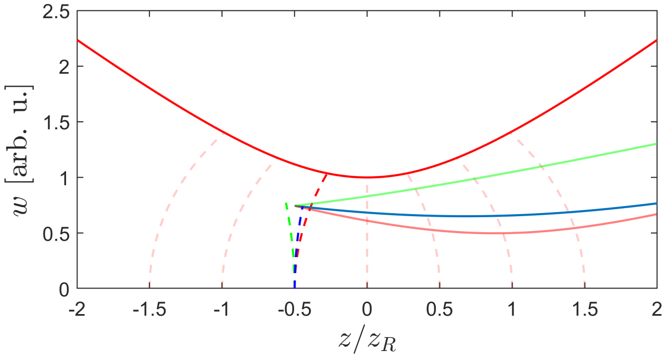

Fig. 5.1: The illustration of the optics-less focusing mechanism: the summing of the two curvatures. There is the driving IR-beam (red) and the thin target (radiating plane) is placed at -0.5. The inherited phase is in red and the intrinsic atomic phase induced the green curvature. Both of them are summed to form the XUV beam (blue).

5.2.2 Key principle: summing two curvatures

The set-up to is composed of a thin target placed perpendicularly to the driving beam at point z_0 along the propagation axis, where the origin of the coordinates is chosen at the focus of the driving beam as shown in Fig. 5.1.

A basic physical model is to consider the XUV field for each harmonic as a Gaussian beam. This model is justified by two arguments. First, the generated XUV beam is well-approximated by a Gaussian beam by inserting the phenomenological dipole (2.19) into the Gaussian profile of the driving beam. This approximation describes well the quadratic profile of the phase because the highest XUV contribution is near the maximum on the optical axis. Second, it agrees well with experimental findings. This model was already presented in [126] and this section is adapted from it.

The ABCD propagation of Gaussian beams

All the parameters defining a Gaussian beam in one plane perpendicular to its propagation direction at the point z can be obtained from the complex parameter $\mathscr{Q}$ [189], Chapter III.6;[2] that is defined by

$$\frac{1}{\mathscr{Q}_z} = \frac{1}{R(z)} - \mathbf{i}\frac{\lambda}{\pi w^2(z)} \,. \tag{5.8}$$

R is the radius of curvature of the beam wavefront, $w(z)$ is the beam radius, i.e. the radius where the intensity is equal to $1/\mathrm{e}^2$ of the on-axis intensity. The advantage of this formalism is that the

---

[2] We denote the parameter by the calligraphic $\mathscr{Q}$ because we already use q for the harmonic order.

evolution of $\mathscr{Q}$ from an initial state, $\mathscr{Q}^{(i)}$, to a final state, $\mathscr{Q}^{(f)}$, is given by

$$\mathscr{Q}^{(f)} = \frac{A\mathscr{Q}^{(i)} + B}{C\mathscr{Q}^{(i)} + D} \tag{5.9}$$

for a linear optical system described by the matrix $\left(\begin{smallmatrix} A & B \\ C & D \end{smallmatrix}\right)$. The indices i and f denote the initial and final values, respectively. The free propagation matrix is $\left(\begin{smallmatrix} 1 & d \\ 0 & 1 \end{smallmatrix}\right)$, where d is the propagation distance. We find the formula

$$\mathscr{Q}_{z_0+d} = \mathscr{Q}_{z_0} + d \tag{5.10}$$

for propagation from z_0 to $z_0 + d$.

As stated above, a Gaussian beam is fully defined by the parameter $\mathscr{Q}_{z_0}$ at a given point z_0 (5.8). For the analysis, the parameters of the Gaussian beam (w_0, z_R and the position of the focal point) are needed. Using (5.8) and (5.10), one obtains

$$w^2(z_0 + d) = \frac{\pi^2 w^4(z_0)\left(R(z_0) + d\right)^2 + d^2\lambda^2 R^2(z_0)}{\pi^2 R^2(z_0) w^2(z_0)} \,. \tag{5.11}$$

The minimization of that function with respect to d gives the focal point in the position $z_0 + d_f$. Next, we use the definition of the Gaussian beam, (B.6), and we find the waist and Rayleigh length. All these parameters are given by

$$d_f = -\frac{R(z_0)}{1 + \left(\frac{\lambda R(z_0)}{\pi w^2(z_0)}\right)^2}\,, \quad w_0^2 = w_0^2(z_0 + d_f) = \frac{w^2(z_0)}{1 + \left(\frac{\pi w^2(z_0)}{\lambda R(z_0)}\right)^2}\,, \quad z_R = \frac{\pi\lambda R^2(z_0) w^2(z_0)}{\lambda^2 R^2(z_0) + \pi^2 w^4(z_0)}\,. \tag{5.12}$$

The generated field as a Gaussian beam

The qualitative insight into the origin of the spatial distribution can be obtained from the theory of Gaussian-beam propagation and from the dipole model (2.19). We are analysing the generated field for a given harmonic order q. Let us look at the radial distribution of the field modulus and phase, that defines the beam radius and curvature, respectively. The field modulus follows the law $|\mathcal{E}_q| \propto |\mathcal{E}_{\mathrm{IR}}|^{q_{\mathrm{eff}}}$ (see (2.19)), thus the beam waist of the harmonic q is $w_q(z_0) = w(z_0)/\sqrt{2q_{\mathrm{eff}}}$. The spatial distribution of the phase is the sum of the IR-beam phase and the additional intensity dependent phase ($-\alpha I_{\mathrm{IR}}$). The intensity distribution in the first order expansion is (see (B.6))

$$I_{\mathrm{IR}}(\rho) = \left(\frac{w_0}{w(z_0)}\right)^2 I_0 \mathrm{e}^{-\frac{2\rho^2}{w^2(z_0)}} \approx \left(\frac{w_0}{w(z_0)}\right)^2 I_0 - \frac{2w_0^2 I_0 \rho^2}{w^4(z_0)}\,, \tag{5.13}$$

Substituting this expansion in (2.19) and adding the IR-beam phase, we find the effective curvature, R_q, of the harmonic q as the solution of

$$\frac{k_q\rho^2}{2R_q(z_0)} = \frac{k_q\rho^2}{2R(z_0)} - \alpha I_{\mathrm{IR}}(\rho) \approx \frac{k_q}{2}\left(\frac{1}{R(z_0)} + \frac{4\alpha w_0^2 I_0}{k_q w^4(z_0)}\right)\rho^2 \quad \Rightarrow \quad \frac{1}{R_q(z_0)} \approx \frac{1}{R(z_0)} + \frac{4\alpha w_0^2 I_0}{k_q w^4(z_0)}\,. \tag{5.14}$$

This equation expresses the reciprocal sum of two curvatures. The first, $R(z_0)$, is simply that of the driving beam, while the second, $R_{\mathrm{atom}} = k_q w^4(z_0)/\left(4\alpha w_0^2 I_0\right)$, is the *intrinsic curvature of the generating process*.

Finally, the waist, w_q, of the harmonic q is found inserting the proper curvature and waist in (5.11):

$$w_q^2(z_0+d) = \frac{\pi^2 w_q^4(z_0)\left(R_q(z_0)+d\right)^2 + d^2\lambda_q^2 R_q^2(z_0)}{\pi^2 R_q^2(z_0) w_q^2(z_0)}\,, \tag{5.15}$$

where λ_q and R_q are the wavelength of the harmonic field and radius of curvature respectively and d is the distance from the studied plane.

The summation of the curvatures is illustrated in Fig. 5.1. We also show in Appendix F that the expansion of the phase of the microscopic dipole within the first order is inherent to the Gaussian optics, and higher orders of phase would go beyond the Gaussian optics.

5.2.3 Methodology, microscopic dipoles

We use several levels of complexity to model the harmonic dipole and the propagation of the XUV field. We start with the dipole coming from SFA including the Saddle-point calculation (2.17) together with the phenomenological approach (2.19):

1. A constant α: This model of the intensity-dependent phase $\varphi = \alpha I$ is already capable to explain the main effect in the spatial structure of the harmonics in the far-field [33].
2. A linear evolution with the harmonic order: $\alpha_q = Aq + B$.
3. The exact fit of the phase computed by FSPA: $\alpha_q = \alpha(q, I)$, where its value is retrieved from the Full Saddle Point Approximation. This model actually fully reproduces the phase, $\varphi(q\omega_0, I) = \alpha(q, I)I$, computed from FSPA.[3] However, we have to take this value constant and evaluate it on the optical axis of the beam at the point of the XUV generation to be consistent with the Gaussian-optics model (5.14).

---

[3] We could point out that there is also another strategy for approximating $\alpha(q, I)$, see formula (6) in [190]. They used a numerical solution to find a larger set of fit parameters to find a global fitting function. Our strategy is that we take the numerical solution anywhere and we then use a first-order local fit in the variable of our interest.

4. Fully numerical treatment using a numerical 1D-TDSE solver for the microscopic dipole combined with the numerical propagation (5.3).

The comparison of the model of the XUV phase based on SFA in the points 2 and 3 is shown in Fig. 5.2.

The parameters of simulations were chosen according to the experiment: $w_0 = 85\ \mu$m, $I_0 = 4 \times 10^{14}$ W/cm^2, $\lambda = 800$ nm, pulse (FWHM) duration 40 fs; the ionisation potential: $I_P = 0.792$ a.u.; of neon is the only parameter describing the target in this model. Harmonics from 29 to 47 were studied. Using these values, we may find the region interesting for studies. The initial experimental campaign [34] recognised the region of the interest being within the Rayleigh range $z_R \approx 30$ mm (computed in our conditions). Second, the study remains in the plateau regime, where the harmonics are efficiently produced, see Fig. 5.3. We thus retrieve the region of interest for $z \in [-20, 0]$ mm.

In the second part, we study the filtering by a pinhole placed at $z_{\text{pinhole}} = 37$ cm and with the radius $\rho_{\text{p}} = 70\ \mu$m.

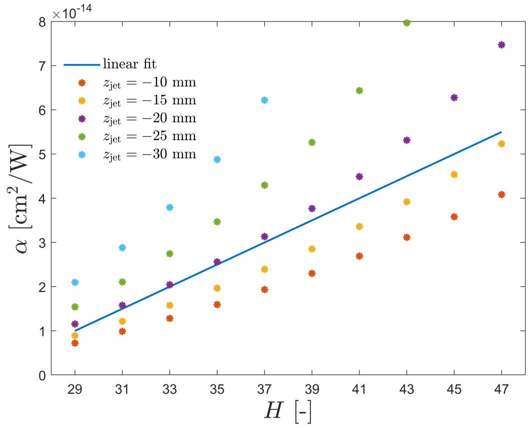

Fig. 5.2: The evolution of α with the harmonic order. We compare there three cuts for intensities in the positions of the generation that we discuss further. There are also two extra placements for comparison. Finally, there is the linear fit that we used in the part of the study.

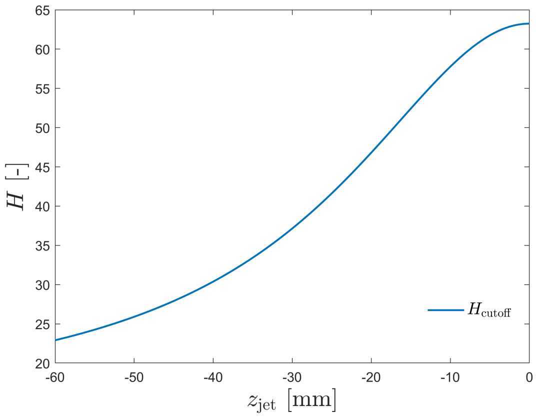

Fig. 5.3: The on-axis harmonic cutoff in our conditions.

The fundamental quantity of interest is the generated electric field $\mathcal{E}$. It is computed from (5.3) by assuming thin targets:

$$\hat{\mathcal{E}}(z_{\text{jet}}; z, \rho, \omega) \propto \int_0^{+\infty} \frac{\mathrm{e}^{-\mathbf{i}\frac{k(\omega)\tilde{\rho}^2}{2D}}}{D} \widehat{\partial_t j}\,(\tilde{\rho}, \omega)\, J_0\left(\frac{k(\omega)\rho\tilde{\rho}}{D}\right) \tilde{\rho}\,\mathrm{d}\tilde{\rho}\,, \qquad D = z - z_{\text{jet}}\,. \tag{5.16}$$

We keep the coordinate frame fixed by the coordinates of IR-beam (the focus at $z = \rho = 0$). Next, we classify the corresponding beam by the S_q-metric introduced by (5.6). Next, we use FWHM, energy passed through a given disc and root-mean-square characteristics (ISO recommended [191]); we denote them, respectively, $\rho_{q,\mathrm{FWHM}}(z_{\mathrm{jet}};z)$, $E_q(z_{\mathrm{jet}};z,\rho)$ and $\rho_{q,\mathrm{rms}}(z_{\mathrm{jet}};z)$.[4]

5.2.4 XUV beams & spectra

We start with an example of beams for the jet placed 15 mm before the IR-focus for the harmonics 29, 37 and 49. These beams are shown in Fig. 5.4. We present in this figure the results from the linear-phase model, FSPA and TDSE as explained in Section 5.2.3. The beam S_{29} is irregular and defocused, it suggests a more structured profile for lower harmonics. S_{37} is a low-divergent and regular beam. The last beam, S_{47}, is divergent and regular.

These three beams suggest that there is the desired focusing property as S_{37} is less divergent than the others. Complementary to the shown far-field distributions, we place a virtual observation screen in the position of the pinhole and move the jet. Figure 5.5 shows the full spectra, $|\mathcal{E}(z_{\mathrm{jet}} = z_{\mathrm{jet},0}; z = z_{\mathrm{pinhole}}, \rho, \omega)|^2$, for different positions of the jet, $z_{\mathrm{jet},0}$. We can trace the spectral selectivity with moving the jet position, z_{jet}, in these spectra. For the spectrum corresponding to the beams from Fig. 5.4, $z_{\mathrm{jet}} = -15$ mm, there is a minimum of the divergence in the plateau around H37-H39. Tracing the minimum divergence with z_{jet} approaching the IR-focus, we find the minimum moving from the cutoff towards lower frequencies in the plateau (note that the cutoff position varies with z_{jet} as depicted in Fig. 5.3).

---

[4] $E_q(z_{\mathrm{jet}};z,\rho) = \int_0^\rho S_q(z_{\mathrm{jet}};z,\rho')\,\rho'\mathrm{d}\rho'$ and $\rho_{q,\mathrm{rms}}(z_{\mathrm{jet}};z) = \sqrt{\int_0^{+\infty} \rho^2 S_q(z_{\mathrm{jet}};z,\rho)\,\mathrm{d}\rho / \int_0^{+\infty} S_q(z_{\mathrm{jet}};z,\rho)\,\mathrm{d}\rho}$.

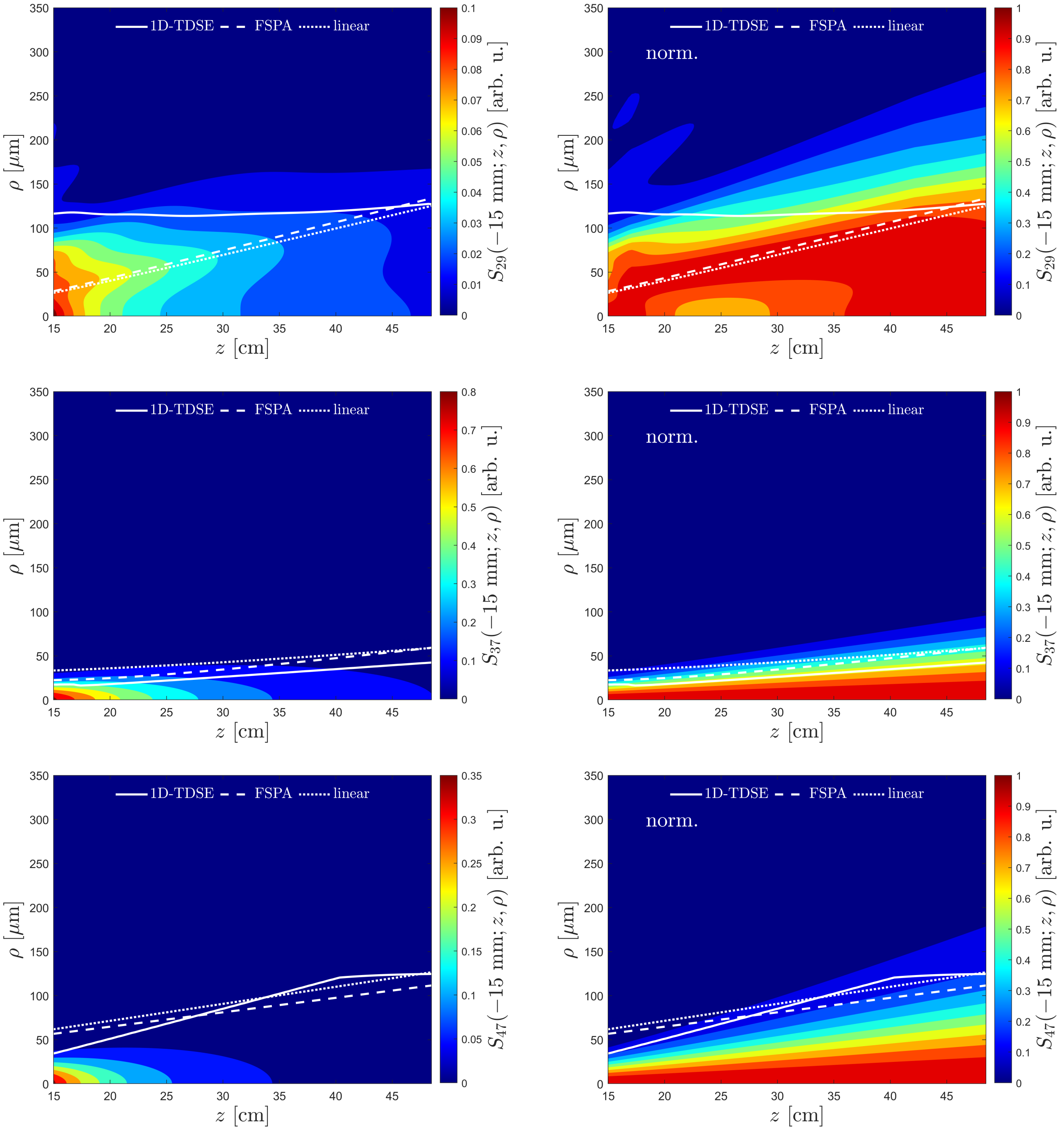

Fig. 5.4: The harmonic beams $S_H(z_{\text{jet}} = -15\text{ mm}, z, \rho)$ for harmonics, H, within the range of our interest. We show various versions of the beams. The color-scale correspond to the fully numerical of the diffraction from the TDSE dipoles, the corresponding metric of the beam is ρ_{rms} shown by the full white lines. There are also Gaussian beams obtained from the linear and FSPA-models; dotted and dashed lines, respectively. Next, the beams are shown both in the original scale and normalised by $S_{\text{norm.}}(\rho, z) = S(\rho, z)/\max_{\rho} S(\rho, z)$. To recall the conditions, the harmonics are generated in a thin neon jet by a driving field defined by $w_0 = 85\ \mu\text{m}$, $I_0 = 4 \times 10^{14}\ \text{W/cm}^2$, $\lambda = 800\text{ nm}$, $\tau_{\text{FWHM}} = 40\text{ fs}$, the intensity for $z_{\text{jet}} = -15\text{ mm}$ is inferred from Fig. 5.3 or Tab. 5.1.

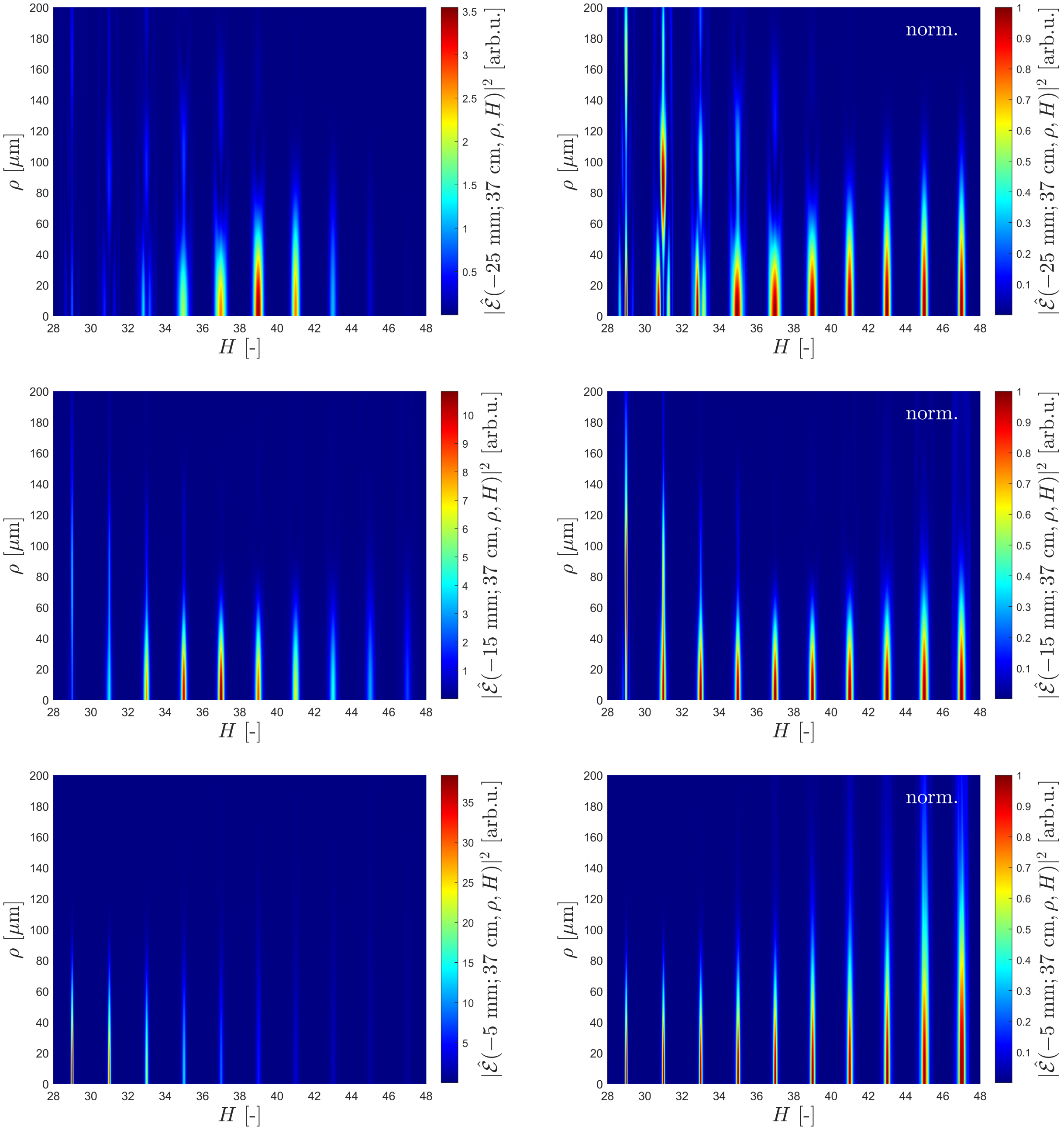

Fig. 5.5: The spatially resolved spectra in the position of the pinhole. The minimum of divergence traverse throughout the plateau as the jet moves towards the focus. Denoting $S = \mathcal{E}(z_{\text{jet}} = z_{\text{jet},0}, z = z_{\text{pinhole}}, \rho, H)$, the normalisation around a given harmonic, H_i, is defined as $S_{\text{norm}} = S/\left(\max_{(\rho,H)\in\mathbb{R}^+\times[H_i-1/2,H_i+1/2]}|S|\right)$. The parameters correspond to Fig. 5.4

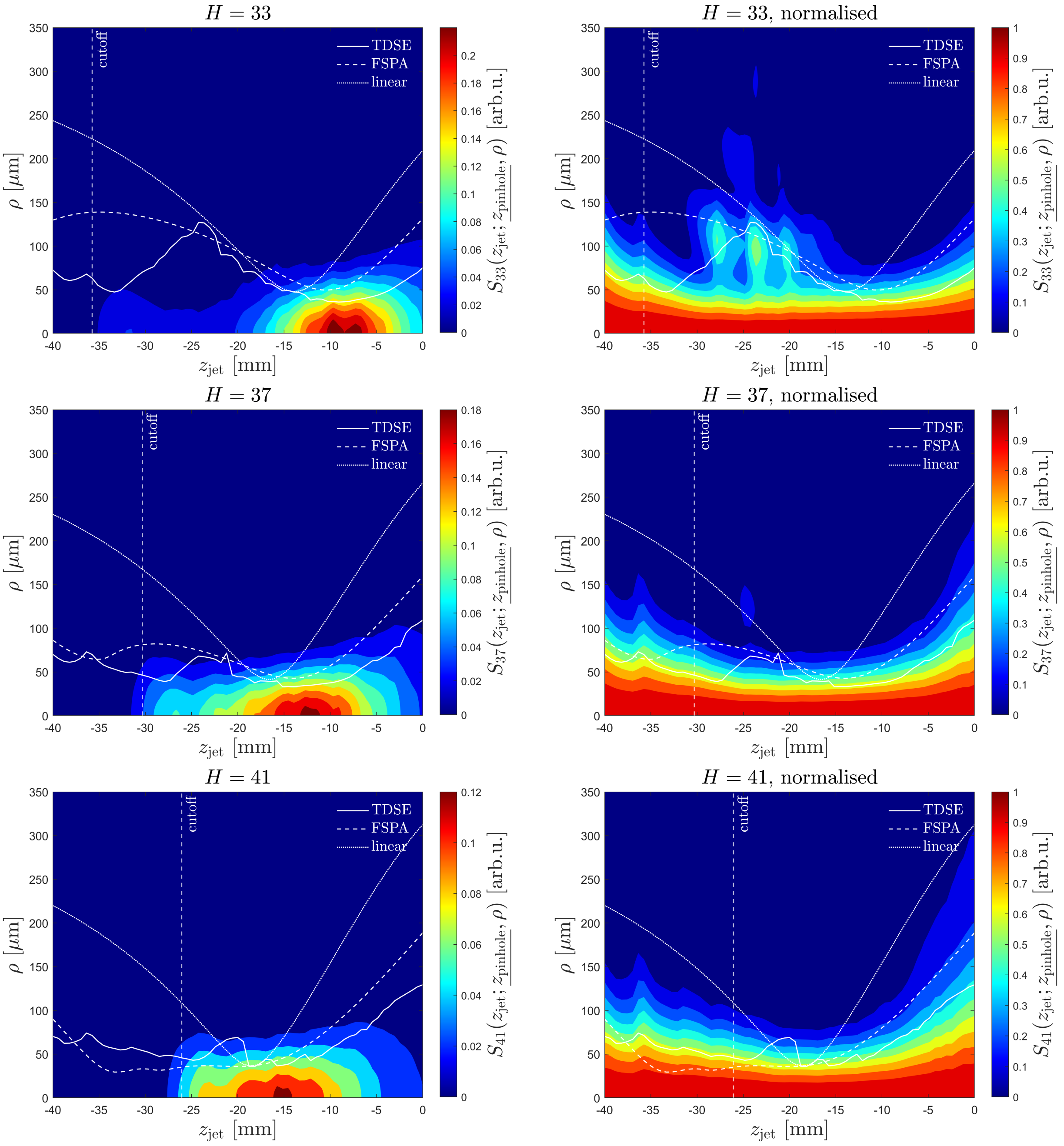

Fig. 5.6: These panels show $S_q(z_{\text{jet}}, z = z_{\text{pinhole}}, \rho)$, that represents the beam sections at the position of the pinhole as functions of the jet positions. The solid, dashed and dotted lines represent ρ_{rms} for 1D-TDSE-, FSPA- and linear-model-beam, respectively. The parameters correspond to Fig. 5.5; $z_{\text{pinhole}} = 37$ cm.

To combine the previous two pictures – the beams and the spectra at the pinhole position –, we show also the cut through the beam of H29, H37 and H47 at the position of the pinhole as a function of z_{jet} in Fig. 5.6. It agrees and complements the picture of the spectral selectivity as a function of the jet position. There is clearly seen the variation of the minimal spot-size at the position of the pinhole as a function of the position of the jet.

In summary, Figs. 5.4, 5.5 and 5.6 have provided us a comprehensive picture of the generation scheme. We did cuts in the three principal variables of this generating scheme: the harmonic order H, the propagation distance z and the position of the jet z_{jet}. It basically confirmed the key idea using all the models: the divergence of the harmonics is controlled by the placement of the jet, i.e. by the curvature of the driving beam, and this control is spectrally selective. To get a better insight we analyse in detail the generation regime of the harmonics (plateau vs. cutoff, ...) and study the XUV field also after the filtering by the pinhole in the following Sections.

5.2.5 Transmittances: probing XUV beams by pinhole

Here, we qualitatively estimate the focusing by the same methodology as done in the experiment: the pinhole is placed in the XUV beam, and we compute the transmittance through it. The experimental results are shown in Fig. 5.7. It should be noted that the absolute strength of the signal is not kept because the cutoff changes with z_{jet}. We summarise the expected cutoffs in Tab. 5.1.

z_{jet} [mm]	H_{cutoff} [-]
-5	61.8
-10	57.8
-15	52.4
-20	46.8
-25	41.6

Tab. 5.1: The cutoffs corresponding to the positions of jets of the interest.

Figure 5.8 shows the transmittances both as a function of harmonic order and of various jet positions.

The first dependence we trace in Fig. 5.8 is the evolution with the harmonic order, i.e. the spectral selectivity. It confirms the picture inferred from the incident XUV beams, Fig. 5.5, – transmittances increase as the beam radii decrease. Here we also compare different dipole models. All of them qualitatively agree. Let us describe the linear model: the transmittance in the region of the interest decreases with the harmonic order once the jet is close to the focus, $z_{\text{jet}} \in \{-5, -10\}$ mm. The maximum of the transmittance then traverses the region as it forms a bell-shaped curve for

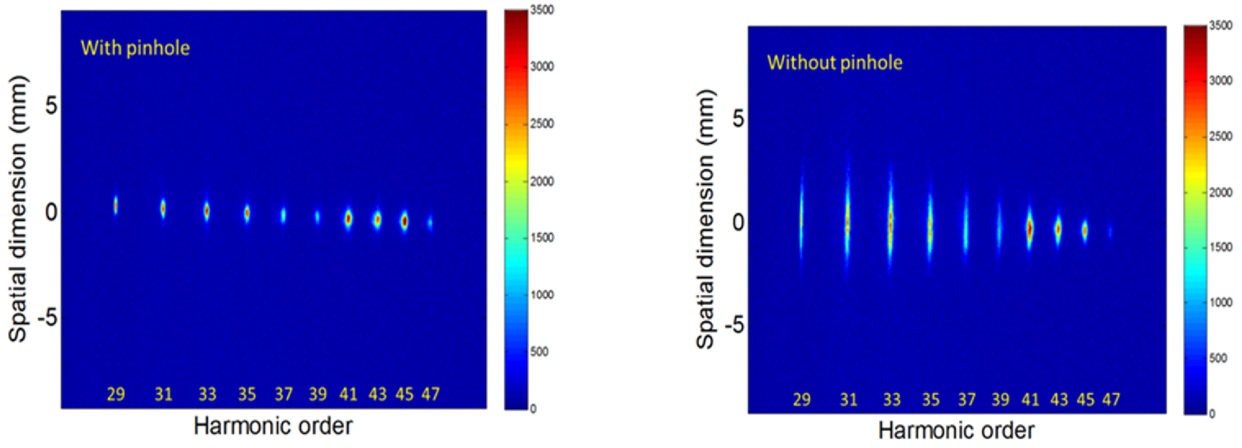

(a) With pinhole

(b) Without pinhole

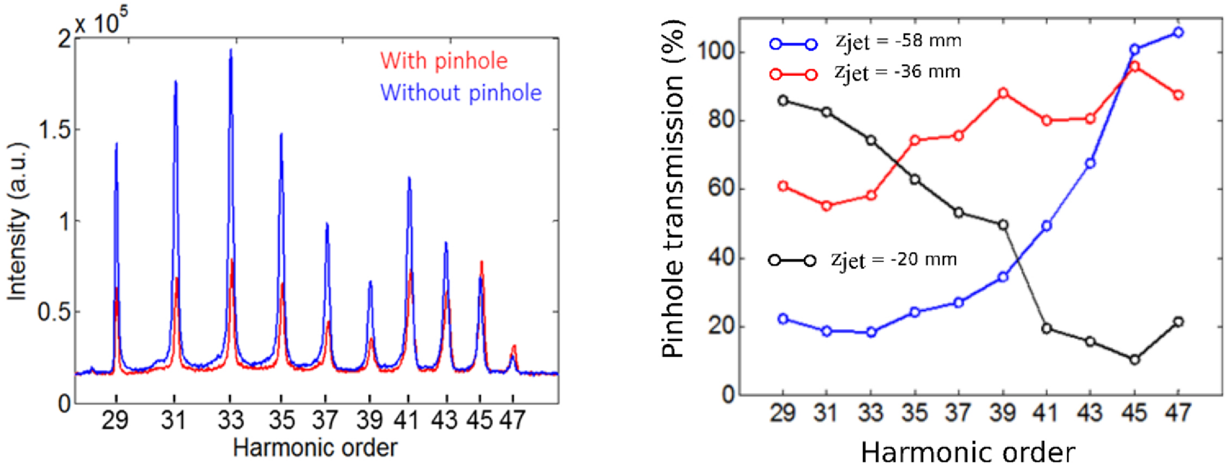

(c) Spatially integrated spectra

(d) Transmission

Fig. 5.7: Far-field spatially-resolved HHG spectrum measured for $z_{\text{jet}} = -58$ mm with (a) and without (b) the pinhole centered on the XUV path. (c) Corresponding HHG spectra after summing over the spatial coordinate. (d) Measured transmission of harmonics H29 to H47 for $z_{\text{jet}} = -58$ (blue), -36 (red) and -20 mm (black). The error bar of the transmittance (not shown here) is estimated to be within 10 %. The figure is adapted from [35].

$z_{\text{jet}} = -15$ mm. At the end it reaches a decreasing regime for $z_{\text{jet}} \in \{-20, -25\}$ mm. The evolution is similar for the other models but slightly shifted.

The second comparison in Fig. 5.8 is the evolution of the transmittance with z_{jet}. There are two maxima of transmittance for H37 presented in the FSPA- and TDSE-models. Considering the cutoffs, one maximum is in the plateau region and the second in the cutoff. In fact, this is

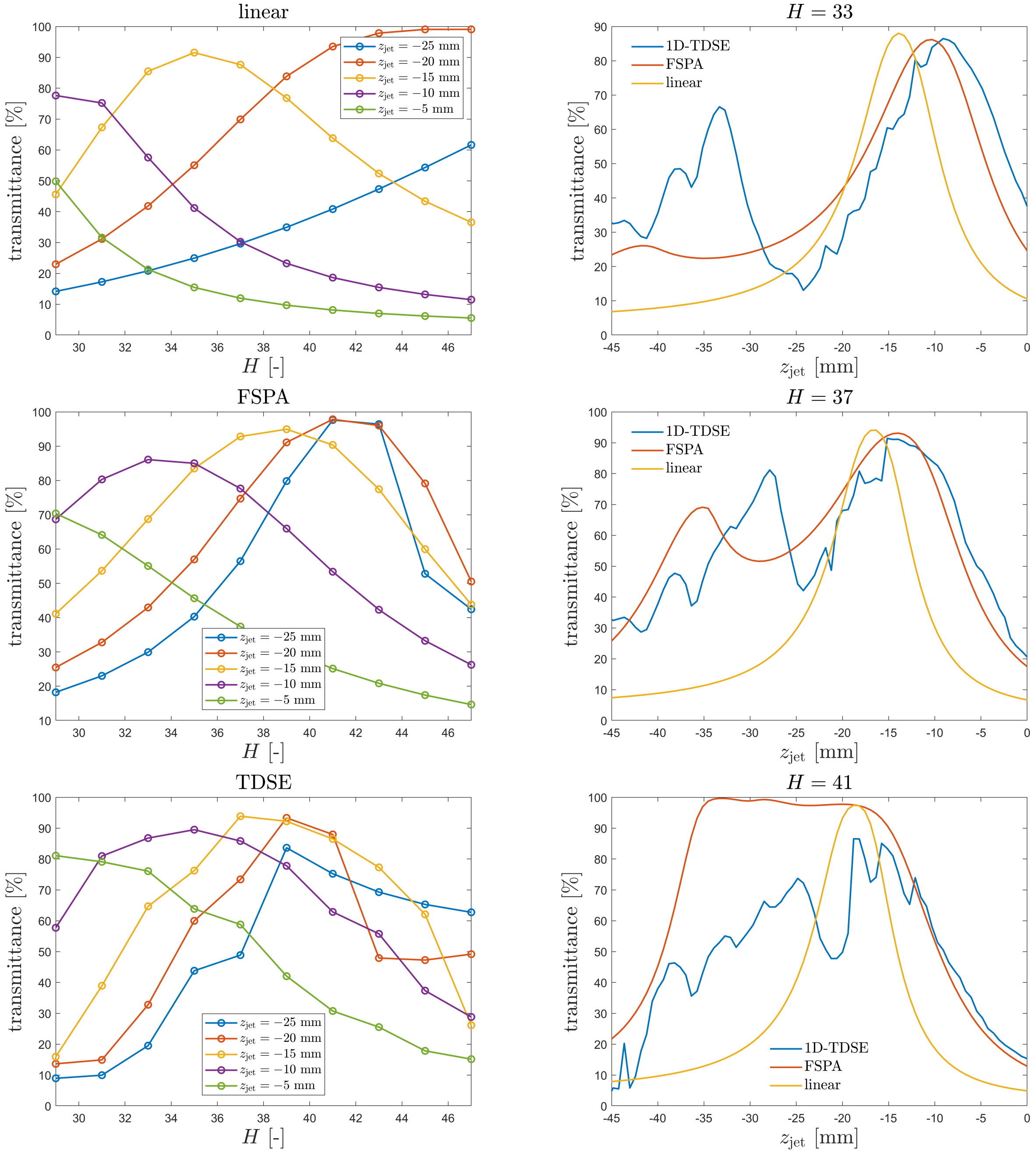

Fig. 5.8: The transmittances through the pinhole as functions of the harmonic orders (left panels) and the positions of the jet, $z_{\rm jet}$, (right panels). Different models are used. Each of the right panels compares various methods for a given harmonic H, different panels are for different harmonics. Right panels show the spectral selectivity of the transmittance both for different models and different positions of the jet. The parameters correspond to Fig. 5.4; $z_{\rm pinhole} = 37$ cm. See Fig. 5.7(d) for corresponding experimental transmittances.

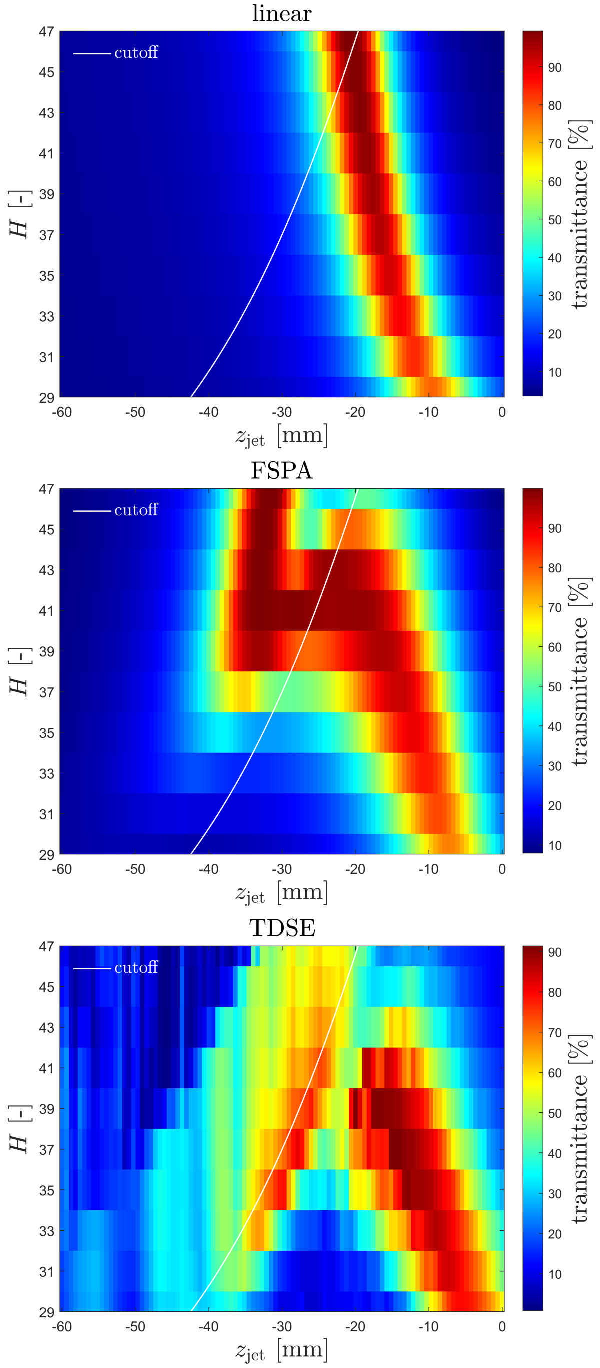

Fig. 5.9: The transmittance in the (H, z_{jet})-space computed from the different models. The white line represents the cutoff. The parameters correspond to Fig. 5.4; $z_{\mathrm{pinhole}} = 37$ cm.

not surprising as the evolution of the dipole phase is steeper in the cutoff. Translating the phase evolution into the curvature, the condition $R_{\text{atom}} = -R(z_0)$ inferred from (5.14) is met twice for these regimes. This effect is not present in the model of the linear phase $\alpha_q = Aq + B$ explained in the point 2 of the list from Section 5.2.3. This is expected as a monotonic evolution of the phase cannot describe the change of the regime from the plateau to the cutoff.

Finally, we put the precedent findings together by scanning the transmittance in both harmonic order, H, and jet position, z_{jet}, at once. This is shown in Fig. 5.9. It provides a complete picture of the focusing. One focusing regime is in the plateau: The minimum of the divergence moves towards the the cutoff while increasing z_{jet}. The second focusing regime is the cutoff region, where the minimum of the divergence is also met in the studied geometry. It also confirms the previous findings: the focusing related to the cutoff region is completely omitted by the linear model. It is partially included in our FSPA model; however, it still does not matches the TDSE model. It means that even the FSPA model in the current implementation is not accurate in this region.

In conclusion, this study added a quantitative picture of the transmittance and also revealed the different contributions by the cutoff and the plateau.

5.2.6 Far-field XUV profiles

We started with the beam profiles for z_{jet} before the pinhole, then we investigated the transmittance through the pinhole and now we examine the field after the pinhole. To do so, we propagate the field after the pinhole by the composition of two Hankel transforms to obtain the filtered far-field profiles. Since the integral over a circular aperture is analytical, we have a similar expression for the resulting field:

$$\mathcal{E}(z_{\text{jet}}; z, \rho, \omega) \propto \frac{\rho_{\text{p}}}{k(\omega)} \int\limits_{T_1} \mathrm{e}^{\mathbf{i}\frac{k(\omega)\rho_1^2}{2D_1}} \mathcal{J}(\rho, \rho_1, \omega) d\left(\rho_1, \omega\right) \rho_1 \mathrm{d}\rho_1 \,, \tag{5.17}$$

where ρ_{p} is the radius of the pinhole. The integral is similar to the Hankel transform, only the kernel of the transform, $\mathcal{J}$, differs, see (D.6) for details. Basically this formula is valid if both the propagation from z_{jet} to z_{pinhole} and from z_{pinhole} to z are sufficiently modelled by the Hankel transforms.

We start with the spatially resolved spectra, Figs. 5.10 and 5.11. Figure 5.10 is basically the same as Fig. 5.5 except the scale. It is expected as the propagation is homothetic in the far-field region. Figure 5.11 is the counterpart of Fig. 5.10 with the pinhole employed. The beams are truncated in all the cases and all the harmonics in the region of the interest have similar radii.

There is clear spectral filtering after the pinhole. Let us take the apertured case for $z_{\text{jet}} = -25$ mm, the strongest signal is around H40. Note that the expected cutoff, $H_{\text{cutoff},z_{\text{jet}}=-25\text{ mm}} \approx 41$, so the strong signal is at the end of the plateau; in contrast, these harmonics are deeply in the plateau for $z_{\text{jet}} = -5$ mm. The weak observed signal for this case is thus purely by the macroscopic defocusing of the beam.

In summary, we added the spatially resolved harmonics with and without the pinhole. We show that the radial distribution is truncated by the pinhole and the main contribution is in the region with the highest transmittance, it then confirms the spectral filtering in the proposed scheme.

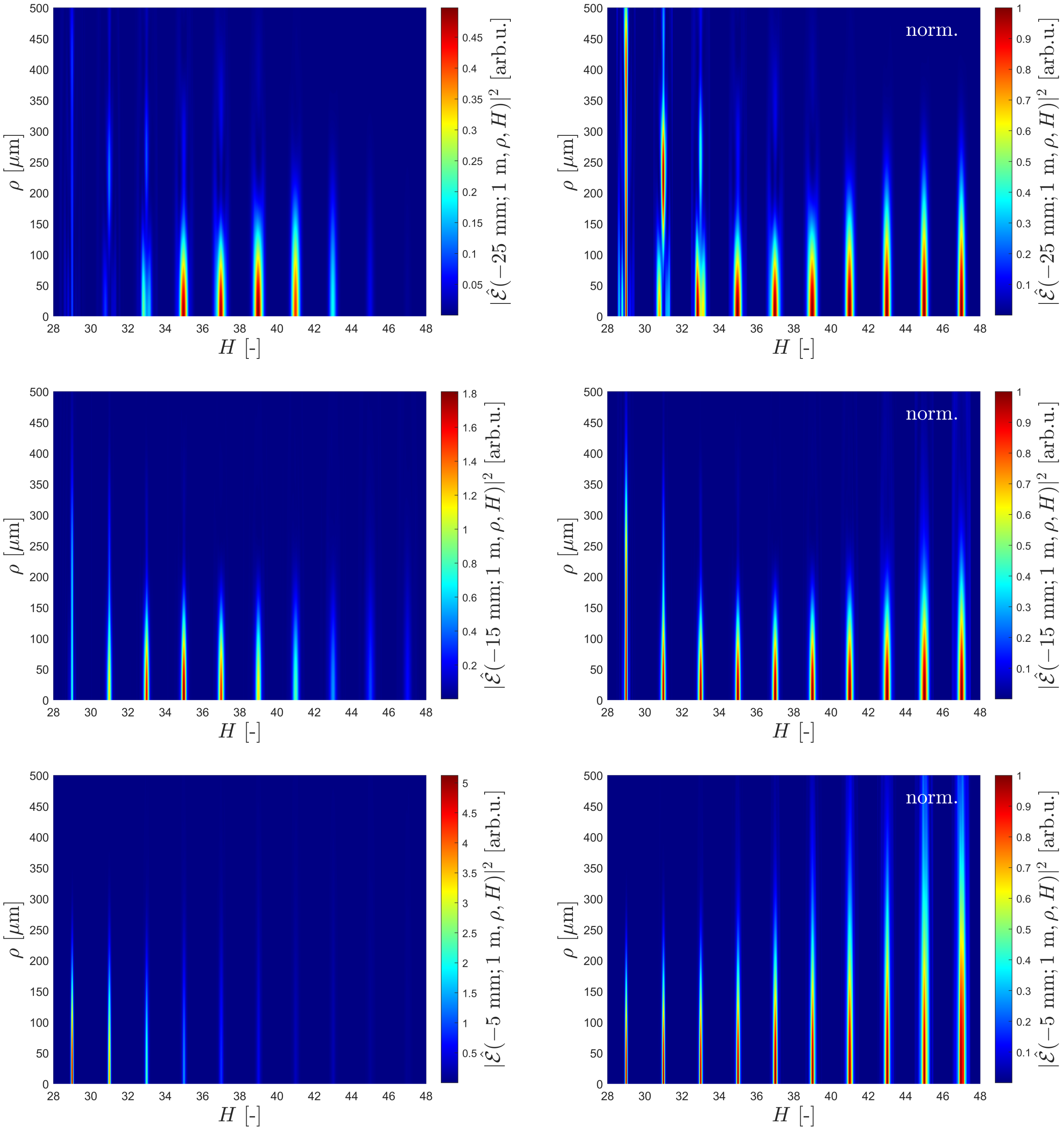

Fig. 5.10: The harmonic spectra at 1 m after the focus without the pinhole for various jet positions. The organisation and methodology is the same as in Fig. 5.5. The parameters correspond to Fig. 5.4.

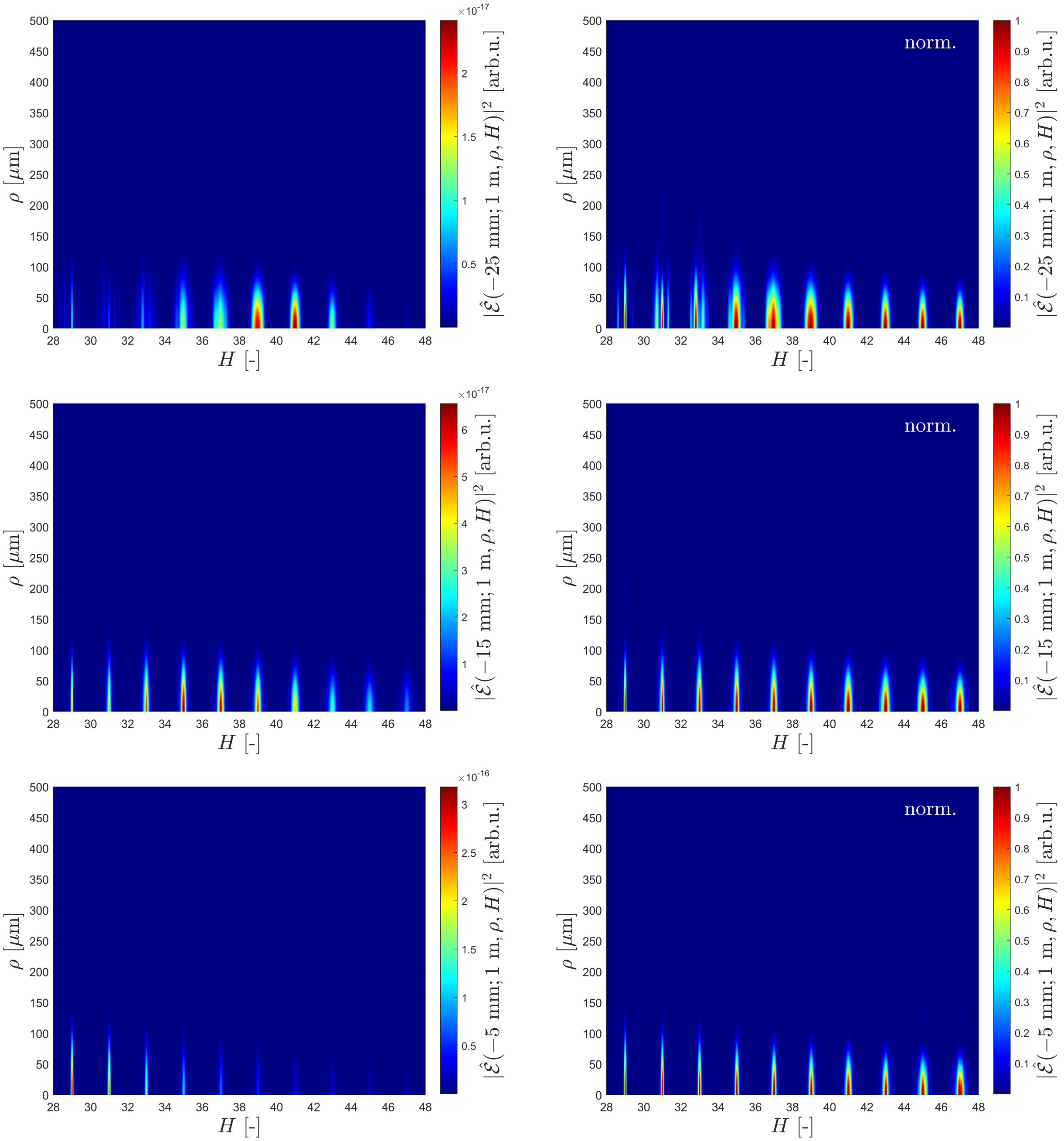

Fig. 5.11: The harmonic spectra at 1 m after the focus with the pinhole for various jet positions. The organisation and methodology is the same as in Fig. 5.5. The parameters correspond to Fig. 5.4; $z_{\mathrm{pinhole}} = 37$ cm. See Figs. 5.10 and 5.7(a,b) for comparisons with experimental spatially resolved spectra with and without the pinhole.

5.2.7 Spectro-temporal profiles: Gabor transforms

We will link the spectral and temporal aspect of the generation process in this section. A tool to show the field in both frequency and time domains directly is the so-called Gabor transform $G_{\mathcal{E}}^{(\alpha)}$ [192]: it is basically the Fourier transform of the signal in time on which a sliding Gaussian window is applied to select only a portion of the signal. Mathematically, $G_{\mathcal{E}}^{(\alpha)}(\omega,\tau) = \mathscr{F}_t\left[w_\alpha(\tau,t)\mathcal{E}(\cdots,t)\right](\omega)$, where $w_\alpha(\tau,t) \propto \exp\left(((t-\tau)/\alpha)^2\right)$. We use $\alpha = 5$ a.u.[5] The Gabor transform reveals times when a given frequency is contained in the harmonic signal.

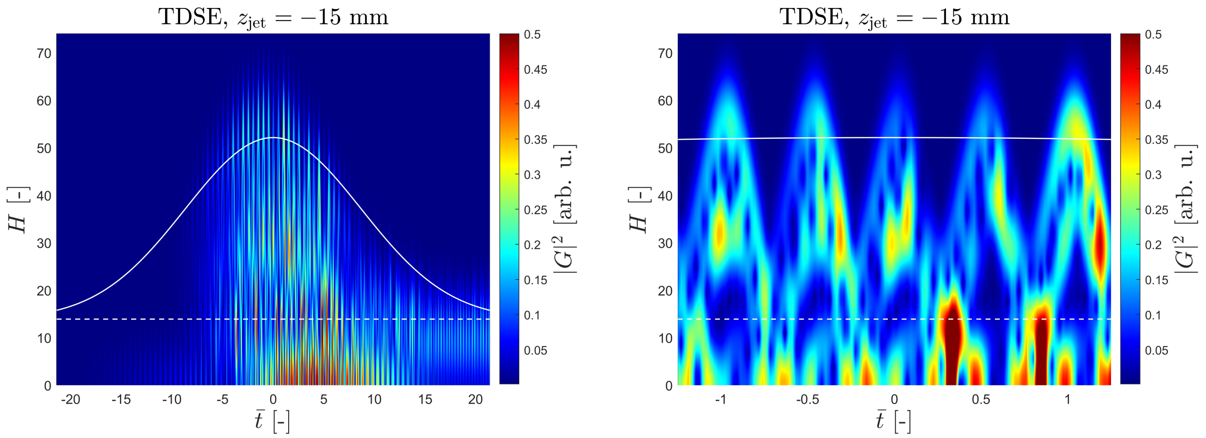
TDSE, $z_{\mathrm{jet}} = -15$ mm

TDSE, $z_{\mathrm{jet}} = -15$ mm

Fig. 5.12: The Gabor transform of the generating dipole placed at $(\rho, z_{\mathrm{jet}}) = (0, -15)$ mm. (The right panel is only a zoom of the right panel and it provides the insight within the sub-cycle structures). The full line shows the cutoff and the dashed line the ionisation potential I_P. The normalised time is defined as $\bar{t} = t/T_0$, where T_0 is the period of the fundamental field. The parameters correspond to Fig. 5.4.

An example of the Gabor transform is shown in Fig. 5.12. There is the transformation $G_{\partial_t j}$ of the microscopic on-axis source term, $\partial_t j$, placed at $z_{\mathrm{jet}} = -15$ mm. From the viewpoint of one half-cycle, there are ”arcs”. These arcs correspond to the short and long trajectories from the classical model. The leading edge of an arc matches the short trajectories, the top of the arc represents a single trajectory in the cutoff, and the trailing edge of the arc matches the long trajectories. It reveals that the generation process contains a lot of anharmonic components – the structures within the arcs. We will discuss this further once the picture is completed with the far-field distribution.

Let us move to the perspective of the whole pulse. Within this scale, the generation follows the cutoff law (1.1) with the two families of the trajectories merging at this point. We also notice the asymmetry of the generating process with respect to the peak of the pulse. The structure is richer at the trailing edge of the pulse in this case. Both, there are more hal-cycles contributing to the generation and there is also visible electron dynamics around the ionisation potential I_P.

---

[5] One cycle of an 800nm-laser corresponds to $T_0 \approx 110$ a.u.. The length of the window, α, cannot be neither too short nor too long to recognise the spectral features with a sufficient resolution, see Appendix E of [126] for details.

Figure 5.13 shows the Gabor transforms of the on-axis for $z_{\text{jet}} \in \{-25, -15, -5\}$ mm. It allows to infer various effects. First, the structures are much more regular than for a single microscopic emitter. Second, we easily obtain further informations about the focusing completing the discussion of the previous Sections: a) From the viewpoint of the whole pulse, the region of efficient generation moves towards lower harmonic as the jet approaches the focus (in agreement with the previous studies). b) We have a detailed insight within a single cycle. The maximum of the signal slides along the short trajectories, starting in the cutoff for $z_{\text{jet}} = -25$ and moving towards the ionisation threshold while approaching the focus. Finally, a sub-cycle analysis (Fig. 5.14) provides also details about possible interferences present in Fig. 5.10; for example: a) H31 and H33 for $z_{\text{jet}} = -25$ mm are split in three contributions when filtered by the pinhole. Comparing this with the respective region of the Gabor transform, there are indeed present three peaks in $|G|^2$. Two correspond to short- and long trajectories; the principal contribution, however, is between them. b) For the same conditions as in a) but without the pinhole, H39 is split into two for $\rho = 250$ μm. There is a local minimum of $|G|^2$ in the transition between the short trajectories and the cutoff merged with the long trajectories. The spacing there also explains the split in the spectrum.

In summary, we introduced the temporal aspect in our study and also explained the generation in the means of short and long trajectories and compared their contributions. The Gabor transform also revealed the origin of fine structures within one harmonic signal due to the interferences within a single cycle.

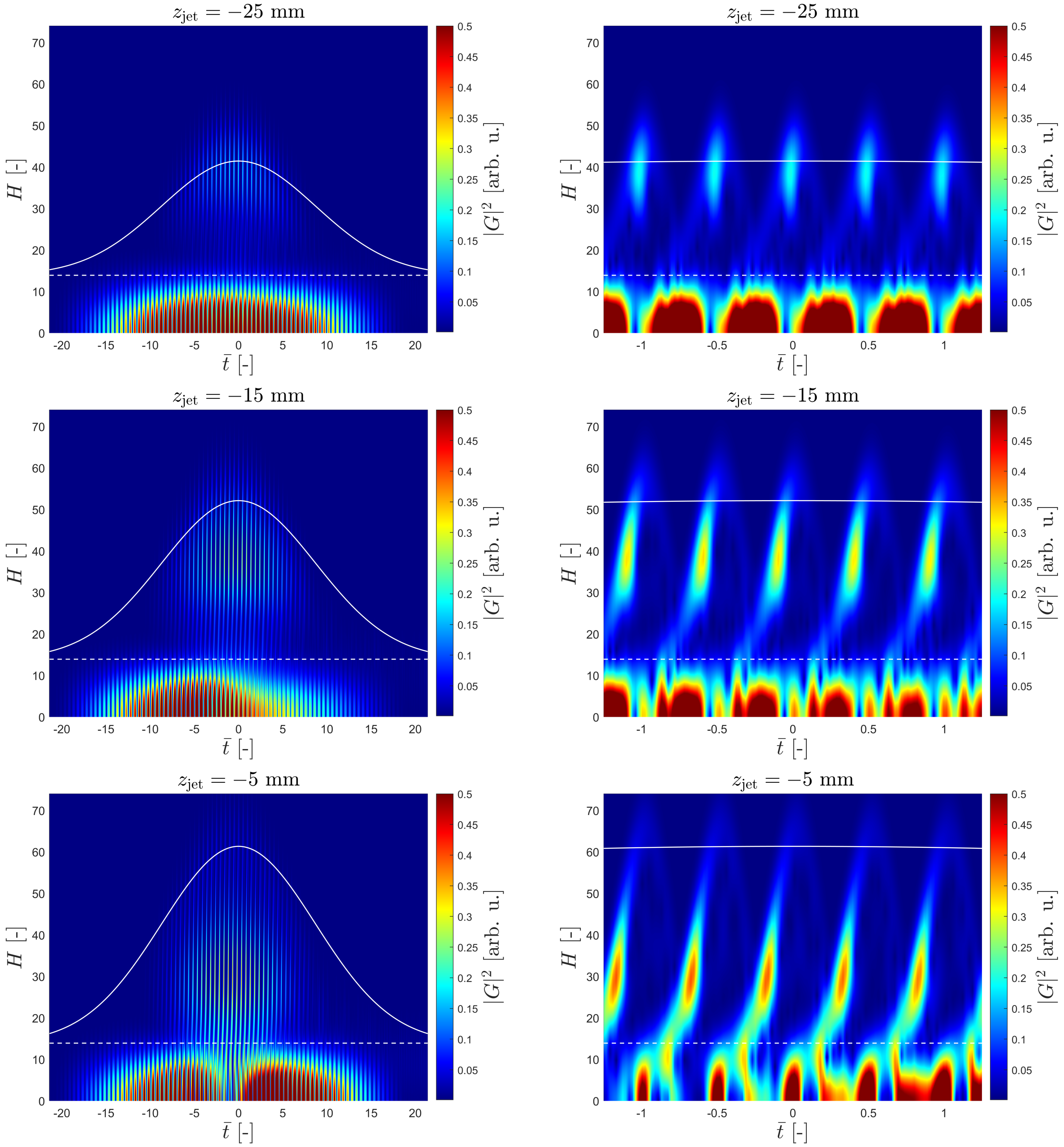

$z_{\text{jet}} = -25$ mm

$z_{\text{jet}} = -15$ mm

$z_{\text{jet}} = -5$ mm

Fig. 5.13: The Gabor transforms of the on-axis far-field obtained from the jets placed as in the previous studies. It shows $|G|^2$ in the linear scale. The parameters correspond to Fig. 5.4.

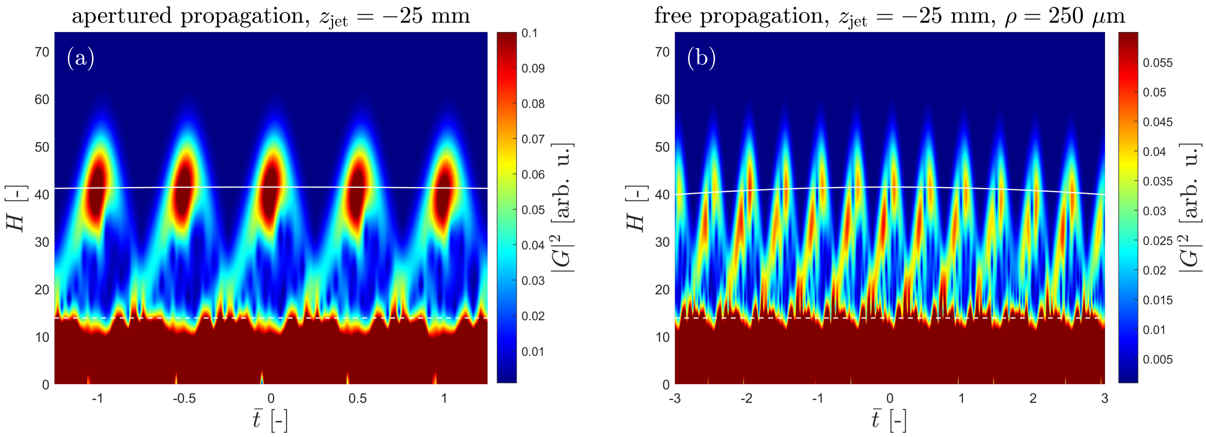

Fig. 5.14: (a) The Gabor transform of the apertured signal generated by a jet placed at $z_{\text{jet}} = -25$ mm. (b) The Gabor transform of the off-axis signal showing the origin of the split of the harmonics around H41. The parameters correspond to Fig. 5.4; $z_{\text{pinhole}} = 37$ cm.

5.2.8 Spectra & time profiles

Finally, we fully decouple the spectral and temporal domains. Figure 5.15 shows both the on-axis spectra and XUV intensity in time for the jet positions of the interest. Next, we also present the microscopic on-axis response at the generating plane. The signals in time are spectrally filtered by the frequency window selecting H28-H48.

The microscopic responses in the plateau region are "jittery" compared to the far-field signals, both in the time and spectral domain. It shows that the far-field spectrum is given by the coherent sum of the microscopic source terms. It means that the incoherent component of the process is removed by the propagation. Next, the harmonics in the cutoff are much cleaner, the explanation is that there is only a single trajectory and reduced contribution of higher-order recombinations. This explains the nature of the harmonic signal plotted in the introductory chapter.[6]

The spectra provide further details about the filtering. We confirm the "homogenisation" of the signal for $z_{\text{jet}} = -15$ mm. Next, the drop in the plateau for $z_{\text{jet}} = -5$ mm is exponential starting around H30 and the plateau is ended by the usual cutoff (with a faster exponential damping) around H60.

Changing to the time domain, the harmonic radiation forms a train of pulses where the duration of each particular pulse may go down to 200 as. It also compares the signal with the time profile of the source term, $\partial_t j$, in the generating medium. In agreement with the spectral profile, this profile contains a lot of irregular structures compared to the far-field profile of the field.

---

[6] Figure 1.2 used to illustrate the spectrum is taken from here and correspond to the case $z_{\text{jet}} = -15$ mm.

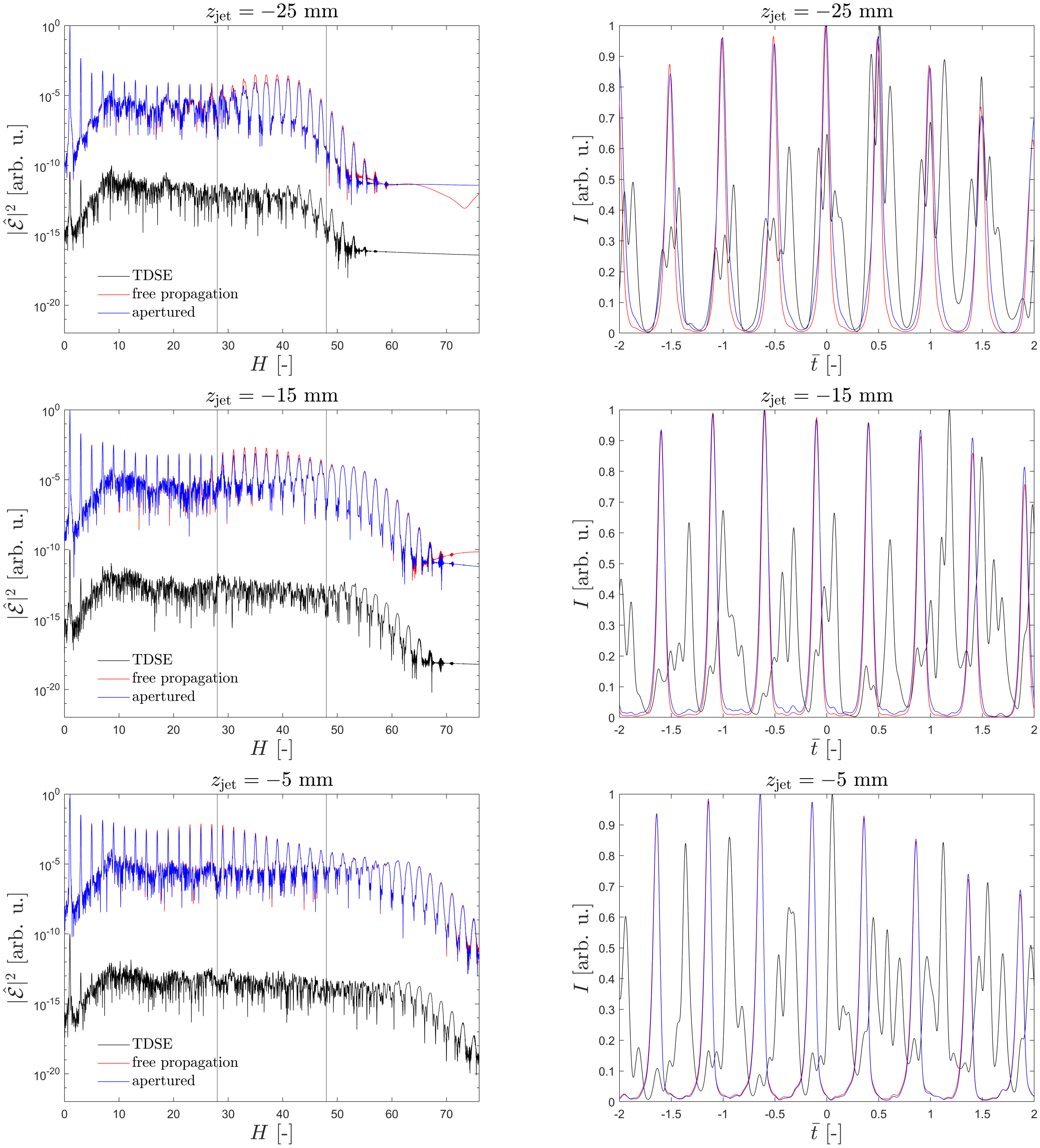

Fig. 5.15: Left panels: The on-axis harmonic spectra for different positions of the jets z_{jet}. Red and blue lines compare the free propagation and the signal apertured by the pinhole. The black curves show the on-axis spectra of the source term (see (5.1) for the relation with the local field). Right panels: the intensity profiles in time by filtering using the spectral window H28–H48 as indicated in the respective spectra. The lines match the spectra. $\bar{t}$ is normalised to optical signals of the driving laser. The parameters correspond to Fig. 5.4; $z_{\mathrm{pinhole}} = 37$ cm.

5.2.9 Conclusion

The conclusion of this example is twofold. First, we investigated in detail the physics necessary to control the divergence of the XUV beams generated from thin targets and recognised the key mechanisms. Second, we provide a methodological example of the use of the multi-scale approach to HHG and show several possible stages of complexity of the used model.

The simple picture that takes the XUV beam for each respective harmonic defined by two curvatures – the inherited from IR-beam and intrinsic from the generated process – explains the key physical mechanisms. It means that the simple model of the linear evolution of the phase with intensity together with Gaussian-beam theory for the respective harmonics is capable to explain the main features.

We have also shown that the process is spectrally selective. We have employed the pinhole and we have proved it may be used for trimming different spectral components of the XUV beam. This mechanism leads to homogenisation of the trimmed beam. Furthermore, we have shown the regular profiles of the XUV field in the time domain, where the field forms a regular attosecond train with a single pulse duration down to 200 as. Altogether with the complementary experimental work, we designed and verified a generation scheme that allows to control the harmonic beams with keeping the intensity as there is no XUV optics involved.

These theoretical and numerical studies have been a part of collaborative work with experimentalists [34, 35]. We have reached to the agreement in the main features and trends.

From a more general perspective, the direct control by the wavefront profile of the driver paves the way to engineer XUV beams by shaping the driving beams. This mechanism is particularly interesting as it does not resort on any XUV optics, which cannot be fabricated today without high losses in the XUV region.

Putting this example in the context of the multi-scale model, the several stages of approximations in the model allowed to access more subtle details of the process. We have reached a good agreement of the employed models together with the experimental measurements that motivated our work.

5.3 Continuous on-axis model

We provided a detailed study of the generation from thin targets accompanied by the example where the multi-scale model was applied for quantitatively modelling of a real experiment. It contained only the transversal aspects of HHG. Now, we move to long media. This will be done by considering an on-axis model by suppressing the transversal dimensions. In other words, we consider only $\rho = \rho' = 0$ in (5.3) from the beginning. This model is applied, e.g., in [193].

The longitudinal model emerges from the integration over z' in (5.3):

$$\int_{z_\mathrm{entry}}^{z_\mathrm{exit}} \frac{\mathrm{e}^{-\mathbf{i}k(\omega)z'}\mathrm{e}^{\mathbf{i}\frac{k(\omega)\rho^2}{2(z-z')}}}{z-z'} \left.\widehat{\left(\frac{\partial \boldsymbol{j}_Q}{\partial t}\right)}\right|_{\rho'=0} \mathrm{d}z' \,.$$

The harmonic signal, precisely the spectral intensity[7] is then given by

$$I(\omega) \propto \left| \int_{z_\mathrm{entry}}^{z_\mathrm{exit}} \mathrm{e}^{-\frac{z_\mathrm{exit}-z}{L_\mathrm{abs}}} \mathrm{e}^{-\mathbf{i}\,\mathsf{Re}(k(\omega))z'} \left.\widehat{\left(\frac{\partial \boldsymbol{j}_Q}{\partial t}\right)}\right|_{\rho'=0} \mathrm{d}z' \right|^2 , \tag{5.18}$$

where we dropped out the denominator $z - z'$; this is valid if the far-field region is much further compared to the length of the medium, i.e. $|z - z_\mathrm{exit}| \gg |z_\mathrm{exit} - z_\mathrm{entry}|$. An insight comes from the refractive index, n, that is introduced by $k(\omega) = \omega n(\omega)/c$. The refractive index is complex: the real part is related to the dispersion of the field in the medium, while the imaginary part is related to the absorption length

$$L_\mathrm{abs}(\omega) = \frac{c}{2\omega\,\mathsf{Im}(n(\omega))} = \frac{1}{\varrho\sigma(\omega)} \,. \tag{5.19}$$

This equation also defines the absorption cross-section $\sigma(\omega)$. This formulation is valid if $\mathsf{Im}(n(\omega))$ scales with the medium density ϱ. This condition is satisfied for gaseous media. A practical implementation of the absorption comes from Eq. (3.9) of [194] and is discussed in Chapter 9.

The phase related to the propagation of the IR-field is still encoded in $\widehat{\partial_t \boldsymbol{j}_Q}$. We further disentangle it for a better insight. Let us assume that only the phase of the IR-field is driven by the propagation and not the amplitude. Considering the phase accumulated by the refractive index, Φ_IR, the source is then

$$\left.\widehat{\left(\frac{\partial \boldsymbol{j}_Q}{\partial t}\right)}\right|_{\rho'=0} = \hat{A}_0(\omega)\mathrm{e}^{\mathbf{i}\frac{\omega}{\omega_0}\Phi_\mathrm{IR}} \,, \tag{5.20}$$

where $\hat{A}_0(\omega)$ is the response of a single microscopic system, i.e. it is a constant for the different z-contributions. We further model the phase Φ_IR being accumulated by the driving field propagating

---

[7] We recall that the intensity is the energy flux, see Appendix B.2. The dimensionality is then related with the omitted transversal integration.

in the medium, it gives[8,9]

$$\Phi_{\mathrm{IR}}(z) = \int_{z_{\mathrm{entry}}}^{z} k_{\mathrm{IR}}(\omega_0, z')\,\mathrm{d}z'\,, \qquad k_{\mathrm{IR}}(\omega_0, z) = \frac{\omega_0 n_{\mathrm{IR}}(\omega_0, z)}{c}\,. \tag{5.21}$$

Using this phase in (5.18), we obtain the XUV signal

$$I(\omega) \propto \hat{A}_0 \left| \int_{z_{\mathrm{entry}}}^{z_{\mathrm{exit}}} \mathrm{e}^{-\frac{z_{\mathrm{exit}}-z'}{L_{\mathrm{abs}}(\omega)}} \mathrm{e}^{\mathrm{i}\int_{z_{\mathrm{entry}}}^{z'} \Delta k(\omega, z'')\,\mathrm{d}z''}\,\mathrm{d}z' \right|^2, \quad \Delta k(\omega, z) = \frac{\omega}{\omega_0} k_{\mathrm{IR}}(\omega_0, z) - \mathsf{Re}(k_{\mathrm{XUV}}(\omega))\,. \tag{5.22}$$

This equation is a continuous version of (1.8) and it then justifies the intuitive phenomenological model introduced in Section 1.3. In this sense, (5.22) then represents a continuous sum of the elementary emitters along the propagation axis. This formulation is instrumental to understand the phase matching. Let us investigate the signal for a given harmonic order q, which means $\omega = q\omega_0$. The resulting signal is affected by $\hat{A}_0$, L_{abs} and $\Delta k(\omega, z)$. The phase-matching is related only to $\Delta k(\omega, z)$ that is rewritten:

$$\Delta k = q k_{\mathrm{IR}} - k_{\mathrm{XUV}} = \frac{q\omega_0}{c}\left(n_{\mathrm{IR}} - n_{\mathrm{XUV}}\right) = q\omega_0 \left(\frac{1}{v_p^{(\mathrm{IR})}} - \frac{1}{v_p^{(\mathrm{XUV})}} \right)\,. \tag{5.23}$$

The difference of the wavenumbers is the usual form to classify the phase-matching. The last expression links the phase-matching with the phase velocities, v_p, of the driver and the generated harmonic field. If they are the same, the signal is maximal and there is no modulation of the signal due to the difference in the phase. Finally, the middle form measures the phase-matching via the refractive indexes.

An advantage of the refractive index is that various processes may be included just by summing the respective susceptibilities (1.4). As the ionisation is naturally time-dependent, it leads to there-mentioned time-dependent refractive indexes. This is tricky as it mixes the conjugate domains of time and frequency. A pragmatic approach is to fix the time in the part of the pulse of our interest and analyse the phase at this moment [195]. A more advanced approach resolves cases while the time evolution is the dominant effect, and we may neglect small corrections of the refractive index in the vicinity of the carrier frequency. An exhaustive mathematical formulation assuming the

---

[8] The subscripts of k_{IR} and n_{IR} are redundant because the refractive index, or more generally the dispersion relation is a single function along the spectrum. However, we use this notation in the cases where we compare the phase inherited from the driver with the phase due to the propagation of the XUV field to emphasise their different origin.

[9] The phase shift $\Phi_{\mathrm{IR}}(z)$ is then easily visualised as the corresponding delay: The driving field carries its phase from z_{entry} to z. Indeed, the related time is $T(z) = \int_{z_{\mathrm{entry}}}^{z} \mathrm{d}z'/v(z')$, which is proportional by ω_0 to the presented phase shift.

refractive-index changing linearly in time, $n(t) = \bar{n} + at$, with $\bar{n}$ being the average value of the refractive index, is in [196]. The advantage of the linear form of $n(t)$ is its simple counterpart in the frequency domain – only a frequency shift. However, once the formal evolution of the refractive index becomes non-trivial in both ω and t, the frontier of the concept of the refractive index is reached; and it cannot give a self-consistent model.

In conclusion, we have completed the model for the propagation of the XUV field by addressing both transversal and longitudinal aspects of the XUV generation within the use of a simplified dipole. We have also reached the limit of describing the generation from pulses with a non-trivial spatio-temporal profile (including also non-trivial evolution in frequency as the conjugate variable to time). To resolve the raised limits, we complete the multi-scale model including the full profile of the driving pulse and the microscopic response from TDSE in the following chapter.

6. FULL MULTISCALE MODEL

We have shown how separately handle the transversal and longitudinal effects characterising HHG and we have procedure to join them easily by computing the full integral (5.3) in the previous chapter. Although we have already used some simplistic models of the IR-pulse propagation, a full model of the non-linear propagation of the IR-driving pulse is still a crucial missing element. This chapter completes the multi-scale model together with its application to the HHG in pre-ionised media.

A more detailed description of the model using non-linear optics is the subject of Section 6.1. The final coupling procedure used in this work is described in Section 6.2. Finally, this model is applied on a real physical configuration and compared with experiments done at ELI-Beamlines. This generation scheme led, jointly with an experimental study, to one of the outcomes of this work [72], and the details are presented in Section 6.3.

6.1 *Unidirectional pulse propagation equation (UPPE)*

Although we have the necessary description by the wave equation (4.6), there is still missing a specific expression of its right-hand side. The objective of this section is then to introduce the model of the non-linear response and simplify the equation into a first-order partial differential equation.

First, we recall the equation and specify the directions of the coordinate system. Let z be the direction of propagation, the equation reads

$$\left(\frac{\partial^2}{\partial z^2} + k^2(\omega) + \triangle_\perp\right)\hat{\mathcal{E}} = -\mu_0\omega^2\left(\hat{P}_{\text{non-lin}} + \mathbf{i}\frac{\hat{\jmath}}{\omega}\right) . \tag{6.1}$$

An ultimate solution for the right-hand side would be to compute it directly from the microscopic model as discussed in the introduction of Chapter 4, where we have called it the strong coupling. Such a coupling would include a loop for computing the source term by the TDSE. This would be ideal from the theoretical viewpoint. However, this is potentially very expensive from the computational viewpoint since it requires to calculate the microscopic response from numerical microscopic model in a fine grid due to the large spectral range that is then included in the field.

Furthermore, the single-active electron approximation becomes questionable for some non-linear effects. Such an approach would also need a lot of work in the design of a numerical implementation. We then change the computation of the source term and use simpler models of the non-linear response only including the IR-range.

The relevant effects in this frequency region are the ionisation and Kerr effect. We now present the approach used in our implementation. I was fortunate to be able to collaborate with Stefan Skupin and the computational core of the code is adopted from [197, 80], where is also an exhaustive description of the physics. Further details may be found in [198].

6.1.1 Unidirectional pulse propagation approximation (UPPA)

The wave equation (6.1) is a second-order partial differential equation and it describes solutions propagating in both direction: z an $(-z)$. Intuitively, the propagation in the direction of $(-z)$ corresponds to *backscattering*. To treat the backscattering, the solutions advanced in z – i.e. the field $\mathcal{E}(z+\Delta z,\dots)$ – would necessarily affect the precedent field $\mathcal{E}(z,\dots)$. It means a solver advancing step-by-step in the z-direction cannot be constructed. Essentially, if the backscattering cannot be neglected, usual approaches do not simplify Maxwell's equations much, and the procedure is to solve them directly [199]. A practical implementation is, for example, *Particle-in-cell* codes [104] or the model introduced in [88]. However, if the backscattering can be neglected; there would be an algorithm going step-by-step in the direction of propagation. This idea is mathematised by rewriting $\partial_z^2 + k^2(\omega) = (\partial_z - \mathbf{i}k(\omega))(\partial_z + \mathbf{i}k(\omega)) = D_+(\omega)D_-(\omega)$ and separating the solution into forward- and backward-propagating parts: $\hat{\mathcal{E}} = \hat{U}_+ \mathrm{e}^{\mathbf{i}k(\omega)z} + \hat{U}_- \mathrm{e}^{-\mathbf{i}k(\omega)z}$.

If we neglect the backward component $\hat{U}_-$, the propagation equation transforms into

$$\frac{\partial \hat{\mathcal{E}}}{\partial z} = \frac{\mathbf{i}}{2k(\omega)} \triangle_\perp \hat{\mathcal{E}} + \mathbf{i}k(\omega)\hat{\mathcal{E}} + \frac{\mathbf{i}\mu_0\omega^2}{2k(\omega)}\hat{\mathcal{F}}\,, \qquad \hat{\mathcal{F}} = \hat{P}_{\text{non-lin}} + \mathbf{i}\frac{\hat{\jmath}}{\omega}\,. \tag{6.2}$$

This is written in the desired form of a first-order partial differential equation in z.

6.1.2 Enveloped pulse

Here, we characterise the field in time domain by a complex envelope[1] and adjust it into a co-moving frame; this description in the unidirectional propagation was originally introduced in this form in [200]. The envelope function U is defined for a complexified field by (see (B.3) for the

---

[1] The complex envelope means that it contains not only the shape of the averaged field but also the phase difference respective to the carrier frequency. It means that for example a chirp may be included within the complex envelope.

details about the complexification)

$$\mathscr{E}(\boldsymbol{r},t) = U(\boldsymbol{r},t)\mathrm{e}^{-\mathbf{i}(\omega_0 t - k_0 z)}\,. \tag{6.3}$$

This decomposition assumes a pulse centred around a carrying frequency ω_0; but it is still for convenience without assuming a slowly varying envelope. The dispersion relation is Taylorised around ω_0:

$$k(\omega) = k_0 + k'(\omega - \omega_0) + \hat{\mathcal{D}}_2(\omega)\,, \qquad \hat{\mathcal{D}}_2(\omega) = \sum_{n=2}^{+\infty} \frac{k^{(n)}}{n!}(\omega-\omega_0)^n\,, \tag{6.4}$$

$k_0 = k(\omega_0)$, $k' = \partial_\omega k(\omega_0)$, etc. To obtain the evolution of U, the equation (6.2) is used for $\hat{\mathscr{E}}$ and transformed back into time domain; it yields

$$\begin{aligned} &\mathrm{e}^{-\mathbf{i}(\omega_0 t - k_0 z)} \left(\partial_z + k'\partial_t\right) U(\boldsymbol{r},t) = \\ &\qquad \mathbf{i}\mathrm{e}^{\mathbf{i}k_0 z} \int \left(\frac{\triangle_\perp}{2k(\omega)} + \hat{\mathcal{D}}_2(\omega)\right) \hat{U}(\boldsymbol{r},\omega-\omega_0)\mathrm{e}^{-\mathbf{i}\omega t}\,\mathrm{d}\omega + \frac{\mathbf{i}\mu_0}{2}\int \frac{\omega^2}{k(\omega)}\hat{\mathcal{F}}(\boldsymbol{r},\omega)\mathrm{e}^{-\mathbf{i}\omega t}\,\mathrm{d}\omega\,. \end{aligned} \tag{6.5}$$

The last step transforms the equation into the co-moving frame with the group velocity $v_g = 1/k'$ via the retarded time $\tilde{t} = t - k'z$ and approximates $k(\omega)$ in the denominators. The final propagation equation reads

$$\partial_z U = \frac{\mathbf{i}\mathcal{T}^{-1}\triangle_\perp}{2k_0}U + \mathcal{D}_2 U + \frac{\mathbf{i}\mu_0\omega_0^2}{2k_0}\mathcal{T}\mathcal{F}^{(\mathrm{env.})}(U)\,, \tag{6.6}$$

where $\mathcal{T} = 1 + \mathbf{i}\partial_t/\omega_0$ and $\mathcal{D}_2 = \sum_{n=2}^{+\infty}\left(\mathbf{i}\partial_t\right)^n/n!$. The last term, $\mathcal{F}^{\mathrm{env.}}$, is the non-linear and plasma effects, it is averaged over the fast oscillations of the carrier frequency ω_0.

We now have the first-order equations (6.2) and (6.6), that are favourable to be numerically advanced from an initial plane. The difference is that the latter uses only the complex envelope U of the field; it thus allows coarser discretisation, but some sub-cycle phenomena may not be treated well.

6.1.3 Principal non-linear effects

To complete the description of propagation, we need to write-down an explicit form of $\hat{\mathcal{F}}$. We discuss here the principal non-linear effects included in this term.

– *Kerr effect* –

This is a standard non-linear effect of the third order,[2] it contributes to the non-linear source as

$$P^{(3)}_{\text{non-lin}}(t) = P^{(3)}_{\text{Kerr}}(t) = \frac{4n_0^2 c}{3} n_2 \left|\bar{\mathcal{E}}\right|^2 \mathcal{E}\,. \tag{6.7}$$

where $\bar{\mathcal{E}}$ is the averaged field with fast oscillations removed. The pre-factor is chosen to link the non-linear constant n_2 with the refractive-index $n = n_0 + n_2 I$; where $n_0 = ck(\omega_0)/\omega_0$ is the linear refractive index; see the section 4.1 of [36] for details about the normalisation.

Since the Kerr effect is one of the key processes to understand the non-linear propagation, we provide the context for further reading. The self-focusing of radiation due to the non-linearity, later identified with the Kerr effect in gases, was recognised in 1962 [201]. The stability of a laser beam due to the Kerr effect became intensively studied soon after, and theory started to develop employing various approaches as analytical [202], variational [203, 204] and numerical [85] (see also the reviews [205, 79]).

– *Plasma: free electrons and ionisation* –

We arrive to the term combining the generation (and absorption) of free electrons due to the ionisation (and recombination) processes together. Similarly as for the Kerr effect, the role of the ionisation in the stability of the beam has been addressed in detail in literature [206, 207, 78, 208, 209].

We present a model arising from two-fluid hydrodynamical description [210] (see Appendix J and Sections 2.4 and 2.5 of [211] for further details):

$$\frac{\partial \varrho_e}{\partial t} + \triangledown(\varrho_e \boldsymbol{v_e}) = S\,, \tag{6.8a}$$

$$\frac{\partial \boldsymbol{v}_e}{\partial t} + (\boldsymbol{v}_e \cdot \triangledown)\boldsymbol{v}_e = -\frac{e}{m_e}\left(\boldsymbol{\mathcal{E}} + \boldsymbol{v}_e \times \boldsymbol{B}\right) - \nu_e \boldsymbol{v}_e - S\frac{\boldsymbol{v}_e}{\varrho_e}\,, \tag{6.8b}$$

The first equation is the continuity equation, where S is the source of free electrons. The second equation is the electronic motion driven by the Lorentz force; additionally, there is a friction force due to collisions with the collisional frequency ν_e. The frequency is taken as a constant within our model; however, it is only a simplification and we refer to the aforementioned literature for further details. The source term S couples the equations with the model of ionisation. A fast link with the microscopic model is the rate equation (3.3), it then provides the source of the electrons $S = -\Gamma(|\mathcal{E}|)\varrho_e$.

---

[2] See [121] for a quantum-mechanical description of the Kerr effect.

The source term for the field equations is the current, it is given by $\boldsymbol{j} = -e\varrho_e \boldsymbol{v}_e$ in this approach. We express it from (6.8) as

$$(\partial_t + \nu_e)\boldsymbol{j} = \frac{e^2 \varrho_e}{m_e}\boldsymbol{\mathcal{E}} + \boldsymbol{\Pi}\,, \qquad \boldsymbol{\Pi} = -\frac{e}{m_e}\boldsymbol{j} \times \boldsymbol{B} - \boldsymbol{v}_e\left(\triangledown \boldsymbol{j}\right) - \left(\boldsymbol{j} \cdot \triangledown\right)\boldsymbol{v}_e\,. \tag{6.9}$$

$\boldsymbol{\Pi}$ describes ponderomotive forces that may be neglected in the range of intensities and pulse durations of our interest. Posing $\boldsymbol{\Pi} \approx 0$, the current is then easily found in the Fourier space:

$$\hat{\boldsymbol{j}}(\omega) = \left(\frac{\nu_e e^2}{m_e\left(\omega^2 + \nu_e^2\right)} + \frac{\mathbf{i}\omega e^2}{m_e\left(\omega^2 + \nu_e^2\right)}\right)\mathscr{F}_t\left[\varrho_e \boldsymbol{\mathcal{E}}\right](\omega)\,. \tag{6.10}$$

The first term is responsible for the ionisation losses as it vanishes for $\nu_e \to 0$, the second term is thus the plasma response.

– Further effects included in the code –

Finally, the code we use contains more functionalities that we do not use in our work. There is a 5th-order analogue of the Kerr effect, $n_4|\bar{\mathcal{E}}|^4\mathcal{E}$. Another phenomenon is the retarded Kerr effect, where the response is given by a convolution $\left(\int \bar{R}(t-t')|\mathcal{E}(t')|\,\mathrm{d}t\right)\mathcal{E}(t)$, which may include also the Raman scattering. There is also possibility to include the third-order harmonic generation and also quintic non-linear effects. However, some of these effects require a finer phase-matching and the propagation equation is different as the envelope function U is not used. Consequently, a finer resolution in a numerical solver is needed.

Although these effects are not within the scope of this work, we mention them in the case this manuscript is used to help the orientation in the code.

6.1.4 Final propagation equation

Finally, we arrive to an explicit expression for $\mathcal{F}^{(\mathrm{env.})}$ in (6.6). The equation used in the solver is then

$$\partial_z U = \frac{\mathbf{i}}{2k_0}\mathcal{T}^{-1}\triangle_\perp U + \mathbf{i}\mathcal{D}_2 U + \mathbf{i}\frac{\omega_0}{c}n_2\mathcal{T}|U|^2 U - \frac{\mathbf{i}e^2 k_0}{2n_0^2\omega_0^2 m_e \varepsilon_0}\mathcal{T}^{-1}\left(\varrho_e U\right) - \frac{e^2\nu_e}{2m_e\varepsilon_0 n_0 c\left(\nu_e^2 + \omega^2\right)^2}\varrho_e U \tag{6.11}$$

We recapitulate the included effects on the right-hand side. The term containing $\triangle_\perp U$ is the diffraction directly from the transverse Laplacian in the wave-equation. $\mathbf{i}\mathcal{D}_2 U$ is the reduced dispersion relation since the 0th and 1st orders are included in the envelope and co-moving frame, respectively. The term containing $n_2\mathcal{T}|U|^2U$ is responsible for the Kerr effect. The last two terms are the rescaled expressions from (6.10) describing the free electrons and absorption due to the ionisation.

Each physical effect may be linked directly with their actions on the laser pulse [80]. $\triangle_{\perp} U$ is a spatio-temporal effect leading to self-steepening of the pulse. The Kerr and plasma generation are leading to focusing and defocusing effects, respectively.

The equation (6.11) completes all the ingredients needed for the multi-scale model. The next step is to assemble all the parts in the final multi-scale model.

6.2 Assembling multiscale model

We have discussed all the necessary physical models required to construct the full multiscale model. A fully numerical counterpart of an experiment is the weak coupling procedure:

1. We compute the propagation of the driving laser using a solver implementing (6.11). The output is $\mathcal{E}(\boldsymbol{r}, t)$.
2. The microscopic source term (discussed in Section 2.3) is calculated on a grid covering the macroscopic medium by a numerical solution of TDSE using $\mathcal{E}(\boldsymbol{r}, t)$ from the previous point.
3. The XUV field in the far-field region is integrated using (5.3).

This is the central result of this work: each of the points above is represented by its respective model described in previous chapters. An indispensable part of the solution is the ”translation” into numerical algorithms that is described in Part III of this thesis.

Here, we use the multi-scale model for studying high-harmonic generation in a pre-ionised medium. As this problem is of practical interest, we first explain the physical background and motivation. The multi-scale model is then applied in Section 6.3.5. The purpose of this study is then twofold. First, it is a practical example of the capabilities of the code. Second, it contributes to the development of a novel method used to optimise HHG yield.

6.3 HHG from long media: phase-matching controlled by pre-ionisation

One issue one faces in HHG in long media is the phase matching: the physical picture is that the driving pulse propagates through the macroscopic medium and it induces microscopic dynamics at all points. This dynamics leads to the generation of an XUV field that is generated only in a short window of re-collision times from the three-step model, which leads to highly coherent generated field. The XUV field co-propagates with the driver; which is the second important property of this source: the XUV field is well-spatially confined and it forms a beam as discussed in Section 5.2. Both mentioned properties – coherence and spatial localisation – are extremely important for applications. There is a complication in long generating media: the phase velocity of the driver and XUV differs; consequently, they may become dephased at some point. Once this is reached, the generating window does not match with the co-propagated XUV and it kills the efficiency of the process. Our goal is to provide a mechanism to control and suppress this dephasing. We propose a scheme, where the medium is homogeneously pre-ionised. It gives us a further tunable parameter of the medium to control the phase velocity via the plasma response of the medium. A rough picture is that we tune the linear response of the medium by controlling the base index of refraction n_0.[3] If this is reached, the driving and generated fields "run together" and all the generated radiation add constructively.

In this section, we explain the approach used to accompany experimental campaigns done at ELI-Beamlines. The mechanism of pre-ionisation was to use an electric discharge. The experimental setup was a long cell filled with argon or krypton. The conditions were adjusted so that the discharge creates a homogeneous free-electron density compared to the beam diameter.

This section is thus organised as follows: 1) We present a simple picture by investigating the local phase mismatch. 2) We introduce the metrics applied on macroscopic scale to recognise the principal mechanisms of the generation in long media. 3) We apply the fully numerical model for quantitative modelling.

6.3.1 Local dephasing

We recall the simple approach to phase-matching presented in the introductory chapter, Section 1.3. Locally, XUV field corresponding to the qth harmonic is perfectly phase-matched if the difference between the wavenumbers is zero, $\Delta k_q = 0$. We recall the usual contributions for the phase-matching [37]:

$$\Delta k_q = \Delta k_{\text{disp.}} + \Delta k_{\text{plasma}} + \Delta k_{\text{geom.}} + \Delta k_{\text{atom}} \,. \tag{6.12}$$

The dispersion term contains the dephasing due to the difference in the linear dispersion from the refractive index, we recall their expressions: $\Delta k_{\text{disp.}} = qk_0(n_{\text{IR,disp.}} - n_{\text{XUV,disp.}})$; where only the contribution of neutrals is included, $n_{\cdot,\text{disp}} = \sqrt{1+\chi_{\cdot,\text{disp.}}}$. The plasma refractive index for plasma is $n_{\text{plasma}} = \sqrt{1-(\varrho_e e^2)/(\varepsilon_0 m_e \omega^2)}$, where ϱ_e is the density of free electrons. A general way to include susceptibilities attributed to various processes is given by (1.4). The geometry of the beam contributes as $\Delta k_{\text{geom.}} = \partial_z \Phi_G(z)$. The atomic phase comes from the empiric dipole (2.19), $\Delta k_{\text{atom}} = -\alpha \partial_z I$.

---

[3] We discussed the plasma generation as extremely non-linear process. Indeed, the self-generated plasma by a pulse introduces it due to its time-profile. Contrary, a homogeneous pre-ionisation acts as a constant background contributing dominantly only to the linear refractive index.

The decomposition (6.12) is possible only for analytically written phases of laser fields. Once only the profile $\mathcal{E}(\boldsymbol{r},t)$ is known, the contributions from dispersion, plasma and beam geometry cannot be disentangled easily. A way to obtain Δk is directly obtained from the phase of the field $\Phi(\boldsymbol{r},t) = \mathrm{Arg}(\mathscr{E}(\boldsymbol{r},t))$, where the complexified electric field $\mathscr{E}(\boldsymbol{r},t)$ is assumed. The wave-vector is then $\boldsymbol{k} = \bigtriangledown\Phi(\boldsymbol{r},t)$, which leads to Δk_q. In our particular case, the only effects not included in the phase obtained from the driving-laser propagation are: the dispersion of the XUV and the intrinsic phase. The phase-mismatch is

$$\Delta k_q = \partial_z \Phi + k_q(n_{\mathrm{XUV,disp.}} - 1) - \alpha \partial_z I\,, \tag{6.13}$$

where $k_q = q\omega_0/c$ is the wave-number of the corresponding harmonic.

The local dephasing, Δk_q, provides a good insight in the phase-matching conditions, and it is a starting point to design a phase-matching scheme. Because it considers the optimisation only locally, the same approach may be applied for example in guided geometries [212].

6.3.2 General phase-matching schemes

Equation (6.12) is an initial point to design phase-matching schemes. $\Delta k_{\mathrm{disp.}}$ is a material constant and cannot be modified microscopically. A way to use this term is to change the macroscopic shape of the target; for example, [70] proposes to use a series of equally spaced plasma jets to cumulate the phase constructively in the jets and use the spaces to overcome the destructively interfering part. A whole branch of HHG uses guided driving beams [64]. Another option is to shape the wavefronts of the driving beam to control $\Delta k_{\mathrm{geom.}}$. For example [61] proposes to use a two-foci scheme. A disadvantage of the mentioned methods is a difficult scalability. Once the driving beam is significantly distorted due to non-linear propagation. Another possibility is to use an intense pulse that ionises the medium itself to a sufficient level [48, 39]. The possible disadvantages are 1) a short temporal window in time reaching an optimal value, which gives the name of the method – *transient phase-matching*; 2) the difficulty to control and stabilise an intense pulse if a long medium is used. Another use of ionised media is to guide the driving beam in a plasma channel to prevent defocusing of the beam [67, 68, 66].

The scheme we propose based on the homogeneous pre-ionisation relies on the control of $\Delta k_{\mathrm{plasma}}$. This effect have been briefly discussed as a part of the ”ionisation-driven” generating scheme [68]. We study a set-up of a long medium with loosely focused laser. In this case, the guiding of the beam and the gradient of intensity are minor effects. Considering only plasma, $\Delta k_{\mathrm{plasma}}$, and neutrals, $\Delta k_{\mathrm{disp.}}$; the mismatch is

$$\Delta k_q = \frac{q\omega_0\varrho}{2c}\left(\Delta\alpha^{(\mathrm{p})} - \eta\frac{e^2}{\varepsilon_0 m_e \omega_0^2}\right) . \tag{6.14}$$

We use the polarisability $\alpha^{(\mathrm{p})}$ related to the susceptibility by $\chi_{\cdot,\mathrm{disp.}} = \varrho\alpha^{(\mathrm{p})}$.[4] It shows an explicit scaling of the dephasing with the density. There is only the difference $\Delta\alpha^{(\mathrm{p})} = \alpha^{(\mathrm{p})}_{\mathrm{IR,disp.}} - \alpha^{(\mathrm{p})}_{\mathrm{XUV,disp.}}$ needed for the analysis. Next, we have defined the ionisation degree η so that the plasma density is written $\varrho_e = \eta\varrho$. This provides a simple way to find the corresponding degree of ionisation for a given coherence length

$$L_{\mathrm{coh}} = \frac{\pi}{|\Delta k_q|} . \tag{6.15}$$

The relation is

$$\eta = \frac{\omega_0^2\varepsilon_0 m_e}{e^2}\left(\Delta\alpha^{(\mathrm{p})} \mp \frac{2\pi c}{q\omega_0\varrho L_{\mathrm{coh}}}\right) , \qquad \eta_{\mathrm{opt.}} = \frac{\omega_0^2\varepsilon_0 m_e \Delta\alpha^{(\mathrm{p})}}{e^2} . \tag{6.16}$$

The optimal ionisation $\eta_{\mathrm{opt.}}$ is reached by letting $L_{\mathrm{coh}} \to +\infty$.

The microscopic mechanism is clear, the next step is to zoom out to macroscopic scale. A rough estimate of a region interfering constructively is directly L_{coh} as its characteristic dimension.

6.3.3 Longitudinal simple model

The longitudinal aspect comes from the integration along the propagation (5.18), this model was introduced in [38]. It gives the XUV-signal:

$$\begin{aligned} I(\omega) = {} & \frac{4\varrho^2 L_{\mathrm{abs}}^2 \left|\widehat{\partial_t j}\right|^2}{1 + 4\pi^2\left(\frac{L_{\mathrm{abs}}}{L_{\mathrm{coh}}}\right)^2}\left(1 + \mathrm{e}^{-\frac{L_{\mathrm{med}}}{L_{\mathrm{abs}}}} - 2\mathrm{e}^{-\frac{L_{\mathrm{med}}}{2L_{\mathrm{abs}}}}\cos\left(\frac{\pi L_{\mathrm{med}}}{L_{\mathrm{coh}}}\right)\right) = \\ = {} & \frac{16\varrho^2 L_{\mathrm{abs}}^2 \left|\widehat{\partial_t j}\right|^2}{1 + 4\pi^2\left(\frac{L_{\mathrm{abs}}}{L_{\mathrm{coh}}}\right)^2}\mathrm{e}^{-\frac{L_{\mathrm{med}}}{2L_{\mathrm{abs}}}}\left(\sinh^2\left(\frac{L_{\mathrm{med}}}{4L_{\mathrm{abs}}}\right) + \sin^2\left(\frac{\pi L_{\mathrm{med}}}{2L_{\mathrm{coh}}}\right)\right) . \end{aligned} \tag{6.17}$$

Because $\widehat{\partial_t j}$ is constant in this model, this equation provides a direct macroscopic insight in the generation process driven by the absorption length, L_{abs}, coherence length, L_{coh}, and the length of the medium L_{med}. The expected signal is further simplified if $L_{\mathrm{med}} \gg L_{\mathrm{abs}}$, this is called

---

[4] This scaling is justified for our use of gaseous media. In a general case, the link is provided by the Clausius-Mossotti relation.

absorption-limited generation because L_{med} vanishes from the expression: the signal is given by the pre-factor only. We consider the absorption-limited case for the rest of this analytical approach.

We can substitute the coherence length from the dephasing (6.14) and $L_{\mathrm{abs}} = 1/\varrho\sigma$ from (5.19), the signal is then

$$I_q(\eta) \approx \frac{4\left|\widehat{\partial_t j}\right|^2}{\sigma^2 + \frac{q^2\omega_0^2}{c^2}\left(\Delta\alpha^{(\mathrm{p})} - \eta\frac{e^2}{\omega_0^2\varepsilon_0 m_e}\right)^2}\,. \tag{6.18}$$

We use a suitable notation for studying HHG in pre-ionised media: the signal is evaluated at a given harmonic order q, and we emphasise that the variable of interest is η. An important property is that the signal is density-independent. An explanation is that with increasing the medium density: there is more signal generated, but the same amount is absorbed. The main property of this equation is that it quantitatively shows the expected signal tuned by the ionisation η. The maximal signal is $I_q(\eta_{\mathrm{opt.}}) = 4\left|\widehat{\partial_t j}\right|^2/\sigma^2$, we call the generation in this regime as *ideal absorption-limited generation.*

6.3.4 Experimental results

The goal of the numerical study in this part is to provide a detailed analysis to the experimental campaign that studied the XUV signal from a long medium filled with krypton gas for various pressures and pre-ionisation degrees created by an electric discharge. The details of the experiment are described in [72]. The key parameters are the dimension of the capillary: 15-mm long with the diameter of 1 mm. The Ti:Sapphire laser system used for the experiment delivers up to 10 mJ, 40 fs, 798 nm pulse, that is focused by a spherical mirror with the focal length of 5-m down to the beam radius of 100 μm. We study in detail the following set-up: the discharge is fixed and pressure is varied. Because the response of the medium to the discharge is non-linear, the pre-ionisation varies with the pressure as well. The basic result, that will be discussed later, is that the ionisation decreases with the increasing pressure.

The experimental results for the 17th harmonic in krypton are shown in Fig. 6.1. It compares a reference measurement of the XUV signal without the pre-ionisation as a function of the medium pressure and a run with a fixed discharge current. There are two key features in this result. First, the signal without the discharge is flat as a function of the pressure, it confirms the expected absorption limited generation – the signal independent on the pressure. Second, there is an amplification of the signal with a peak around $p = 35$ mbar for 40 A. It seems that the peak may be shifted even to higher pressures for 50 A; however, the uncertainty is high in this region. The reason is that the discharge is more unstable with both a higher pressure and discharge current.

The measurement was, in principle, a single-shot experiment: about 10 measurements per point.

Figures 6.3 and 6.4 show the experimental spectra with and without the pre-ionisation, respectively. There are also histograms of the signals. The histograms show the relative stability of the set-up without the discharge. When the discharge is applied, the set-up is more unstable; however, there is a clear enhancement of the signal. The normalisation to arb. u. is respective to the maximum of the signal observed for the 17th harmonic. The spectra are collected from the raw data from a camera, and an example of these data is shown in Fig. 6.6.

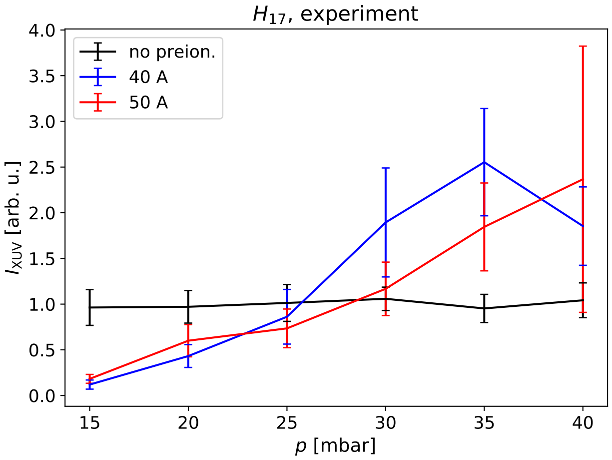

Fig. 6.1: The experimental results of the 17th harmonic generated in long cell filled by pre-ionised krypton gas. There are shown three cases: without the pre-ionisation and pre-ionised by 40-A- and 50-A-discharge current. The data are averaged from 10 shots.

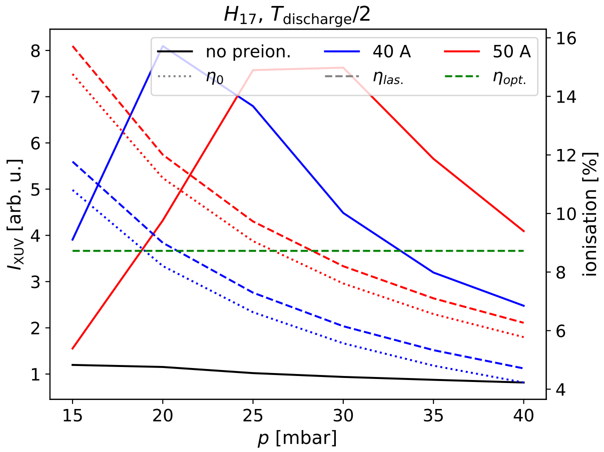

Fig. 6.2: The simulated XUV signal (full lines). There are also corresponding ionisations (the right y-axis): by the discharge (dotted lines), by the laser at the peak of the IR-pulse (dashed lines). The green dashed line shows $\eta_{\mathrm{opt.}}$ given by (6.16). The generation conditions are a 15-mm long gas call filled by krypton, Gaussian beam & pulse focused in the middle of the cell with $w_0 = 110\ \mu\mathrm{m}$, $I_0 = 0.9 \times 10^{14}\ \mathrm{W/cm^2}$, $\tau_{\mathrm{FWHM}} = 35$ fs.

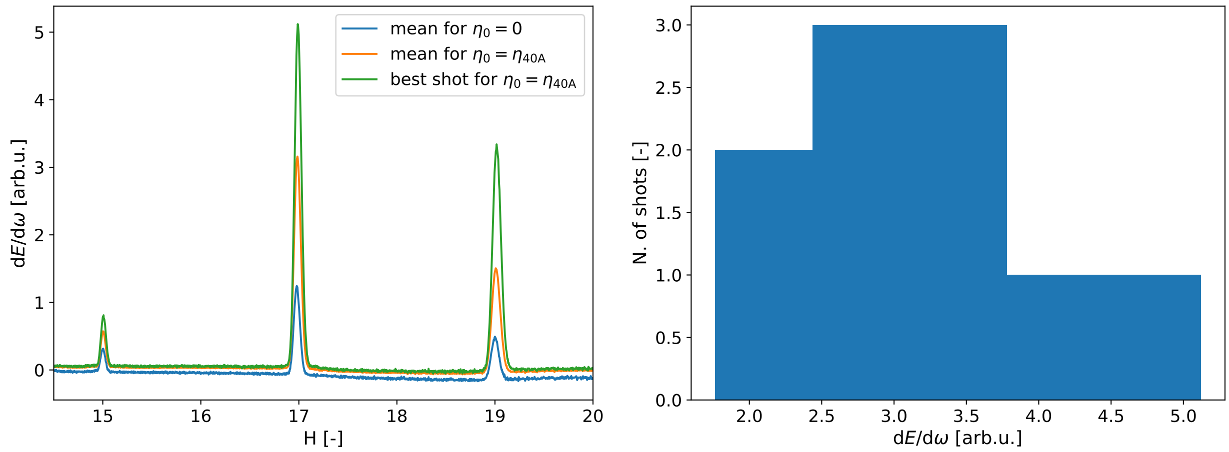

Fig. 6.3: (Left:) The experimental spectra for $p = 35$ mbar and without the pre-ionisation and pre-ionisation by 40 A discharge. There are plotted means of all 10 shots and the shot with the largest enhancement. (Right:) The histogram of the maxima of the 10 shots with the discharge. The $\mathrm{d}E/\mathrm{d}\omega$-axes are normalised to the mean without the pre-ionisation (see Fig. 6.4), it thus correspond to the enhancement of the XUV signal.

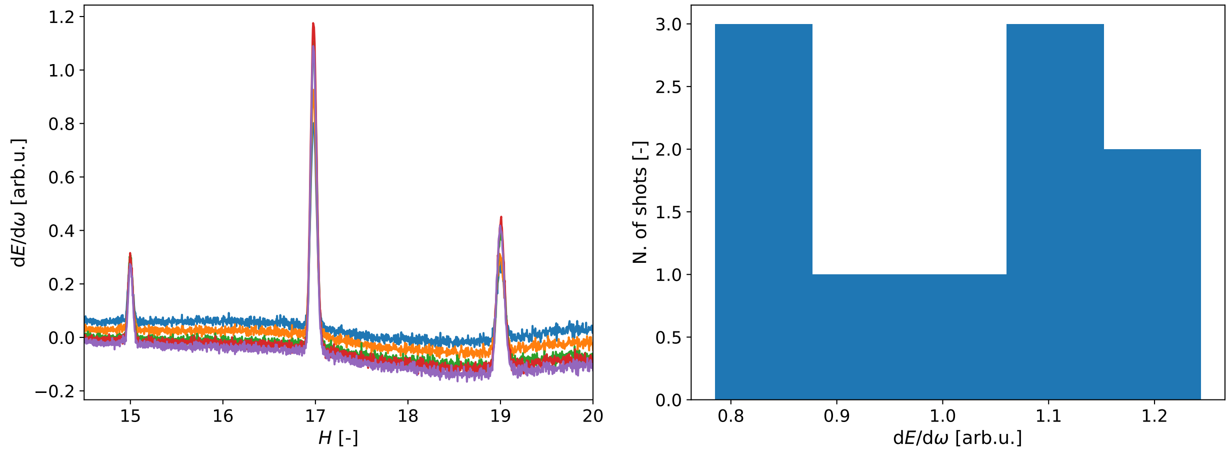

Fig. 6.4: (Left): The XUV spectra for all 10 shots for $p = 30$ mbar without the pre-ionisation. (Right:) The histogram of the maxima of these shots.

6.3.5 Full numerical model: introduction

Here, we apply the full weak-coupling procedure to model the generation process. The numerical model does not rely on any considerations from the analytic model and provides a full numerical counterpart to experiments. We then use various metrics to characterise and compare the results.

One of the inputs of the simulation is the initial value of the ionisation degree by the discharge. The development of such a model is not a subject of this work. We used values computed by Nadya Bobrova from the model introduced in [213]. The result of these computations are the values of the ionisation during the discharge. The computed duration of the discharge is 500 ns. It means that the time scale of the discharge is far beyond the femtosecond scale of the laser pulse, the ionisation by the discharge is thus static during the generation. The laser is master-clocked with the discharge circuit assuring synchronisation, the laser arrives 250 ns after the discharge is triggered. Next, the discharge is well-approximated by a homogeneous plasma within the capillary dimensions. Under these assumptions the pre-ionisation degree by the discharge, η_0, is a constant within the generating medium.

We start with a direct comparison with the experiment. On one hand, this is a "rough" starting point, as the whole multi-scale simulation is reduced to a single number: the strength of the signal in the far field for a given harmonic. On the other hand, it is the most desired result and provides a clear grasp of the modelled physics. Subsequently, we will go into finer detail, which help to understand the underlying mechanisms.

The initial conditions were estimated to agree with the experimental values: the waist of the beam $w_0 = 110\ \mu$m, Gaussian focus intensity $I_0 = 0.9 \times 10^{14}$ W/cm^2, assumed Gaussian focus in the middle of a 15mm-long krypton medium,[5] the duration of the pulse 35 fs (FWHM). Throughout the chapter, we measure the intensity also in the units of the harmonic cutoff derived from (1.1) as

$$\text{Cutoff} = \frac{E_{\text{cutoff}}}{\hbar\omega_0} = \frac{1}{\hbar\omega_0}\left(I_p + \frac{3.17e^2}{2c\varepsilon_0 m_e \omega_0^2} I\right) . \tag{6.19}$$

6.3.6 Numerical simulation of experiment

The signal is computed for a given harmonic q from (5.7) as $I_q = \int_0^{+\infty}\int_{\omega_0(q-1/2)}^{\omega_0(q+1/2)} |\mathcal{E}(\omega,\rho)|^2\, \rho \mathrm{d}\rho \mathrm{d}\omega$. Figure 6.2 shows the XUV intensities for a discharge currents 40 A and 50 A. The full lines correspond to I_{17} – without the pre-ionisation and for the two currents. The signal without the pre-ionisation is flat, this agrees both with the experiment and the analytical model. Next, the signal with the pre-ionisation is amplified, but there is a systematic shift compared to experiment;

---

[5] The gas is mainly characterised by the ionisation potential $I_P^{(\mathrm{Kr})} = 14.00$ eV [214], see Section 8.2 for the specification of other material constants in the model.

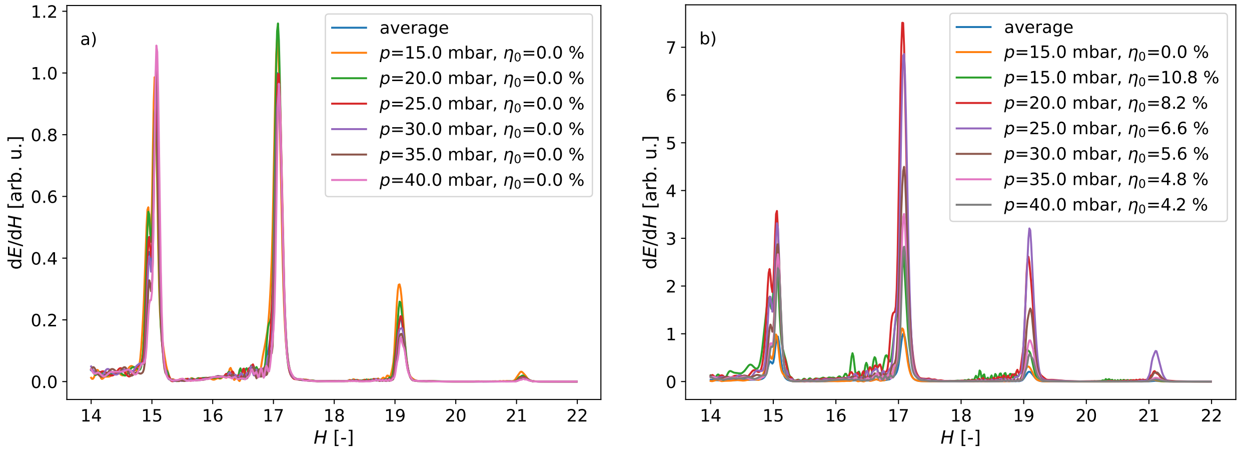

Fig. 6.5: The XUV spectra as functions of pressure. The right panel show the signal without the pre-ionisation, $\eta_0 = 0$ %. The left panel shows the case corresponding to the 40A discharge. The *average* value is taken from the values without the pre-ionisation. The generation conditions are a 15-mm long gas call filled by krypton, Gaussian beam & pulse focused in the middle of the cell with $w_0 = 110$ μm, $I_0 = 0.9 \times 10^{14}$ W/cm^2, $\tau_{\mathrm{FWHM}} = 35$ fs.

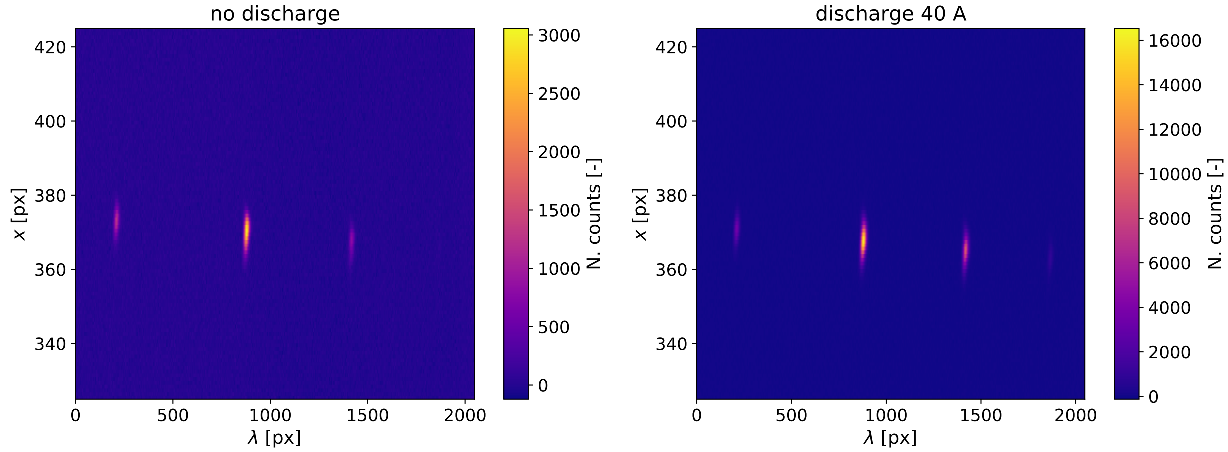

Fig. 6.6: An example of raw data from camera. (Left:) A shot for 35 mbar without the pre-ionisation. (Right:) A shot for 35 mbar for the 40A discharge. The enhancement of the signal is characterised by the number of counts (N. counts).

the peak is moved to lower values of the pressure. It may suggest that the initial ionisation is underestimated in the model. Another difference is in the overall amplification ratio that is ~ 7 compared to ~ 2.5 in the experiment. The difference could originate from the fact that the experimental data are acquired and averaged over many shots, where one faces various instabilities in the laser and discharge. The numerical simulations give an "ideal" single-shot. This is compared in Figs. 6.3 and Fig. 6.5, where the ideal experimental shot is closer to numerical results in the

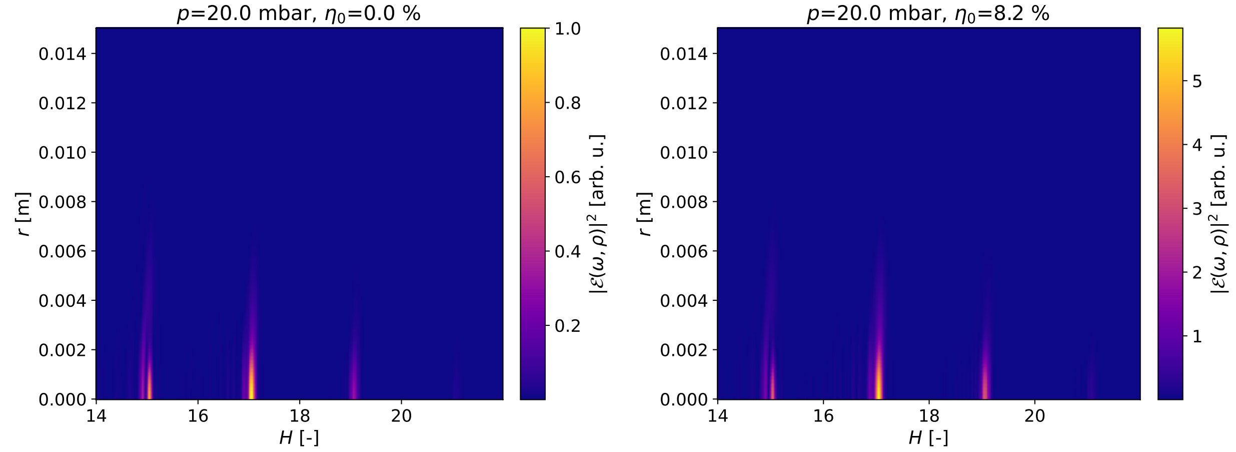

Fig. 6.7: Numerically computed spectra. The generation conditions are a 15-mm long gas call filled by krypton, Gaussian beam & pulse focused in the middle of the cell with $w_0 = 110\ \mu$m, $I_0 = 0.9 \times 10^{14}$ W/cm^2, $\tau_{\mathrm{FWHM}} = 35$ fs.

means of the enhancement (~ 5). Finally, the analogy of the full spatially resolved spectra are compared in Figs. 6.6 and 6.7.

Now, we can go into more detail of the key effect – the effect of the (pre-)ionisation – in Fig. 6.2. The initial conditions for the simulations are the pre-ionisation degrees by the discharges; as it is homogeneous, it is a clear quantity. However, the additional ionisation by the optical field itself depends on the pulse, it is a function of both space and time, i.e. $\eta = \eta(\boldsymbol{r}, t)$. The shown value in the figure is reduced to the on-axis value at the peak of the pulse, where we expect the maximal generation of the XUV. It means that the ionisation shown in the figure is $\eta_{\mathrm{las.}} = \eta(\rho = 0, z = z_{\mathrm{exit}}, t = t_{\mathrm{peak}})$. The results shows that the dominant ionisation comes from the pre-ionisation. This is a desired result as the optimal ionisation shall be seen by the whole pulse and not only transiently.

Next, we have a look at the position of the maximum based on the ionisation. The maximum is expected to be in the crossing of the ionisation from the laser field $\eta_{\mathrm{las.}}$ with $\eta_{\mathrm{opt.}}$. This is confirmed in Fig. 6.2. We investigate this also in different conditions in Fig. 6.9. First, we increase the ionisation. As we mentioned above, the ionisation by the discharge evolves on much longer time-scales than the pulse. The discharge ionisation increases in time, we used the value at the end of the discharge as a different initial condition for the multi-scale model. The maxima again follows the crossings of $\eta_{\mathrm{las.}}$ with $\eta_{\mathrm{opt.}}$. Second, there is the signal for the 19th harmonic. It turns out that the difference between the harmonics is not negligible: the refractive index for the XUV, $n_{\mathrm{XUV,disp.}}$, varies in this region leading to a different $\eta_{\mathrm{opt.}}$, the crossing is then moved along the pressure because of the small gradient of $\eta_{\mathrm{las.}}$ with the pressure. This is again confirmed in Fig. 6.9.

6.3.7 Far-field spectra

The numerical study provides us a deeper insight by: 1) analysing the processes inside the generating medium; 2) studying in great detail the frequency contain with high resolution. Figure 6.8 shows the same spectra as Fig. 6.7 in the logarithmic scale. These figures reveal interference patterns within the spatially resolved spectrum.

The origin of the (ω, ρ)-plane interferences in the HHG process may be of different natures. The arcs (clearly visible for $\eta_0 = 8.2$ % around H19) are related to the modulation of the dipole phase for long trajectories in space and time due to the intensity profiles [33]. This modulation is clear from the phenomenological dipole (2.19): $d \propto \mathrm{e}^{-\mathbf{i}\alpha I_{\mathrm{IR}}}$. Another known interference mechanisms are 1) Maker fringes due to the longitudinal phase modulated attributed to the modulation of the phase due to Δk_q from the phase-matching [195, 215, 216], or 2) the interference between different microscopic electron paths – the long and short trajectories [31]. Generally, any modulation of the XUV phase either in space or time would lead to an interference.

The detailed study of interferences in long targets is out of scope of the pre-ionisation-driven phase-matching. The fine characterisation of XUV could be then a following project.

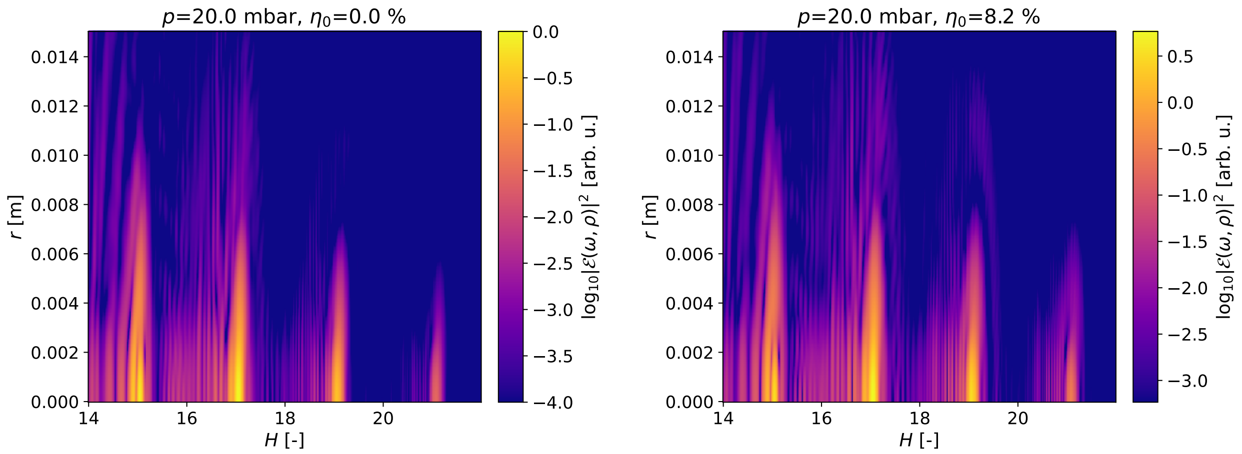

Fig. 6.8: The same spectra as in Fig. 6.7 in the logarithmic scale.

6.3.8 Applicability of the analytic model

An important question is the applicability of the analytical model (6.18) that gives a direct relation between the ionisation degree expressed in η and the XUV signal. Once we have the signal and the ionisation degree from the full numerical model, we can compare this equation both ways: We can estimate 1) the signal from the numerical ionisation plugged in (6.18) and 2) the ionisation from the numerical signal by inverting the relation. A difficulty is that we do not know $\left|\widehat{\partial_t j}\right|^2$. We use the average in pressure without the pre-ionisation, $\eta = 0$, for a calibration:

$$\left|\widehat{\partial_t j}\right|^2 = \frac{\sigma^2 \overline{I_q(\eta = 0)}}{4}\,, \qquad \overline{I_q(\eta = 0)} = \frac{1}{N}\sum_{i=1}^{N} I_q(\eta = 0; p_i)\,,$$

and $\{p_i\}_{i=1}^{N}$ are the pressures for which we done the simulations. The comparisons are in Fig. 6.10. There are two curves estimating the ionisation; because (6.18) is not an injective function, there are two branches of the inverse for η. The lower branch is for η below the optimal ionisation and vice versa for the upper branch. The estimate of the ionisation differs the most close to the optimal generation. This may be due to the steep evolution of $I_q(\eta)$ around $\eta_{\mathrm{opt.}}$. The opposite procedure: the signal estimated from the ionisation follows the numerical results well in both cases. In summary, the analytic model fits well the full *ab initio* computations.

The benchmark of the analytical model is of high interest – the computation of the source term from the numerical solution of the Schrödinger equation is computationally the most expensive part of the model. Relying only on the ionisation from the numerical model is cheap compared to the full computation. Finally, if the optical ionisation is small compared to the pre-ionisation – as shown for this particular case in the previous figures – only reaching the value $\eta_{\mathrm{opt.}}$ becomes sufficient to design phase-matching mechanisms.

In conclusion, we must clarify up to which point it is a true benchmark of two independent approaches to avoid possible circular reasoning. In both cases, the initial values – the ionisation and the electric field as functions of $(\boldsymbol{r}, t)$ in the whole medium – comes from CUPRAD, but the computation splits at this moment. 1) The analytic model is a short-cut to get the result directly from the ionisation relying on $\Delta\alpha^{(\mathrm{p})}$. 2) The full study first computes numerically TDSE's and then sums the elementary dipoles by the Hankel transform. The refractive indexes, $n_{\mathrm{IR,disp.}}$ and $n_{\mathrm{XUV,disp.}}$, within the multi-scale model are sourced from the same data as $\Delta\alpha^{(\mathrm{p})}$.[6] It means that both models share this quantity: this part is thus not an independent check. However, the multi-scale model surpasses analytic model in two key aspects: the time profile of the pulse – the envelope – and transversal profile of the beam. This benchmark thus cannot answer if there are any inaccuracies due to the refractive indexes, but it answers that the spatio-temporal profile of the pulse does not destroy the phase-matching in our conditions.

---

[6] However, they are decoupled in the multi-scale model. $n_{\mathrm{IR,disp.}}$ is used only in the code propagating the IR-laser, while $n_{\mathrm{XUV,disp.}}$ is in the independent code for collecting the dipoles. Thus, it is still a self-consistency check of the multi-scale model.

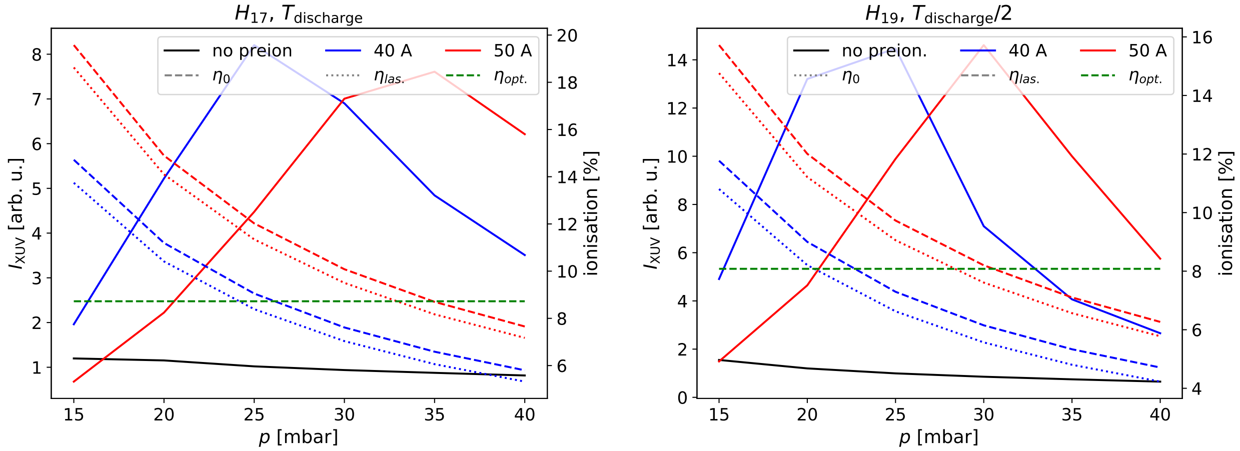

Fig. 6.9: The sensitivity of the XUV signal on the optimal ionisation $\eta_{\mathrm{opt.}}$. The left panel shows the H17-signal for different pre-ionisation curves obtained at the end of discharges for 40 A and 50 A. The right panel shows the signals for H19 for the pre-ionisations at the half of the discharges. There are also shown the initial ionisations, η_0, and ionisation by the IR pulse, $\eta_{\mathrm{las.}}$. The generation conditions are a 15-mm long gas cell filled by krypton, Gaussian beam & pulse focused in the middle of the cell with $w_0 = 110\ \mu$m, $I_0 = 0.9 \times 10^{14}$ W/cm^2, $\tau_{\mathrm{FWHM}} = 35$ fs.

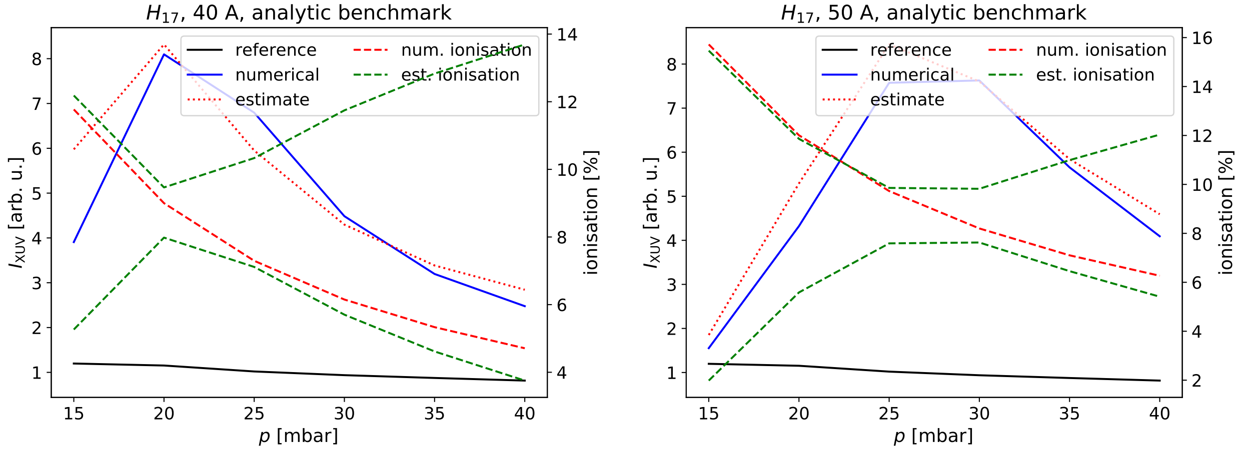

Fig. 6.10: The comparison of numerical model with the analytic model (6.18). The *reference*, *numerical* and *num. ionisation* are obtained from the multi-scale model. The *estimates* are obtained from (6.18) (inverted for the *est. ionisation*) by using respective values from the numerical model. The generation conditions are a 15-mm long gas cell filled by krypton, Gaussian beam & pulse focused in the middle of the cell with $w_0 = 110\ \mu$m, $I_0 = 0.9 \times 10^{14}$ W/cm^2, $\tau_{\mathrm{FWHM}} = 35$ fs.

6.3.9 Detailed characterisation of HHG in multi-parametric space

We have investigated the physics corresponding to experiments, confirmed the key principle and benchmarked the analytic model. We extended the analyses in two directions compared to the

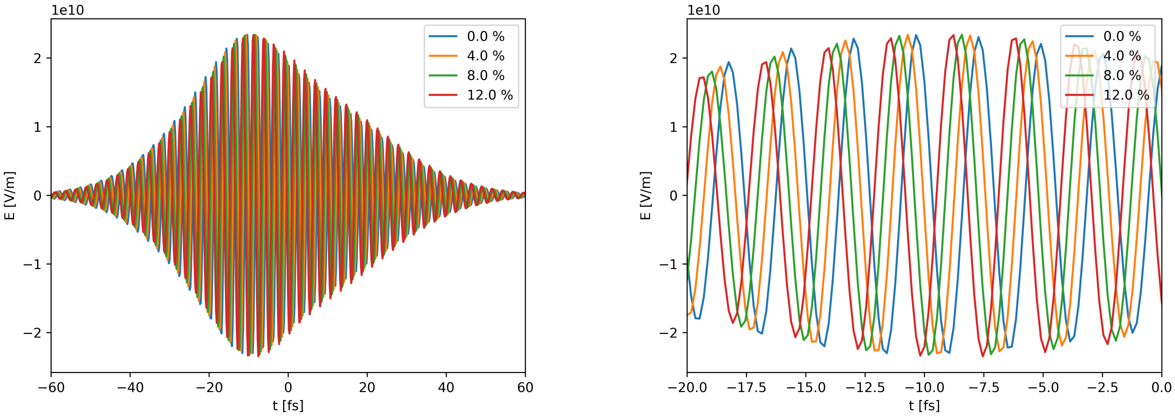

Fig. 6.11: The electric fields, $\mathcal{E}(\rho = 0, z = z_{\text{exit}}, t)$ for $p = 25$ mbar, $z_{\text{exit}} = 15$ mm and the input peak intensity 1.2×10^{14} W/cm^2, at the exit of the gas cell for various pre-ionisations. The time is adjusted to the co-propagating frame by c. The key features are the stability of the envelope and the shifts of the fast oscillating parts.

experiment: 1) We may get insight of the physics inside the medium during the generation. For example, the electric field, $\mathcal{E}$, and microscopic source terms, $\partial_t j$. 2) A single run is a realisation of the experiment in a multi-parametric space of input parameters. In simulations, some of them may be easier or more precisely controlled. We thus may inspect HHG in a broader perspective. We add these parameters as the quantities of the interest. For example, $\mathcal{E}(\boldsymbol{r}, t; p, I_0, \eta_0)$ denotes the electric field in its natural variables $\boldsymbol{r}$ and t, together with the conditions p, I_0 and η_0 that denote respectively: the pressure of the gas p, the peak intensity in the vacuum focus of the driving beam I_0 and the pre-ionisation η_0.

6.3.10 *Stability of beam with respect to* η_0

We mentioned that one of the key advantages of the homogeneous pre-ionisation is that we tune the linear part of the refractive index. In other words, we control the phase velocity of the driving laser without affecting the focusing properties, the pulse shapes, etc. We verify this by our simulations. As examples, we show the evolution of the electric field for various degrees of pre-ionisation in Fig. 6.11. The electric field is plotted in two scales: The envelope of the pulse is not affected and the fast oscillations fit within in all the cases. Zooming only few cycles of the field, the fields for various pre-ionisations are shifted by the pre-ionisation. This is a clear straightforward demonstration of the mechanism as the electric field is one of the most fundamental characteristics of the field.

Figure 6.12 shows the profile of the (ρ, z)-profile of the peak intensity of the pulse for $\eta_0 = 0$ %

and ionisation degrees at corresponding times for $\eta_0 \in \{0\ \%, 8\ \%\}$. Note that the ionisation degree is only shifted by η_0 for the two cases. There were no noticeable differences in the intensity profile.

In conclusion, these results prove the expected scalability with the pre-ionisation and that it really acts as a background changing the phase velocity. We verified this behaviour also for other configurations within the region of the initial conditions of our interest; we thereafter will not show the beam profiles for different values of η_0 as $\eta_0 = 0$ is representative enough.[7]

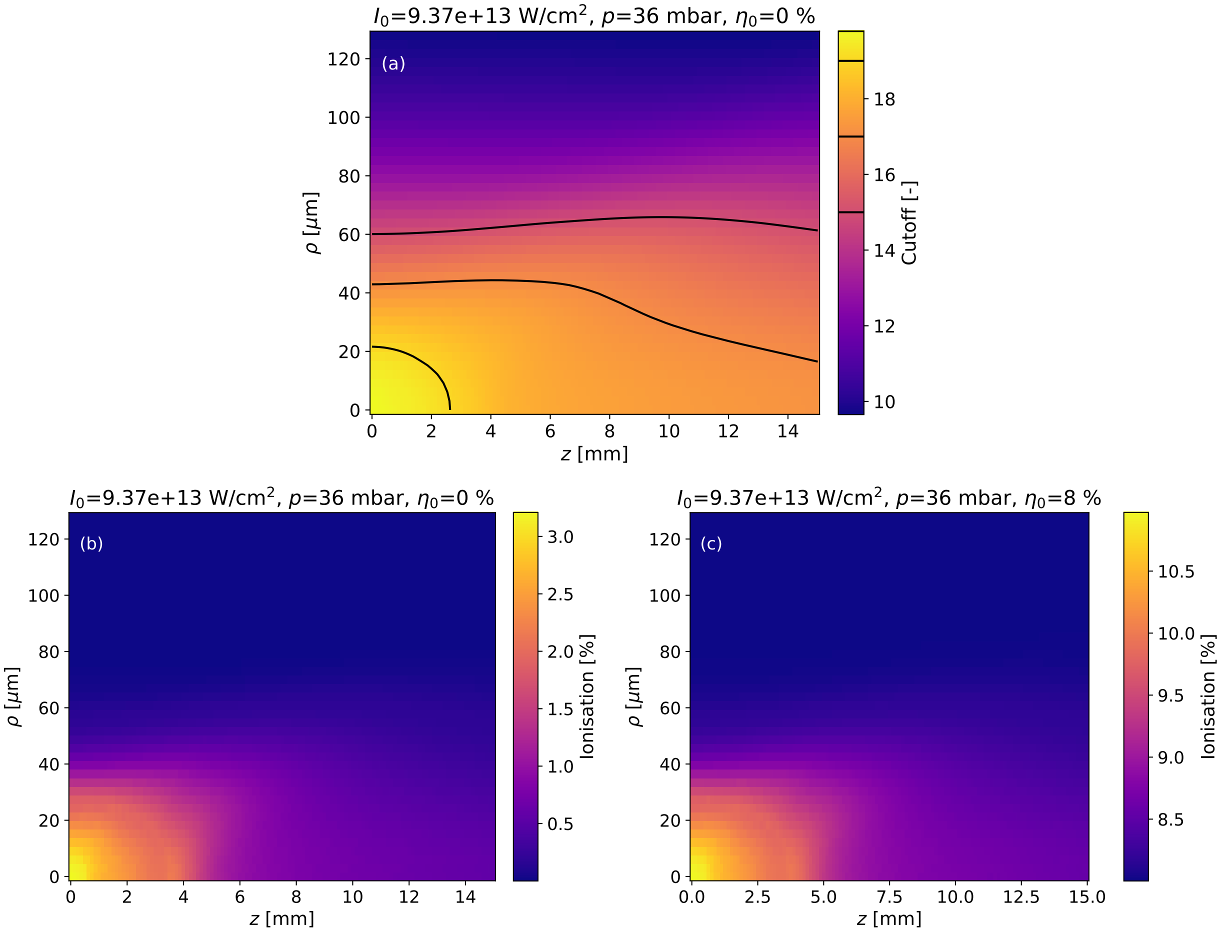

Fig. 6.12: (a): The peak intensity profile $I(\rho, z)$ for the given input conditions I_0, p and η_0. (Measured by the harmonic cutoff (6.19).) (b): The corresponding ionisation of the medium. (c): The ionisation profile for the case differing only in η_0. The intensity profile corresponding to (c) is not shown as there is no recognisable difference compared to (a). We see that also (b) and (c) differ only by a constant shift of the scale.

---

[7] Note, this is not a general proof in all the cases. For example, once multiple-ionisation becomes to play a role, the propagation may be more complicated; however, this is beyond our interest at the instant.

6.3.11 Beam shape, intensity clamping

Now, we move to the shaping of the pulse in space and time due to the propagation and study the impacts to the phase-matching conditions. The pulse is expected to be heavily distorted once the intensity is high enough to induce strong non-linear response. The plasma-induced defocusing due to the ionisation prevails in our conditions [73, 74, 75, 217]. Here we investigate in detail this effect from our simulations.

We start with the intensity distribution on the axis. Figure 6.13 shows the intensity and phase-mismatch evolution for various initial peak intensities and pressures. The first panel, (a), shows the on-axis peak intensity profiles as for various pressures and initial intensities of the pulse. It illustrates the key mechanism of the long-media generation in our conditions. The intensity is clamped at the first part of the medium for $z \lesssim 6$ mm (region I) and is stabilised after this region, $z \gtrsim 6$ mm, with only a mild decrease (region II). Moreover, the stabilised intensity in the region II is driven also by the pressure. Generally, lower pressure can accommodate beams with lower peak intensity as expected: the the two cases with sufficiently high intensity are above all the others in the region II, while the others fall to approximately the same peak intensity. Next panels, (b) and (c), show also the corresponding scaled phase mismatches $|\Delta k_{17}/p|$ for different pre-ionisation degree η_0. It directly shows the reduction of the mismatch by the order of magnitude (note y-axis scales). Moreover, it shows the scaling with pressures: the limit value in the region II is very similar for higher pressures and slightly different for the lowest pressure (but still far below the differences between the two cases of various η_0).

This study gives us the insight in the generation: our medium is long enough so that the intensity is clamped at its first part, region I, and then we generate in a relatively stable region of the beam evolution. Note $L_{\mathrm{abs}} \approx 1$ mm for H17 at 15 mbar in krypton from the scattering coefficients [218, 219], it means that the relevant contribution to the signal comes from the rear part of the medium.

Off-axis intensity, fluence

Next, we look into more detail on the off-axis physics. We have seen the on-axis defocusing in Fig. 6.13 and also the corresponding beam shape and ionisation in Fig. 6.12 for $p = 36$ mbar, which is an intermediate case of the defocusing. ”Limit cases” are shown in Fig. 6.14. These two cases use (a) low intensity and low pressure and (b) high intensity and high pressure. Concerning the case (a), the focusing is preserved in the middle of the medium as the intensity increases with z. Contrary, the beam is heavily distorted for the case (b). Notably, the peak of the intensity is reached off the axis at the edge of the beam for $z < 8$ mm. It means that a significant portion of the energy is pushed off the axis due to defocusing before an equilibrium is reached, in agreement with what is

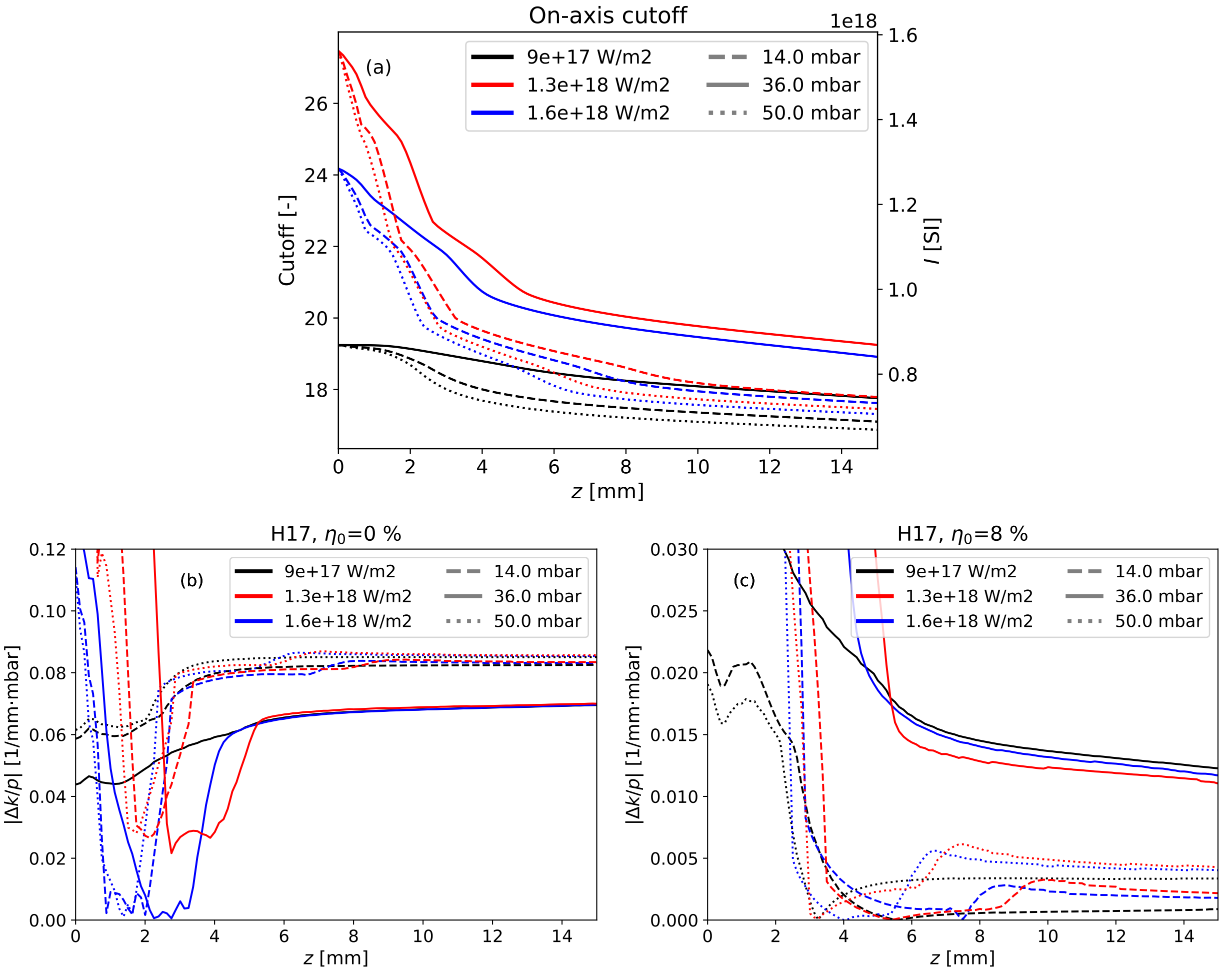

Fig. 6.13: (a) shows the on-axis intensity profiles in the harmonic cutoff units (6.19) for various initial pressures and intensities. The initial intensity is given by the value at $z = 0$ and pressures by various styles of the lines. Next panels show the corresponding scaled phase mismatches $|\Delta k/p|$ without the pre-ionisation, $\eta_0 = 0$ % (b), and for $\eta_0 = 8$ % (c).

observed as the stable region II. Next, the ionisation acts as a fast defocusing mechanism in our conditions: high amount of the ionisation degree, η, is reached in approximately the first 2 mm of the propagation.

The intensity provides an image of the pulse profile. Mainly, we find the cases when the pulse is distorted. However, a part of the information is still not complete by this methodology: the time aspect of the generation is partially suppressed because we have evaluated the quantities of interest at the peak of the pulse in time. We complete this discussion in Section 6.3.13. Now, we restrict our analysis to the main concept characterising the phase-matching conditions.

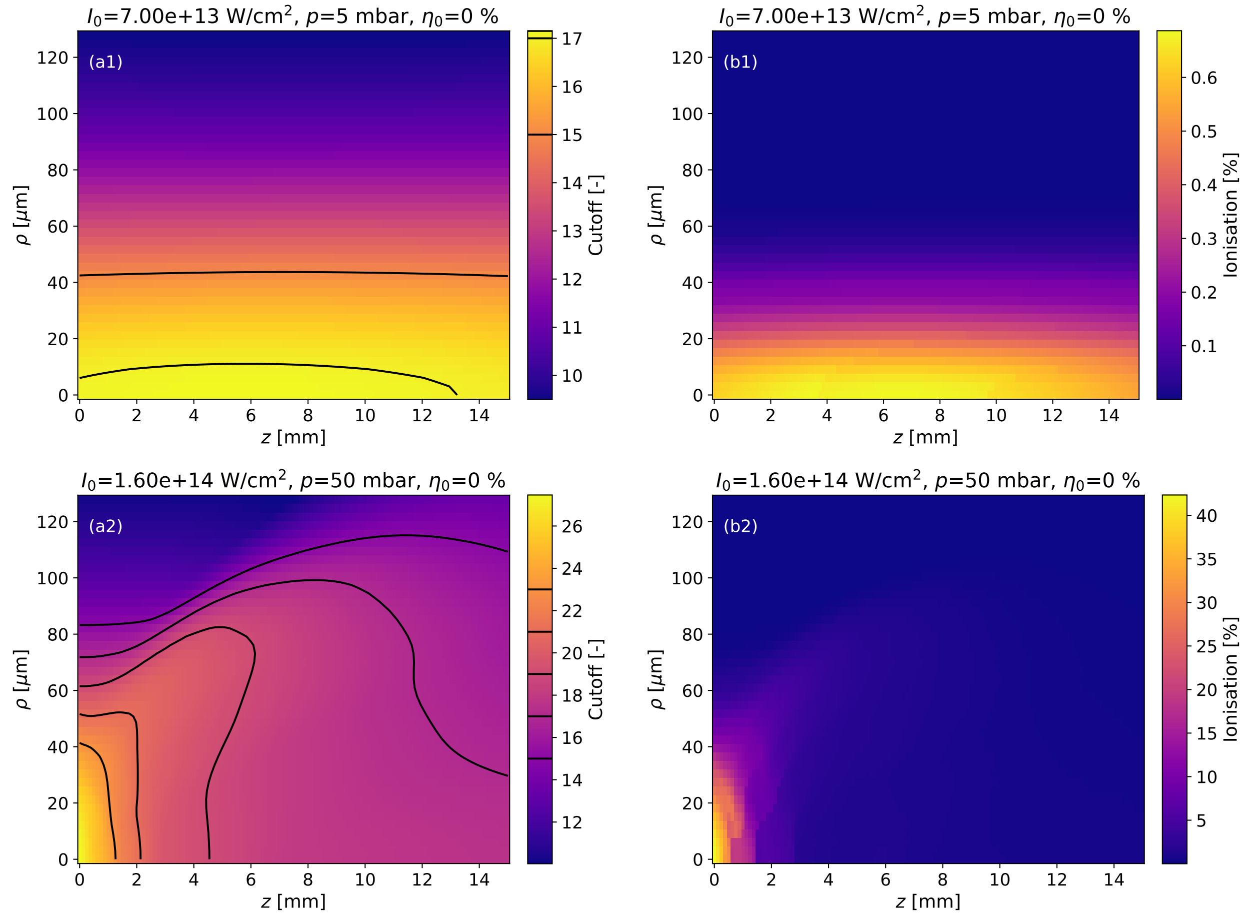

Fig. 6.14: The peak intensities and ionisation for two ”limit cases”: 1) low pressure and low initial intensity, 2) high pressure and high initial intensity.

Coherence maps

Because the ionisation affects the phase, which together with the intensity drives HHG, we link these quantities in the map of the coherence length L_{coh} given by (6.15). We continue with the beam characteristics presented in Fig. 6.12. Considering the effect of η_0, the intensity profile is unaffected and η is only shifted by η_0. The corresponding coherence lengths for H17 are shown in Fig. 6.15. There is a significant difference in the coherence maps. The case of $\eta_0 = 8$ % indicates an optimal generation in a large part of the region II both on- and off-axis, which agrees well with the already discussed results in sections 6.3.6 and 6.3.8.

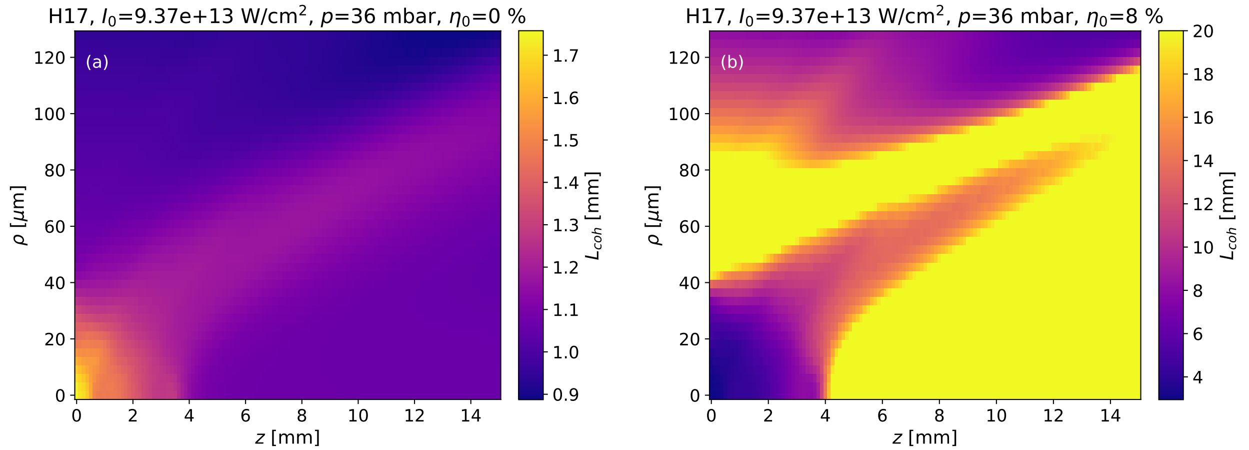

Fig. 6.15: The coherence lengths, see (6.15), at the peak of the pulse without the pre-ionisation (a) and near optimal η_0 (b). Note different scales.

6.3.12 Measures to optimise phase-matching

We defined two different metrics of the phase-matching: the coherence length $L_{\mathrm{coh}} = |\pi/\Delta k_q|$ and the dephasing Δk_q. These quantities are very intuitive and we could infer a good qualitative picture of phase-matching. The question is: how do they stand quantitatively?

We list the difference between the dephasing (6.13), coherence length and the expected intensity I_q (6.18):

Δk: It is a "notorious" quantity in optics and it naturally emerges from the superposition of the waves to find its constructiveness. It is also a natural quantity of the local viewpoint.

L_{coh}: It is a very instructive quantity, it gives the spatial dimension of the region, where we expect a constructive addition of the signal. It is a natural quantity of the global viewpoint.

I_q: This is the most specific quantity, it is fitted for our problem and aligned with our goal: optimise the expected signal. Its largest advantage is that it is properly scaled with the density. Both aforementioned quantities are not, it means that one must keep in mind the scaling while working with them.

Either of them can be used to optimisation. However, some care is needed. Their mutual relations are non-linear, which has to be considered once one applies them. The quantities Δk or L_{coh} are commonly used. But we suggest that I_q should be used as a fitness function to optimise the intensity. The difference between $|\Delta k_q|$-, L_{coh}- and I_q-map is shown in Fig. 6.16. The main trend is still covered by all the metrics. However, I_q includes the proper scaling with the pressure, which extends the ridge-shape in the centre of the L_{coh}-map.

The information contained in all three measures is thus similar. However, the key information is about setting a proper threshold – the value we accept to call the generation optimised – for each of them. Such an information is naturally contained in I_q as it measures directly the expected XUV signal.

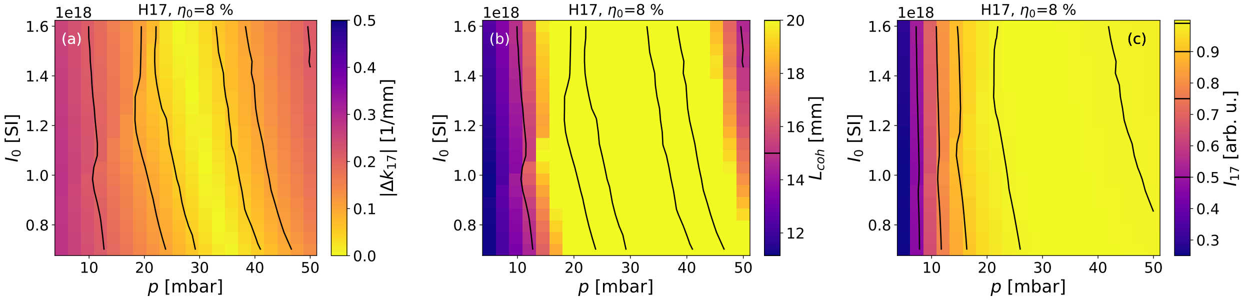

Fig. 6.16: There are various measures of phase matching for H17. From left to right: $|\Delta k|$, L_{coh} and I. These graphs show the values at the peak of the pulse, on the axis at the end of the medium, using the notation of the multi-parametric space, the cuts are $|\Delta k(z = z_{\mathrm{exit}}, \rho = 0, t = t_{\mathrm{peak}}; p, I_0, \eta_0 = 8\ \%)|$ and correspondingly for the others. The units of I are normalised to the maximal possible signal of the ideal absorption-limited generation.

6.3.13 Time aspect of the generation

To complete the study, we infer the role of time and finish the introduction from Section 6.3.11. The motivation is that some dimensions are always removed if we intend to visualise multidimensional quantities. To slice out the temporal dependence, we present the quantities at the peak of laser intensity (Figs. 6.12, 6.13, 6.14, 6.15 and 6.16). This choice is logical as we expect the maximum of the XUV to be generated at this point. It is also consistent with the methodology used in, e.g., [75]. However, this may put together unsynchronised parts of the pulse if it is seriously distorted due to its propagation in the medium. We address the question of the time profile in this section. This will also help us to understand the shaping of the pulse during the propagation.

Before we go into detail, we need to synchronise the clock along the propagation. Our convention for this section is to use a frame co-moving with the pulse by the speed of light c along the laser propagation.

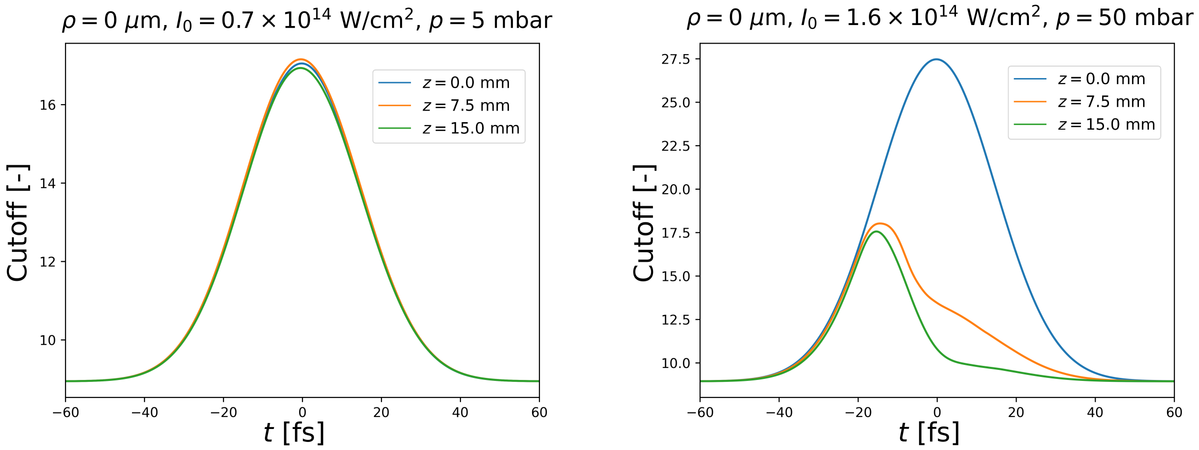

Fig. 6.17: The evolution of the on-axis time-intensity profile during the numerical propagation of the driving pulse, the difference between the panels is the pressure and the initial peak intensity. In the case of the lower pressure and intensity, the pulse is not strongly shaped and also the maximum of intensity is inside the medium. The intensity drops throughout the propagation for the higher pressure and intensity; the trailing edge is suppressed; and the actual peak of the pulse moves towards the leading edge. It is expected as the propagation is generally more affected in a denser medium.

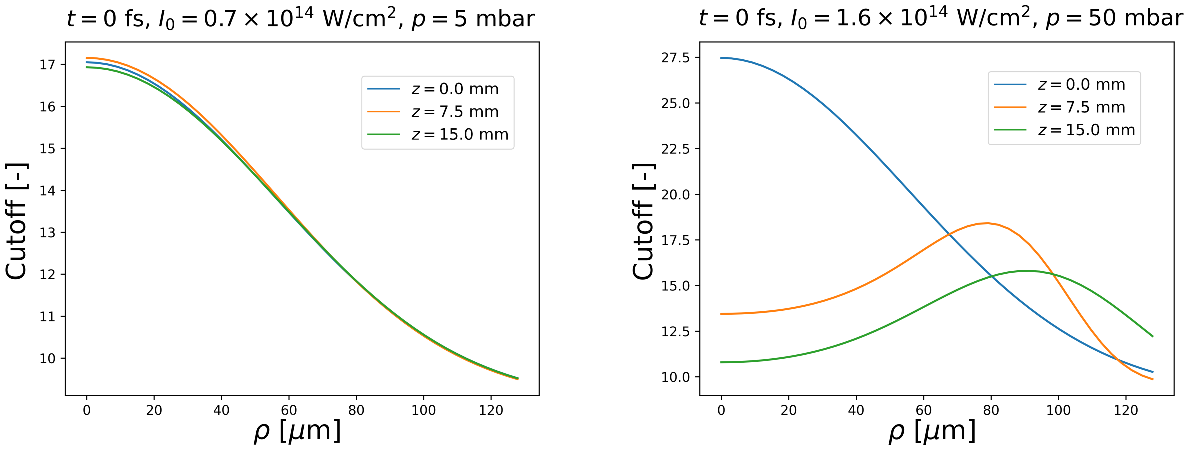

Fig. 6.18: The radial intensity profiles for fixed times along the propagation corresponding to the points and conditions from Fig. 6.17. It confirms that the profile remains Gaussian also in the radial coordinate in the case of the lower pressure and intensity; while the intensity is pressed outwards the on-axis region for the higher pressure and intensity.

One-dimensional cuts

We start with simple one-dimensional cuts of the intensity profiles. Figures 6.17 and 6.18 show respectively the intensity evolution in time at different points in the gas cell and corresponding radial distribution for a fixed time. There are the two limit cases from Fig. 6.14 used for the illustration. (They represent low-intensity, low-pressure and high-intensity, high-pressure cases.) The pulse is almost undistorted in low pressure and preserves also its focusing property: the peak at 7.5 mm is higher than that at the entry and exit. The radial profile also follows the Gaussian shape during the whole propagation. The situation is very different in high pressure. The defocusing clearly affects the pulse from the trailing edge as this part of the pulse is mostly defocused. The peak of the intensity is reduced and moved into the raising edge. The pulse shape is at the end quite close to the low-pressure case, only shifted in time. It also complements Fig. 6.13, where the peak intensity is stabilised at similar values.

The conclusion from these findings is that the peak of the intensity moves in time towards the original raising edge of the pulse once the intensity surpasses the threshold of defocusing. The surplus of the intensity from the peak and the trailing edge is pushed out from the propagation axis. It causes the formation of wings at the radial edge of the pulse, where the peak intensity may be even higher than on the axis.

2D-scans: wings of pulse

Having introduced the basic picture, we go into more detail by scanning the profile. First, there are snapshots of the pulse at the entry and at the exit of the medium shown in Fig. 1.3. The pressure is 50 mbar and the peak entry intensity is 1.2×10^{14} W/cm^2. (The figure shows the instantaneous intensity that is doubled compared with the usual intensity that is averaged over the fast oscillations, see Appendix B.2.) It shows the formation of the wings at the trailing of the pulse.

Now, let us see the formation of the wings along the passage through the medium and compare it with the "peak-intensity" methodology. Figure 6.19 shows the intensity in the (z, ρ)-cut at different times of the co-moving frame. The snapshot on the leading edge ($t \approx -5$ fs) shows a regular profile similar to Gaussian focused at the entry of the medium. The wings with the off-axis intensity are clearly formed at the trailing edge of the pulse ($t \approx 5$ fs). The intensity taken at the peak of the pulse, Fig. 6.19(d), demonstrates that the maximum of the intensity is not reached at a fixed time. It suggests that the peak of the intensity is reached later in the pulse in the wings rather than on the optical axis. It is natural as the wings are formed later in the pulse.

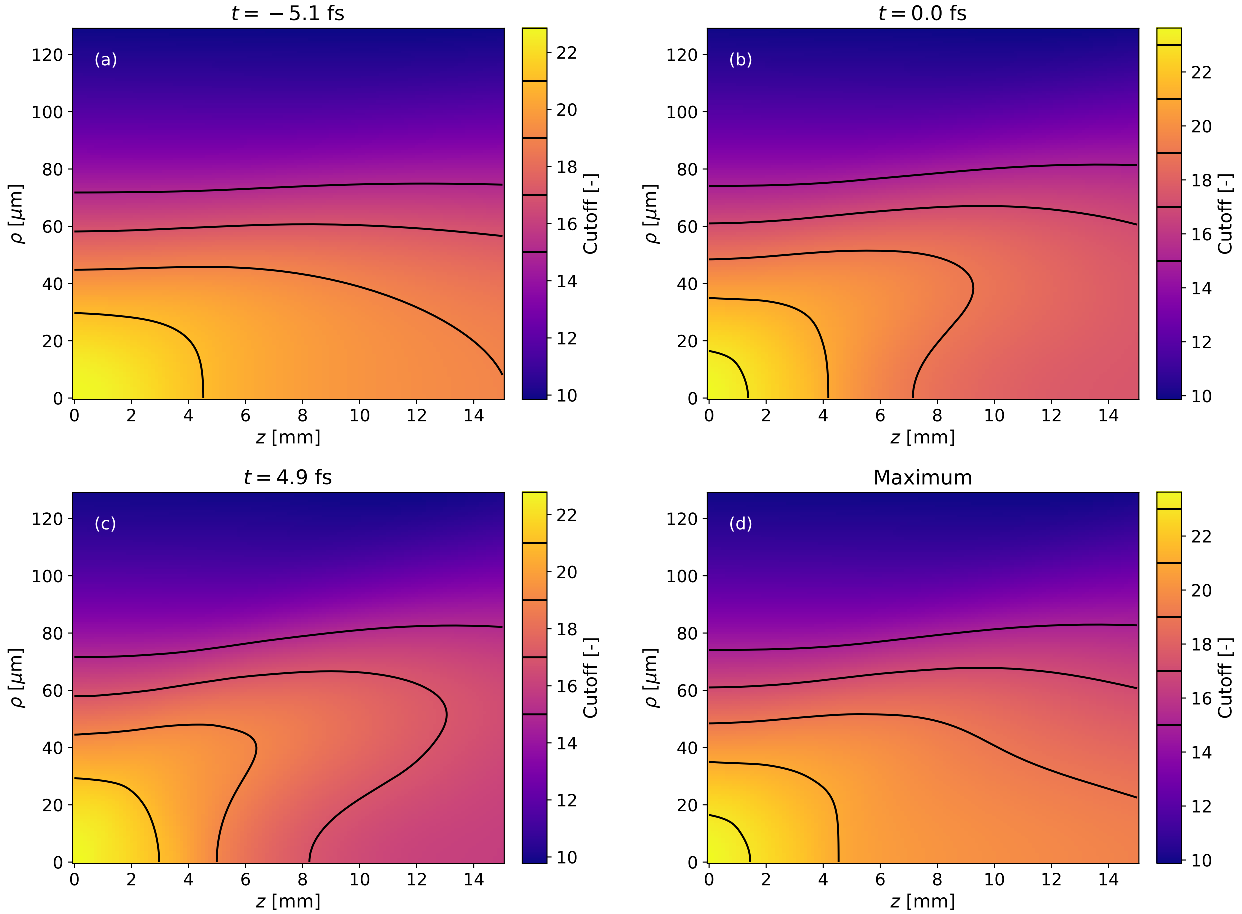

Fig. 6.19: The spatial intensity profiles of the IR-field at various times of the pulse. Panels (a)-(c) show the intensity profiles at a fixed time, $I(t = t_{\mathrm{fix}}, \rho, z)$. (d) is the intensity profile at the peak of the pulse at every point.

Insight into focusing

The profile of the pulse from the previous study demonstrates that each part of the pulse may have different focusing properties. Here we show a way to quantify this property.

Let us recall the spatio-temporal distribution of the phase for a Gaussian beam (B.6),

$$\Phi_{\mathrm{Gauss}}(\boldsymbol{r}, t) = \omega_0 t - k_0 z - \frac{k_0 \rho^2}{2R(z)} + \phi_G(z)\,. \tag{6.20}$$

Subtracting the "plane-wave" oscillations $\omega_0 t - k_0 z$, we obtain the spatial variations of phase

$$\tilde{\Phi}_{\mathrm{Gauss}}(\boldsymbol{r}) = \frac{k_0 \rho^2}{2R(z)} + \phi_G(z)\,, \qquad \phi_{\mathrm{Curv.,Gauss}}(\boldsymbol{r}) = \frac{k_0}{2R(z)} \rho^2\,. \tag{6.21}$$

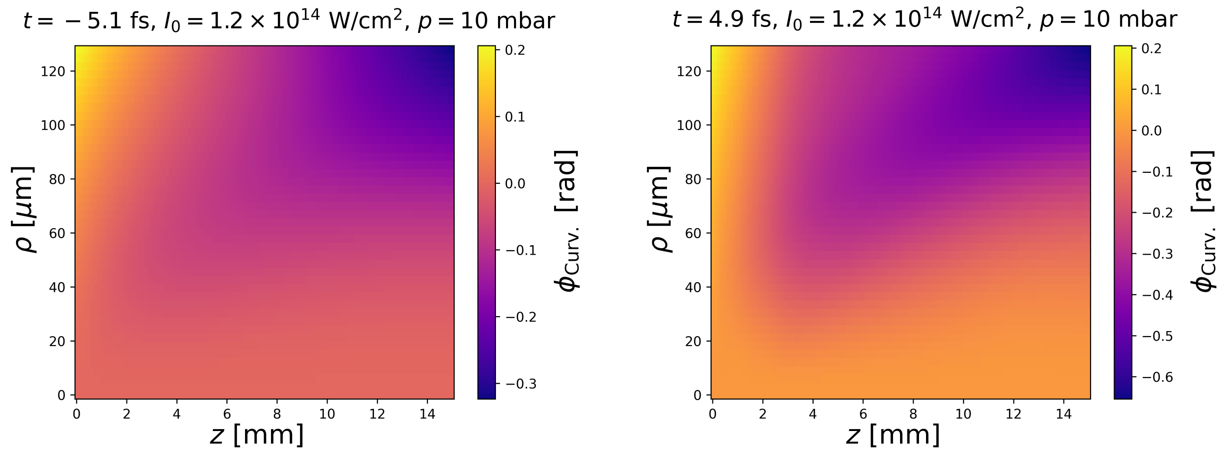

Fig. 6.20: The curvatures $\phi_{\mathrm{Curv.}}(\rho, z, t = t_{\mathrm{fix}})$ for $t_{\mathrm{fix}} \approx \pm 5$ fs, corresponding to Fig. 6.19. The positive values of $\phi_{\mathrm{Curv.}}$ give the focusing property, while negative values are the defocusing. The initial conditions correspond to a Gaussian beam focused in the middle of the medium, $z = 7.5$ mm.

$\tilde{\Phi}_{\mathrm{Gauss}}$ contains both the curvature and the geometrical (Gouy) phase $\phi_G(z)$. The second term, $\phi_{\mathrm{Curv.,Gauss}}$, contains only the curvature related to focusing. We can extract a corresponding quantity from a numerical field as

$$\phi_{\mathrm{Curv.}}(\rho, z, t) = \Phi(\rho, z, t) - \Phi(\rho = 0, z, t)\,. \tag{6.22}$$

Note, that the Gaussian curvature, $\phi_{\mathrm{Curv.,Gauss}}$, is t-independent, while the general case is not. This means that each part of the pulse may be focused at a different spot. This is exactly the case for our defocusing of the trailing edge of the pulse.

These considerations are illustrated in Fig. 6.20. It shows the curvatures for fixed times in Figs. 6.19(a) and 6.19(c). The case for the raising edge of the pulse is close to "vacuum" Gaussian beam focused in the middle of the medium, which corresponds to the initial parameters at the entry of the medium. The difference is that slight defocusing starts to occur for $(\rho, z) \approx (2\text{ mm}, 40\ \mu\text{m})$. The profile differs much more at the trailing edge, $t \approx 5$ fs. It starts to defocus significantly around $z = 2$ mm. Furthermore, the scale is twice the scale compared to $t \approx -5$ fs.

This analysis showed: a) the capability of the code to study the focusing properties in detail; b) that the pulse is significantly distorted at the trailing edge of the pulse while the raising edge remains close to Gaussian.

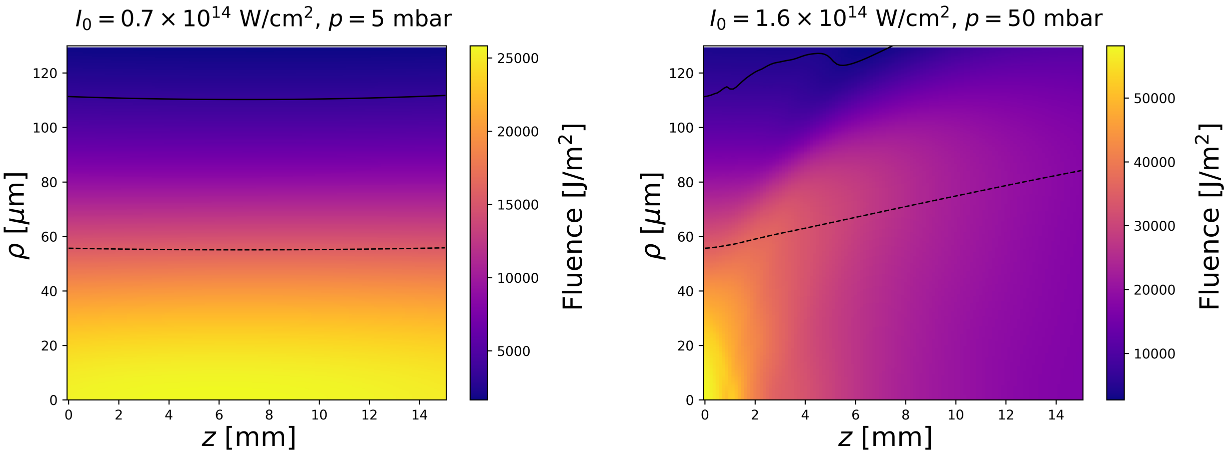

Fig. 6.21: The beam trace given by the fluence $F(\rho, z) = \int_{-\infty}^{+\infty} I(\rho, z, t)\,\mathrm{d}t$, we show further the radii of the beam defined by $\rho_{\mathrm{rms}}(z) = \int_0^{+\infty} \rho^2 F(\rho, z)\,\mathrm{d}\rho / \int_0^{+\infty} F(\rho, z)\,\mathrm{d}\rho$ and $F(\rho_{1/\mathrm{e}^2}(z), z) = F(\rho = 0, z)/\mathrm{e}^2$, shown in respectively dashed and full lines. The conditions of the limit cases are the same as in Figs. 6.17 and 6.18.

Aggregated time: fluence

Finally, we apply the measurements of the pulse by its fluence F, defined in (B.4). The snapshots at time – either fixed or corresponding to the peak of the intensity – are appropriate to HHG as it is an instantaneous process. However, a snapshot of the field in time may be difficult to reach experimentally. On the other hand, it is easy to measure the energy integrated over the pulse at a given radius.[8] This is exactly the fluence.

The fluences corresponding to the two limit cases from Figs. 6.17 and 6.18 are shown in Fig. 6.21. Note that the drop of the fluence with the radial coordinate is not necessarily a drop in energy, as the scaling includes the Jacobian, i.e. the differential energy is $\mathrm{d}E/\mathrm{d}\rho = 2\pi\rho F(\rho, z)$.

6.4 Conclusion and discussion

This chapter has followed two goals. First, we have presented the multi-scale model of HHG, which is an important result of this thesis. Second, we have investigated a real scheme to optimise HHG, where the model is complemented with an experiment. The multi-scale model has provided a detailed insight into the underlying physical processes. This approach is indispensable to comprehend the key mechanisms which are then turned into a design of optimised HHG.

We have shown that the phase matching in long-media HHG can be controlled by pre-ionising the medium. Moreover, we have proved that it is almost an independent parameter of the control

---

[8] For example, this is exactly the way the harmonics are measured experimentally, Fig. 6.6. The frequency resolution is obtained by grating placed in the beam.

within the investigated range. Next, we have recognised that the pre-ionisation degree is the key parameter of the optimisation and we have found a great agreement with the analytical model, which confirms the applicability of the analytical model in designing phase-matching schemes. The numerical model may be then used for confirmations and further refinements of the designs. Additionally, the robustness of the pre-ionisation scheme has been shown for various parameters.

The model has also been compared with the experiments, and we have reached quantitative agreement of all the approaches. The XUV signal has enhanced up to 8 times. Applying the verified model beyond the experimental conditions, it indicates that even higher enhancement is reachable in some configurations, at instant up to 25 for H45 in neon.[9]

Finally, we return to another goal of the thesis – the model itself. We had access to the physics of the HHG in the generating medium. Mainly, we have been able to retrieve the spatio-temporal profile of the driving laser, together with detailed analyses of its phase, plasma density and others. We have also presented various approaches to proceed. Beside the numerical solution of HHG based on the coupling with the Schrödinger equation (that is computationally expensive), we have found a great utility of simpler models based on the phenomenological dipole. Such an approach allows to scan larger portion of multi-parametric space given by various initial conditions of the incident laser and generating medium relatively cheaply from a computation viewpoint. In conclusion this part of the work should be seen not only as a complement to the particular experiment, but also as a demonstration of the capability of the code.

---

[9] This estimate is obtained by using (6.18) for 800 nm input laser for $\eta_{\text{opt.}} \approx 6.8$ %, the material constants are obtained from [218, 219].

Part III

NUMERICAL CONSIDERATION OF MODELLING

7. NUMERICS OF MICROSCOPIC SCALE

This chapter introduces the numerical procedures used to solve the TDSE and the related eigenvalue problem in a static field. First, we pose the problems of interest mathematically. Then, we present the general framework: the tools to represent states by vectors $|\psi\rangle$ from a Hilbert space (Sections 7.1 and 7.2) and the Hamiltonian H driving the dynamics (Section 7.3). Last, the procedure describing the evolution in time of the system is presented in Section 7.4. This general framework is then applied to our 1D-TDSE solver, 3D-TDSE solver and the complex rotation in Sections 7.5, 7.6 and 7.7, respectively. Last, we provide details about the calculation of the dipole using the FSPA in Section 7.8.

The central equations are[1]

$$\mathbf{i}\partial_t |\psi(t)\rangle = H(t) |\psi(t)\rangle \ , \tag{7.1a}$$

$$H |\psi_E\rangle = E |\psi_E\rangle \ . \tag{7.1b}$$

The first equation describes the evolution of the state $|\psi(t)\rangle$, the second equation is the eigenvalue problem for the eigenvector $|\psi_E\rangle$ associated with the eigenvalue E. There are three main points to address before we implement an algorithm to find a numerical solution:

- The choice of a proper Hamiltonian H and the respective Hilbert space $\mathscr{H}$. At this stage, we need to resolve the degree of complexity of physics that we want to include in the model. For example: How many electrons will be described? Do we further reduce the size of $\mathscr{H}$ by using "1D-atoms"? Do we include spin interactions? This is intimately related to the approximations discussed in detail in Section 2.1. Here in Section 7.3, we will discuss the implementation of 3D- and 1D-atoms using the approximations.
- Next point is the choice of the representation of $|\psi\rangle$. Basically, it means to choose a finite-dimensional subspace $\mathscr{G}$ of $\mathscr{H}$.
- The last point is the evolution in time. It means to discretise t and use finite differences to find $|\psi(t)\rangle$.

---

[1] As stated in Section 2.1, we stay within the frame of non-relativistic quantum mechanics. See, at instant, [220, 221] for recent numerical methods for a relativistic case.

Before we address these points in the respective section, there is a place for a mathematical insertion about the nature of finite- and infinite-dimensional Hilbert spaces in relation to numerical modelling because the dimensionality may significantly change the mathematical nature of a space.

Finite- vs. infinite-dimensional Hilbert spaces

The goal is to approximate functions and other mathematical structures of the infinite-dimensional spaces using only finite representations. This problem is shared in all numerical treatments in last decades, it is thus well-grounded today. However, one should be aware about some of these details as it may lead to non-trivial consequences. We thus only recapitulate some of the main points.

The functions may be approximated with arbitrary precision as shown by the *Stone-Weierstrass theorem* [222]. It is not very restrictive to physical problems as it holds for a large set of functions. Difficulties occur once we arrive to differential equations. The requirements are stronger in this case. According to a given problem, only some numerical schemes converge to the desired solution. An important result in this area is the *Lax–Richtmyer theorem*, see Theorem 10.5.1 of [223] or Chapter 10.5 of [224].

To conclude this remark, we recall two examples from quantum mechanics. First, we recall the Heisenberg commutation relations $[x_i, p_j] = \mathbf{i}\delta_{ij}$, which are obeyed by the position $\boldsymbol{x}$ and momentum $\boldsymbol{p}$ operator. This relation can never be represented exactly in a finite-dimensional space, see Chapter 8, Problem 10 of [225]. The second example is the spectral property of the Hamiltonian under the complex rotation [151]. We have already discussed this property in the relation to (3.5) recalling the existence of an infinite dimensional linear operator with an empty spectrum. This case is more dramatic, as an n-dimensional linear operator can never have the empty spectrum.

7.1 Numerical methods for TDSE: representation of $|\psi\rangle$

A way to represent $|\psi\rangle$ is usually to choose an orthonormal basis of $\mathscr{H}$. Let us denote the basis $A = \{|\alpha\rangle\}_{\alpha\in\mathcal{I}}$. The state is thus written

$$|\psi\rangle = \sum_{\alpha} \langle\alpha|\psi\rangle\,|\alpha\rangle + \int \langle\alpha|\psi\rangle\,|\alpha\rangle\;\mathrm{d}\alpha\,, \tag{7.2}$$

where the summation and integration run through the discrete and continuous part, respectively, of the index set $\mathcal{I}$. It is a complete description of the state. Roughly said, a numerical treatment of a problem having an infinite number of variables (either discrete or continuous) approximates the problem with a finite number of variables. A way to obtain these variables is to truncate A and use the coefficients of the truncated basis.

There are two families of methods – Spectral methods (SM) and Grid methods (GM)[2] – based on the choice of A. For the SM, we take a finite truncation of any basis of functions as A (for example Gaussian functions); for the GM, we take finite number of points $\boldsymbol{x}$ from the position representation of the wave function.[3] We now list some of the properties of the methods:

(SM): We choose a basis $\{|\varphi_i\rangle\}_{i=1}^{+\infty}$ of $\mathscr{H}$. The state is then given by the finite truncation $|\psi\rangle = \sum_i^N \alpha_i |\varphi_i\rangle$. The unknowns characterising the state are now α_i.

- \+ The number of unknowns may be reduced by the choice of basis suitable for the problem.
- – Its accuracy and performance strongly depend on the choice of the basis thus the method may be limited only to a particular task.
- – It may be difficult to express the matrix elements of the Hamiltonian $\langle\varphi_i|H|\varphi_j\rangle$.[4]

(GM): The wave function is evaluated at the given points in the position space: $\psi_i = \psi(\boldsymbol{x}_i) = \langle\boldsymbol{x}_i|\psi\rangle$. The unknowns are then directly ψ_i.

- \+ The method is very versatile; it provides a direct physical insight since problems are usually formulated in the x-space.
- – Increasing accuracy usually demands very fine grids, which leads to a high computational cost.[5]

Before we proceed to practical examples relevant for our work, we recall the decomposition for Hilbert spaces that may be written as a tensor product of ”smaller” spaces. Let us take $\mathscr{H} = \mathscr{H}_1 \otimes \mathscr{H}_2$. A possible basis is the tensor product of their respective bases, $A = \{|\alpha_1\rangle \otimes |\alpha_2\rangle\}_{\alpha_1\in\mathcal{I}_1,\alpha_2\in\mathcal{I}_2}$. It means that the aforementioned approaches may be applied independently in both $\mathscr{H}_1$ and $\mathscr{H}_2$. An important example are the square-integrable functions in the 3-dimensional space described in spherical coordinates:

$$L^2(\mathbb{R}^3, \mathrm{d}^3x) = L^2(\mathbb{R}^+, r^2\mathrm{d}r) \otimes L^2(S^2, \mathrm{d}\Omega)\,, \tag{7.3}$$

where S^2 denotes the 2-dimensional sphere. A convenient basis for $L^2(S^2, \mathrm{d}\Omega)$ are the spherical harmonics Y_l^m, which can be mixed with an arbitrary method for the radial part $L^2(\mathbb{R}^+, r^2\mathrm{d}r)$.

---

[2] We adopt the classic definition of the spectral methods [226, 227]. These methods are defined in Preface of [226] as: *”Spectral methods involve seeking the solution to a differential equation in terms of a series of known, smooth functions.”* In atomic physic, a spectral method may be narrowed to use, for example, the basis of the corresponding field-free Hamiltonian. We do not restrict the definition in this sense here.

[3] In both cases, the computation is then a restriction to a finite-dimensional subspace $\mathscr{G} \subset\subset \mathscr{H}$. The representation of operators $\tilde{O}$ is then given by the projection $\tilde{O} = P_{\mathscr{G}} O P_{\mathscr{G}}$, where $P_{\mathscr{G}}$ is the projector on $\mathscr{G}$. It means that $\mathscr{G} = P_{\mathscr{G}}\mathscr{H}$.

[4] For example, if $|\varphi_i\rangle$ is an orthogonal polynomial, the integration of the scalar products for large values of i contains fast oscillations.

[5] This is meant by comparing to the SM, where – with a suitable basis – the accuracy grows faster with the number of additional basis functions compared to the number of additional points in GM.

7.1.1 Grid methods

We present how to represent the wave function and differential operators in this section. If we adjust the above scheme to an N-dimensional space, the wave function is represented by a finite number of points in the chosen representation,

$$\psi_J(t) = \psi(\boldsymbol{x}_J, t) = \langle \boldsymbol{x}_J | \psi(t) \rangle = \langle x_1^{(J_1)}, \dots, x_N^{(J_N)} | \psi(t) \rangle \ , \tag{7.4}$$

we adopted the multi-index notation $J = (J_1, \dots, J_N)$, where any of J_i runs in a given finite range.

All the differential operators are thus represented by finite differences on the grid. For example

$$\partial_{x_2} \psi(\boldsymbol{x}_J, t) \approx \frac{\psi_{(J_1, J_2+1, J_3, \dots)}(t) - \psi_{(J_1, J_2, J_3, \dots)}(t)}{x_2^{(J_2+1)} - x_2^{(J_2)}} \ , \tag{7.5}$$

using the forward-difference approximation of the first order. The important property is that all the derivatives are still represented by linear operations and may be thus described by matrices.

Numerov's approximation of derivatives

The idea leading to the finite differences approximation used in (7.5) comes from the Taylor's expansion of $f(x + kh) = f(x) + (kh) f'(x) + \cdots$, subtractions of these series would give the required order of precision [228]. There is another way to increase the accuracy. Let us consider an equation $y'' = f$ for a single-variable function y. The Numerov's method (see [229] and [230], chapter III.10, Implicit Störmer Methods) increases the accuracy of the derivatives by using more grid points on both sides of the approximation, the discretised version of $y'' = f$ is:

$$\frac{y_{i-1} - 2y_{i-1} + y_{i+1}}{(\Delta x)^2} \approx \frac{f_{i-1} + 10 f_{i-1} + f_{i+1}}{12} \qquad \Leftrightarrow \qquad \Delta_2 \boldsymbol{y} \approx M_2 \boldsymbol{f} \ . \tag{7.6}$$

Δ_2 and M_2 represent the linear operations and are defined by the first equation, we may then modify the approximation of the second derivative as $\tilde{\Delta}_2 \boldsymbol{y} = \boldsymbol{f}$, $\tilde{\Delta}_2 = M_2^{-1} \Delta_2$. The newly defined operator $\tilde{\Delta}_2$ gives a new approximation of the second derivative with the accuracy $\mathcal{O}(\Delta x^5)$ compared to $\mathcal{O}(\Delta x^2)$ included in Δ_2. Further details including non-uniform grids or the approximation of the first-order derivative necessary for the interaction term in the velocity gauge can be found in, e.g., [231, 232, 233].

A disadvantage of this approach is the inversion in $\tilde{\Delta}_2$ that generally mixes all the grid points, but it could be avoided in some cases as we will see later.

7.1.2 Spectral representation

This paradigm focuses on the discrete-type decompositions in (7.2). We use an example of a 3D-Hamiltonian including a Coulomb-tail in the effective potential, which we will use later for the diagonalisation with the complex rotation. We use a basis defined by the solution of the following equation:

$$\left(-\frac{1}{2}\frac{\mathrm{d}^2}{\mathrm{d}r^2}+\frac{l(l+1)}{2r^2}-\frac{\lambda n}{r}+\frac{\lambda^2}{2}\right)S^{\lambda}_{nl}(r)=0\,, \tag{7.7}$$

these functions are called *Sturmians* [234].[6] If we fix n, the Sturmians solve a Coulomb problem with a charge $Z=\lambda n$. However, the enumeration of the Sturmians is not linked with the scaling in the energy as the Coulomb-problem eigenfunctions are. The Sturmians are scaled in the *charge* λn (n is a varying parameter of the Sturmian). The Sturmians then seems to be a suitable basis for Coulomb-tailed problems analytically introduced by (2.1) since the short-range potential W may be attributed to the local change of the charge seen by the electron as it will be seen in (7.26b).

The Sturmians resolve only the radial part, the full description includes also angular part. The full basis is then $\langle \boldsymbol{r}|ilm\rangle = S^{\lambda}_{l+i,l}(r)Y^{m}_{l}(\Omega_{\boldsymbol{r}})$, where i and l enumerate the Sturmians and m is the usual magnetic quantum number. Although we used the Sturmians as an example of spectral methods, they do not obey (7.2) because this basis is not orthonormal. Its overlap matrix, also called Gramian, is written

$$\mathbb{G}=\begin{pmatrix}\mathbb{S}_1 & & \\ & \ddots & \\ & & \mathbb{S}_{l_{\max}}\end{pmatrix}\,, \tag{7.8a}$$

$$(\mathbb{G}_l)_{jk}=\left\langle S^{\lambda}_{l+j,l}\,\middle|\,S^{\lambda}_{l+k,l}\right\rangle\,, \tag{7.8b}$$

and is a tridiagonal matrix. The decomposition in (7.2) is then still possible, it is replaced by

$$|\psi\rangle=\sum_{\alpha}\xi_\alpha\,|\alpha\rangle+\int\xi(\alpha)\,|\alpha\rangle\,\mathrm{d}\alpha\,. \tag{7.9}$$

The coefficients ξ_α and $\xi(\alpha)$ are still uniquely defined, but they cannot be obtained by the scalar

---

[6] In broader sense, the Sturmians are the eigenfunctions of a general *Sturm-Liouville operator*

$$\mathcal{L}=-\frac{1}{w(x)}\left(\frac{\mathrm{d}}{\mathrm{d}x}\left(p(x)\frac{\mathrm{d}}{\mathrm{d}x}\right)+q(x)\right)\,.$$

However, we restrict the term only for solutions of the Sturm-Liouville equation corresponding to the Coulomb problem in this work.

products $\langle \alpha | \psi \rangle$ any more.

7.1.3 Discrete variable representation (DVR)

We introduce a methodology benefiting from the advantages of GM and SM in this section. The idea is to bind a basis with a grid, in other words to construct the basis on the grid. The underlying structure is similar to B-splines [235, 236, 237, 238], but its technical realisation is different. We use the so-called Discrete variable representation (DVR), see, e.g., [239, 240] and references therein for the overview of the method.

Our starting point is the Gaussian quadrature rules for the integration using orthogonal polynomials p_i with respect to a weight function w. The orthogonality and the integration rule are, respectively,

$$\int_\Omega w(x) p_i(x) p_j(x)\,\mathrm{d}x = \delta_{ij}\,, \qquad \int_\Omega w(x) f(x)\,\mathrm{d}x \approx \sum_{i=1}^{N} w_i f(x_i)\,, \tag{7.10}$$

w_i are called *weights* and x_i *abscissae*. The role of the polynomials is that weights are related to them and abscissae are zeros of the $(N-1)$st polynomial.

Based on the abscissae x_i, we define *the cardinal functions* and *DVR-basis functions*

$$\mathcal{C}_i(x) = \sqrt{\frac{w(x)}{w(x_i)}} \prod_{\substack{j=1\\ j\neq i}}^{N} \left(\frac{x - x_j}{x_i - x_j} \right) = \frac{1}{\mathcal{P}_N'(x_i)} \frac{\mathcal{P}_N(x)}{x - x_i}\,, \qquad f_i(x) = \sqrt{\frac{w(x_i)}{w_i}} \mathcal{C}_i(x)\,, \tag{7.11}$$

respectively, $\mathcal{P}_i(x) = \sqrt{w(x)} p_i(x)$ and $\{x_i\}_{i=1}^N$ are the zeros of p_N.[7] By construction, the DVR-basis functions satisfy $f_i(x_j) = \sqrt{\frac{w(x_i)}{w_i}} \delta_{ij}$.

Next, the matrix elements in the DVR-basis are calculated from the quadrature rule[8]

$$\langle f_i | f_j \rangle = \int_\Omega f_i^*(x) f_j(x)\,\mathrm{d}x = \sum_{k=1}^{N} w_k f_i^*(x_k) f_j(x_k) = \sum_{k=1}^{N} w_k \frac{\delta_{ik}}{\sqrt{w_i}} \frac{\delta_{jk}}{\sqrt{w_j}} = \delta_{ij} \tag{7.12a}$$

$$\langle f_i | V | f_j \rangle = \int_\Omega f_i^*(x) V(x) f_j(x)\,\mathrm{d}x \approx V(x_i) \delta_{ij}\,. \tag{7.12b}$$

The important consequences are that the basis is orthonormal (compared to the aforementioned

---

[7] In the vicinity of x_j, the Cardinal function may be found by Taylor expansion

$$\mathcal{C}_i(x) = \delta_{ij} + \frac{1}{\mathcal{P}_N'(x_i)} \sum_{k=2}^{+\infty} \frac{\mathcal{P}_N^{(k)}(x_j)}{k!} (x - x_j)^{k-1}\,,$$

note, that the expansion is generally infinite since $\mathcal{P}_N$ includes $\sqrt{w(x)}$.

[8] The calculation of $\langle f_i | f_j \rangle$ is exact because of Theorem 2.4.1 [241].

B-splines), and the expression of local operators V is diagonal in the DVR basis. Furthermore, only the evaluation of the potential in abscissae is required to construct the matrix. Conversely, the expression of the kinetic term is usually a full matrix.

The above derivation uses the machinery of spectral methods and the solution is thus given by the expansion $|\psi\rangle = \sum_{i=1}^{N} \alpha_i |f_i\rangle$. On the other hand, the basis is entangled with the choice of the grid. It leads to

$$\psi(x_i) = \sum_{j=1}^{N} \alpha_j f_j(x_i) = \frac{\alpha_i}{\sqrt{w_i}} \,. \tag{7.13}$$

If we define $\psi_i = \frac{\alpha_i}{\sqrt{w_i}}$, we have a straightforward resemblance with GM.

DVR as spectral method

DVR is closely related to spectral methods. A simple analysis of the dimensionality shows that using $\mathcal{P}_N$ leads to an N-dimensional subspace of $\mathscr{H}$, which is of the same dimensionality as for a truncated expansion

$$\psi(x) = \sum_{i=0}^{N-1} \beta_{i+1} \mathcal{P}_i(x) \,. \tag{7.14}$$

We included the weight in the basis and thus the wave function is expanded in $\mathcal{P}_i$. This makes sense since the orthonormality corresponds to the standard scalar product, $\langle \mathcal{P}_i | \mathcal{P}_j \rangle = \delta_{ij}$. Furthermore, the factor $\sqrt{w(x)}$ suppresses the function for large values of x. This suppression can be exactly seen as a closure of the wave function in a *finite soft-box*, which we will describe further in Section 7.1.5. A natural question is to find a relation between $\mathscr{G}_1 = \operatorname{span}\{|\mathcal{P}_i\rangle\}_{i=0}^{N-1}$ and $\mathscr{G}_2 = \operatorname{span}\{|f_i\rangle\}_{i=1}^{N}$. We will prove that $\mathscr{G}_1 = \mathscr{G}_2$:

First, we compute $\langle f_i | \mathcal{P}_j \rangle$ for an arbitrary i and j:

$$\langle f_i | \mathcal{P}_j \rangle = \frac{1}{\sqrt{w_i} \mathcal{P}'_N(x_i)} \int_\Omega w(x) \frac{p_N(x)}{x - x_i} p_j(x) \, \mathrm{d}x = \frac{1}{\sqrt{w_i} \mathcal{P}'_N(x_i)} \int_\Omega w(x) g_i(x) p_j(x) \, \mathrm{d}x \,,$$

$g_i(x) = \frac{p_N(x)}{x - x_i}$. The calculation can be now performed first for $j < N$, since the order of the polynomial $g_i p_j$ is $(N - 1 + j) \leq (2N - 1)$, the quadrature rule gives the exact result,

$$\begin{aligned}\langle f_i | \mathcal{P}_j \rangle &= \frac{1}{\sqrt{w_i} \mathcal{P}'_N(x_i)} \sum_k w_k \frac{p_N(x_k)}{x_k - x_i} p_j(x_k) = \frac{1}{\sqrt{w_i}} \sum_k \frac{w_k}{\sqrt{w(x_k)}} \left(\frac{\sqrt{w(x_k)} p_N(x_k)}{\mathcal{P}'_N(x_i)(x_k - x_i)} \right) p_j(x_k) = \\ &= \frac{1}{\sqrt{w_i}} \sum_k \frac{w_k}{\sqrt{w(x_k)}} \delta_{ik} p_j(x_k) = \sqrt{\frac{w_i}{w(x_i)}} p_j(x_i) = \frac{\sqrt{w_i}}{w(x_i)} \mathcal{P}_j(x_i) \,, \qquad \forall j \leq N - 1 \,.\end{aligned} \tag{7.15a}$$

For higher values of j, we have g_i being $(N-1)$st order polynomial, and such a polynomial is orthogonal by construction to all p_j, $j \geq N$. We conclude

$$\langle f_i | \mathcal{P}_j \rangle = 0\,, \qquad \forall j \geq N\,. \tag{7.15b}$$

Since $\mathscr{G}_1 \perp \mathscr{G}_2^{\perp}$ and from the fact, that any vector from $\mathscr{G}_1$ is contained in $\mathscr{G}_2$, we have proven $\mathscr{G}_1 = \mathscr{G}_2$.

It is a particularly important result. From a mathematical point of view, working in any of these two subspaces is fully equivalent. It means that there no further information is obtained by DVR with respect to the spectral methods. Vice-versa, it provides a grid representation to the corresponding spectral methods and links them to the representation on the grid. The difference may be in the numerical implementation, mainly that $\langle f_i | V | f_j \rangle$ forms a diagonal matrix, if we impose the quadrature rule for evaluating the integral.[9]

Furthermore, we have an explicit unitary transform between our two orthonormal bases,

$$\boldsymbol{\beta} = \mathbb{U}\boldsymbol{\alpha}\,, \qquad\qquad \mathbb{U}_{ij} = \sqrt{\frac{w_i}{w(x_i)}}\mathcal{P}_j(x_i) = \sqrt{w_i}p_j(x_i)\,. \tag{7.16}$$

Finally, there may be seen a difference between the two bases. For the spectral method, we just extend the space by adding next $|\mathcal{P}_i\rangle$ in the sequence and others remain the same. In DVR, all the basis vectors are shuffled by adding a new vector.

7.1.4 DVR from different truncating function, multidimensional DVR

The choice of an orthogonal polynomial, $\mathcal{P}_N$, as a reference function to construct the DVR basis has been motivated by the quadrature rules for integration. It was useful for explaining the idea of the method, but the machinery may be repeated also using various reference functions; i.e. the replacemet $\mathcal{P}_N \mapsto v$, v being the new *truncating* function; e.g. a Coulomb wave function [242]. The requirement on these functions is that they should be somehow properly adjusted to the task (proper tails for $x \to \pm\infty$, generally boundary conditions, adapted to the singularities in the problem, etc.), their zeros should construct a good grid, and a quadrature rule derived from v should be possible to construct on this grid. We should note that the procedure is not completely universal [240].

Another generalisation comes in the direction of multidimensional domains [243]. This generalisation is straightforward if we write the domain as a tensor product of one-dimensional domains. However, a direct method using a multivariate basis that is not a tensor product is non-trivial [244, 245]. See e.g. [246] for a recent computational method to cover the multidimensional

---

[9] For example, if V changes in time, we need only $\mathcal{O}(n)$ matrix operations per one time step compared to $\mathcal{O}(n^2)$ with a full matrix.

domains.

7.1.5 *Boundaries and* finite soft-box

Here, we make a remark about the boundaries in GM and SM. The DVR is used to enlighten the SM, because it provides the insight from GM. A usual procedure to construct a GM is to close the system in a box defined by the first and last point of the grid. This is then complemented by boundary conditions. However, it is more subtle. Let us consider the 1D case. A particle in a unit box can be described by

$$H = \frac{p^2}{2m} + V(x)\,, \qquad V(x) = \begin{cases} V_0, & x \in [-1,1]\,, \\ +\infty, & \text{otherwise.} \end{cases} \tag{7.17}$$

A correct mathematical definition is to restrict the Hilbert space and use $\mathscr{H} = L^2(]-1,1[\,,\mathrm{d}x)$, the particle is then effectively closed in the box $[-1,1]$. This creates a clear well-defined boundary.

The situation is a bit different for spectral methods, the basis functions usually contain tails spanning the expansion into infinity. However, there are two properties to consider: 1) The last point containing some information is the last zero of $\mathcal{P}_N$.[10] There is thus much limited space to include any information about the system beyond this point. 2) Finite systems without external effects (i.e. no time-dependent Hamiltonians or absorbers) always evolve in time periodically, this inevitably leads to a reflection at some point. In conclusion, the effect of the boundary in this case may be called as a *finite soft-box* [247].

Let us focus more on the reflections. If there is no real physical boundary within the system, the reflections are numerical artefacts, which we want to remove. One possibility is to choose the box large enough to contain the propagated wavepacket within the time T of interest. The size can be simply estimated as $s = vT$, where v is the maximal estimated within the process. However, this can potentially lead to very large ”boxes”, while the part of the wavefunction describing the processes of interest remains close to the center, but the reflections lead to artificial interferences even at this point. A resolution is to employ an absorber on the boundary. One option is, for example, to clamp the function on the boundary by using a continuous transition; which can be done by the cosine attenuation scaled from $[0,\pi/2]$ to an interval near the edge of the box. Another option is to include an absorber in the potential, or to use the exterior complex scaling, see [248, 249, 250, 251] and references therein for details.

---

[10] For example, the farthest zero of the nth Sturmian (7.7) is approximately $2n/\lambda$ [247].

7.1.6 Piecewise DVR

Up to this point, we have been staying with a general basis for DVR. Concerning practical numerical applications, the choice of a suitable basis is important. It may be useful to think about the domain of the problem in a piecewise manner. For example, atomic potential and respective wavefunctions are characterised by different regions: First, there is the region near the nuclei placed in the origin of the coordinate system, which is linked to a cusp condition on the wavefunction [252, 253, 254]. Moving away from the nucleus, there is the principal region where bound states reside. The last region, far from the nucleus, contains continuum states. This region is also characterised by the asymptotic of the potential at infinity. In our problems, the asymptotic behaviour is governed by the Coulomb tail.

It may be then natural to use different numerical descriptions in these regions. An advantage of DVR is that it can be easily constructed from a piecewise basis. The DVR-method is then suitable even for potential containing discontinuities [255]. The boundary intervals may include the required conditions: 1) The cusp condition may be included near the origin. 2) The last interval may include an infinitely spanned basis discussed in the previous section. Another suitable approach is to use the aforementioned ideal absorber given by the complex scaling to eliminate possible artificial reflections at the boundaries [249].

The last question to resolve is then the connection of neighbouring segments. To describe flows between the elements, the basis must contain overlapping functions. These links are called the *bridge functions* [256, 257]. A direct way to link two functions is to include the limits point of the interval as done in, e.g., the Gauss-Lobatto quadrature. We denote the grid points $\{x_i^{(j)}\}_{i=0,j=1}^{N_j+1,N_s}$, where i enumerates the points of the jth segment including the limit points $x_0^{(j)}$ and $x_{N_j+1}^{(j)}$. N_j is the number of points in the jth segment and N_s is the number of segments. Because two consecutive segments share the limit points, we have $x_{N_j+1}^{(j)} = x_0^{(j+1)}$. Using the same indexing in the definition of the DVR-basis (7.11), we have two functions being unity at this point: $f_{N_j+1}^{(j)}$ and $f_0^{(j+1)}$. The bridge function is then given by

$$f_b^{(j)} = \frac{f_{N_j+1}^{(j)} + f_0^{(j+1)}}{\sqrt{2}}\,, \qquad j = 1, \dots, N_s - 1\,. \tag{7.18}$$

The final DVR-basis is then $\{f_i^{(j)}\}_{i=1,j=1}^{N_j,N_s} \cup \{f_b^{(j)}\}_{j=1}^{N_s-1}$. We note that the matrix representing local operators V stays diagonal, and the representation of the kinetic terms forms a band-matrix for the Gauss-Lobatto quadrature [256].

In conclusion, the piece-wise DVR provides a way to use different bases for different regions, this allows to fit the asymptoticity of the problem or to use different discretisations. Next, it also allows to use many segments reducing the degree of the polynomials within one piece, which may be seen as an analogy to B-splines [236].

7.2 Discretised continuum states

One important aspect to clarify regarding all the numerical methods is the approximation of the continuous part of spectra. Let us take, for the sake of simplicity a Hamiltonian H with purely continuous spectrum, $\sigma(H) = \sigma_{\mathrm{c}}(H) = [0, +\infty[$. Choosing a finite-dimensional subspace $\mathscr{G}$ of $\mathscr{H}$ always leads to a finite set of eigenvalues of the restriction of H to $\mathscr{G}$. Let us call this restriction $\tilde{H}$. The eigenvectors of $\tilde{H}$ approximate the formerly continuous basis of $\mathscr{H}$. Let us take a normalised state $|\psi\rangle \in \mathscr{H}$,

$$|\psi\rangle = \int \mathrm{d}E \; c(E) \, |\psi_E\rangle \;, \tag{7.19}$$

where $|\psi_E\rangle \in \mathscr{H}$ is the generalised eigenvector corresponding to $E \in \sigma_{\mathrm{c}}(H)$. The normalisation of the eigenvectors is $\langle \psi_{E'} | \psi_E \rangle = \delta(E - E')$. The normalisation condition is[11,12]

$$\begin{aligned}\langle \psi | \psi \rangle = \int \mathrm{d}E \int \mathrm{d}E' \; c^*(E') c(E) \, \langle \psi_{E'} | \psi_E \rangle = \int \mathrm{d}E \int \mathrm{d}E' \; c^*(E') c(E) \delta(E - E') \approx \\ \approx \int_0^{E_{\max}} |c(E)|^2 \, \mathrm{d}E \approx \sum_n |c(E_n)|^2 \frac{E_{n+1} - E_{n-1}}{2} \;,\end{aligned} \tag{7.20}$$

the discretisation corresponds to the finite restriction of the Hamiltonian, $\tilde{H} \, |\tilde{\psi}_{E_n}\rangle = E_n \, |\tilde{\psi}_{E_n}\rangle$. The normalisation of these states is $\langle \tilde{\psi}_{E_n} | \tilde{\psi}_{E'_n} \rangle = \delta_{nn'}$ in the finite dimension. The approximation of the original state given by

$$|\tilde{\psi}\rangle = \sum_n c(E_n) \, |\tilde{\psi}_{E_n}\rangle \;, \tag{7.21}$$

which is not normalised because $\langle \tilde{\psi} | \tilde{\psi} \rangle = \sum_n |c(E_n)|^2$. The way to establish the correspondence with the original normalisation is to define a new state

$$|\varphi_{E_n}\rangle = \rho(E_n) \, |\tilde{\psi}_{E_n}\rangle \;, \qquad \rho(E_n) = \sqrt{\frac{2}{E_{n+1} - E_{n-1}}} \,. \tag{7.22}$$

If we use this new basis $|\tilde{\psi}\rangle = \sum_n c(E_n) \, |\varphi_{E_n}\rangle$ instead of (7.21), the normalisation is correct correspondingly to $|\psi\rangle$. A further analysis may be found, e.g., in [258].

---

[11] We may restrict the integration because the finiteness of the integral ensures that for all $\varepsilon > 0$, there exists $E_{\max} > 0$ satisfying $\int_{E_{\max}}^{+\infty} |c(E)|^2 \, \mathrm{d}E < \varepsilon$.

[12] The approximation of the integral is given as the average of the left and right Riemann sum (omitting the outermost intervals).

7.3 Finite approximations of Hamiltonians

We presented various methods to represent states, but they are still quite general and allows to accommodate various physical descriptions. Now, we describe the two models used in this work.

7.3.1 1D-Hamiltonians

The multi-scale model uses "1D-atoms" for which the field-free-Hamiltonian is

$$H_0^{(1\mathrm{D})} = -\frac{1}{2}\frac{\mathrm{d}^2}{\mathrm{d}x^2} - \frac{1}{\sqrt{a^2+x^2}}\,. \tag{7.23}$$

The atom is modelled by the soft-Coulomb potential $-1/\sqrt{a^2+x^2}$.[13,14] The only free parameter of the description is a, which allows to set the ionisation energy of the atom. Table 7.1 summarises its values for the rare gases of our interest. Our implementation allows to switch between length and velocity gauges

$$H_L^{(1\mathrm{D})} = -\frac{1}{2}\frac{\mathrm{d}^2}{\mathrm{d}x^2} - \frac{1}{\sqrt{a^2+x^2}} + \mathcal{E}(t)x\,, \qquad H_V^{(1\mathrm{D})} = -\frac{1}{2}\left(\frac{\mathrm{d}}{\mathrm{d}x} - \mathbf{i}A(t)\right)^2 - \frac{1}{\sqrt{a^2+x^2}}\,, \tag{7.24}$$

in the dipole approximation, see (2.8). Both of them may be chosen for an analytic field. However, the multi-scale model limits to the length gauge as its input is a numerical solution of $\mathcal{E}$.

The Hamiltonians (7.24) are directly represented by standard techniques of either finite differences replacing derivatives, in the case of GM; or by evaluating the matrix elements $\langle\varphi_i|H_G^{(1\mathrm{D})}|\varphi_j\rangle$ with a suitable numerical approach while using SM or DVR.

7.3.2 3D-Hamiltonians

Now, we present the 3D-Hamiltonian. First, we fix the gauge, which turns out to be an important question in the 3D-geometry. A computationally convenient choice is the velocity gauge, mainly due to its fast convergence in the angular subspace $L^2(S^2, \mathrm{d}\Omega)$. Therefore, we use it in our treatment. Although we simply stated our choice, the reasoning behind is non-trivial and we provide a brief overview of related references. A detailed discussion is in Section 2.3 of [231] and in [260]. Further details and the transformations between different gauges are in [261]. Find also a direct comparison of the length and velocity gauges in [262], where is also discussed the retrieval of the source term

---

[13] The term *soft-Coulomb* is chosen because there is no singularity in the potential. Let us denote that there is a difference in the singularities in the classic ("hard") Coulomb potential depending on the dimension because a singularity $\sim 1/r$ is integrable in all dimensions higher than 1.

[14] This potential gives also the correct asymptotic behaviour $1/x$ for $x \to +\infty$, see also [259] for further details and generalisations.

	I_P[eV]	I_P[a.u.]	a[a.u.]
He	24.59	0.9036	0.6950
Ne	21.56	0.7924	0.8161
Ar	15.76	0.5792	1.1893
Kr	14.00	0.5145	1.3676
Xe	12.13	0.4458	1.6171

Tab. 7.1: The ionisation potentials of rare gases of our interest taken from [214] and the corresponding a-parameters of the soft-Coulomb potential used in (7.23). The ground state energy is verified by diagonalising the Hamiltonian using various bases. We have implemented grid methods (with and without Numerov approach), Hermite-spectral basis, Hermite-DVR basis, sinus-cardinal-DVR basis and B-splines for testing 1D-diagonalisations.

complementary to the the approach presented in Section 2.3. A mix of the length and velocity gauge for different interaction regions is discussed in [263].

The next step is to represent a state $|\psi\rangle$ in the spherical coordinates

$$\langle r, \Omega_{\boldsymbol{r}} | \psi \rangle = \sum_{l,m} R_{lm}(r) Y_l^m(\Omega_{\boldsymbol{r}}) \,, \qquad \Omega_{\boldsymbol{r}} = (\vartheta, \varphi) \text{ stands for the spherical angles.} \tag{7.25}$$

The full-form of the 3D-Hamiltonian derived from (2.1) reads under these assumptions

$$H = -\frac{1}{2}\left(\frac{\partial^2}{\partial r^2} + \frac{2}{r}\frac{\partial}{\partial r} - \frac{\boldsymbol{L}^2}{r^2}\right) + V_C(r) + V_I(t, \boldsymbol{r}, \boldsymbol{p}) \,, \tag{7.26a}$$

where $\boldsymbol{L}$ is the angular momentum operator.

The Coulomb potential, V_C, includes the screening short-range potential W, introduced by (2.2). A common approach is to obtain the form of W from the Hartree-Fock screening,

$$V_C(r) = -\frac{Z_{+\infty}}{r} - \frac{1}{r}\left(\sum_{i=1}^{N} \alpha_i \mathrm{e}^{-\beta_i r}\right) \,, \tag{7.26b}$$

where $Z_{+\infty}$ is the asymptotic ionic charge and α_i and β_i the coefficient from the Hartree-Fock procedure, which are tabulated for several atoms [264]. The second asymptotic condition is $V_C(r) \sim Z_{\text{nucl}}$, as $r \to 0$, where Z_{nucl} is the nuclear charge number.

The interaction term reads

$$V_I(t, \boldsymbol{r}, \boldsymbol{p}) = -\mathbf{i}\boldsymbol{A}(t) \cdot \boldsymbol{p} + \mathbf{i}\frac{[\boldsymbol{A}(t), \boldsymbol{p}]}{2} + \frac{\boldsymbol{A}^2(t)}{2} \approx -\mathbf{i}\boldsymbol{A}(t) \cdot \boldsymbol{p} \,. \tag{7.26c}$$

The last two term are disregarded in the dipole approximation. The commutator $[\boldsymbol{A}, \boldsymbol{p}]$ vanishes directly, while $\boldsymbol{A}^2/2$ changes only the global phase (see Eq. (2.25) of [265]).

In the case of a linearly polarised field, it is convenient to choose the z-axis in the direction of the field. The interaction term is then simply

$$V_I(t,\boldsymbol{r},\boldsymbol{p}) = -\mathbf{i}A(t)p_z = -\mathbf{i}A(t)\left(\cos\vartheta\partial_r + \frac{\sin\vartheta}{r}\partial_\vartheta\right). \tag{7.27}$$

Furthermore, the linear field does not include any coupling of different quantum numbers m. The dimensionality of the problem is then further reduced because we can fix $m = m_0$ in (7.25).

Now, we find a more suitable form of the Hamiltonian. The standard substitution $R_{lm}(r) = \chi_{lm}(r)/r$ transforms (7.26a) into

$$H = \left(-\frac{1}{2}\frac{\mathrm{d}^2}{\mathrm{d}r^2} + V_C(r)\right)\otimes\left(\sum_l \mathbb{I}_l\right) + \sum_l\left(\frac{l(l+1)}{2r^2}\otimes\mathbb{I}_l\right) + \tilde{V}_I(t,\boldsymbol{r},\boldsymbol{p}), \tag{7.28}$$

where the radial part is now given by χ_{lm}. The respective Hilbert space with the fixed m_0 is decomposed into a tensor product: $\mathscr{H}_{m_0} = L^2(]0,+\infty], \mathrm{d}r)\otimes\operatorname{span}_{l\geq|m_0|}\{|l,m_0\rangle\}$.[15] The angular part is spanned by spherical harmonics, $\langle\Omega_{\boldsymbol{r}}|l,m_0\rangle = Y_l^{m_0}(\Omega_{\boldsymbol{r}})$. The radial part is then reduced into a 1D-problem. The boundary condition of χ_{lm} is $\chi_{lm}(0) = 0$; however, it does not impose any constraints on $R_{lm}(0)$ due to the substitution. The boundary should be treated with care; namely including cusp conditions for $r\to 0$ imposed by (7.26b), which may improve the accuracy of the approximation [231].

An important structure of (7.28) is the decomposition into the sum of tensor products in the first two terms. These terms are thus block-diagonal. The coupling of various blocks is given only due to the coupling terms in $\tilde{V}_I$, the tilde denotes there, that the representation of V_I is changed due to the substitution of R_{lm}. Due to the selection rules, there are only couplings of neighbouring values of l. This results into a block tridiagonal matrix. The final representation is obtained by truncating the expansion in l and choosing a finite representation of the radial subspace. In summary, the desired matrix representation is:

$$\mathbb{H} = \begin{pmatrix} \mathbb{H}_0(|m_0|) & \mathbb{V}_I(|m_0|) & & & \\ \mathbb{V}_I^\dagger(|m_0|) & \mathbb{H}_0(|m_0|+1) & \mathbb{V}_I(|m_0|+1) & & \\ & \mathbb{V}_I^\dagger(|m_0|+1) & \mathbb{H}_0(|m_0|+2) & \ddots & \\ & & \ddots & \ddots & \mathbb{V}_I(l_{\max}-1) \\ & & & \mathbb{V}_I^\dagger(l_{\max}-1) & \mathbb{H}_0(l_{\max}) \end{pmatrix}. \tag{7.29}$$

---

[15] The measure in the radial subspace is different that of (7.3). However, these are isometric as $\int_0^{+\infty}|R_{lm}(r)|^2 r^2\,\mathrm{d}r = \int_0^{+\infty}|\chi_{lm}(r)|^2\,\mathrm{d}r$.

The size of each elementary block is given by the finite representation in r, and $|m_0| \leq l \leq l_{\max}$. The diagonal blocks, $\mathbb{H}_0(l)$, represent the field-free interaction of (7.28). The interaction terms $\mathbb{V}_I^{\dagger}(l)$ are computed directly from $\tilde{V}_I$ with the respective spherical harmonic $Y_l^{m_0}$. It is interesting to note, that the block tridiagonal form is due to the dipole approximation. Going beyond the dipole approximation would significantly enlarge the numerical description: The couplings are not limited to $\Delta l = \pm 1$ by the selection rules. Furthermore, there occur transitions in the quantum number m (cf. the couplings discussed in Appendix C).

Finally, the formulae to find the original wavefunction in the case of GM and SM are respectively

$$\psi(r_i, \Omega_{\boldsymbol{r}}) \approx \sum_{l=|m_0|}^{l_{\max}} \frac{\chi_{ilm_0}}{r_i} Y_l^{m_0}(\Omega_{\boldsymbol{r}}) \,, \qquad \psi(r, \Omega_{\boldsymbol{r}}) \approx \sum_{l=|m_0|}^{l_{\max}} \sum_{i=1}^{N} \frac{\alpha_{ilm_0}\varphi_i(r)}{r} Y_l^{m_0}(\Omega_{\boldsymbol{r}}) \,. \tag{7.30}$$

The coefficients χ_{ilm_0} correspond to the grid, $\chi_{ilm_0} = \langle r_i | \chi_{lm_0} \rangle$. The coefficients α_{ilm_0} correspond to the finite basis spanning the radial subspace, $\mathrm{span}\{|\varphi_i\rangle\}_{i=1}^{N} \subset L^2(]0, +\infty[\,, \mathrm{d}r)$.

7.4 Evolution in time

Once we have a state $|\psi(t = t_0)\rangle = |\psi_0\rangle$ and its suitable finite representation, we need to solve the evolution in time driven by (7.1a). We first recall a mathematically exact solution and then discuss the approximations.

The evolution is unitary in quantum mechanics, $|\psi(t)\rangle = U(t, t_0)\,|\psi_0\rangle$; where U is a unitary operator called *evolution operator*. If H would be time-independent, the solution is directly:

$$U(t, t_0) = \mathrm{e}^{-\mathbf{i}(t-t_0)H} \,. \tag{7.31}$$

Otherwise, more care is needed – the solution incorporates possible non-commutativity of the Hamiltonian at different times – and the unitary evolution is given by the Magnus expansion

$$U(t, t_0) = \mathrm{e}^{-\mathbf{i}\Omega(t,t_0)} \,, \tag{7.32a}$$

$$\Omega(t, t_0) = \int_{t_0}^{t} \mathrm{d}t_1 H(t_1) + \frac{1}{2}\int_{t_0}^{t} \mathrm{d}t_1 \int_{t_0}^{t_1} \mathrm{d}t_2\, [H(t_1), H(t_2)] + \cdots \,. \tag{7.32b}$$

The exact form of the next terms in the sum is given recursively in Eq. (3.31) of [266]. Note that the higher terms in the sum (7.32b) contain recursively more commutators, they thus provides corrections due to non-commutativity and vanish for a commutative H; the solution then reduces to (7.31). Furthermore, as these terms contain multiple integrals, the nth term goes in $\mathcal{O}(\Delta t^n)$ if integrated over Δt.

Although we have a formally exact solution, we need only an approximate solution in a numerical scheme. The elementary idea is to evolve the solution by a small amount of discretised time, we thus need to solve $|\psi(t+\Delta t)\rangle = U(t+\Delta t, t)\,|\psi(t)\rangle$. A straightforward approximation is

$$U(t+\Delta t, t) \approx \mathrm{e}^{-\mathbf{i}\Delta t H(t')}\,, \tag{7.33}$$

where $t' \in [t, t+\Delta t]$. Such an approximation may be seen as $\mathcal{O}(\Delta t)$ from the viewpoint of (7.32), but we need to mention an important point related to our problem. The changes of the Hamiltonian with time are related with the evolution of the external field. This evolution is much slower than the electronic motion (cf. the adiabatic approach to the ionisation in section 3.1.1 and the dipole approximation). It suggests that neither this approximation nor including higher orders in (7.32b) are a bottleneck in the accuracy. A potential limitation is the need of the computation of the matrix exponential, which is computationally expensive. We thus discuss another candidate, *the Crank-Nicolson scheme (CN)*:

$$U(t+\Delta t, t) \approx \left(1 + \mathbf{i}H\left(t'\right)\frac{\Delta t}{2}\right)^{-1}\left(1 - \mathbf{i}H\left(t'\right)\frac{\Delta t}{2}\right)\,. \tag{7.34}$$

An advantage is that this scheme is per-construction norm-preserving. The stability of this solver for the Schrödinger equation using grid methods is proven in [267].

7.4.1 Krylov-subspace methods

Here we discuss another possible numerical scheme to reduce the dimensionality of the inverse problem solved in each time step.

Since the proposed method is implicit, there is a need for an inverse problem in a space with the dimensionality of the subspace $\mathscr{G}$ at every time step. For an efficient solver, we may seek for reducing the dimensionality. Both for the original exponential (7.33) or CN (7.34), the propagator may be expanded in a series

$$|\psi(t+\Delta t)\rangle = |\psi(t)\rangle + \sum_{n=1}^{+\infty} \beta_n (\Delta t)^n H^n(t)\,|\psi(t)\rangle \tag{7.35}$$

(we do not need to write down the coefficients β_n exactly). The main idea is to truncate the series to reduce the dimensionality as the higher terms contributes with $\mathcal{O}(\Delta t^n)$. The Krylov subspace at a given time t is defined as $\mathscr{K}(t) = \operatorname{span}\{|K_i(t)\rangle\}_{i=0}^{N}$, where $|K_i(t)\rangle = H^i(t)\,|\psi(t)\rangle$. The propagation is then computed within $\mathscr{K}(t) \subset\subset \mathscr{G}$ at every time step, this procedure is discussed in detail in Chapter 6 of [268]. A key intermediate step is to use an orthonormal basis of $\mathscr{K}(t)$ as the vectors $\{|K_i(t)\rangle\}_{i=0}^{N}$ may be close to linearly dependent and leading to a numerically stiff problem in $\mathscr{K}(t)$. A standard way that may remove the stiffness is to use an orthonormal basis, which may be always constructed by the Gram-Schmidt procedure. Due to the used algorithms [268], the orthonormalised basis is called the Lanczos basis $\{|L_i(t)\rangle\}_{i=0}^{N}$. The dimensionality of the original problem is then reduced in $\mathscr{K}(t)$.

We summarise the main idea of this approach. First, $\mathscr{K}(t)$ is constructed using the Lanczos basis together with the respective representation of the Hamiltonian, $H^{(\mathscr{K})}$. The dimensionality n of $\mathscr{K}(t)$ could be really small as it should include the propagation within the order $\mathcal{O}(\Delta t^n)$. The propagator is thus computationally cheap in $\mathscr{K}(t)$ even, for example, for full inverses.

7.4.2 Split-operator technique

To conclude this part about general methods for solving TDSE, we briefly present the so-called split-operator technique. Let us use a typical case of this technique with the Hamiltonian

$$H(t) = H_0 + V(t)\,, \tag{7.36}$$

where H_0 is a static part of the Hamiltonian and $V(t)$ is a time-dependent part. Because H_0 and $V(t)$ generally do not commute,

$$\mathrm{e}^{-\mathbf{i}\Delta t(H_0+V(t))} \neq \mathrm{e}^{-\mathbf{i}\Delta t H_0}\mathrm{e}^{-\mathbf{i}\Delta t V(t)}\,.$$

A similar problem was discussed in (7.32). The approach here is reformulated in a different way. It uses the Trotter formula, which can be found in [225], Theorem 5.9.7. Using only the approximation in the first order (consistently with the approximations in the Magnus expansion), the Trotter formula gives

$$\mathrm{e}^{-\mathbf{i}\Delta t H(t)} \approx \mathrm{e}^{-\mathbf{i}\frac{\Delta t}{2}H_0}\mathrm{e}^{-\mathbf{i}\Delta t V(t)}\mathrm{e}^{-\mathbf{i}\frac{\Delta t}{2}H_0}\,. \tag{7.37}$$

An implementation is then straightforward, the exponentials are applied in the chain given by (7.37).[16] Each exponential in the chain may be treated by a suitable technique for this particular term (e.g. by CN or direct calculation).

Now, we have a palette of possible approaches, we then proceed to the motivation of the choices applied in our work.

---

[16] The separated action of $\exp(-\mathbf{i}\Delta t H_0)$ makes this technique a cornerstone of the time evolution in the Dirac picture because this term vanishes in that case.

7.5 1D-TDSE solver

Now, we recapitulate all the ingredients used in the workhorse tool of our microscopic model: the 1D-TDSE solver. We use a uniform-grid to represent the wavefunction and evolve it with the length-gauge Hamiltonian (7.24). We use the Crank-Nicolson scheme with splitting H_0 and the interaction $V_I = \mathcal{E}(t)x$, while applying Numerov's refinement (7.6) in H_0. Summing this up, a single step is

$$\begin{aligned} \tilde{\boldsymbol{\psi}}^{n+1} &= \left(M_2 + \frac{\mathbf{i}\Delta t}{2}\Delta_2 - \mathbf{i}\Delta t M_2 V_C \right) \boldsymbol{\psi}^n \,, & \text{(7.38a)} \\ \left(M_2 - \frac{\mathbf{i}\Delta t}{2}\Delta_2 + \mathbf{i}\Delta t M_2 V_C \right) \tilde{\tilde{\boldsymbol{\psi}}}^{n+1} &= \tilde{\boldsymbol{\psi}}^{n+1} \,, & \text{(7.38b)} \\ \psi_i^{n+1} &= \mathrm{e}^{-\mathbf{i}\Delta t \mathcal{E}(t_n) x_i} \tilde{\tilde{\psi}}_i^{n+1} \,. & \text{(7.38c)} \end{aligned}$$

The notation of the discretised wavefunction is $\psi(x_i, t_n) = \psi_i^n$ and $\boldsymbol{\psi}^n = (\psi_1^n, \ldots, \psi_N^n)$.

Note, that the inversion of the Numerov's matrix, M_2, is not needed because it can be used to modify the Crank-Nicolson scheme:

$$\begin{aligned} \left(1 + \mathbf{i}H_0\frac{\Delta t}{2}\right)^{-1} \left(1 - \mathbf{i}H_0\frac{\Delta t}{2}\right) &= \left(1 + \mathbf{i}H_0\frac{\Delta t}{2}\right)^{-1} M_2^{-1} M_2 \left(1 - \mathbf{i}H_0\frac{\Delta t}{2}\right) = \\ &= \left(M_2\left(1 + \mathbf{i}H_0\frac{\Delta t}{2}\right)\right)^{-1} \left(M_2 - \mathbf{i}M_2H_0\frac{\Delta t}{2}\right) = \\ &= \left(M_2 + \mathbf{i}\frac{\Delta t}{2}\left(-\frac{\Delta_2}{2} + M_2V_C\right)\right)^{-1} \left(M_2 - \mathbf{i}\frac{\Delta t}{2}\left(-\frac{\Delta_2}{2} + M_2V_C\right)\right) \,. \qquad \text{(7.39)} \end{aligned}$$

Because V_C is diagonal, M_2V_C is still tridiagonal, and there is just some extra multiplication by a tridiagonal matrix in the propagator step. All the matrices in the expression are tridiagonal, thus the inversion can be done very efficiently.

One can note that the action of the electric external field (7.38c) is not applied using explicitly the Trotter formula (7.37). The error is negligible in this case because the evolution of the field $\mathcal{E}(t)$ is much slower than the studied dynamics as discussed directly after (7.33). The Trotter formula is then retrieved by composing two consecutive steps by considering the half of the action (7.38c) being a part of the $(n+1)$st step leading to $\boldsymbol{\psi}^{n+2}$.

The solver we presented (7.38) uses directly the electric field, which provides a straightforward link with the outputs of the macroscopic propagation, and there is no significant difference for various gauges unlike for the 3D-geometry. In the case of an analytic field, the solver implements velocity gauge as well. It then replaces only the action of $\exp\left(-\mathbf{i}\Delta t\mathcal{E}(t_n)x\right)$ by its counterpart in the velocity gauge. (Practically, it is included in the CN-steps and (7.38c) is not applied.)

7.6 3D-TDSE solver

A part of this work is dedicated to the development of an efficient 3D-TDSE solver. The starting point is a direct implementation in the velocity gauge using a grid method in the radial subspace $L^2(\mathbb{R}^+, r^2\mathrm{d}r)$ and spherical harmonics in the angular subspace $L^2(S^2, \mathrm{d}\Omega)$. Last, the main goal is to find the parameters and propagators of the solver using the Krylov subspace and focusing in the extent in the angular subspace.

The parameters of the grid in time and space are: the step in space, Δr, the size of the grid, N_r, and the step in time Δt. We used their values from a precedent solver that computed the propagation without the Lanczos basis. The parameters of interest to optimise the solver are the size of the Lanczos basis N_L, the maximal angular momentum $l_{\max}$ and the form of the propagator.

We used the Hydrogen atom for the study and a single-photon process in a linear field. The parameters of the field are chosen as: $\omega = 1$ a.u., $\mathcal{E}_0 = 0.01$ a.u., $\sin^2$-envelope spanning three cycles of the fundamental field. The aforementioned numeric parameters with verified convergence are $\Delta t = 0.005$ a.u., $\Delta r = 0.2$ a.u. and $N_r = 2000$.

We use the radial density at the end of the interaction to measure the differences. It is obtained from the wavefunction $\rho_r(r) = \int_\Omega |\psi(r, \Omega_{\boldsymbol{r}}, t = t_{\text{end}})|^2 \,\mathrm{d}\Omega$. After testing various propagators in $\mathscr{K}(t)$, we observed the best results for the Crank-Nicolson propagator (7.34).[17]

We have found that the dimensionality results converged with the rather low $N_L = 5$, which makes no problem to use arbitrary method within such a small subspace. We also confirmed that our test problem is indeed a single-photon process, the solution was stable for $l_{\max} = 2$ and few higher values. However, one of the purposes of the study was to extend the possible number of angular momenta as they become large for more complicated problems. Having a well behaved solver with a large $l_{\max}$ is a necessary condition for the solver to be successful in that extended case. We observed a poor performance in that case as shown in Fig. 7.1: The solution is not stable with increasing l. The culprit has not been easily identified, the Hamiltonian in the Krylov subspace provide a clue since its eigenvalues has grown with $l_{\max}$. Recently to our study, this issue has been recognised by [269], the high energies are introduced by the centrifugal term in the kinetic operator.[18] The kinetic operator for a given l is found from (7.29):

$$T_r(l) = -\frac{1}{2}\frac{\mathrm{d}^2}{\mathrm{d}r^2} + \frac{l(l+1)}{r^2} = T_0 + V_c(l)\,. \tag{7.40}$$

---

[17] The step without the inverse would be easy to apply directly as the action of $H(t)$ is required anyway to construct $\mathscr{K}(t)$. However, different techniques for each half-steps of CN would not assure the unitarity of the propagator.

[18] Interestingly, very analogical problem is also recognised in the Kapler problem in classical mechanics and it causes also numerical difficulties [270].

The problem can be explicitly recognised here, the centrifugal term $V_c(l) \sim 10^6$ for the discretisation $\Delta r \sim 0.1$ a.u. and maximal angular momenta $l_{\max} \sim 100$.

The solution of this problem is to apply the split-operator on the centrifugal term, which may be applied exactly because it acts diagonally. The resulting one step of the scheme is

$$|\psi(t+\Delta t)\rangle = \mathrm{e}^{-\mathbf{i}\frac{\Delta t}{2}V_c}\mathrm{e}^{-\mathbf{i}\Delta t H_1(t)}\mathrm{e}^{-\mathbf{i}\frac{\Delta t}{2}V_c}\,|\psi(t)\rangle \ , \tag{7.41}$$

where $H_1 = T_0 + \tilde{V}_I$ as described in (7.28). The part of the Hamiltonian H_1 does not contain the problematic term and does not present difficulties in the evolution operator.

Our finding are summarised in Figs. 7.1 and 7.2. We make 2 comments: the unstable solution with increasing l in Fig. 7.1; and the difference between the solver within the Krylov subspace and the direct CN applied without using the subspace. The results with the split-operator are not presented as we verified that they strictly overlap the reference solution in the Krylov subspace up to $l_{\max} = 80$.

The result we have discussed so far consider only a linear field. It reduces the dimensionality if the problem as $m = m_0$ is fixed. The dimensionality of the matrix representation (7.29) grows significantly in the case of an arbitrary polarised field because there are $(2l+1)$ possibilities for m in that case.

Unfortunately, the 3D-TDSE solver was not incorporated or further developed in the timespan of this work. Its further development and deployment in the model is one of the nearest follow-up projects. One of the important goals is a comparison with other codes as some available solver have been published recently, for example [271, 272, 248].

7.7 Eigenvalue problem of complex rotation

We return to the eigenvalue problem in the last section of the microscopic scale and provide some details about the calculation we used for the computation of the complex rotation presented in Section 3.1.

We use the Sturmian basis, (7.7), for computing the ionisation rates (3.6b) in the 3D-geometry defined by the Hamiltonian (7.26) with the following modifications: 1) The interaction term is replaced by the length gauge, $V_I = \mathcal{E}z$, as required by the machinery of the static-field methods. 2) The radial coordinate is complexly scaled by $r \mapsto \mathrm{e}^{\mathbf{i}\theta}r$. The matrix representation is similar to (7.29) but with one crucial difference: The Hamiltonian is no longer Hermitian, which affects also the Hermiticity of the matrix. Compared to the 3D-TDSE solver, the radial subspace is treated with the spectral method instead of the grid.

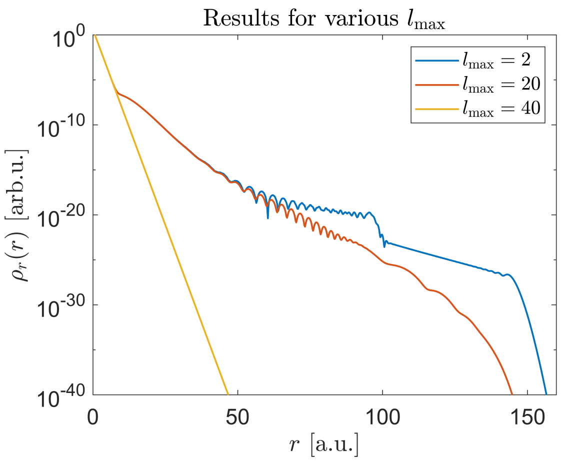

Fig. 7.1: The radial distribution of the wave function after the interaction with the single-photon-process pulse for various truncations in $l_{\max}$. The results are computed by the Crank-Nicolson propagator with Lanczos basis and without the split-operator technique.

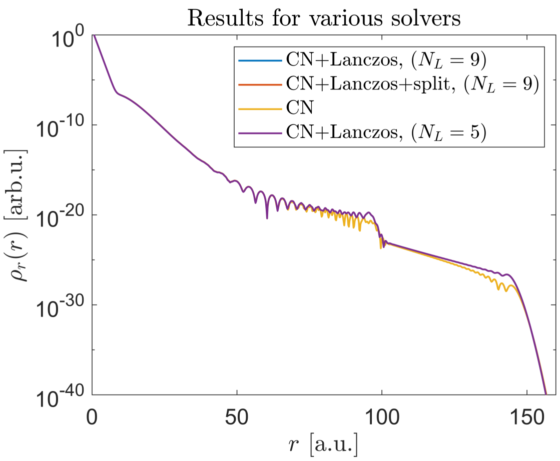

Fig. 7.2: Different propagators used in the propagation. The conditions are the same as in Fig. 7.1. All the results except CN coincide in our precision.

7.7.1 Eigenvalue problem in non-orthogonal bases

The Sturmians do not form an orthogonal basis, the matrix form of the eigenvalue problem includes explicitly the Gramian. Let us take any non-orthogonal basis span $\{|e_i\rangle\}_{i\in\mathcal{I}}$. We seek a solution $|\psi\rangle$ of an eigenvalue problem $H|\psi_E\rangle = E|\psi_E\rangle$. This solution can be expanded in the considered basis $|\psi_E\rangle = \sum_i \xi_i |e_i\rangle$. The original eigenvalue problem is thus rewritten as

$$(H-E)|\psi\rangle = 0 \quad \Leftrightarrow \quad \sum_i \xi_i (H-E)|e_i\rangle = 0 \quad \Leftrightarrow$$

$$\sum_i \xi_i \langle e_k|(H-E)|e_i\rangle = 0\,, \forall k \quad \Leftrightarrow \quad (\mathbb{H} - E\mathbb{G})\boldsymbol{\xi} = 0\,, \tag{7.42}$$

$\mathbb{H}_{ij} := \langle e_i|H|e_j\rangle$, $\boldsymbol{\xi}$ is now a vector from the l^2-space. Since the overlap matrix $\mathbb{G}$ is not the identity matrix, this problem is usually called *generalised eigenvalue problem.*[19]

7.7.2 Matrix elements

Now, we specify the matrix representation given by the Sturmians. The solution of (7.7) is

$$S_{nl}^{\lambda}(r) = N_{nl}^{\lambda}(2\lambda r)^{l+1}\mathrm{e}^{-\lambda r}\, L_{n-l-1}^{2l+1}(2\lambda r)\,, \qquad N_{nl}^{\lambda} = \sqrt{\frac{\lambda}{n}\frac{(n-l-1)!}{(n+l)!}}\,, \tag{7.43}$$

---

[19] $\mathbb{G}$ is regular in our case, thus it is equivalent to the eigenvalue problem for the matrix $\mathbb{G}^{-1}\mathbb{H}$.

L_k^α are the generalised Laguerre polynomials. The normalisation N_{nl}^λ is chosen so that $\left\langle S_{nl}^\lambda \middle| S_{nl}^\lambda \right\rangle = 1$. The values of l follows from (7.43); it starts with $n = l + 1$, the first polynomial is then L_0^{2l+1} for each value of l. The finite basis of each l-subspace is $\{|S_{l+i,l}^\lambda\rangle\}_{i=1}^N$. The full basis is then $|e_{il}\rangle$ defined by $\langle \boldsymbol{r}|e_{il}\rangle = S_{l+i,l}^\lambda(r) Y_l^{m_0}(\Omega_{\boldsymbol{r}})$.

The first series of the matrix elements is

$$\langle e_{il'} \,|\, e_{jl}\rangle \;, \quad \left\langle e_{il'} \middle| \mathrm{e}^{\mathrm{i}\theta} r \cos\vartheta \middle| e_{jl} \right\rangle \;, \quad \left\langle e_{il'} \middle| \frac{1}{\mathrm{e}^{\mathrm{i}\theta} r} \middle| e_{jl} \right\rangle \;, \quad \left\langle e_{il'} \middle| -\frac{1}{2\mathrm{e}^{2\mathrm{i}\theta}} \frac{\mathrm{d}^2}{\mathrm{d}r^2} + \frac{l(l+1)}{2\mathrm{e}^{2\mathrm{i}\theta} r^2} \middle| e_{jl} \right\rangle \;. \tag{7.44}$$

All the elements except the second one stays within the radial subspace and are sufficient to treat for $l = l'$. It thus means that for any angular-independent operator Ξ: $\langle e_{il'} \,|\, \Xi \,|\, e_{jl}\rangle = \left\langle S_{l+i,l}^\lambda \middle| \Xi \middle| S_{l+j,l}^\lambda \right\rangle \delta_{ll'}$. Let us compute the coupling element of the interaction,

$$\begin{aligned} &\mathrm{e}^{\mathrm{i}\theta} \left\langle S_{l'+j,l'}^\lambda \middle| r \middle| S_{l+k,l}^\lambda \right\rangle \int_\Omega \left(Y_{l'}^{m_0}\right)^* (\Omega_{\boldsymbol{r}}) \cos(\vartheta) Y_l^{m_0}(\Omega_{\boldsymbol{r}}) \, \mathrm{d}\Omega = \\ &\quad = (-1)^{m_0} \mathrm{e}^{\mathrm{i}\theta} \sqrt{(2l+1)(2l+3)} \begin{pmatrix} l & 1 & l+1 \\ 0 & 0 & 0 \end{pmatrix} \begin{pmatrix} l & 1 & l+1 \\ -m_0 & 0 & m_0 \end{pmatrix} \left\langle S_{l+1+j,l+1}^\lambda \middle| r \middle| S_{l+k,l}^\lambda \right\rangle \;. \end{aligned} \tag{7.45}$$

The selection rules of the Wigner 3j-symbols, $\left(\begin{smallmatrix} l_1 & l_2 & l_3 \\ m_1 & m_2 & m_3 \end{smallmatrix}\right)$, reveal the coupling of only neighbouring l's and provides the respective coupling constants. The remaining computation is thus only the last scalar product.

The required scalar products are

$$\left\langle S_{il}^\lambda \middle| S_{jl}^\lambda \right\rangle = \begin{cases} 1 \,, & i = j \,, \\ -\frac{1}{2}\sqrt{\frac{(j+l)(j-l-1)}{j(j-1)}} \,, & i = j-1 \,, \\ -\frac{1}{2}\sqrt{\frac{(j-l)(j+l+1)}{j(j+1)}} \,, & i = j+1 \,, \\ 0 \,, & \text{otherwise,} \end{cases} \tag{7.46a}$$

$$\left\langle S_{il'}^\lambda \middle| \mathrm{e}^{\mathrm{i}\theta} r \middle| S_{jl}^\lambda \right\rangle = \begin{cases} -\frac{\mathrm{e}^{\mathrm{i}\theta}}{4\lambda}\sqrt{\frac{(j+l)(j-l-1)(j-l-2)(j-l-3)}{j(j-2)}} \,, & i = j-2 \,, \\ -\frac{\mathrm{e}^{\mathrm{i}\theta}}{4\lambda}\sqrt{\frac{(j-l)(j+l+1)(j+l+2)(j+l+3)}{j(j+2)}} \,, & i = j+2 \,, \\ -\mathrm{e}^{\mathrm{i}\theta}\frac{2j+l}{2\lambda}\sqrt{\frac{(j-l-1)(j-l-2)}{j(j-1)}} \,, & i = j-1 \,, \\ -\mathrm{e}^{\mathrm{i}\theta}\frac{2j-l}{2\lambda}\sqrt{\frac{(j+l+1)(j+l+2)}{j(j+1)}} \,, & i = j+1 \,, \\ -\frac{3\mathrm{e}^{\mathrm{i}\theta}}{2\lambda}\sqrt{(j+l+1)(j-l-1)} \,, & i = j \,, \\ 0 \,, & \text{otherwise,} \end{cases} \tag{7.46b}$$

$$\left\langle S^{\lambda}_{il'} \middle| \frac{1}{\mathrm{e}^{\mathrm{i}\theta} r} \middle| S^{\lambda}_{jl} \right\rangle = \mathrm{e}^{-\mathrm{i}\theta} \frac{\lambda}{j} \delta_{ij}\,, \tag{7.46c}$$

$$\left\langle S^{\lambda}_{il'} \middle| -\frac{1}{2\mathrm{e}^{2\mathrm{i}\theta}} \frac{\mathrm{d}^2}{\mathrm{d}r^2} + \frac{l(l+1)}{2\mathrm{e}^{2\mathrm{i}\theta} r^2} \middle| S^{\lambda}_{jl} \right\rangle = \begin{cases} \frac{\mathrm{e}^{-2\mathrm{i}\theta}\lambda^2}{2}\,, & i = j\,, \\ \frac{\mathrm{e}^{-2\mathrm{i}\theta}\lambda^2}{4} \sqrt{\frac{(j+l)(j-l-1)}{j(j-1)}}\,, & i = j-1\,, \\ \frac{\mathrm{e}^{-2\mathrm{i}\theta}\lambda^2}{4} \sqrt{\frac{(j-l)(j+l+1)}{j(j+1)}}\,, & i = j+1\,, \\ 0\,, & \text{otherwise,} \end{cases} \tag{7.46d}$$

The first three are obtained using tabled integrals [273] and the expansion of the Wigner 3j-symbols; the last element comes from the definition of Sturmians (7.7) and already known elements of (7.46). The element (7.46b) also present a band-diagonal structure of the interaction matrix-block.

The last missing element to construct the matrix representation is the short-range term of the potential. It reads

$$\left\langle S^{\lambda}_{n'l} \middle| \frac{\mathrm{e}^{-qr\mathrm{e}^{\mathrm{i}\theta}}}{\mathrm{e}^{\mathrm{i}\theta} r} \middle| S^{\lambda}_{nl} \right\rangle = \mathrm{e}^{-\mathrm{i}\theta} \mathcal{N}^{\lambda}_{n'nl} \int_0^{+\infty} \frac{\mathrm{e}^{-\tilde{q}r}}{r} (2\lambda r)^{2l+2} \mathrm{e}^{-2\lambda r} L^{2l+1}_{n'-l-1}(2\lambda r) L^{2l+1}_{n-l-1}(2\lambda r)\, \mathrm{d}r \tag{7.47a}$$

$$= \mathrm{e}^{-\mathrm{i}\theta} \mathcal{N}^{\lambda}_{n'nl} \int_0^{+\infty} \mathrm{e}^{-\left(1+\frac{\tilde{q}}{2\lambda}\right)x} x^{2l+1} L^{2l+1}_{n'-l-1}(x) L^{2l+1}_{n-l-1}(x)\, \mathrm{d}x \tag{7.47b}$$

$$= \frac{\mathrm{e}^{-\mathrm{i}\theta} \mathcal{N}^{\lambda}_{n'nl} \Gamma(n'+n)}{(n'-l-1)!(n-l-1)!} \frac{{}_2F_1\left(-n'+l+1, -n+l+1, -(n'+n-1); z\right)}{\left(\frac{\tilde{q}}{2\lambda}\right)^{2l+2} \left(1+2\frac{\lambda}{\tilde{q}}\right)^{n'+n}} \tag{7.47c}$$

$$= \frac{\mathrm{e}^{-\mathrm{i}\theta} \lambda \sqrt{\frac{a!b!}{nn'(n+l)!(n'+l)!}}}{\left(\frac{\tilde{q}}{2\lambda}\right)^{2l+2} \left(1+2\frac{\lambda}{\tilde{q}}\right)^{n'+n}} \sum_{m=0}^{\min\{a,b\}} \frac{(c-m)!}{(a-m)!(b-m)!} \frac{(-z)^m}{m!}\,, \tag{7.47d}$$

$$\mathcal{N}^{\lambda}_{n'nl} = N^{\lambda}_{n'l} N^{\lambda}_{nl}\,, \quad \tilde{q} = q\mathrm{e}^{\mathrm{i}\theta}\,, \quad a = n'-l-1\,, \quad b = n-l-1\,, \quad c = n+n'-1\,, \quad z = 1 - \left(\frac{2\lambda}{\tilde{q}}\right)^2 .$$

see [273], Eq. (7.714.4). We have tried several approaches to compute various expressions enlisted under (7.47); this problem arises as numerically non-trivial and unstable.[20] We noted a recurrence in the matrix calculation of the corresponding short-range potential term

$$[\mathbb{V}_{\mathrm{SR}}(l)]_{i,j} = \left\langle S^{\lambda}_{l+i,l} \middle| \frac{\mathrm{e}^{-qr\mathrm{e}^{\mathrm{i}\theta}}}{\mathrm{e}^{\mathrm{i}\theta} r} \middle| S^{\lambda}_{l+j,l} \right\rangle , \tag{7.48}$$

---

[20] The explicit integration seems suitable for quadrature rules, the last sum is finite, there are procedures to evaluate the hypergeometric function ${}_2F_1$, [274, 275]. However, all the procedures occurred inaccurate for large n and/or n'.

because (7.47) is symmetric in n and n', also $\mathbb{V}_{\mathrm{SR}}(l)$ is symmetric. The recurrence reads

$$\frac{[\mathbb{V}_{\mathrm{SR}}(l)]_{i,j+1}}{[\mathbb{V}_{\mathrm{SR}}(l)]_{i,j}} = \frac{2l+2+j+i}{1+\frac{2\lambda}{\tilde{q}}}\sqrt{\frac{j+l+1}{(j+1)(j+l+2)(2l+j+2)}} \frac{{}_2F_1\left(-i,-j,-(2l+j+i+2);z\right)}{{}_2F_1\left(-i,-(j+1),-(2l+j+i+1);z\right)}\,, \tag{7.49}$$

where the ratio of the hypergeometric functions ${}_2F_1$ can be obtained from the Gauss's continued fraction (Eq. (15.3.3) of [276]):

$$\frac{{}_2F_1\left(a+1,b,c;z\right)}{{}_2F_1\left(a,b,c+1;z\right)} = 1 + \mathop{\mathrm{K}}_{i=1}^{+\infty}\left(\frac{k_i z}{1}\right)\,, \qquad \begin{aligned} k_{2j+1} &= -\frac{(b+j)(c-a+j)}{(c+2j)(c+2j+1)}\,, \quad j\in\mathbb{Z}_+\,,\\ k_{2j} &= -\frac{(a+j)(c-b+j)}{(c+2j-1)(c+2j)}\,, \quad j\in\mathbb{N}\,, \end{aligned} \tag{7.50}$$

and the symmetry in the first two arguments of ${}_2F_1$. A general continued fraction is given by

$$b_0 + \mathop{\mathrm{K}}_{i=1}^{+\infty}\left(\frac{a_i}{b_i}\right) = b_0 + \cfrac{a_1}{b_1+\cfrac{a_2}{b_2+\cfrac{a_3}{b_3+\ddots}}}\,. \tag{7.51}$$

Combining these equations, we compute recurrently (7.47) from the initial point

$$[\mathbb{V}_{\mathrm{SR}}(l)]_{1,1} = \frac{\mathrm{e}^{-\mathbf{i}\theta}{}_2F_1\left(0,0,0;z\right)}{(l+1)\left(1+\frac{\tilde{q}}{2\lambda}\right)^{2l+2}} = \frac{\mathrm{e}^{-\mathbf{i}\theta}}{(l+1)\left(1+\frac{\tilde{q}}{2\lambda}\right)^{2l+2}}\,. \tag{7.52}$$

All the other elements follows from the symmetry and the recurrence. Note that the continued fraction is finite as the first three arguments of ${}_2F_1$ are integers. Using this approach, we are able to construct the matrix up to 1000 Sturmians involved in the standard double precision.

7.7.3 Ionisation rates

We constructed all the required matrices and implemented the task in FORTRAN using lapack [277] procedure `ZGGEV` to compute the generalised eigenvalue problem. Here we show examples of complexly rotated spectra and conclude this section by explaining how the ionisation rates are retrieved.

The spectra of the rotated 3D-Hamiltonian are shown in Figs. 7.3 and 7.4. These examples show the spectra of an argon atom given by the potential (7.26b) with the parameters from [264]. The parameters of the calculation was chosen to reach the precision 10^{-16} estimated by the imaginary part of the bound states of the field-free spectrum.

The spectrum of the field-free Hamiltonian is in Fig. 7.3. A general field-free spectrum fulfils the following properties [278, 279]:

1. $\sigma_\mathrm{d}(H_0(\theta)) = \sigma_\mathrm{d}(H_0(0))$,
2. $\sigma_\mathrm{c}(H_0(\theta)) = \mathrm{e}^{-2\mathbf{i}\theta}\sigma_\mathrm{c}(H_0(0))$,

where σ_p and σ_d are the *discretised* and *continuum spectrum*, respectively. The unscaled field-free Hamiltonian is $H_0(0)$, and $H_0(\theta)$ is scaled by $r \mapsto \mathrm{e}^{\mathbf{i}\theta} r$. The points on the negative real axis correspond to the bounded states of the model potentials, these are 2s, 2p, 3s, 3p,. . . (1s states is out of the range of the figure). The continuum, σ_c, is rotated by 2θ as expected.

The spectrum of the Hamiltonian with the external field $\mathcal{E} = 0.05$ a.u., Fig. 7.4, exhibits more structures. The most important feature is the imaginary value of the bound states, which is related to the ionisation rate of interest $\Gamma = -2\,\mathsf{Im}(E_n)$. A new structure are the eigenenergies sorted along the red line $\mathrm{e}^{\mathbf{i}\theta}$. Although it seems natural to link them with the scaled interaction term $\mathcal{E} r \mathrm{e}^{\mathbf{i}\theta}\cos\vartheta$, this part of the spectrum is a pure numerical artefact linked with the finite dimension.[21]

The final task is to automatise the retrieval of the ionisation rates from the spectra that looks alike Fig. 7.4. We need to find the proper eigenvalue. We use its geometrical placement that

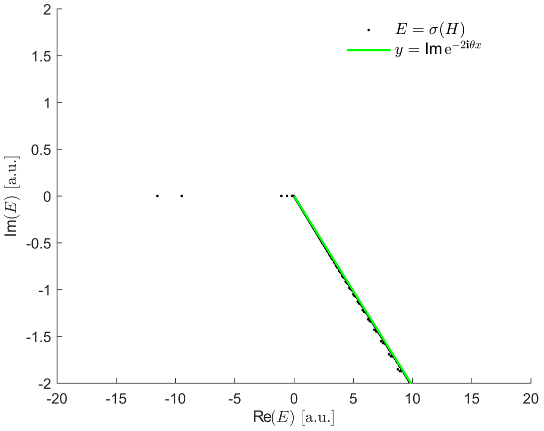

Fig. 7.3: The complexly rotated spectrum of the field-free case.

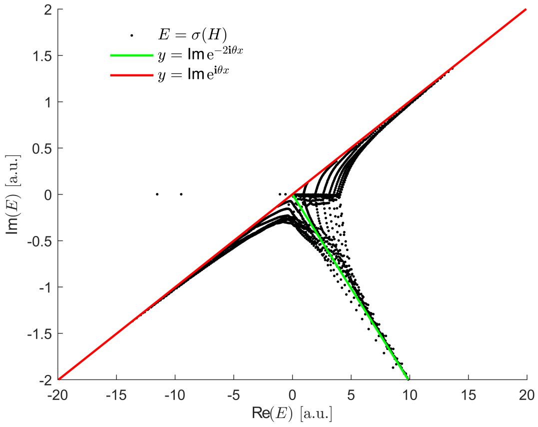

Fig. 7.4: The complexly rotated spectrum with an external field $\mathcal{E} = 0.05$ a.u..

---

[21] We recall the discussion from [151] and [108, 108]. The core of the artefact is the emptiness of the spectrum is imposed by $\sigma\left(-\frac{\triangle}{2} + \alpha x\right) = \emptyset$ for $\mathsf{Im}\,\alpha \neq 0$; *theorem II.1* in [108]. It is also interesting to note the characteristic value $\theta = \pi/3$ mentioned as the bound of the applicability. If we omit the Coulomb potential, the Hamiltonian reads $\tilde{H}(\theta) = \mathrm{e}^{-2\mathbf{i}\theta}\left(-\frac{\triangle}{2} + \mathcal{E}\mathrm{e}^{3\mathbf{i}\theta} r\right)$. Considering only the part in the bracket and accounting the theorem, the field $\mathcal{E}\mathrm{e}^{3\mathbf{i}\theta}$ only changes its sign for $\theta = \pi/3$ and both terms in $\tilde{H}$ are scaled by the same angle. If $\theta > \pi/3$ is chosen, the artificial part of the spectrum is flipped around the red line.

clearly distinguishes it from the others. The complex rotation separates this value until this value lies above the red line $e^{\mathbf{i}\theta}$. The scaling θ must then be chosen appropriately to this condition. Next, this value lies close to the unscaled eigenenergy, while its real part is shifted according to the Stark shift. Our approach was to choose a polygon containing only the eigenenergy of the interest. For example for argon as shown in Fig. 3.2 with $I_p \approx 0.58$ a.u., we used the rectangle $[-0.7, -0.4] \times [-0.4, 0.01]$, which lies above $e^{\mathbf{i}\theta}$ and contains the ionisation rates up to $\mathcal{E} = 0.3$ a.u. (the corresponding intensity is $\sim 3.2 \times 10^{15}$ W/cm^2).

7.8 Calculation of FSPA

Here we reproduce the implementation of a solver of (2.17) that was introduced in [126]. The set of equations to solve is

$$\omega = \frac{(\boldsymbol{k} + \boldsymbol{A}(t_r))^2}{2} - E_g\,, \qquad E_g = \frac{(\boldsymbol{k} + \boldsymbol{A}(t_i))^2}{2}\,, \qquad \boldsymbol{k} = -\frac{\int_{t_i}^{t_r} \boldsymbol{A}(t'')\,\mathrm{d}t''}{(t_r - t_i)}\,.$$

We solve these equations for a monochromatic field, $\boldsymbol{A}(t) = (A_0 \cos(\omega_0 t), 0, 0)$, and given E_g and ω. The unknowns are then t_i, t_r and $\boldsymbol{k}$. The last equation may be substituted to the other ones, reducing the unknowns to t_i and t_r. The equations to solve are then

$$\left(\frac{A_0}{\omega_0}\right)^2 \left(\omega_0 \cos(\omega_0 t_r) - \frac{\sin(\omega_0 t_r) - \sin(\omega_0 t_i)}{t_r - t_i}\right)^2 - 2E_g - 2\omega = 0\,, \tag{7.53a}$$

$$\left(\frac{A_0}{\omega_0}\right)^2 \left(\omega_0 \cos(\omega_0 t_i) - \frac{\sin(\omega_0 t_r) - \sin(\omega_0 t_i)}{t_r - t_i}\right)^2 - 2E_g = 0\,. \tag{7.53b}$$

We use the Newton iterative method[22] to obtain the solutions [280]. Using this method, we reach a converged solution ($\|\boldsymbol{t}_i - \boldsymbol{t}_{i-1}\| < 10^{-10}$) in $\lesssim 10$ iterations for the initial guesses $\boldsymbol{t}_0 = (0.3T_0 + 2T_0\mathbf{i}, 0.44T_0 + 2T_0\mathbf{i})^\intercal$ and $\boldsymbol{t}_0 = (0.15T_0 + 2T_0\mathbf{i}, 0.75T_0 + 2T_0\mathbf{i})^\intercal$, $T_0 = 2\pi/\omega_0$, for the short and long trajectories, respectively. With these conditions, the merged solution in the cutoff is the extension of the long trajectories. Because we require the calculation of the dipoles also in the frequency range corresponding to the transition between the plateau and cutoff, we use polynomial interpolation linking the short trajectories to the cutoff.

The FSPA approach is computationally cheap compared to the other methods. It then provides a fast estimate of the harmonic signal once the intensity of the driver is known. Although this solution is formally obtained only for a monochromatic plane wave, it can be easily extended for pulses with well-defined carrying frequency ω_0 until the variation of the amplitude in time and space is slow compared to the carrying frequency. In other words, until the slowly varying envelope

---

[22] The iterative scheme reads $\boldsymbol{t}_{i+1} = \boldsymbol{t}_i - \mathbb{A}^{-1}\boldsymbol{F}(\boldsymbol{t}_i)$, where $\boldsymbol{t} = (t_i, t_r)^\intercal$ and $\boldsymbol{F}$ is given by (7.53a).

approximation may be applied. In this case, the harmonic response is obtained by a simple masking of the intensity profile. The macroscopic source of the qth harmonic is then

$$d_q^{(\text{macro})}(\boldsymbol{r}, t) = d(q\omega_0; I_{\text{IR}}(\boldsymbol{r}, t))\,, \tag{7.54}$$

where $d(q\omega_0; I_{\text{IR}}(\boldsymbol{r}, t))$ is given by (2.18) with the amplitude of the field corresponding to the respective IR-intensity at $(\boldsymbol{r}, t)$.

8. CUPRAD: DRIVING LASER PROPAGATION

Because the development of the computational kernel of this part of the model is not a subject of this thesis, we only briefly plot its functionality. The main work done during this project is: 1) creating an interface to be sorted within the multi-scale model; 2) modifying the ionisation module and creating the "pre-ionisation" module.

8.1 Main routines

While we were describing the physics of non-linear propagation of laser pulses, we found convenient to represent a part of it in spectral domain and part of it in time domain. In this implementation, this is not only about the words, but it is actually a crucial concept of the code. Profiting from a parallelised fast implementation of the Fourier transform (FFT), it switches the domains at each step.

The objective of the code is the implementation of (6.11) to evolve U, which correspond to the electric field in the co-moving frame with removed fast oscillations. We recall the equation here:

$$\partial_z U = \frac{\mathbf{i}}{2k_0}\mathcal{T}^{-1} \triangle_\perp U + \mathbf{i}\mathcal{D}_2 U + \mathbf{i}\frac{\omega_0}{c} n_2 \mathcal{T}|U|^2 U - \frac{\mathbf{i}e^2 k_0}{2n_0^2\omega_0^2 m_e \varepsilon_0}\mathcal{T}^{-1}\left(\varrho_e U\right) - \frac{e^2 \nu_e}{2m_e\varepsilon_0 n_0 c \left(\nu_e^2 + \omega^2\right)^2}\varrho_e U$$

The code uses a grid representation in all the discretised dimensions, namely: time/frequency, radial coordinate ρ and z. The desired quantity is the electric field $\mathcal{E}$ that is obtained from U as explained in the derivation of (6.11). Second, the plasma density ϱ_e is retrieved from the ionisation model.

Algorithm 1 shows the schematic of the main operation procedure. It explains the key philosophies of the code. The evolution is done by the Crank-Nicolson operator, already introduced for TDSE (7.34). There is implemented adaptive-step control governed by $\Delta\varphi$, which symbolises the change of the phase of the field from one plane to the next one (note that the fast oscillations are removed and co-moving frame is applied, i.e. $\Delta\varphi = 0$ for a free linear propagation). The step-size Δz is then reduced or enlarged if the phase is outside the interval of changes $[\varphi_{\min}, \varphi_{\max}]$.[1] The core of the code uses the FFT implemented by the FFTW3 [281] and the application of the

---

[1] To be rigorous, there is possible to set also a maximal possible advancement $\Delta z_{\max}$.

Algorithm 1 Main CUPRAD routine

```
Initialise
while $z < z_{\text{exit}}$ do                                  ▷ loop until the end of the medium is reached
    if $z \geq z_{\text{print}}$ then
        Save data
        $z_{\text{print}} \leftarrow z_{\text{print}} + \Delta z_{\text{print}}$
    FFT: $U \to \hat{U}$
    Crank-Nicolson + the physics in the $\omega$-domain: $U \leftarrow U(z + \Delta z)$; $z \leftarrow z + \Delta z$
    inverse FFT: $\hat{U} \to U$
    physics in $t$-domain
    FFT: $U \to \hat{U}$
    Crank-Nicolson + the physics in the $\omega$-domain: $U \leftarrow U(z + \Delta z)$; $z \leftarrow z + \Delta z$
    inverse FFT: $\hat{U} \to U$
    Absorbing boundaries                                 ▷ avoid artificial reflections on boundaries
    if $\Delta\varphi > \Delta\varphi_{\max}$ then                                   ▷ adaptive-step control
        decrease $\Delta z$
    else if $\Delta\varphi < \Delta\varphi_{\min}$ then
        increase $\Delta z$
Finalise
```

respective physical effects in their natural time or frequency domains. Further details about the implementation are in Appendix B.1 of [197].

There are two points where physical effects are treated: *the physics in the t-domain* and *the physics in the ω-domain*. The physics in the ω-domain means basically applying of the differential operator and dispersive effects $k(\omega)$. These effects are contained in

$$\frac{\mathbf{i}}{2k_0}\mathcal{T}^{-1} \triangle_{\perp} U + \mathbf{i}\mathcal{D}_2 U \,. \tag{8.1}$$

The rest of (6.11) is natural to treat in the t-domain as there stands either the plasma density ϱ or the intensity of the field $|U|^2$.

Next, we infer that the storing of data is not done at every iteration, the data are stored with an independently prescribed spacing Δz_{print}. Note, that the adaptive-steps does not ensure this spacing exactly. It means, that the outputs within the medium are not equidistant. This has to be considered, if one would finely compare simulations with different inputs as the output z-grids would not match exactly.

One has to pay attention to the use of the units in the code. Internally, the code constructs its own computational units (C.U.) adjusted to the input parameters based on a Gaussian beam. The normalisations are done respective to 4 Rayleigh ranges in the longitudinal dimension, beam waist w_0 in the radial dimension, pulse duration in time and the density is expressed using the critical plasma density $\varrho_c = \varepsilon_0 m_e \omega_0^2 / e^2$.

Finally, we mention, that our description of the code is not limited to the actual needs of the multi-scale model. The code may be used for broader range of cases. For example, the approximations due to the use of the enveloped description from section 6.1.2 is optional. It is possible to use the routine directly for the complexified field $\mathscr{E}$ (as introduced in (6.3)), see the equation (43) of [80].[2]

8.2 Code modules

Beside the main routine, we mention two important modules of the code: the ionisation module and I/O processing.

- The ionisation is computed in all the cases by the rate equation $\partial_t \varrho = -\Gamma(|U(t)|)\varrho$ (see (3.3)), computed locally at each point. There are two options implemented within the module for HHG in gases. First, there is the PPT-formula, [110]. Second, it is possible to load an external table $\Gamma(|U|)$, which is considered as an input of the code. One alternative we tested was the complex rotation.
- I/O processing is the interface of the code with user inputs and outputs linked with either post-processing or the TDSE-solver. One of the tasks of these procedures is to convert the units from SI to C.U. and vice versa, so C.U. remains encapsulated in the code.
    - The inputs are of three natures: i) the set-up of the laser pulse and medium; ii) the material constants, i.e. the pre-set parameters of the medium; iii) the numerical parameters of the computation. There are now implemented pre-sets for rare gases in the code: the dispersion relation for $k(\omega)$ from [282], the ionisation potentials from [214], the Kerr-effect refractive index n_2 from [283] (please find a discussion of various sources for n_2 in [284]). The laser pulse is constructed in the pre-processor, we currently use Gaussian beams and pulses, but from the viewpoint of the main code, the input is an arbitrary $\mathscr{E}(t, \rho, z = z_{\text{entry}})$.
    - The key outputs – the electric field $\mathcal{E}$ and plasma density ϱ – are stored on-the-fly in the main routine, Algorithm 1. There are also some other characteristics stored throughout the computation and stored during the *Finalise* phase.

---

[2] One case where this approach is required is to treat correctly the third harmonic generation. Next, this approach would give also the "ionisation ladder" on the sub-cycle resolution. A disadvantage is higher computational cost as the sub-cycle resolution is required.

9. XUV SIGNAL: THE HANKEL TRANSFORM

Here we present the last module of the multi-scale model: the propagation of the XUV field. From the implementation viewpoint, we use a solution expressed in the means of the integral (5.3):

$$\hat{\boldsymbol{\mathcal{E}}}(\omega,\rho,z) \approx -\frac{\mu_0 \mathrm{e}^{\mathbf{i}k(\omega)z}}{4\pi} \int_{z_{\mathrm{entry}}}^{z_{\mathrm{exit}}} \frac{\mathrm{e}^{-\mathbf{i}k(\omega)z'}\mathrm{e}^{\mathbf{i}\frac{k(\omega)\rho^2}{2(z-z')}}}{z-z'} \int_{\Delta_T} \mathrm{e}^{\mathbf{i}\frac{k(\omega)(\rho')^2}{2(z-z')}} \widehat{\left(\frac{\partial \boldsymbol{j}_Q}{\partial t}\right)} J_0\left(\frac{k(\omega)\rho\rho'}{z-z'}\right) \rho' \,\mathrm{d}\rho' \,\mathrm{d}z' \,.$$

There is thus no need to solve a partial differential equation as in the previous two sections.

We implement it straightforwardly by first integrating over the radial coordinate ρ' to obtain the signal from a single plane. Second, the planes are integrated over z' in the case of long media. We need to take some care about the correct reference frames, especially when treating the phase-matching.

The reference frame imposed by the CUPRAD, F_g, is co-moving with the pulse with the group velocity v_g. The original integral (5.3) is in the laboratory frame F_l. We now adjust the phases in the integral. First, we transform the source term in the laboratory frame

$$\widehat{\left(\frac{\partial \boldsymbol{j}_Q}{\partial t}\right)}_{F_l} = \mathrm{e}^{\mathbf{i}\frac{\omega z'}{v_g}} \widehat{\left(\frac{\partial \boldsymbol{j}_Q}{\partial t}\right)}_{F_g} . \tag{9.1}$$

Second, we adjust $k(\omega)$ for the harmonics. Because we consider only the linear dispersion and absorption, it can be written as

$$k(\omega) = \frac{\omega n(\omega)}{c} \,, \qquad n(\lambda) = 1 - \frac{N r_e \lambda^2}{2\pi}\left(f_1(\lambda) - \mathbf{i} f_2(\lambda)\right) \,, \tag{9.2}$$

where $n(\lambda)$ is the refractive index conventionally written (see Eq. (3.9) of [194]) using the atomic scattering factors f_1 and f_2 for the dispersion and absorption, respectively. We implemented the option from the tabulated values from [218] and [219, 285]. λ is the vacuum wavelength, r_e the classical electron radius $\hbar\alpha_0/(m_e c)$ and N the density of the gas atoms.

Now, we substitute the adjustments in (5.3). The final integral expression for the generated field in th far-field region reads

$$\hat{\boldsymbol{\mathcal{E}}}(\omega,\rho,z) \approx -\frac{\mu_0 \mathrm{e}^{\mathbf{i}k_r(\omega)z}}{4\pi} \int_{z_{\mathrm{entry}}}^{z_{\mathrm{exit}}} \int_{\Delta_T} \frac{\mathrm{e}^{\Phi(\rho,\rho',z,\omega)}}{z-z'} \widehat{\left(\frac{\partial \boldsymbol{j}_Q}{\partial t}\right)}_{F_g} J_0\left(\frac{k_r(\omega)\rho\rho'}{z-z'}\right) \rho' \,\mathrm{d}\rho' \,\mathrm{d}z' \,, \tag{9.3a}$$

$$\Phi\left(\rho,\rho',z,\omega\right) = \mathbf{i}\omega z' \left(\frac{1}{v_g} - \frac{n_r(\omega)}{c}\right) + \mathbf{i}\frac{k_r(\omega)\rho^2}{2(z-z')} + \mathbf{i}\frac{k_r(\omega)\left(\rho'\right)^2}{2(z-z')} - \frac{z_{\mathrm{exit}}-z}{L_{\mathrm{abs}}(\omega)} \,. \tag{9.3b}$$

We use n_r and k_r to denote the real parts of n and k, respectively. The terms involved in the phase Φ can be assigned to various effects:

- The first term, $\mathbf{i}\omega z'(1/v_g - n(\omega)/c)$, adjust the frames and gives the principal contribution to the phase-matching. An intuition about the phase-matching comes from the difference of the phase-velocities of the IR-driver and the XUV-field as explained earlier (see (5.23) for instant). The expression (9.3) contains explicitly the group velocity v_g instead of the phase velocity v_p to adjust the phase. This is specific for our model that describes the physics in the co-moving frame with v_g: The other phase effects are encoded directly in $\widehat{\partial_t j_Q}_{F_g}$. The proper phase is then restored by matching the reference frames.
- The first curvature term, $\mathbf{i}k_r(\omega)\rho^2/\left(2(z-z')\right)$, basically gives the wave-front profile of the beam in the far-field region.
- The second curvature term, $\mathbf{i}k_r(\omega)\left(\rho'\right)^2/\left(2(z-z')\right)$, is the correction that allows the focusing of the generated beam and goes beyond the Fraunhofer diffraction as explained in Appendix D.
- The last term, $(z_{\mathrm{exit}} - z)/L_{\mathrm{abs}}(\omega)$, is the attenuation due to the absorption with $L_{\mathrm{abs}}(\omega) = c/\left(\omega\,\mathsf{Im}(n(\omega))\right)$.

The propagation of the XUV field completed the numerical part of the multi-scale model and we can assemble the modules.

10. COUPLED MODEL

The last part is completion of the code. We recall that our approach is sequential: 1) We compute the non-linear propagation by CUPRAD; 2) We run TDSE solvers on a grid covering the medium; 3) We use the Hankel transform to obtain the far-field XUV. Because there is no real-time communication between the processes, we can simply pipeline the process, and each stage is inputted by the outputs of the previous one.

There is then no fundamental challenge in the implementation of the multi-scale model itself. However, we consider the computational needs as non-trivial from the viewpoint of the resources needed. This chapter introduces our specific implementation of the model. The linear operation of the three main modules is introduced in Section 10.1. Section 10.2 mentioned the post-processing of the results. Section 10.3 shows the roadmap of the multiscale model including also computationally cheaper modules and possible outputs. A complementary analysis of the computational cost of the model is done in Appendix E.

One of the main philosophies is to keep data from the whole calculation together and the modularity of the model: to easily change one part of the process. It suggests some level of standardisation in the process.

We opted for the HDF5-data format [286]. We briefly introduce its features. The elementary block of an hdf5-archive is a dataset: This is an N-dimensional array of either integer or real numbers in single or double precision. Complementary to numbers, strings can be also stored. The archive may contain many of datasets ordered in a hierarchical structure, which is similar to a directorial structure in usual file-systems. Because there are interfaces to many programming languages and software (Python, MATLAB®, Fortran, c, Java, . . .), it provides portability across these platforms. Last, the HDF5-library supports the parallel file access. All these features are demanded and used in the multi-scale model for all the data-flows.

10.1 Multi-scale model work-flow

Here we present the work-flow of the code. The input of the code are various parameters that can be divided into 3 groups:

- *The driving IR laser:* This input is generally the electric field at the entry plane of the medium,

$\mathcal{E}(z = z_{\text{entry}}, \rho, t)$. A standard model of the driving laser is a Gaussian profile (B.6). This profile is fully defined by its: wavelength λ, peak intensity I_0, waist w_0, focus position z_{focus} and pulse duration τ_{FWHM}. We frequently use a *vacuum Gaussian profile* as a reference. It means that we first consider a virtual set-up without medium with analytically defined Gaussian beam. Second, we place the medium in the path of the beam at a given position compared to the vacuum focus.

- *The specification of the target:* There are two aspects of the target: 1) the macroscopic properties as pressure, the length of the gas-cell and eventually further specifications as pre-ionisation as applied in Section 6.3; 2) the microscopic property is basically only the type of atoms in the medium. For the rare gases of our interest, we use pre-set values discussed in the previous chapters.
- *The parameters of the numerics:* This set of parameters defines the discretisations of grids and their sizes, it also contain the driving variables of the code as the number of processors.

The last set of parameters are the properties of the *analyser* – the Hankel transform. These are the properties of the observation plane: its size and distance from the target.

All the modules of the model are prepared to be executed as jobs on a computer cluster using the slurm workload manager [287]. These jobs are submitted in the sequence of the weak-coupling model. There are some details about the implementation

1. *CUPRAD*: The first step of the calculation is the propagation of the IR-laser. This is done in two steps, first, the data are pre-processed. The pre-processor constructs the beam profile and convert the inputs into the computational units of CUPRAD. The second step is the computation of the propagation itself. The output of this code is the electric field and plasma density. The actual implementation is done in FORTRAN [288] for both pre-processor and the main code.
2. *1D-TDSE*: The 1D-TDSE solver is executed for all the required points covering the macroscopic medium. The desired output is $\widehat{\partial_t j}$ on the same grid. The main computational challenge is the need to execute a large amount of the simulation. Even though there is no communication between the simulations, it is not possible to separate the jobs easily. For example, the typical amount of TDSE's per one simulation is about 10^5 for the set-up required in Section 6.3.6 (approximately 15 mm of the propagation of a beam about 100μm radius and pressure in the order of 10^1-10^2 mbar). This is beyond reasonable limits both for number of jobs submitted to slurm and the files used. The solver is then encapsulated into an MPI-scheduler, which executes all the TDSE's within a single parallelised job. The actual

implementation uses a 1D-solver introduced in the Section 7.5, which is implemented in the c-language [289, 290].

3. *Hankel transform*: This is the last step of the computation. As the current approach is the least expensive part of the computation, it can be comparable with post-processing. The actual implementation is done in Python [291, 292].[1]

The final result is then the XUV field in the far-field region. However, a valuable result is also intermediate outputs of CUPRAD. Most of the physics can be inferred from these profiles directly, which provides a short-cut over the TDSE computation.

10.2 Post-processing

The post-processing is mainly the visualisation of the data. Because they are stored in the HDF5-archives, it can be easily ported into Python [293], MATLAB® [294] or similar tools. We use mainly the two mentioned.

Complementary to these ”trivial” post-processing, we may consider also the use of the full-saddle points tabulated from (2.17) and implemented in Section 7.8 as a post-processing. It provides a table of the required source terms for the XUV only as functions of the actual intensity of the field: $d = d(I)$. This can be applied then only as ”masking” of the electric fields from CUPRAD. The study in Section 6.3 confirmed that it can provide a good insight of the physics without the need of large computational resources. The advantage is that these resources may be used in other way: to scan the large parametric space of a given task. These results provide a valuable initial point for possible detailed simulations with the full model.

---

[1] Beyond these standard references, we use many of packages that are contained in usual Python distributions.

10.3 Computational models roadmap

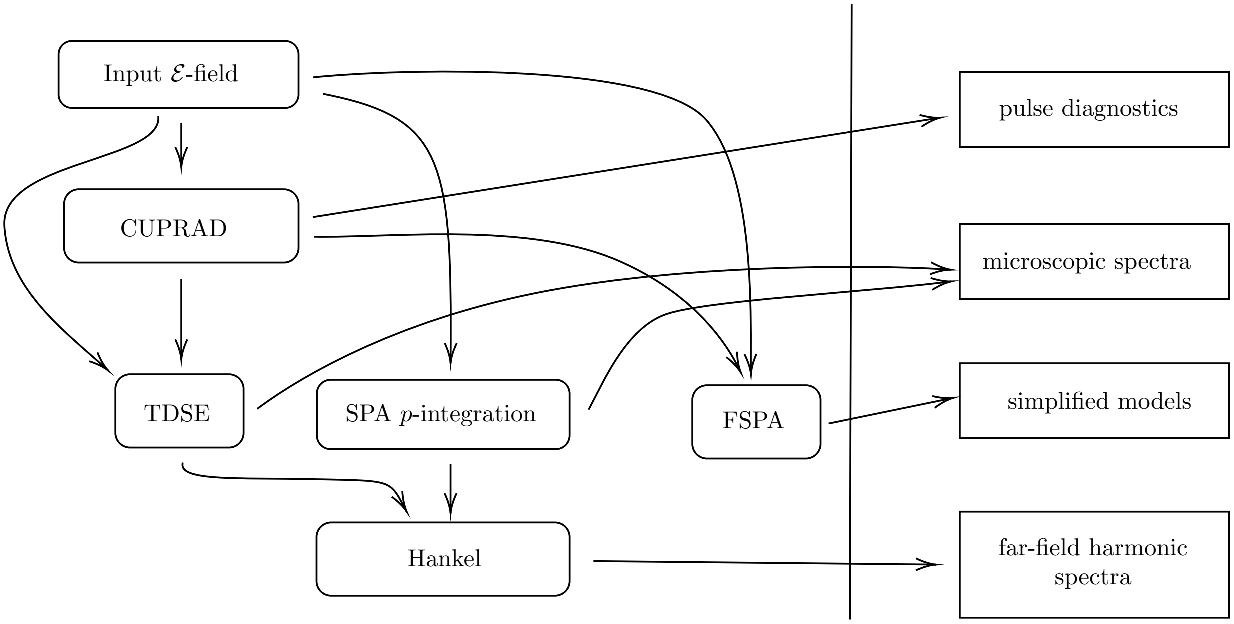

Fig. 10.1: Computational models roadmap: The left part of the schematic represents possible process chains initiated by the input electric field $\mathcal{E}$. The right part represents possible outputs.

The schematic of the operation of various modules of the multi -scale model is shown in Fig. 10.1:

- *Input $\mathcal{E}$-field*: The computation is started by the input electric field $\mathcal{E}$. It is generally a macroscopic field at the entry plane of the medium $\mathcal{E}(\rho, t)$. Another option is to perform only a microscopic study, the input is then only $\mathcal{E}(t)$ within the dipole approximation.
- *CUPRAD*: It computes the electric field in the whole medium $\mathcal{E}(\rho, z, t)$. This output may be input in the *TDSE* or *FSPA*, or this field may be directly diagnosed by the *pulse diagnostics*.
- *TDSE*: Its primary function is to transform an input field $\mathcal{E}(t)$ into the source term $\partial_t j$. Complementary, it also provides the profile of the degree of ionisation.
- *SFA p-integration*: The source term is computed by (2.16) in this module. It allows to work with two-colour arbitrary polarised pulses. This method is used in [126] to study polarisation gating. However, the current implementation relies on analytic models of the input field, the reason is that there are required quantities up to $\int \boldsymbol{A}\,\mathrm{d}t$, where $\boldsymbol{A}$ is the vector potential corresponding to $\boldsymbol{\mathcal{E}}$. This module is thus unlinked to the *CUPRAD* now.
- *FSPA*: This module allows to infer basic properties of harmonics by masking the intensity profile of the field. These sudies are, so far, limited to the regions where different semi-

classical trajectories (long and short in the plateau or the single trajectory in the cutoff) may be distinguished.

- *Hankel*: This module collects microscopic source terms and transforms them into far-field spatially resolved spectra.

The purpose of the model is to provide various physical quantities considered as outputs indicated in Fig. 10.1:

- *pulse diagnostics*: These diagnostics include the intensity profiles, ionisation maps or spectra of the driving field.
- *microscopic spectra*: The source terms, $\widehat{\partial_t j}$, at a given point of the medium.
- *simplified models*: This indicates models directly linked with the *FSPA*. It mainly provides a fast model of the phase of the generated field. We have proven that this approach is sufficient in the two geometries – the optics-free XUV focusing and pre-ionisation driven phase matching – studied in Sections 5.2 and 6.3, respectively.
- *far-field harmonic spectra*: This is one of the most important outputs because it gives a direct link with experiments.

10.4 Optimisation

We have reviewed the operation of the multi-scale model and its typical cost in the actual implementation is discussed in Appendix E. It shows possible ways to make the model more efficient both computationally and in its usage. There seem to be two significant bottlenecks at the instant. First, the computational cost may be probably reduced. The resolution needed at different regions is probably different. Using again Fig. 6.14 as a practical example, we ensured the convergence in the region with the fast changes of the field and fixed this grid. A coarser grid would be probably sufficient in less critical regions. The second point is related to the first one, there is needed a non-negligible effort to run the code and check the results manually.

Both of these points should be avoided by using adaptive steps and other internal metrics, which choose automatically computational parameters according to some heuristics and verify the convergence and other requirements. This task is non-trivial as it needs a) to define these metrics and implement them; b) the management of the computational resources, which dynamically allocate them.

Part IV

CONCLUSION & PERSPECTIVE

11. CONCLUSIONS

We have developed a comprehensive numerical model of the High-order harmonic generation in gaseous media in this thesis. Our model has been applied to two different generation schemes in Sections 5.2 and 6.3, which have been investigated in close collaboration with experimentalists and have brought novel ways to control HHG process. The first scheme allows for the control of the harmonic beams via optics-free mechanism: the wavefront is driven directly by the generation process in thin media[34, 35]. The second method provides the control of the phase-matching in a long medium by homogeneously pre-ionising the medium [72].

Aside the results directly synthesised with experiments, another important outcome the comprehensive study of the ionisation, Chapter 3, and the work on the development of the 3D-TDSE solver, Section 7.6. For the former, the summary of different perturbative approaches is complemented by a rigorous treatment based on the resolvent technique. This work is summarised in [111]. The development of the TDSE solver consists of the experiments with the Krylov subspace method and treatment of high-energy components from the large angular momenta in the solver, this work contributes to ongoing development of a 3D-solver that shall be deployed soon after the thesis.

These results demonstrated the use of the multi-scale model, which is the primary goal of this thesis. It may be then used to study other HHG schemes without significant changes. An example of recently introduced techniques is the generation in the so-called ”over-driven” regime [295, 60, 296], it is characterised by higher intensity than the usual HHG schemes. This intensity is linked to plasma generation leading to the re-shaping of the pulse. Another possibility goes towards the use of gradually changing phase along the phase induced by the chirp of the driving pulse [297].

The code also provides a basis for possible future development. One of the advantages of the discussed and not fully implemented 3D-TDSE is the reach of arbitrary polarised driving IR pulses. Complementary to this approach, it would be favourable to link the model with other methods to describe these fields based on SFA, e.g. [137, 298, 299, 300]. Extending also the dimensionality of CUPRAD, there is a sibling code beyond the cylindrical symmetry, see e.g. [197, 301, 302, 303]. The implementation of these extensions would help to cover broader range of phenomena in HHG. More details about possible follow-up topics are in Section 11.2.

11.1 Scientific significance of designed HHG schemes

Here we return to the details about the two HHG designs to control and optimise HHG. We have studied the XUV beams on thin targets leading to the optics-free focusing mechanism in the first study. The main contribution of the work consists in the recognition of the key principle of the formation of the harmonic beams in thin targets. The XUV wavefront is the sum of 1) the curvature inherited from the driving IR-beam, and 2) the intrinsic phase of the process as a function of the intensity. We have investigated a particular set-up in Section 5.2 and in [35], there were used a IR beam with the waist 85 μm and a thin neon jet. It is possible to focus the XUV beams down to approximately 5–20 μm. Another key feature is the spectral selectivity of the mechanism: each harmonic beam is focused differently. This is another key principle of the set-up, it allows to create a low-pass, high-pass or broadband filter in the given spectral region.

The second multi-scale study has discussed the HHG in long pre-ionised media [72]. The pre-ionisation has been proposed and verified as a mechanism to control the phase-matching. We have shown that the pre-ionisation acts as an independent tuning parameter in the studied range of the input intensities: the phase or intensity profile of the beam is not affected by the homogeneous pre-ionisation. Consequently, the shape of the generated XUV beams is also not affected. We have used the full multi-scale model in this work and we have shown the possible enhancement of the order of 8 for the 17th harmonic in krypton generated in the absorption-limited regime. We have also recognised that this regime puts the limit on the intensity in long media due to the defocusing. This intensity is in our case $I \sim 0.9 \times 10^{14}$ W/cm^2. Two important consequences of the defocusing limit are: 1) it imposes the generation regime and the investigated H17 in krypton is near the cutoff; 2) the driving beam itself cannot ionise sufficiently the generating medium. The pre-ionisation can overcome this problem as being an external mechanism. Finally, the low ionisation induced by the driving pulse itself can be taken as an advantage. The XUV signal can be optimised in long pulses avoiding transient ionisation to over-ionise the medium during the interaction.

In the microscopic study of the ionisation, the resolvent technique has allowed to find an unambiguous view on the energy distribution of the electron during the ionisation process. The ambiguity caused by the gauge freedom is resolved by the removal of the potential energy of the external field, which coincides with the velocity gauge. Furthermore, the spectrum is stable – i.e. unitarily equivalent to the field-free case – within the dipole approximation. The developed methodology of the energy measurement has been applied in three typical regimes of ionisation (perturbative singe-photon linear, perturbative multi-photon, and tunnelling). There is no conceptual obstacle to extend this methodology on more complex setups and benchmark usual practical methods based on perturbative approaches.

11.2 Perspective

The research carried out in this thesis has proven that our developed computer model can be used to provide both qualitative and quantitative analyses of the discussed configurations. We believe that our model can be further developed and various follow-up projects are possible. We sketch some of the ideas in the following points (sorted thematically, not by their impact or difficulty to implement):

- *3D-TDSE solver*: Unfortunately, the completion of the development of the 3D-TDSE solver has not fit within the timespan of the PhD project. However, significant effort was made, and the completion of the solver with the DVR method in the radial subspace still seems promising to be computationally affordable to link even with the multi-scale model.

  The completion of this model is not only a numerical exercise, but it is crucial for some effects in the XUV. Namely, 1D-TDSE cannot contain arbitrary polarised field. As generation schemes including polarisation states of the generating beam are one of widely studied approaches [304, 305, 306]. The polarisation represents the spin angular momentum of light, the generation becomes particularly interesting when combined with the orbital angular momentum of the light – helical beams – [307, 308, 309]. Another aspect is the geometry of the atom itself. One dimension contains parity of states, which include some of the symmetry properties. However, the full symmetry contained in, e.g., p-orbitals are correctly included only in 3 dimensions. Furthermore, 3D-potentials, (7.26b), contain more parameters to describe subtle structures as e.g. Rydberg atoms.

  The incorporation of the efficient 3D-TDSE is then one of the most prioritised follow-up projects.

- *Strong coupling*: The basic idea of the strong coupling is to use the TDSE solver to replace the sources from non-linear optics. Such an approach for coupling directly with Maxwell's equations was introduced by [88, 90, 89, 91]. In our case, it basically means to run both codes together. The unidirectional laser propagation calls the microscopic responses at every plane. This becomes challenging even from the viewpoint of computer science. It would require an efficient design of the microscopic solvers and implementing the coupling with parallelising the procedures.

- *FSPA library*: As a part of the complementary models, we modelled harmonics by the Full-Saddle-Point Approximation given by the set of non-linear equations (2.17). We have proved that this approximation provides a good insight and also a sufficient quantitative analysis in the problems we investigated. We solved these equations ad-hoc for our purposes. However, it can be easily generalised to tabulate the dipoles for different targets as a function of the frequency and intensity. The treatment of the transition between the plateau and the cutoff may be improved by [310]. At this stage, we can provide API to use the dipoles or linearised phases for various models of HHG.

- *Accessibility & open-sourcing of the code*: One of the issues of the actual multi-scale model is that it is not published and accessible. Because the availability of codes and the possibility to be used and verified by scientific community pairs with one of the pillars of science: reproducibility, the publication of the code is one of priorities as well.

  An inspiration can be nowadays well-established PIC-codes in plasma physics; as for example EPOCH [311], SMILEI [312], FLUKA [313, 314].[1]

- *User interface*: This project follows the previous point and it is even more challenging. The main goal of such a project is to create an interface for users to operate the multi-scale model. Another aspects of this part is the modularity and accessibility of the code to user-created sub-modules and other modifications.

  Complementary to the physical motivation, the processing linked with software-engineering should made the code more user-friendly.

- *Code optimisation & modularity*: This work confirmed the applicability of the multi-scale model, which is now fully operational. However, the performance of the code should be further optimised for wider applications. We can see this optimisation from two sides. First, the numerical techniques may be advanced as, for example, by using adaptive steps in the TDSE solvers. Generally, the goal is to implement internal convergence checks etc. to let the code itself to choose optimal numerical parameters of calculation. Second, the code should be done easily deployable on various architectures, so it can be used more on the user-base as defined in the *user interface*.

  Regarding the computational part, we can consider also more advanced methods as parallelisation. For that, we spent significant effort in the development of a general MPI-scheduler of the sub-tasks. Unfortunately, we did not succeed to scale and deploy it on the architecture available. We are able to use a simplified version of the 1D-TDSE code, where the runtime of the processes with a fixed discretisation may be considered as constant. However, more sophisticated approaches as the aforementioned adaptive step-size control would require improvement also in this overhead of the execution of the code. Finally, we consider to port the code using GPU's or employing techniques as machine learning.

  Another way to extend the model is to use different modules with an optimal cost-accuracy balance for a given problem. We have already mentioned the 3D-TDSE, which includes finer microscopic effects. A different way could be to use SFA-based modules for the microscopic

---

[1] See [104] for a comparison of various codes.

response. Regarding the model of the XUV, we could include near-field XUV and different strategies to calculate the XUV signal. It would be beneficiary to compare our work with other treatments, such as [94, 99, 91]

- *Porting the code for other media*: We study only atomic targets in this thesis. There is high interest in other targets since there are fundamental limits in the generation in gases. One comes from the recombination as the last step of the three-step model. The wavepacket spreads in the continuum during the second step, which reduces the efficiency of the recombination according to the atomic cross-section. It suggests to use larger targets. A direct extension is to use molecules or even macromolecules as C_{60} [315]. The situation may be dramatically different in solids [316] or nanostructures [317]. In atomic cases, the electron is in a "free-space" continuum during the second step and propagates almost as a free particle. This is not generally true any more for the different targets, the electron stays within the strong influence of the material even during the "propagation".[2] Although this sounds as a dramatic change of the setup at the first glance, we believe the code can be adapted to these cases with a reasonable effort as both kernels of CUPRAD and TDSE are shared with codes used to model analogical processes in solids [80, 318].

- *Electron dynamics near the ionisation threshold, non-linear optics*: Our invariant study of the ionisation is a) challenging exactly the coupling point of the microscopic and macroscopic physics, b) providing insight into the mechanisms of both ionisation and HHG. This can be further extended by including complementary spatial resolution of the problem. Another aspect to include is the dimensionality of the problem and investigate the dynamics in elliptical fields including the couplings of various orbitals differing in the magnetic quantum number m.

  The second direction of research is the approach to the non-linear optics from quantum mechanics. This approach is manifested theoretically in (2.11) and (4.2). However, the practical computation of the optical response of the medium in the IR-region is based on non-linear optics. The TDSE solver opens a way to compare these approaches on the microscopic scale as a building bricks of the proposed *strong coupling*.

  Finally, this may be used to systematically study the validity of the ionisation formulae providing rate equations and to extend the them into, e.g., multi-colour fields.

- *Optics-free harmonic beam control & off-axis contributions*: We have recognised the two effects defining the curvature of harmonic beams – the inherited phase from the IR-driver and the intrinsic phase induced by the intensity profile $\varphi_{\mathrm{XUV}} = -\alpha I_{\mathrm{IR}}$. We have limited our applications to Gaussian driving fields. A possible generalisation is to engineer the driving-field profile to achieve arbitrary shape of the generated field (see for instant [319] using annular

---

[2] The nature of the corresponding continuum in the spectrum is, e.g., a conduction band.

beams) .

- *Multi-scale studies*: We have studied the effect of the pre-ionisation in long media. This model should be ready to study different set-ups without large modifications. For example, the generation from the first region when high intensity is used corresponds to the over-driven regime [60, 296]. This process can be studied directly by our approach. Next, we have been interested mainly in the harmonic yield. The ab-initio model contains more subtle effects as the interplays of the microscopic and macroscopic effects. Another logical continuation is to connect the formation of XUV beams in thin targets and do a similar analysis for long media.
- *Off-axis contributions*: A direct simplification of the generation process is to consider only the on-axis contribution. Considering only the energetic perspective of a Gaussian beam, the energy distribution is $f_E(\rho) = \rho \exp\left(-2\rho^2/w^2\right)$. It means that the highest energetic contribution is at the $\rho = w/2$, i.e. the half of the waist of a beam. It suggests that the off-axis region may contribute significantly.[3]
- *Data management, tabulations*: The multi-scale model becomes non-trivial in both computational resources and the amount of the produced data. The data then may become valuable to store or we may need to keep many results to some larger analyses. The management of the data is then another space to improve. At the time of this work, the author participated on the development of an SQL database system, which is now used for listing experimental data. The design of this database reflected these considerations and its further development should be able to include the data from numerical simulations. The basic idea is to list characteristics of each simulation (inputs and some metrics of the outputs), which allows to run a fast database over these data.
- *Automatised optimisation procedures*: In the previous points, we touched several optimisation or controllability problems. During this work, we have seen that there is a large amount of parameters of the generation, for the instant, the arbitrary profiles of the radial intensity and phase from the *optics-free harmonic beam control*. To investigate such a space systematically requires some automatic optimisation technique. This consideration sounds exactly as a starting point of *machine-learning*, *genetic algorithms* and similar approaches. Our multi-scale model then becomes an underlying structure of such a model. The challenges of this approach is to design a proper optimisation function and handle the computations with a reasonable computation cost.

Basically these points provide a direct perspective for the continuation of the multi-scale model. These are quite straightforward: the actual topic of HHG are advanced generation schemes. All

---

[3] To be precise, the non-linear processes reduce the size at the non-linear response is induced by the local intensity. On the other hand, we observed the radial redistribution of the energy due to the defocusing (cf. Figs. 6.17 and 6.18).

these points address further development either to expand the capabilities of the multi-scale model or to investigate different physics related to HHG.

BIBLIOGRAPHY

[1] P. K. Maroju, C. Grazioli, M. D. Fraia, M. Moioli, D. Ertel, H. Ahmadi, O. Plekan, P. Finetti, E. Allaria, L. Giannessi, G. D. Ninno, C. Spezzani, G. Penco, S. Spampinati, A. Demidovich, M. B. Danailov, R. Borghes, G. Kourousias, C. E. S. D. Reis, F. Billé, A. A. Lutman, R. J. Squibb, R. Feifel, P. Carpeggiani, M. Reduzzi, T. Mazza, M. Meyer, S. Bengtsson, N. Ibrakovic, E. R. Simpson, J. Mauritsson, T. Csizmadia, M. Dumergue, S. Kühn, H. N. Gopalakrishna, D. You, K. Ueda, M. Labeye, J. E. Bækhøj, K. J. Schafer, E. V. Gryzlova, A. N. Grum-Grzhimailo, K. C. Prince, C. Callegari, and G. Sansone, "Attosecond pulse shaping using a seeded free-electron laser," *Nature*, vol. 578, pp. 386–391, Feb. 2020.

[2] P. H. Bucksbaum, "Sources and science of attosecond light," *Opt. Photon. News*, vol. 26, pp. 28–35, May 2015.

[3] M. Drescher, M. Hentschel, R. Kienberger, M. Uiberacker, V. Yakovlev, A. Scrinzi, T. Westerwalbesloh, U. Kleineberg, U. Heinzmann, and F. Krausz, "Time-resolved atomic inner-shell spectroscopy," *Nature*, vol. 419, pp. 803–807, Oct. 2002.

[4] F. Calegari, G. Sansone, S. Stagira, C. Vozzi, and M. Nisoli, "Advances in attosecond science," *Journal of Physics B: Atomic, Molecular and Optical Physics*, vol. 49, p. 062001, feb 2016.

[5] S. Haessler, M. Ouillé, J. Kaur, M. Bocoum, F. Böhle, D. Levy, L. Daniault, A. Vernier, J. Faure, and R. Lopez-Martens, "High-harmonic generation and correlated electron emission from relativistic plasma mirrors at 1 khz repetition rate," *Ultrafast Science*, vol. 2022, pp. 1–9, June 2022.

[6] T. Gaumnitz, A. Jain, Y. Pertot, M. Huppert, I. Jordan, F. Ardana-Lamas, and H. J. Wörner, "Streaking of 43-attosecond soft-x-ray pulses generated by a passively cep-stable mid-infrared driver," *Opt. Express*, vol. 25, pp. 27506–27518, Oct 2017.

[7] Y. He, L. He, P. Lan, B. Wang, L. Li, X. Zhu, W. Cao, and P. Lu, "Direct imaging of molecular rotation with high-order-harmonic generation," *Phys. Rev. A*, vol. 99, p. 053419, May 2019.

[8] M. Kübel, Z. Dube, A. Y. Naumov, D. M. Villeneuve, P. B. Corkum, and A. Staudte, "Spatiotemporal imaging of valence electron motion," *Nature Communications*, vol. 10, Mar. 2019.

[9] A. Autuori, D. Platzer, M. Lejman, G. Gallician, L. Maëder, A. Covolo, L. Bosse, M. Dalui, D. Bresteau, J.-F. Hergott, O. Tcherbakoff, H. J. B. Marroux, V. Loriot, F. Lépine, L. Poisson, R. Taïeb, J. Caillat, and P. Salières, "Anisotropic dynamics of two-photon ionization: An attosecond movie of photoemission," *Science Advances*, vol. 8, no. 12, p. eabl7594, 2022.

[10] J. Itatani, J. Levesque, D. Zeidler, H. Niikura, H. Pépin, J. C. Kieffer, P. B. Corkum, and D. M. Villeneuve, "Tomographic imaging of molecular orbitals," *Nature*, vol. 432, pp. 867–871, Dec. 2004.

[11] C. Zhai, L. He, P. Lan, X. Zhu, Y. Li, F. Wang, W. Shi, Q. Zhang, and P. Lu, "Coulomb-corrected molecular orbital tomography of nitrogen," *Scientific Reports*, vol. 6, Mar. 2016.

[12] I. Orfanos, I. Makos, I. Liontos, E. Skantzakis, B. Förg, D. Charalambidis, and P. Tzallas, "Attosecond pulse metrology," *APL Photonics*, vol. 4, no. 8, p. 080901, 2019.

[13] Y. Fu, K. Nishimura, R. Shao, A. Suda, K. Midorikawa, P. Lan, and E. J. Takahashi, "High efficiency ultrafast water-window harmonic generation for single-shot soft x-ray spectroscopy," *Communications Physics*, vol. 3, May 2020.

[14] E. J. Takahashi, P. Lan, O. D. Mücke, Y. Nabekawa, and K. Midorikawa, "Attosecond nonlinear optics using gigawatt-scale isolated attosecond pulses," *Nat. Commun.*, vol. 4, no. 1, p. 2691, 2013.

[15] M. Chini, K. Zhao, and Z. Chang, "The generation, characterization and applications of broadband isolated attosecond pulses," *Nature Photonics*, vol. 8, pp. 178–186, Feb. 2014.

[16] C. M. Heyl, H. Coudert-Alteirac, M. Miranda, M. Louisy, K. Kovacs, V. Tosa, E. Balogh, K. Varjú, A. L'Huillier, A. Couairon, and C. L. Arnold, "Scale-invariant nonlinear optics in gases," *Optica*, vol. 3, pp. 75–81, Jan 2016.

[17] R. Weissenbilder, S. Carlström, L. Rego, C. Guo, C. M. Heyl, P. Smorenburg, E. Constant, C. L. Arnold, and A. L'Huillier, "How to optimize high-order harmonic generation in gases," *Nature Reviews Physics*, vol. 4, pp. 713–722, Oct. 2022.

[18] R. W. Boyd, "Order-of-magnitude estimates of the nonlinear optical susceptibility," *Journal of Modern Optics*, vol. 46, pp. 367–378, Mar. 1999.

[19] A. McPherson, G. Gibson, H. Jara, U. Johann, T. S. Luk, I. A. McIntyre, K. Boyer, and C. K. Rhodes, "Studies of multiphoton production of vacuum-ultraviolet radiation in the rare gases," *J. Opt. Soc. Am. B*, vol. 4, pp. 595–601, Apr 1987.

[20] M. Ferray, A. L'Huillier, X. F. Li, L. A. Lompre, G. Mainfray, and C. Manus, "Multiple-harmonic conversion of 1064 nm radiation in rare gases," *Journal of Physics B: Atomic, Molecular and Optical Physics*, vol. 21, pp. L31–L35, feb 1988.

[21] X. F. Li, A. L'Huillier, M. Ferray, L. A. Lompré, and G. Mainfray, "Multiple-harmonic generation in rare gases at high laser intensity," *Phys. Rev. A*, vol. 39, pp. 5751–5761, Jun 1989.

[22] M. Y. Kuchiev, "Atomic antenna," *Soviet Journal of Experimental and Theoretical Physics Letters*, vol. 45, p. 404, Apr. 1987.

[23] P. B. Corkum, "Plasma perspective on strong field multiphoton ionization," *Phys. Rev. Lett.*, vol. 71, pp. 1994–1997, Sep 1993.

[24] K. J. Schafer, B. Yang, L. F. DiMauro, and K. C. Kulander, "Above threshold ionization beyond the high harmonic cutoff," *Phys. Rev. Lett.*, vol. 70, pp. 1599–1602, Mar 1993.

[25] M. Lewenstein, P. Balcou, M. Y. Ivanov, A. L'Huillier, and P. B. Corkum, "Theory of high-harmonic generation by low-frequency laser fields," *Phys. Rev. A*, vol. 49, pp. 2117–2132, Mar 1994.

[26] P. M. Paul, E. S. Toma, P. Breger, G. Mullot, F. Augé, P. Balcou, H. G. Muller, and P. Agostini, "Observation of a train of attosecond pulses from high harmonic generation," *Science*, vol. 292, no. 5522, pp. 1689–1692, 2001.

[27] E. Brunetti, R. Issac, and D. A. Jaroszynski, "Quantum path contribution to high-order harmonic spectra," *Phys. Rev. A*, vol. 77, p. 023422, Feb 2008.

[28] J. Jiang, P. Wei, Z. Zeng, J. Miao, Y. Zheng, X. Ge, C. Li, R. Li, and Z. Xu, "Spatially and spectrally resolved quantum-path tracing in high-order harmonic generation," *Opt. Express*, vol. 22, pp. 15975–15981, Jun 2014.

[29] F. Schapper, M. Holler, T. Auguste, A. Zaïr, M. Weger, P. Salières, L. Gallmann, and U. Keller, "Spatial fingerprint of quantum path interferences in high order harmonic generation," *Opt. Express*, vol. 18, pp. 2987–2994, Feb 2010.

[30] T. Auguste, P. Salières, A. S. Wyatt, A. Monmayrant, I. A. Walmsley, E. Cormier, A. Zaïr, M. Holler, A. Guandalini, F. Schapper, J. Biegert, L. Gallmann, and U. Keller, "Theoretical and experimental analysis of quantum path interferences in high-order harmonic generation," *Phys. Rev. A*, vol. 80, p. 033817, Sep 2009.

[31] A. Zaïr, M. Holler, A. Guandalini, F. Schapper, J. Biegert, L. Gallmann, U. Keller, A. S. Wyatt, A. Monmayrant, I. A. Walmsley, E. Cormier, T. Auguste, J. P. Caumes, and P. Salières, "Quantum path interferences in high-order harmonic generation," *Phys. Rev. Lett.*, vol. 100, p. 143902, Apr 2008.

[32] R. Feynman, A. Hibbs, and D. Styer, *Quantum Mechanics and Path Integrals.* Dover Books on Physics, Dover Publications, 2010.

[33] F. Catoire, A. Ferré, O. Hort, A. Dubrouil, L. Quintard, D. Descamps, S. Petit, F. Burgy, E. Mével, Y. Mairesse, and E. Constant, "Complex structure of spatially resolved high-order-harmonic spectra," *Phys. Rev. A*, vol. 94, p. 063401, Dec 2016.

[34] L. Quintard, V. Strelkov, J. Vabek, O. Hort, A. Dubrouil, D. Descamps, F. Burgy, C. Péjot, E. Mével, F. Catoire, and E. Constant, "Optics-less focusing of xuv high-order harmonics," *Science Advances*, vol. 5, no. 4, 2019.

[35] K. Veyrinas, J. Vábek, C. Valentin, D. Descamps, C. Péjot, F. Burgy, E. Constant, E. Mével, and F. Catoire, "Spectral filtering of high-order harmonics via optics-free focusing," *Opt. Express*, vol. 29, pp. 29813–29827, Sep 2021.

[36] R. W. Boyd, *Nonlinear Optics, Third Edition.* Academic Press, 3rd ed., 2008.

[37] C. Delfin, C. Altucci, F. D. Filippo, C. de Lisio, M. B. Gaarde, A. L'Huillier, L. Roos, and C.-G. Wahlström, "Influence of the medium length on high-order harmonic generation," *Journal of Physics B: Atomic, Molecular and Optical Physics*, vol. 32, pp. 5397–5409, nov 1999.

[38] E. Constant, D. Garzella, P. Breger, E. Mével, C. Dorrer, C. Le Blanc, F. Salin, and P. Agostini, "Optimizing high harmonic generation in absorbing gases: Model and experiment," *Phys. Rev. Lett.*, vol. 82, pp. 1668–1671, Feb 1999.

[39] J. Schötz, B. Förg, W. Schweinberger, I. Liontos, H. A. Masood, A. M. Kamal, C. Jakubeit, N. G. Kling, T. Paasch-Colberg, S. Biswas, M. Högner, I. Pupeza, M. Alharbi, A. M. Azzeer, and M. F. Kling, "Phase-matching for generation of isolated attosecond xuv and soft-x-ray pulses with few-cycle drivers," *Phys. Rev. X*, vol. 10, p. 041011, Oct 2020.

[40] G. Lerner, T. Diskin, O. Neufeld, O. Kfir, and O. Cohen, “Selective suppression of high-order harmonics within phase-matched spectral regions,” *Opt. Lett.*, vol. 42, pp. 1349–1352, Apr 2017.

[41] P. L. Shkolnikov, A. Lago, and A. E. Kaplan, “Optimal quasi-phase-matching for high-order harmonic generation in gases and plasma,” *Phys. Rev. A*, vol. 50, pp. R4461–R4464, Dec 1994.

[42] P. Balcou, P. Sali‘eres, A. L’Huillier, and M. Lewenstein, “Generalized phase-matching conditions for high harmonics: The role of field-gradient forces,” *Phys. Rev. A*, vol. 55, pp. 3204–3210, Apr 1997.

[43] P. Salières, A. L’Huillier, P. Antoine, and M. Lewenstein, “Study of the spatial and temporal coherence of high-order harmonics,” vol. 41 of *Advances In Atomic, Molecular, and Optical Physics*, pp. 83–142, Academic Press, 1999.

[44] P. Balcou, A. S. Dederichs, M. B. Gaarde, and A. L'Huillier, “Quantum-path analysis and phase matching of high-order harmonic generation and high-order frequency mixing processes in strong laser fields,” *Journal of Physics B: Atomic, Molecular and Optical Physics*, vol. 32, pp. 2973–2989, jan 1999.

[45] M. Geissler, G. Tempea, and T. Brabec, “Phase-matched high-order harmonic generation in the nonadiabatic limit,” *Phys. Rev. A*, vol. 62, p. 033817, Aug 2000.

[46] G. Tempea, M. Geissler, M. Schnürer, and T. Brabec, “Self-phase-matched high harmonic generation,” *Phys. Rev. Lett.*, vol. 84, pp. 4329–4332, May 2000.

[47] P. Balcou, R. Haroutunian, S. Sebban, G. Grillon, A. Rousse, G. Mullot, J.-P. Chambaret, G. Rey, A. Antonetti, D. Hulin, L. Roos, D. Descamps, M. B. Gaarde, A. L’Huillier, E. Constant, E. Mevel, D. von der Linde, A. Orisch, A. Tarasevitch, U. Teubner, D. Klöpfel, and W. Theobald, “High-order-harmonic generation: towards laser-induced phase-matching control and relativistic effects,” *Appl. Phys. B*, vol. 74, pp. 509–515, Apr. 2002.

[48] S. Kazamias, D. Douillet, F. Weihe, C. Valentin, A. Rousse, S. Sebban, G. Grillon, F. Augé, D. Hulin, and P. Balcou, “Global optimization of high harmonic generation,” *Phys. Rev. Lett.*, vol. 90, p. 193901, May 2003.

[49] M. B. Gaarde, J. L. Tate, and K. J. Schafer, “Macroscopic aspects of attosecond pulse generation,” *Journal of Physics B: Atomic, Molecular and Optical Physics*, vol. 41, p. 132001, jun 2008.

[50] T. Popmintchev, M.-C. Chen, A. Bahabad, M. Gerrity, P. Sidorenko, O. Cohen, I. P. Christov, M. M. Murnane, and H. C. Kapteyn, “Phase matching of high harmonic generation in the soft and hard x-ray regions of the spectrum,” *Proceedings of the National Academy of Sciences*, vol. 106, no. 26, pp. 10516–10521, 2009.

[51] A. Bouhal, P. Salières, P. Breger, P. Agostini, G. Hamoniaux, A. Mysyrowicz, A. Antonetti, R. Constantinescu, and H. G. Muller, “Temporal dependence of high-order harmonics in the presence of strong ionization,” *Phys. Rev. A*, vol. 58, pp. 389–399, Jul 1998.

[52] A. S. Sandhu, E. Gagnon, A. Paul, I. Thomann, A. Lytle, T. Keep, M. M. Murnane, H. C. Kapteyn, and I. P. Christov, “Generation of sub-optical-cycle, carrier-envelope-phase—insensitive, extreme-uv pulses via nonlinear stabilization in a waveguide,” *Phys. Rev. A*, vol. 74, p. 061803, Dec 2006.

[53] T. Pfeifer, A. Jullien, M. J. Abel, P. M. Nagel, L. Gallmann, D. M. Neumark, and S. R. Leone, “Generating coherent broadband continuum soft-x-ray radiation by attosecond ionization gating,” *Opt. Express*, vol. 15, pp. 17120–17128, Dec 2007.

[54] A. Jullien, T. Pfeifer, M. J. Abel, P. M. Nagel, M. J. Bell, D. M. Neumark, and S. R. Leone, “Ionization phase-match gating for wavelength-tunable isolated attosecond pulse generation,” *Appl. Phys. B*, vol. 93, pp. 433–442, Nov. 2008.

[55] M. J. Abel, T. Pfeifer, P. M. Nagel, W. Boutu, M. J. Bell, C. P. Steiner, D. M. Neumark, and S. R. Leone, “Isolated attosecond pulses from ionization gating of high-harmonic emission,” *Chemical Physics*, vol. 366, no. 1, pp. 9–14, 2009. Attosecond Molecular Dynamics.

[56] C. Hernández-García, T. Popmintchev, M. M. Murnane, H. C. Kapteyn, L. Plaja, A. Becker, and A. Jaron-Becker, “Isolated broadband attosecond pulse generation with near- and mid-infrared driver pulses via time-gated phase matching,” *Opt. Express*, vol. 25, p. 11855, May 2017.

[57] V. S. Yakovlev, M. Ivanov, and F. Krausz, “Enhanced phase-matching for generation of soft x-ray harmonics and attosecond pulses in atomic gases,” *Opt. Express*, vol. 15, pp. 15351–15364, Nov 2007.

[58] T. Popmintchev, M.-C. Chen, O. Cohen, M. E. Grisham, J. J. Rocca, M. M. Murnane, and H. C. Kapteyn, “Extended phase matching of high harmonics driven by mid-infrared light,” *Opt. Lett.*, vol. 33, pp. 2128–2130, Sep 2008.

[59] C. Vozzi, M. Negro, F. Calegari, S. Stagira, K. Kovács, and V. Tosa, "Phase-matching effects in the generation of high-energy photons by mid-infrared few-cycle laser pulses," *New Journal of Physics*, vol. 13, p. 073003, jul 2011.

[60] A. S. Johnson, D. R. Austin, D. A. Wood, C. Brahms, A. Gregory, K. B. Holzner, S. Jarosch, E. W. Larsen, S. Parker, C. S. Strüber, P. Ye, J. W. G. Tisch, and J. P. Marangos, "High-flux soft x-ray harmonic generation from ionization-shaped few-cycle laser pulses," *Science Advances*, vol. 4, no. 5, p. eaar3761, 2018.

[61] L. Roos, E. Constant, E. Mével, P. Balcou, D. Descamps, M. B. Gaarde, A. Valette, R. Haroutunian, and A. L'Huillier, "Controlling phase matching of high-order harmonic generation by manipulating the fundamental field," *Phys. Rev. A*, vol. 60, pp. 5010–5018, Dec 1999.

[62] E. Constant, A. Dubrouil, O. Hort, S. Petit, D. Descamps, and E. Mével, "Spatial shaping of intense femtosecond beams for the generation of high-energy attosecond pulses," *Journal of Physics B: Atomic, Molecular and Optical Physics*, vol. 45, p. 074018, mar 2012.

[63] J. L. Ellis, K. M. Dorney, C. G. Durfee, C. Hernández-García, F. Dollar, C. A. Mancuso, T. Fan, D. Zusin, C. Gentry, P. Grychtol, H. C. Kapteyn, M. M. Murnane, and D. D. Hickstein, "Phase matching of noncollinear sum and difference frequency high harmonic generation above and below the critical ionization level," *Opt. Express*, vol. 25, pp. 10126–10144, May 2017.

[64] Y. Tamaki, J. Itatani, Y. Nagata, M. Obara, and K. Midorikawa, "Highly efficient, phase-matched high-harmonic generation by a self-guided laser beam," *Phys. Rev. Lett.*, vol. 82, pp. 1422–1425, Feb 1999.

[65] T. Popmintchev, M.-C. Chen, D. Popmintchev, P. Arpin, S. Brown, S. Ališauskas, G. Andriukaitis, T. Balčiunas, O. D. Mücke, A. Pugzlys, A. Baltuška, B. Shim, S. E. Schrauth, A. Gaeta, C. Hernández-García, L. Plaja, A. Becker, A. Jaron-Becker, M. M. Murnane, and H. C. Kapteyn, "Bright coherent ultrahigh harmonics in the kev x-ray regime from mid-infrared femtosecond lasers," *Science*, vol. 336, no. 6086, pp. 1287–1291, 2012.

[66] K. Cassou, S. Daboussi, O. Hort, O. Guilbaud, D. Descamps, S. Petit, E. Mével, E. Constant, and S. Kazamias, "Enhanced high harmonic generation driven by high-intensity laser in argon gas-filled hollow core waveguide," *Opt. Lett.*, vol. 39, pp. 3770–3773, Jul 2014.

[67] D. M. Gaudiosi, B. Reagan, T. Popmintchev, M. Grisham, M. Berrill, O. Cohen, B. C. Walker,

M. M. Murnane, H. C. Kapteyn, and J. J. Rocca, “High-order harmonic generation from ions in a capillary discharge,” *Phys. Rev. Lett.*, vol. 96, p. 203001, May 2006.

[68] B. A. Reagan, T. Popmintchev, M. E. Grisham, D. M. Gaudiosi, M. Berrill, O. Cohen, B. C. Walker, M. M. Murnane, J. J. Rocca, and H. C. Kapteyn, “Enhanced high-order harmonic generation from xe, kr, and ar in a capillary discharge,” *Phys. Rev. A*, vol. 76, p. 013816, Jul 2007.

[69] I. Hadas and A. Bahabad, “Periodic density modulation for quasi-phase-matching of optical frequency conversion is inefficient under shallow focusing and constant ambient pressure,” *Opt. Lett.*, vol. 41, pp. 4000–4003, Sep 2016.

[70] V. V. Strelkov and R. A. Ganeev, “Quasi-phase-matching of high-order harmonics in plasma plumes: theory and experiment,” *Opt. Express*, vol. 25, pp. 21068–21083, Sep 2017.

[71] H.-W. Sun, P.-C. Huang, Y.-H. Tzeng, J.-T. Huang, C. D. Lin, C. Jin, and M.-C. Chen, “Extended phase matching of high harmonic generation by plasma-induced defocusing,” *Optica*, vol. 4, pp. 976–981, Aug 2017.

[72] O. Finke, J. Vábek, M. Nevrkla, N. Bobrova, O. Hort, M. Jurkovič, M. Albrecht, A. Jančárek, F. Catoire, S. Skupin, and J. Nejdl, “Phase-matched high-order harmonic generation in pre-ionized noble gases,” *Scientific Reports*, vol. 12, May 2022.

[73] A. Becker, N. Aközbek, K. Vijayalakshmi, E. Oral, C. Bowden, and S. Chin, “Intensity clamping and re-focusing of intense femtosecond laser pulses in nitrogen molecular gas,” *Applied Physics B*, vol. 73, pp. 287–290, Sept. 2001.

[74] E. Takahashi, V. Tosa, Y. Nabekawa, and K. Midorikawa, “Experimental and theoretical analyses of a correlation between pump-pulse propagation and harmonic yield in a long-interaction medium,” *Phys. Rev. A*, vol. 68, p. 023808, Aug 2003.

[75] D. E. Rivas, B. Major, M. Weidman, W. Helml, G. Marcus, R. Kienberger, D. Charalambidis, P. Tzallas, E. Balogh, K. Kovács, V. Tosa, B. Bergues, K. Varjú, and L. Veisz, “Propagation-enhanced generation of intense high-harmonic continua in the 100-ev spectral region,” *Optica*, vol. 5, pp. 1283–1289, Oct 2018.

[76] P. D. Maker, R. W. Terhune, M. Nisenoff, and C. M. Savage, “Effects of dispersion and focusing on the production of optical harmonics,” *Phys. Rev. Lett.*, vol. 8, pp. 21–22, Jan 1962.

[77] C. M. Heyl, J. Güdde, U. Höfer, and A. L'Huillier, "Spectrally resolved maker fringes in high-order harmonic generation," *Phys. Rev. Lett.*, vol. 107, p. 033903, Jul 2011.

[78] S. Rae, "Ionization-induced defocusing of intense laser pulses in high-pressure gases," *Optics Communications*, vol. 97, no. 1, pp. 25 – 28, 1993.

[79] C. Sulem and P. Sulem, *The Nonlinear Schrödinger Equation: Self-Focusing and Wave Collapse*. Applied Mathematical Sciences, Springer New York, 2007.

[80] L. Bergé, S. Skupin, R. Nuter, J. Kasparian, and J.-P. Wolf, "Ultrashort filaments of light in weakly ionized, optically transparent media," *Reports on Progress in Physics*, vol. 70, no. 10, p. 1633, 2007.

[81] J. Crank and P. Nicolson, "A practical method for numerical evaluation of solutions of partial differential equations of the heat-conduction type," *Mathematical Proceedings of the Cambridge Philosophical Society*, vol. 43, no. 1, p. 50–67, 1947.

[82] O. Smirnova and M. Ivanov, *Multielectron High Harmonic Generation: Simple Man on a Complex Plane*, ch. 7, pp. 201–256. John Wiley & Sons, Ltd, 2014.

[83] N. Lewis, "Trinity by the numbers: The computing effort that made trinity possible," *Nuclear Technology*, vol. 207, no. sup1, pp. S176–S189, 2021.

[84] M. W. Evans and F. H. Harlow, "The particle-in-cell method for hydrodynamic calculations," 6 1957.

[85] P. L. Kelley, "Self-focusing of optical beams," *Phys. Rev. Lett.*, vol. 15, pp. 1005–1008, Dec 1965.

[86] E. A. McCullough and R. E. Wyatt, "Quantum dynamics of the collinear (h, h2) reaction," *The Journal of Chemical Physics*, vol. 51, no. 3, pp. 1253–1254, 1969.

[87] H. Gharibnejad, B. Schneider, M. Leadingham, and H. Schmale, "A comparison of numerical approaches to the solution of the time-dependent schrödinger equation in one dimension," *Computer Physics Communications*, vol. 252, p. 106808, 2020.

[88] E. Lorin, S. Chelkowski, and A. Bandrauk, "A numerical maxwell–schrödinger model for intense laser–matter interaction and propagation," *Computer Physics Communications*, vol. 177, no. 12, pp. 908–932, 2007.

[89] E. Lorin, S. Chelkowski, E. Zaoui, and A. Bandrauk, “Maxwell-schrödinger–plasma (masp) model for laser–molecule interactions: Towards an understanding of filamentation with intense ultrashort pulses,” *Physica D: Nonlinear Phenomena*, vol. 241, no. 12, pp. 1059–1071, 2012.

[90] E. Lorin, S. Chelkowski, and A. D. Bandrauk, “The wasp model: A micro-macro system of wave-schrödinger-plasma equations for filamentation,” *Communications in Computational Physics*, vol. 9, no. 2, p. 406–440, 2011.

[91] E. Lorin, M. Lytova, A. Memarian, and A. D. Bandrauk, “Development of nonperturbative nonlinear optics models including effects of high order nonlinearities and of free electron plasma: Maxwell-schrödinger equations coupled with evolution equations for polarization effects, and the SFA-like nonlinear optics model,” *Journal of Physics A: Mathematical and Theoretical*, vol. 48, p. 105201, feb 2015.

[92] E. Priori, G. Cerullo, M. Nisoli, S. Stagira, S. De Silvestri, P. Villoresi, L. Poletto, P. Ceccherini, C. Altucci, R. Bruzzese, and C. de Lisio, “Nonadiabatic three-dimensional model of high-order harmonic generation in the few-optical-cycle regime,” *Phys. Rev. A*, vol. 61, p. 063801, May 2000.

[93] N. H. Shon, A. Suda, and K. Midorikawa, “Generation and propagation of high-order harmonics in high-pressure gases,” *Phys. Rev. A*, vol. 62, p. 023801, Jul 2000.

[94] V. Tosa, E. Takahashi, Y. Nabekawa, and K. Midorikawa, “Generation of high-order harmonics in a self-guided beam,” *Phys. Rev. A*, vol. 67, p. 063817, Jun 2003.

[95] V. Tosa, K. T. Kim, and C. H. Nam, “Macroscopic generation of attosecond-pulse trains in strongly ionized media,” *Phys. Rev. A*, vol. 79, p. 043828, Apr 2009.

[96] V. Tosa, K. Kovács, B. Major, E. Balogh, and K. Varjú, “Propagation effects in highly ionised gas media,” *Quantum Electronics*, vol. 46, pp. 321–326, apr 2016.

[97] C. Jin, *Theory of Nonlinear Propagation of High Harmonics Generated in a Gaseous Medium.* Springer Verlag, 2013.

[98] C. Lin, A. Le, C. Jin, and H. Wei, *Attosecond and Strong-Field Physics: Principles and Applications.* Cambridge University Press, 2018.

[99] C. Hernández-García, J. A. Pérez-Hernández, J. Ramos, E. C. Jarque, L. Roso, and L. Plaja, “High-order harmonic propagation in gases within the discrete dipole approximation,” *Phys. Rev. A*, vol. 82, p. 033432, Sep 2010.

[100] J. A. Pérez-Hernández, L. Roso, and L. Plaja, "Harmonic generation beyond the strong-field approximation: the physics behind the short-wave-infrared scaling laws," *Opt. Express*, vol. 17, pp. 9891–9903, Jun 2009.

[101] E. M. Purcell and C. R. Pennypacker, "Scattering and absorption of light by nonspherical dielectric grains," *The Astrophysical Journal*, vol. 186, pp. 705–714, 1973.

[102] M. Yurkin and A. Hoekstra, "The discrete dipole approximation: An overview and recent developments," *Journal of Quantitative Spectroscopy and Radiative Transfer*, vol. 106, no. 1, pp. 558–589, 2007. IX Conference on Electromagnetic and Light Scattering by Non-Spherical Particles.

[103] N. Metropolis, "The beginning of the monte carlo method," *Los Alamos Science*, vol. 15, pp. 125–130, 1987.

[104] J. R. Smith, C. Orban, N. Rahman, B. McHugh, R. Oropeza, and E. A. Chowdhury, "A particle-in-cell code comparison for ion acceleration: Epoch, lsp, and warpx," *Physics of Plasmas*, vol. 28, no. 7, p. 074505, 2021.

[105] T. Frankel, *The Geometry of Physics: An Introduction.* Cambridge University Press, 2004.

[106] J. R. Oppenheimer, "Three notes on the quantum theory of aperiodic effects," *Phys. Rev.*, vol. 31, pp. 66–81, Jan 1928.

[107] B. M. Smirnov and M. I. Chibisov, "The Breaking Up of Atomic Particles by an Electric Field and by Electron Collisions," *Soviet Journal of Experimental and Theoretical Physics*, vol. 22, p. 585, Mar. 1966.

[108] I. W. Herbst, "Dilation analyticity in constant electric field," *Communications in Mathematical Physics*, vol. 64, pp. 279–298, Oct 1979.

[109] A. I. Nikishov and V. I. Ritus, "Ionization of Systems Bound by Short-range Forces by the Field of an Electromagnetic Wave," *Soviet Journal of Experimental and Theoretical Physics*, vol. 23, p. 168, July 1966.

[110] A. M. Perelomov, V. S. Popov, and M. V. Terent'ev, "Ionization of Atoms in an Alternating Electric Field," *Soviet Journal of Experimental and Theoretical Physics*, vol. 23, p. 924, Nov. 1966.

[111] J. Vábek, H. Bachau, and F. Catoire, "Ionization dynamics and gauge invariance," *Phys. Rev. A*, vol. 106, p. 053115, Nov 2022.

[112] K. Schafer, “The energy analysis of time-dependent numerical wave functions,” *Computer Physics Communications*, vol. 63, no. 1, pp. 427–434, 1991.

[113] F. Catoire and H. Bachau, “Extraction of the absolute value of the photoelectron spectrum probability density by means of the resolvent technique,” *Phys. Rev. A*, vol. 85, p. 023422, Feb 2012.

[114] F. Catoire, R. E. F. Silva, P. Rivière, H. Bachau, and F. Martín, “Molecular resolvent-operator method: Electronic and nuclear dynamics in strong-field ionization,” *Phys. Rev. A*, vol. 89, p. 023415, Feb 2014.

[115] K. Klünder, J. M. Dahlström, M. Gisselbrecht, T. Fordell, M. Swoboda, D. Guénot, P. Johnsson, J. Caillat, J. Mauritsson, A. Maquet, R. Taïeb, and A. L’Huillier, “Probing single-photon ionization on the attosecond time scale,” *Phys. Rev. Lett.*, vol. 106, p. 143002, Apr 2011.

[116] G. Mainfray and G. Manus, “Multiphoton ionization of atoms,” *Reports on Progress in Physics*, vol. 54, pp. 1333–1372, oct 1991.

[117] C. Kern, M. Zürch, and C. Spielmann, “Limitations of extreme nonlinear ultrafast nanophotonics,” *Nanophotonics*, vol. 4, pp. 303–323, Jan. 2015.

[118] J. D. Jackson, *Classical electrodynamics.* New York, NY: Wiley, 3rd ed. ed., 1999.

[119] L. Feng, J. Mccain, and Y. Qiao, “Half-cycle waveform control for producing a broad and intense harmonic spectral continuum and an isolated attosecond pulse,” *Laser Physics*, vol. 31, p. 055301, apr 2021.

[120] R. E. F. Silva, P. Rivière, F. Morales, O. Smirnova, M. Ivanov, and F. Martín, “Even harmonic generation in isotropic media of dissociating homonuclear molecules,” *Scientific Reports*, vol. 6, Sept. 2016.

[121] P. Béjot, E. Cormier, E. Hertz, B. Lavorel, J. Kasparian, J.-P. Wolf, and O. Faucher, “High-field quantum calculation reveals time-dependent negative kerr contribution,” *Phys. Rev. Lett.*, vol. 110, p. 043902, Jan 2013.

[122] J. Sakurai and J. Napolitano, *Modern Quantum Mechanics.* —, Addison-Wesley, 2011.

[123] C. Cohen-Tannoudji, B. Diu, and F. Laloë, *Quantum mechanics.* Quantum Mechanics, Wiley, 1977.

[124] L. Ballentine, *Quantum Mechanics: A Modern Development.* World Scientific, 1998.

[125] G. Russakoff, "A derivation of the macroscopic maxwell equations," *American Journal of Physics*, vol. 38, no. 10, pp. 1188–1195, 1970.

[126] J. Vábek, "High harmonic generation by an elliptically polarized ir-radiation on atomic and molecular targets." `http://physics.fjfi.cvut.cz/publications/mf/2017/dp_mf_17_vabek.pdf`, June 2017.

[127] Wikipedia, "Van der Waals constants (data page) — Wikipedia, the free encyclopedia." `http://en.wikipedia.org/w/index.php?title=Van%20der%20Waals%20constants%20(data%20page)&oldid=1009232216`, 2022. [Online; accessed 23-June-2022].

[128] M. Klaiber, K. Z. Hatsagortsyan, C. Müller, and C. H. Keitel, "Coherent hard x rays from attosecond pulse train-assisted harmonic generation," *Opt. Lett.*, vol. 33, pp. 411–413, Feb 2008.

[129] C. Ullrich, *Time-Dependent Density-Functional Theory: Concepts and Applications.* Oxford Graduate Texts, OUP Oxford, 2011.

[130] J. Feist, "Two-photon double ionization of helium," 2009.

[131] M. K. Lee, P. Hoerner, W. Li, and H. B. Schlegel, "Effect of spin–orbit coupling on strong field ionization simulated with time-dependent configuration interaction," *The Journal of Chemical Physics*, vol. 153, no. 24, p. 244109, 2020.

[132] M. Kircher, F. Trinter, S. Grundmann, I. Vela-Perez, S. Brennecke, N. Eicke, J. Rist, S. Eckart, S. Houamer, O. Chuluunbaatar, Y. V. Popov, I. P. Volobuev, K. Bagschik, M. N. Piancastelli, M. Lein, T. Jahnke, M. S. Schöffler, and R. Dörner, "Kinematically complete experimental study of compton scattering at helium atoms near the threshold," *Nature Physics*, vol. 16, pp. 756–760, Apr. 2020.

[133] S. Grundmann, D. Trabert, K. Fehre, N. Strenger, A. Pier, L. Kaiser, M. Kircher, M. Weller, S. Eckart, L. P. H. Schmidt, F. Trinter, T. Jahnke, M. S. Schöffler, and R. Dörner, "Zeptosecond birth time delay in molecular photoionization," *Science*, vol. 370, no. 6514, pp. 339–341, 2020.

[134] A. Sopena, A. Palacios, F. Catoire, H. Bachau, and F. Martín, "Angle-dependent interferences in electron emission accompanying stimulated compton scattering from molecules," *Communications Physics*, vol. 4, Nov. 2021.

[135] A. Gorlach, O. Neufeld, N. Rivera, O. Cohen, and I. Kaminer, "The quantum-optical nature of high harmonic generation," *Nature Communications*, vol. 11, Sept. 2020.

[136] T. Auguste, F. Catoire, P. Agostini, L. F. DiMauro, C. C. Chirila, V. S. Yakovlev, and P. Salières, “Driving-frequency scaling of high-harmonic quantum paths,” *New Journal of Physics*, vol. 14, no. 10, p. 103014, 2012.

[137] E. Pisanty Alatorre, *Electron dynamics in complex time and complex space.* PhD thesis, 2016.

[138] M. Lewenstein, P. Salières, and A. L’Huillier, “Phase of the atomic polarization in high-order harmonic generation,” *Phys. Rev. A*, vol. 52, pp. 4747–4754, Dec 1995.

[139] L. Rego, J. S. Román, L. Plaja, A. Picón, and C. Hernández-García, “Ultrashort extreme ultraviolet vortices,” in *Vortex Dynamics and Optical Vortices* (H. P. de Tejada, ed.), ch. 9, Rijeka: IntechOpen, 2017.

[140] M. B. Gaarde, F. Salin, E. Constant, P. Balcou, K. J. Schafer, K. C. Kulander, and A. L’Huillier, “Spatiotemporal separation of high harmonic radiation into two quantum path components,” *Phys. Rev. A*, vol. 59, pp. 1367–1373, Feb 1999.

[141] M. D. Perry, O. L. Landen, A. Szöke, and E. M. Campbell, “Multiphoton ionization of the noble gases by an intense 10^{14}-w/cm^2 dye laser,” *Phys. Rev. A*, vol. 37, pp. 747–760, Feb 1988.

[142] M. D. Perry, A. Szoke, O. L. Landen, and E. M. Campbell, “Nonresonant multiphoton ionization of noble gases: Theory and experiment,” *Phys. Rev. Lett.*, vol. 60, pp. 1270–1273, Mar 1988.

[143] S.-F. Zhao, A.-T. Le, C. Jin, X. Wang, and C. D. Lin, “Analytical model for calibrating laser intensity in strong-field-ionization experiments,” *Phys. Rev. A*, vol. 93, p. 023413, Feb 2016.

[144] Y. H. Lai, J. Xu, U. B. Szafruga, B. K. Talbert, X. Gong, K. Zhang, H. Fuest, M. F. Kling, C. I. Blaga, P. Agostini, and L. F. DiMauro, “Experimental investigation of strong-field-ionization theories for laser fields from visible to midinfrared frequencies,” *Phys. Rev. A*, vol. 96, p. 063417, Dec 2017.

[145] M. Labeye, F. Risoud, A. Maquet, J. Caillat, and R. Taïeb, “Tunnel ionization of atoms and molecules: How accurate are the weak-field asymptotic formulas?,” *Journal of Physics B: Atomic, Molecular and Optical Physics*, vol. 51, p. 094001, apr 2018.

[146] X. M. Tong, Z. X. Zhao, and C. D. Lin, “Theory of molecular tunneling ionization,” *Phys. Rev. A*, vol. 66, p. 033402, Sep 2002.

[147] X. M. Tong and C. D. Lin, “Empirical formula for static field ionization rates of atoms and molecules by lasers in the barrier-suppression regime,” *Journal of Physics B: Atomic, Molecular and Optical Physics*, vol. 38, no. 15, p. 2593, 2005.

[148] J. Aguilar and J. M. Combes, “A class of analytic perturbations for one-body schrödinger hamiltonians,” *Communications in Mathematical Physics*, vol. 22, pp. 269–279, Dec 1971.

[149] E. Balslev and J.-M. Combes, “Spectral properties of many-body schrödinger operators with dilatation-analytic interactions,” *Communications in Mathematical Physics*, vol. 22, no. 4, pp. 280–294, 1971.

[150] I. W. Herbst, “Exponential decay in the stark effect,” *Communications in Mathematical Physics*, vol. 75, pp. 197–205, Oct 1980.

[151] C. Cerjan, R. Hedges, C. Holt, W. P. Reinhardt, K. Scheibner, and J. J. Wendoloski, “Complex coordinates and the stark effect,” *International Journal of Quantum Chemistry*, vol. 14, no. 4, pp. 393–418, 1978.

[152] A. Scrinzi, *One- and two-electron atoms in strong external fields.* Universität Innsbruck, 1998.

[153] A. Scrinzi, M. Geissler, and T. Brabec, “Ionization above the coulomb barrier,” *Phys. Rev. Lett.*, vol. 83, pp. 706–709, Jul 1999.

[154] H. R. Reiss, “Unsuitability of the keldysh parameter for laser fields,” *Phys. Rev. A*, vol. 82, p. 023418, Aug 2010.

[155] T. K. Kjeldsen and L. B. Madsen, “Strong-field ionization of n2: length and velocity gauge strong-field approximation and tunnelling theory,” *Journal of Physics B: Atomic, Molecular and Optical Physics*, vol. 37, pp. 2033–2044, may 2004.

[156] L. D. Landau and L. M. Lifshitz, *Quantum Mechanics Non-Relativistic Theory, Third Edition: Volume 3.* Butterworth-Heinemann, 3 ed., Jan. 1981.

[157] R. Wang, Q. Zhang, D. Li, S. Xu, P. Cao, Y. Zhou, W. Cao, and P. Lu, “Identification of tunneling and multiphoton ionization in intermediate keldysh parameter regime,” *Opt. Express*, vol. 27, pp. 6471–6482, Mar 2019.

[158] I. W. Herbst and B. Simon, “Stark effect revisited,” *Phys. Rev. Lett.*, vol. 41, pp. 67–69, Jul 1978.

[159] I. Herbst and R. Mavi, “Can we trust the relationship between resonance poles and lifetimes?,” *Journal of Physics A: Mathematical and Theoretical*, vol. 49, p. 195204, apr 2016.

[160] M. A. Rego-Monteiro and F. D. Nobre, “Classical field theory for a non-hermitian schrödinger equation with position-dependent masses,” *Phys. Rev. A*, vol. 88, p. 032105, Sep 2013.

[161] N. Moiseyev, *Non-Hermitian Quantum Mechanics.* Cambridge University Press, 2011.

[162] M. Gadella, “A rigged hilbert space of hardy-class functions: Applications to resonances,” *Journal of Mathematical Physics*, vol. 24, no. 6, pp. 1462–1469, 1983.

[163] A. Bohm and H. V. Bui, “The marvelous consequences of hardy spaces in quantum physics,” in *Geometric Methods in Physics*, pp. 211–228, Springer Basel, Sept. 2012.

[164] M. Gadella, “Mathematical foundations of time asymmetric quantum mechanics,” *Journal of Physics: Conference Series*, vol. 839, p. 012001, may 2017.

[165] A. M. Perelomov, V. S. Popov, and M. V. Terent’ev, “Ionization of Atoms in an Alternating Electric Field: II.,” *Soviet Journal of Experimental and Theoretical Physics*, vol. 24, p. 207, Jan. 1967.

[166] A. M. Perelomov and V. S. Popov, “Ionization of Atoms in an Alternating Electrical Field. III.,” *Soviet Journal of Experimental and Theoretical Physics*, vol. 25, p. 336, Aug. 1967.

[167] G. L. Yudin and M. Y. Ivanov, “Nonadiabatic tunnel ionization: Looking inside a laser cycle,” *Phys. Rev. A*, vol. 64, p. 013409, Jun 2001.

[168] M. Šindelka and D. Šimsa, “Spontaneous emission from nonhermitian perspective: complex scaling of the photon coordinates,” *Molecular Physics*, vol. 117, no. 15-16, pp. 1989–2009, 2019.

[169] H. R. Reiss, “Effect of an intense electromagnetic field on a weakly bound system,” *Phys. Rev. A*, vol. 22, pp. 1786–1813, Nov 1980.

[170] A. Galstyan, O. Chuluunbaatar, A. Hamido, Y. V. Popov, F. Mota-Furtado, P. F. O’Mahony, N. Janssens, F. Catoire, and B. Piraux, “Reformulation of the strong-field approximation for light-matter interactions,” *Phys. Rev. A*, vol. 93, p. 023422, Feb 2016.

[171] I. Gohberg, S. Goldberg, and M. A. Kaashoek, *Classes of Linear Operators Vol. I.* Birkhäuser Basel, 1990.

[172] F. Catoire and H. Bachau, “Extraction of the absolute value of the photoelectron spectrum probability density by means of the resolvent technique,” *Phys. Rev. A*, vol. 85, p. 023422, Feb 2012.

[173] J.-P. Antoine, “Quantum mechanics beyond hilbert space,” in *Irreversibility and Causality Semigroups and Rigged Hilbert Spaces* (A. Bohm, H.-D. Doebner, and P. Kielanowski, eds.), (Berlin, Heidelberg), pp. 1–33, Springer Berlin Heidelberg, 1998.

[174] D. Gaspard, “Connection formulas between coulomb wave functions,” *Journal of Mathematical Physics*, vol. 59, p. 112104, Nov. 2018.

[175] R. G. Newton, “Analytic properties of radial wave functions,” *Journal of Mathematical Physics*, vol. 1, pp. 319–347, July 1960.

[176] H. R. Reiss, “The tunnelling model of laser-induced ionization and its failure at low frequencies,” *Journal of Physics B: Atomic, Molecular and Optical Physics*, vol. 47, p. 204006, oct 2014.

[177] V. Strelkov, “Role of autoionizing state in resonant high-order harmonic generation and attosecond pulse production,” *Phys. Rev. Lett.*, vol. 104, p. 123901, Mar 2010.

[178] A. Sopena, F. Catoire, A. Palacios, F. Martín, and H. Bachau, “Asymmetric electron angular distributions in h_2 induced by intense ultrashort soft-x-ray laser pulses,” *Phys. Rev. A*, vol. 105, p. 033104, Mar 2022.

[179] P. Agostini, F. Fabre, G. Mainfray, G. Petite, and N. K. Rahman, “Free-free transitions following six-photon ionization of xenon atoms,” *Phys. Rev. Lett.*, vol. 42, pp. 1127–1130, Apr 1979.

[180] P. Colosimo, G. Doumy, C. I. Blaga, J. Wheeler, C. Hauri, F. Catoire, J. Tate, R. Chirla, A. M. March, G. G. Paulus, H. G. Muller, P. Agostini, and L. F. DiMauro, “Scaling strong-field interactions towards the classical limit,” *Nature Physics*, vol. 4, pp. 386–389, Mar. 2008.

[181] C. S. Milsted and C. D. Cantrell, “Vector effects in self-focusing,” *Phys. Rev. A*, vol. 53, pp. 3536–3542, May 1996.

[182] G. Fibich and B. Ilan, “Vectorial and random effects in self-focusing and in multiple filamentation,” *Physica D: Nonlinear Phenomena*, vol. 157, no. 1, pp. 112–146, 2001.

[183] G. Fibich and B. Ilan, “Deterministic vectorial effects lead to multiple filamentation,” *Opt. Lett.*, vol. 26, pp. 840–842, Jun 2001.

[184] M. Abramowitz and I. Stegun, *Handbook of Mathematical Functions: With Formulas, Graphs, and Mathematical Tables.* Applied mathematics series, Dover Publications, 1964.

[185] X. He, M. Miranda, J. Schwenke, O. Guilbaud, T. Ruchon, C. Heyl, E. Georgadiou, R. Rakowski, A. Persson, M. B. Gaarde, and A. L'Huillier, "Spatial and spectral properties of the high-order harmonic emission in argon for seeding applications," *Phys. Rev. A*, vol. 79, p. 063829, Jun 2009.

[186] S. Teichmann, D. Austin, P. Bates, S. Cousin, A. Grün, M. Clerici, A. Lotti, D. Faccio, P. D. Trapani, A. Couairon, and J. Biegert, "Trajectory interferences in a semi-infinite gas cell," *Laser Physics Letters*, vol. 9, pp. 207–211, jan 2012.

[187] M. Kretschmar, C. Hernández-García, D. S. Steingrube, L. Plaja, U. Morgner, and M. Kovačev, "Spatial contributions of electron trajectories to high-order-harmonic radiation originating from a semi-infinite gas cell," *Phys. Rev. A*, vol. 88, p. 013805, Jul 2013.

[188] L. Quintard, *Caractérisation et contrôle des profils spatiaux, spectraux et temporels de faisceaux XUV obtenus par génération d'harmoniques d'ordres élevés dans des gaz.* Theses, Université de Bordeaux, July 2017.

[189] A. Gerrard and J. M. Burch, *Introduction to Matrix Methods in Optics*, ch. III.6, pp. 116–122. New York: Dover Publications, Inc, 1975.

[190] H. Wikmark, C. Guo, J. Vogelsang, P. W. Smorenburg, H. Coudert-Alteirac, J. Lahl, J. Peschel, P. Rudawski, H. Dacasa, S. Carlström, S. Maclot, M. B. Gaarde, P. Johnsson, C. L. Arnold, and A. L'Huillier, "Spatiotemporal coupling of attosecond pulses," *Proceedings of the National Academy of Sciences*, vol. 116, no. 11, pp. 4779–4787, 2019.

[191] ISO, "Lasers and laser-related equipment – test methods for laser beam widths, divergence angles and beam propagation ratios," ISO 11146-2:2005, International Organization for Standardization, Geneva, Switzerland, 2005.

[192] D. Gabor, "Theory of communication," *Journal of the Institution of Electrical Engineers-Part III: Radio and Communication Engineering*, vol. 93, no. 26, pp. 429–441, 1946.

[193] V. E. Nefedova, M. F. Ciappina, O. Finke, M. Albrecht, J. Vábek, M. Kozlová, N. Suárez, E. Pisanty, M. Lewenstein, and J. Nejdl, "Determination of the spectral variation origin in high-order harmonic generation in noble gases," *Phys. Rev. A*, vol. 98, p. 033414, Sep 2018.

[194] D. Attwood, *Soft X-Rays and Extreme Ultraviolet Radiation: Principles and Applications.* New York, NY, USA: Cambridge University Press, 1st ed., 2007.

[195] S. Kazamias, D. Douillet, C. Valentin, F. Weihe, F. Augé, T. Lefrou, G. Grillon, S. Sebban, and P. Balcou, "Observation of high-contrast coherence fringes in high-order harmonic generation," *Phys. Rev. A*, vol. 68, p. 033819, Sep 2003.

[196] M. A. Khokhlova and V. V. Strelkov, "Highly efficient XUV generation via high-order frequency mixing," *New Journal of Physics*, vol. 22, p. 093030, sep 2020.

[197] S. Skupin, *Nonlinear Dynamics of Trapped Beams.* PhD thesis, Friedrich-Schiller-Universität Jena, 2005.

[198] C. Brée, *Self-compression of intense optical pulses and the filamentary regime of nonlinear optics.* PhD thesis, Humboldt-Universität zu Berlin, Mathematisch-Naturwissenschaftliche Fakultät I, 2011.

[199] R. Nuter, M. Grech, P. G. de Alaiza Martinez, G. Bonnaud, and E. d'Humières, "Maxwell solvers for the simulations of the laser-matter interaction," *The European Physical Journal D*, vol. 68, June 2014.

[200] T. Brabec and F. Krausz, "Nonlinear optical pulse propagation in the single-cycle regime," *Phys. Rev. Lett.*, vol. 78, pp. 3282–3285, Apr 1997.

[201] G. A. Askar'yan, "Cerenkov Radiation and Transition Radiation from Electromagnetic Waves," *Soviet Journal of Experimental and Theoretical Physics*, vol. 15, p. 943, Nov. 1962.

[202] V. I. Talanov, "Self Focusing of Wave Beams in Nonlinear Media," *Soviet Journal of Experimental and Theoretical Physics Letters*, vol. 2, p. 138, Sept. 1965.

[203] S. N. Vlasov, V. A. Petrishchev, and V. I. Talanov, "Averaged description of wave beams in linear and nonlinear media (the method of moments)," *Radiophysics and Quantum Electronics*, vol. 14, pp. 1062–1070, Sept. 1971.

[204] R. T. Glassey, "On the blowing up of solutions to the cauchy problem for nonlinear schrödinger equations," *Journal of Mathematical Physics*, vol. 18, no. 9, pp. 1794–1797, 1977.

[205] J. Marburger, "Self-focusing: Theory," *Progress in Quantum Electronics*, vol. 4, pp. 35–110, 1975.

[206] S. C. Rae and K. Burnett, "Detailed simulations of plasma-induced spectral blueshifting," *Phys. Rev. A*, vol. 46, pp. 1084–1090, Jul 1992.

[207] W. P. Leemans, C. E. Clayton, W. B. Mori, K. A. Marsh, P. K. Kaw, A. Dyson, C. Joshi, and J. M. Wallace, "Experiments and simulations of tunnel-ionized plasmas," *Phys. Rev. A*, vol. 46, pp. 1091–1105, Jul 1992.

[208] S. Henz and J. Herrmann, "Self-channeling and pulse shortening of femtosecond pulses in multiphoton-ionized dispersive dielectric solids," *Phys. Rev. A*, vol. 59, pp. 2528–2531, Mar 1999.

[209] L. Bergé and A. Couairon, "Gas-induced solitons," *Phys. Rev. Lett.*, vol. 86, pp. 1003–1006, Feb 2001.

[210] E. Esarey, P. Sprangle, J. Krall, and A. Ting, "Self-focusing and guiding of short laser pulses in ionizing gases and plasmas," *Quantum Electronics, IEEE Journal of*, vol. 33, pp. 1879–1914, Nov 1997.

[211] I. Thiele, *Theoretical investigations of terahertz generation in laser-induced microplasmas.* Theses, Université de Bordeaux, Oct. 2017.

[212] C. G. Durfee, A. R. Rundquist, S. Backus, C. Herne, M. M. Murnane, and H. C. Kapteyn, "Phase matching of high-order harmonics in hollow waveguides," *Phys. Rev. Lett.*, vol. 83, pp. 2187–2190, Sep 1999.

[213] N. A. Bobrova, A. A. Esaulov, J.-I. Sakai, P. V. Sasorov, D. J. Spence, A. Butler, S. M. Hooker, and S. V. Bulanov, "Simulations of a hydrogen-filled capillary discharge waveguide," *Phys. Rev. E*, vol. 65, p. 016407, Dec 2001.

[214] D. R. Lide, "CRC handbook of chemistry and physics, 84th edition edited by david r. lide (national institute of standards and technology). CRC press LLC: boca raton. 2003. 2616 pp. $139.95. ISBN 0-8493-0484-9.," *Journal of the American Chemical Society*, vol. 126, pp. 1586–1586, Dec. 2003.

[215] S. Kazamias and P. Balcou, "Intrinsic chirp of attosecond pulses: Single-atom model versus experiment," *Phys. Rev. A*, vol. 69, p. 063416, Jun 2004.

[216] S. Kazamias, S. Daboussi, O. Guilbaud, K. Cassou, D. Ros, B. Cros, and G. Maynard, "Pressure-induced phase matching in high-order harmonic generation," *Phys. Rev. A*, vol. 83, p. 063405, Jun 2011.

[217] B. Major, K. Kovács, V. Tosa, P. Rudawski, A. L'Huillier, and K. Varjú, "Effect of plasma-core-induced self-guiding on phase matching of high-order harmonic generation in gases," *J. Opt. Soc. Am. B*, vol. 36, pp. 1594–1601, Jun 2019.

[218] B. Henke, E. Gullikson, and J. Davis, "X-ray interactions: Photoabsorption, scattering, transmission, and reflection at e = 50-30,000 ev, z = 1-92," *Atomic Data and Nuclear Data Tables*, vol. 54, no. 2, pp. 181–342, 1993.

[219] C. Chantler, K. Olsen, R. Dragoset, J. Chang, A. Kishore, S. Kotochigova, and D. Zucker, "X-ray form factor, attenuation and scattering tables (version 2.1)." `http://physics.nist.gov/ffast`, March 2022.

[220] X. Antoine, F. Fillion-Gourdeau, E. Lorin, and S. MacLean, "Pseudospectral computational methods for the time-dependent dirac equation in static curved spaces," *Journal of Computational Physics*, vol. 411, p. 109412, 2020.

[221] E. Lorin and X. Yang, "Time-dependent dirac equation with physics-informed neural networks: Computation and properties," *Computer Physics Communications*, vol. 280, p. 108474, 2022.

[222] M. H. Stone, "The generalized weierstrass approximation theorem," *Mathematics Magazine*, vol. 21, no. 4, pp. 167–184, 1948.

[223] J. Strikwerda, *Finite Difference Schemes and Partial Differential Equations*. Other Titles in Applied Mathematics, Society for Industrial and Applied Mathematics (SIAM, 3600 Market Street, Floor 6, Philadelphia, PA 19104), 2004.

[224] R. LeVeque, *Numerical Methods for Conservation Laws*. Lectures in mathematics ETH Zürich, Birkhäuser Basel, 2013.

[225] J. Blank, P. Exner, and M. Havlíček, *Hilbert Space Operators in Quantum Physics*. Theoretical and Mathematical Physics, Springer Netherlands, 2008.

[226] D. Gottlieb and S. Orszag, *Numerical Analysis of Spectral Methods: Theory and Applications*. CBMS-NSF Regional Conference Series in Applied Mathematics, Society for Industrial and Applied Mathematics (SIAM, 3600 Market Street, Floor 6, Philadelphia, PA 19104), 1977.

[227] J. Hesthaven, S. Gottlieb, and D. Gottlieb, *Spectral Methods for Time-Dependent Problems*. Cambridge Monographs on Applied and Computational Mathematics, Cambridge University Press, 2007.

[228] L. F. Richardson and R. T. Glazebrook, "The approximate arithmetical solution by finite differences of physical problems involving differential equations, with an application to the stresses in a masonry dam," *Philosophical Transactions of the Royal Society of London. Series*

A, Containing Papers of a Mathematical or Physical Character, vol. 210, no. 459-470, pp. 307–357, 1911.

[229] M. Pillai, J. Goglio, and T. G. Walker, "Matrix numerov method for solving schrödinger's equation," *American Journal of Physics*, vol. 80, no. 11, pp. 1017–1019, 2012.

[230] E. Hairer, S. Nørsett, and G. Wanner, *Solving Ordinary Differential Equations I: Nonstiff Problems.* Springer Series in Computational Mathematics, Springer Berlin Heidelberg, 2008.

[231] H. G. Muller, "An efficient propagation scheme for the time-dependent schroedinger equation in the velocity gauge," *Laser Physics*, vol. 9, pp. 1341–1350, Aug 1999.

[232] V. Tselyaev, "A generalized numerov method for linear second-order differential equations involving a first derivative term," *Journal of Computational and Applied Mathematics*, vol. 170, no. 1, pp. 103–120, 2004.

[233] L. K. Bieniasz, "A set of compact finite-difference approximations to first and second derivatives, related to the extended numerov method of chawla on nonuniform grids," *Computing*, vol. 81, pp. 77–89, Aug. 2007.

[234] J. Avery and J. Avery, *Generalized Sturmians and Atomic Spectra.* World Scientific, 2006.

[235] C. de Boor, *A Practical Guide to Splines.* New York: Springer Verlag, 1978.

[236] H. Bachau, E. Cormier, P. Decleva, J. E. Hansen, and F. Martín, "Applications of B-splines in atomic and molecular physics," *Reports on Progress in Physics*, vol. 64, pp. 1815–1943, nov 2001.

[237] H. Prautzsch, W. Boehm, and M. Paluszny, *Bezier and B-Spline Techniques.* Berlin, Heidelberg: Springer-Verlag, 2002.

[238] K. Hollig, *Finite Element Methods with B-splines.* Frontiers in Applied Mathematics, Society for Industrial and Applied Mathematics (SIAM, 3600 Market Street, Floor 6, Philadelphia, PA 19104), 2003.

[239] R. G. Littlejohn, M. Cargo, T. Carrington, K. A. Mitchell, and B. Poirier, "A general framework for discrete variable representation basis sets," *The Journal of Chemical Physics*, vol. 116, pp. 8691–8703, May 2002.

[240] J. C. Light and T. Carrington Jr., *Discrete-Variable Representations and their Utilization*, pp. 263–310. John Wiley & Sons, Ltd, 2007.

[241] M. Ismail, *Classical and Quantum Orthogonal Polynomials in One Variable.* Encyclopedia of Mathematics and Its Applications, Cambridge University Press, 2014.

[242] L.-Y. Peng and A. F. Starace, "Application of coulomb wave function discrete variable representation to atomic systems in strong laser fields," *The Journal of Chemical Physics*, vol. 125, no. 15, p. 154311, 2006.

[243] R. G. Littlejohn and M. Cargo, "Multidimensional discrete variable representation bases: Sinc functions and group theory," *The Journal of Chemical Physics*, vol. 116, pp. 7350–7361, May 2002.

[244] J. Hrivnák, L. Motlochová, and J. Patera, "Cubature formulas of multivariate polynomials arising from symmetric orbit functions," *Symmetry*, vol. 8, p. 63, July 2016.

[245] J. F. van Diejen and E. Emsiz, "Cubature rules for unitary jacobi ensembles," *Constructive Approximation*, vol. 54, pp. 145–156, Aug. 2020.

[246] R. I. Saye, "High-order quadrature on multi-component domains implicitly defined by multivariate polynomials," *Journal of Computational Physics*, vol. 448, p. 110720, 2022.

[247] K. Zimmermann, P. Lugan, F. Jörder, N. Heitz, M. Schmidt, C. Bouri, A. Rodriguez, and A. Buchleitner, "Extracting partial decay rates of helium from complex rotation: autoionizing resonances of the one-dimensional configurations," *Journal of Physics B: Atomic, Molecular and Optical Physics*, vol. 48, no. 2, p. 025001, 2015.

[248] A. Scrinzi, "trecx — an environment for solving time-dependent schrödinger-like problems," *Computer Physics Communications*, vol. 270, p. 108146, 2022.

[249] A. Scrinzi, "Infinite-range exterior complex scaling as a perfect absorber in time-dependent problems," *Phys. Rev. A*, vol. 81, p. 053845, May 2010.

[250] Y. Orimo, T. Sato, A. Scrinzi, and K. L. Ishikawa, "Implementation of the infinite-range exterior complex scaling to the time-dependent complete-active-space self-consistent-field method," *Phys. Rev. A*, vol. 97, p. 023423, Feb 2018.

[251] F. He, C. Ruiz, and A. Becker, "Absorbing boundaries in numerical solutions of the time-dependent schrödinger equation on a grid using exterior complex scaling," *Phys. Rev. A*, vol. 75, p. 053407, May 2007.

[252] T. Kato, "On the eigenfunctions of many-particle systems in quantum mechanics," *Communications on Pure and Applied Mathematics*, vol. 10, no. 2, pp. 151–177, 1957.

[253] R. T. Pack and W. B. Brown, “Cusp conditions for molecular wavefunctions,” *The Journal of Chemical Physics*, vol. 45, pp. 556–559, July 1966.

[254] N. H. March, “Spatially dependent generalization of kato’s theorem for atomic closed shells in a bare coulomb field,” *Phys. Rev. A*, vol. 33, pp. 88–89, Jan 1986.

[255] E. Suárez, R. D. Santiago-Acosta, and R. Lemus, “Algebraic dvr approaches applied to piecewise potentials: Symmetry and degeneracy,” *Symmetry*, vol. 14, no. 3, 2022.

[256] B. I. Schneider, L. A. Collins, and S. X. Hu, “Parallel solver for the time-dependent linear and nonlinear schrödinger equation,” *Phys. Rev. E*, vol. 73, p. 036708, Mar 2006.

[257] K. Balzer, S. Bauch, and M. Bonitz, “Finite elements and the discrete variable representation in nonequilibrium green's function calculations. atomic and molecular models,” *Journal of Physics: Conference Series*, vol. 220, p. 012020, apr 2010.

[258] A. Macías, F. Martín, A. Riera, and M. Yáañez, “A practical solution to the “unknown normalization” problem,” *International Journal of Quantum Chemistry*, vol. 33, no. 4, pp. 279–300, 1988.

[259] R. L. Hall, N. Saad, K. D. Sen, and H. Ciftci, “Energies and wave functions for a soft-core coulomb potential,” *Phys. Rev. A*, vol. 80, p. 032507, Sep 2009.

[260] E. Cormier and P. Lambropoulos, “Above-threshold ionization spectrum of hydrogen using b-spline functions,” *Journal of Physics B: Atomic, Molecular and Optical Physics*, vol. 30, p. 77, jan 1997.

[261] A. D. Bandrauk, F. Fillion-Gourdeau, and E. Lorin, “Atoms and molecules in intense laser fields: gauge invariance of theory and models,” *Journal of Physics B: Atomic, Molecular and Optical Physics*, vol. 46, p. 153001, jul 2013.

[262] Y.-C. Han and L. B. Madsen, “Comparison between length and velocity gauges in quantum simulations of high-order harmonic generation,” *Phys. Rev. A*, vol. 81, p. 063430, Jun 2010.

[263] V. P. Majety, A. Zielinski, and A. Scrinzi, “Mixed gauge in strong laser-matter interaction,” *Journal of Physics B: Atomic, Molecular and Optical Physics*, vol. 48, p. 025601, dec 2014.

[264] C. Bunge, J. Barrientos, and A. Bunge, “Roothaan-hartree-fock ground-state atomic wave functions: Slater-type orbital expansions and expectation values for z = 2-54,” *Atomic Data and Nuclear Data Tables*, vol. 53, no. 1, pp. 113 – 162, 1993.

[265] A. Sopena Moros, *Study of relativistic effects in non-linear interaction between molecules andXUV/soft X-ray short laser pulses.* Theses, Université de Bordeaux ; Universidad autonóma de Madrid, Mar. 2021.

[266] W. Magnus, "On the exponential solution of differential equations for a linear operator," *Communications on Pure and Applied Mathematics*, vol. 7, no. 4, pp. 649–673, 1954.

[267] A. Askar and A. S. Cakmak, "Explicit integration method for the time dependent schrodinger equation for collision problems," *The Journal of Chemical Physics*, vol. 68, no. 6, pp. 2794–2798, 1978.

[268] Y. Saad, *Iterative Methods for Sparse Linear Systems: Second Edition.* Other Titles in Applied Mathematics, Society for Industrial and Applied Mathematics, 2003.

[269] W.-C. Jiang and X.-Q. Tian, "Efficient split-lanczos propagator for strong-field ionization of atoms," *Opt. Express*, vol. 25, pp. 26832–26843, Oct 2017.

[270] E. Hairer, C. Lubich, and G. Wanner, *Geometric Numerical Integration: Structure-Preserving Algorithms for Ordinary Differential Equations.* Springer Series in Computational Mathematics, Springer Berlin Heidelberg, 2013.

[271] S. Patchkovskii and H. Muller, "Simple, accurate, and efficient implementation of 1-electron atomic time-dependent schrödinger equation in spherical coordinates," *Computer Physics Communications*, vol. 199, pp. 153–169, 2016.

[272] V. Tulsky and D. Bauer, "Qprop with faster calculation of photoelectron spectra," *Computer Physics Communications*, vol. 251, p. 107098, 2020.

[273] I. S. Gradshteyn and I. M. Ryzhik, *Table of integrals, series, and products.* Elsevier/Academic Press, Amsterdam, seventh ed., 2007. Translated from the Russian, Translation edited and with a preface by Alan Jeffrey and Daniel Zwillinger, With one CD-ROM (Windows, Macintosh and UNIX).

[274] J. W. Pearson, *Computation of hypergeometric functions.* PhD thesis, University of Oxford, 2009.

[275] J. W. Pearson, S. Olver, and M. A. Porter, "Numerical methods for the computation of the confluent and gauss hypergeometric functions," *Numerical Algorithms*, vol. 74, pp. 821–866, Mar 2017.

[276] A. Cuyt, F. Backeljauw, V. Petersen, C. Bonan-Hamada, B. Verdonk, H. Waadeland, and W. Jones, *Handbook of Continued Fractions for Special Functions.* SpringerLink: Springer e-Books, Springer Netherlands, 2008.

[277] E. Anderson, Z. Bai, C. Bischof, S. Blackford, J. Demmel, J. Dongarra, J. Du Croz, A. Greenbaum, S. Hammarling, A. McKenney, and D. Sorensen, *LAPACK Users' Guide.* Philadelphia, PA: Society for Industrial and Applied Mathematics, third ed., 1999.

[278] B. Simon, "Resonances and complex scaling: A rigorous overview," *International Journal of Quantum Chemistry*, vol. 14, no. 4, pp. 529–542, 1978.

[279] B. Simon, "The definition of molecular resonance curves by the method of exterior complex scaling," *Physics Letters A*, vol. 71, no. 2, pp. 211 – 214, 1979.

[280] J.-F. Bonnans, J. C. Gilbert, C. Lemarechal, and C. A. Sagastizábal, *Numerical Optimization: Theoretical and Practical Aspects*, ch. Background, pp. 157–168. Berlin, Heidelberg: Springer Berlin Heidelberg, 2006.

[281] M. Frigo and S. G. Johnson, "The design and implementation of fftw3," *Proceedings of the IEEE*, vol. 93, no. 2, pp. 216–231, 2005.

[282] A. Dalgarno and A. E. Kingston, "The Refractive Indices and Verdet Constants of the Inert Gases," *Proceedings of the Royal Society of London Series A*, vol. 259, pp. 424–431, Dec. 1960.

[283] H. Lehmeier, W. Leupacher, and A. Penzkofer, "Nonresonant third order hyperpolarizability of rare gases and n2 determined by third harmonic generation," *Optics Communications*, vol. 56, no. 1, pp. 67–72, 1985.

[284] C. Brée, A. Demircan, and G. Steinmeyer, "Method for computing the nonlinear refractive index via keldysh theory," *IEEE Journal of Quantum Electronics*, vol. 46, no. 4, pp. 433–437, 2010.

[285] C. T. Chantler, "Detailed tabulation of atomic form factors, photoelectric absorption and scattering cross section, and mass attenuation coefficients in the vicinity of absorption edges in the soft x-ray (z=30–36, z=60–89, e=0.1 keV–10 keV), addressing convergence issues of earlier work," *Journal of Physical and Chemical Reference Data*, vol. 29, pp. 597–1056, July 2000.

[286] The HDF Group, "Hierarchical Data Format, version 5," 1997-2022. https://www.hdfgroup.org/HDF5/.

[287] SchedMD, “slurm workload manager.” `slurm.schedmd.com`, 2022.

[288] M. Metcalf, J. Reid, and M. Cohen, *Modern Fortran Explained: Incorporating Fortran 2018*. Numerical Mathematics and Scientific Computation, OUP Oxford, 2018.

[289] B. Kernighan, D. Ritchie, C. Tondo, and a. O. M. C. Safari, *The C Programming Language*. Prentice-Hall software series, Prentice Hall, 1988.

[290] S. Prata, *C Primer Plus: C Primer Plus_6*. Developer’s Library, Pearson Education, 2013.

[291] G. Van Rossum and F. L. Drake, *Python 3 Reference Manual*. Scotts Valley, CA: CreateSpace, 2009.

[292] C. R. Harris, K. J. Millman, S. J. van der Walt, R. Gommers, P. Virtanen, D. Cournapeau, E. Wieser, J. Taylor, S. Berg, N. J. Smith, R. Kern, M. Picus, S. Hoyer, M. H. van Kerkwijk, M. Brett, A. Haldane, J. F. del Río, M. Wiebe, P. Peterson, P. Gérard-Marchant, K. Sheppard, T. Reddy, W. Weckesser, H. Abbasi, C. Gohlke, and T. E. Oliphant, “Array programming with NumPy,” *Nature*, vol. 585, pp. 357–362, Sept. 2020.

[293] J. D. Hunter, “Matplotlib: A 2d graphics environment,” *Computing in Science & Engineering*, vol. 9, no. 3, pp. 90–95, 2007.

[294] MATLAB, *9.12.0.1884302 (R2022a)*. Natick, Massachusetts: The MathWorks Inc., 2022.

[295] D. Popmintchev, C. Hernández-García, F. Dollar, C. Mancuso, J. A. Pérez-Hernández, M.-C. Chen, A. Hankla, X. Gao, B. Shim, A. L. Gaeta, M. Tarazkar, D. A. Romanov, R. J. Levis, J. A. Gaffney, M. Foord, S. B. Libby, A. Jaron-Becker, A. Becker, L. Plaja, M. M. Murnane, H. C. Kapteyn, and T. Popmintchev, “Ultraviolet surprise: Efficient soft x-ray high-harmonic generation in multiply ionized plasmas,” *Science*, vol. 350, no. 6265, pp. 1225–1231, 2015.

[296] R. Shao, C. Zhai, Y. Zhang, L. He, X. Zhu, P. Lan, and P. Lu, “Efficient soft x-ray high-order harmonic generation via dual-pulse driving lasers in the overdriven regime,” *Journal of Physics B: Atomic, Molecular and Optical Physics*, vol. 54, p. 064001, mar 2021.

[297] S. Petrakis, M. Bakarezos, M. Tatarakis, E. P. Benis, and N. A. Papadogiannis, “Electron quantum path control in high harmonic generation via chirp variation of strong laser pulses,” *Scientific Reports*, vol. 11, Dec. 2021.

[298] E. Pisanty and M. Ivanov, “Slalom in complex time: Emergence of low-energy structures in tunnel ionization via complex-time contours,” *Phys. Rev. A*, vol. 93, p. 043408, Apr 2016.

[299] E. Pisanty and A. Jiménez-Galán, "Strong-field approximation in a rotating frame: High-order harmonic emission from p states in bicircular fields," *Phys. Rev. A*, vol. 96, p. 063401, Dec 2017.

[300] A. Weber, B. Böning, B. Minneker, and S. Fritzsche, "Generation of elliptically polarized high-order harmonic radiation with bi-elliptical two-color laser beams," *Phys. Rev. A*, vol. 104, p. 063118, Dec 2021.

[301] I. Babushkin, W. Kuehn, C. Köhler, S. Skupin, L. Bergé, K. Reimann, M. Woerner, J. Herrmann, and T. Elsaesser, "Ultrafast spatiotemporal dynamics of terahertz generation by ionizing two-color femtosecond pulses in gases," *Phys. Rev. Lett.*, vol. 105, p. 053903, Jul 2010.

[302] L. Bergé, S. Skupin, C. Köhler, I. Babushkin, and J. Herrmann, "3d numerical simulations of thz generation by two-color laser filaments," *Phys. Rev. Lett.*, vol. 110, p. 073901, Feb 2013.

[303] A. Schmitt-Sody, H. G. Kurz, L. Bergé, S. Skupin, and P. Polynkin, "Picosecond laser filamentation in air," *New Journal of Physics*, vol. 18, p. 093005, sep 2016.

[304] C. Chen, Z. Tao, C. Hernández-García, P. Matyba, A. Carr, R. Knut, O. Kfir, D. Zusin, C. Gentry, P. Grychtol, O. Cohen, L. Plaja, A. Becker, A. Jaron-Becker, H. Kapteyn, and M. Murnane, "Tomographic reconstruction of circularly polarized high-harmonic fields: 3d attosecond metrology," *Science Advances*, vol. 2, no. 2, p. e1501333, 2016.

[305] P.-C. Huang, C. Hernández-García, J.-T. Huang, P.-Y. Huang, C.-H. Lu, L. Rego, D. D. Hickstein, J. L. Ellis, A. Jaron-Becker, A. Becker, S.-D. Yang, C. G. Durfee, L. Plaja, H. C. Kapteyn, M. M. Murnane, A. H. Kung, and M.-C. Chen, "Polarization control of isolated high-harmonic pulses," *Nature Photonics*, vol. 12, pp. 349–354, Apr. 2018.

[306] S. D. C. Roscam Abbing, F. Campi, A. Zeltsi, P. Smorenburg, and P. M. Kraus, "Divergence and efficiency optimization in polarization-controlled two-color high-harmonic generation," *Scientific Reports*, vol. 11, Dec. 2021.

[307] L. Rego, K. M. Dorney, N. J. Brooks, Q. L. Nguyen, C.-T. Liao, J. S. Román, D. E. Couch, A. Liu, E. Pisanty, M. Lewenstein, L. Plaja, H. C. Kapteyn, M. M. Murnane, and C. Hernández-García, "Generation of extreme-ultraviolet beams with time-varying orbital angular momentum," *Science*, vol. 364, no. 6447, p. eaaw9486, 2019.

[308] E. Pisanty, L. Rego, J. San Román, A. Picón, K. M. Dorney, H. C. Kapteyn, M. M. Murnane, L. Plaja, M. Lewenstein, and C. Hernández-García, "Conservation of torus-knot angular

momentum in high-order harmonic generation," *Phys. Rev. Lett.*, vol. 122, p. 203201, May 2019.

[309] A. de las Heras, A. K. Pandey, J. S. Román, J. Serrano, E. Baynard, G. Dovillaire, M. Pittman, C. G. Durfee, L. Plaja, S. Kazamias, O. Guilbaud, and C. Hernández-García, "Extreme-ultraviolet vector-vortex beams from high harmonic generation," *Optica*, vol. 9, pp. 71–79, Jan 2022.

[310] C. Figueira de Morisson Faria, H. Schomerus, and W. Becker, "High-order above-threshold ionization: The uniform approximation and the effect of the binding potential," *Phys. Rev. A*, vol. 66, p. 043413, Oct 2002.

[311] T. D. Arber, K. Bennett, C. S. Brady, A. Lawrence-Douglas, M. G. Ramsay, N. J. Sircombe, P. Gillies, R. G. Evans, H. Schmitz, A. R. Bell, and C. P. Ridgers, "Contemporary particle-in-cell approach to laser-plasma modelling," *Plasma Physics and Controlled Fusion*, vol. 57, p. 113001, sep 2015.

[312] J. Derouillat, A. Beck, F. Pérez, T. Vinci, M. Chiaramello, A. Grassi, M. Flé, G. Bouchard, I. Plotnikov, N. Aunai, J. Dargent, C. Riconda, and M. Grech, "Smilei : A collaborative, open-source, multi-purpose particle-in-cell code for plasma simulation," *Computer Physics Communications*, vol. 222, pp. 351–373, 2018.

[313] G. Battistoni, T. Boehlen, F. Cerutti, P. W. Chin, L. S. Esposito, A. Fassò, A. Ferrari, A. Lechner, A. Empl, A. Mairani, A. Mereghetti, P. G. Ortega, J. Ranft, S. Roesler, P. R. Sala, V. Vlachoudis, and G. Smirnov, "Overview of the fluka code," *Annals of Nuclear Energy*, vol. 82, pp. 10–18, 2015. Joint International Conference on Supercomputing in Nuclear Applications and Monte Carlo 2013, SNA + MC 2013. Pluri- and Trans-disciplinarity, Towards New Modeling and Numerical Simulation Paradigms.

[314] C. Ahdida, D. Bozzato, D. Calzolari, F. Cerutti, N. Charitonidis, A. Cimmino, A. Coronetti, G. L. D'Alessandro, A. Donadon Servelle, L. S. Esposito, R. Froeschl, R. García Alía, A. Gerbershagen, S. Gilardoni, D. Horváth, G. Hugo, A. Infantino, V. Kouskoura, A. Lechner, B. Lefebvre, G. Lerner, M. Magistris, A. Manousos, G. Moryc, F. Ogallar Ruiz, F. Pozzi, D. Prelipcean, S. Roesler, R. Rossi, M. Sabaté Gilarte, F. Salvat Pujol, P. Schoofs, V. Stránský, C. Theis, A. Tsinganis, R. Versaci, V. Vlachoudis, A. Waets, and M. Widorski, "New capabilities of the fluka multi-purpose code," *Frontiers in Physics*, vol. 9, 2022.

[315] M. F. Ciappina, A. Becker, and A. Jaro ń Becker, "Multislit interference patterns in high-order harmonic generation in c_{60}," *Phys. Rev. A*, vol. 76, p. 063406, Dec 2007.

[316] S. Ghimire and D. A. Reis, “High-harmonic generation from solids,” *Nature Physics*, vol. 15, pp. 10–16, Nov. 2018.

[317] S. Kim, T.-I. Jeong, J. Park, M. F. Ciappina, and S. Kim, “Recent advances in ultrafast plasmonics: from strong field physics to ultraprecision spectroscopy,” *Nanophotonics*, 2022.

[318] F. Catoire and H. Bachau, “Above-threshold ionization of quasiperiodic structures by low-frequency laser fields,” *Phys. Rev. Lett.*, vol. 115, p. 163602, Oct 2015.

[319] C. Jin, X. Tang, B. Li, K. Wang, and C. D. Lin, “Optimal spatial separation of high-order harmonics from infrared driving lasers with an annular beam in the overdriven regime,” *Phys. Rev. Applied*, vol. 14, p. 014057, Jul 2020.

[320] L. D. Landau and E. M. Lifshitz, *The Classical Theory of Fields.* Butterworth-Heinemann, 4 ed., Jan. 1980.

[321] S. M. Barnett, “Resolution of the abraham-minkowski dilemma,” *Phys. Rev. Lett.*, vol. 104, p. 070401, Feb 2010.

[322] A. Einstein, “Über einen die erzeugung und verwandlung des lichtes betreffenden heuristischen gesichtspunkt,” *Annalen der Physik*, vol. 322, no. 6, pp. 132–148, 1905.

[323] S. Gordienko and A. Pukhov, “Scalings for ultrarelativistic laser plasmas and quasimonoenergetic electrons,” *Physics of Plasmas*, vol. 12, no. 4, p. 043109, 2005.

[324] L. Allen, M. W. Beijersbergen, R. J. C. Spreeuw, and J. P. Woerdman, “Orbital angular momentum of light and the transformation of laguerre-gaussian laser modes,” *Phys. Rev. A*, vol. 45, pp. 8185–8189, Jun 1992.

[325] L. Allen, M. Padgett, and M. Babiker, “Iv the orbital angular momentum of light,” vol. 39 of *Progress in Optics*, pp. 291–372, Elsevier, 1999.

[326] CINES, “Configuration — supercomputer occigen.” `https://web.archive.org/web/20211228223520/https://www.cines.fr/calcul/materiels/occigen/configuration/`, 2022. [Online; accessed 23-June-2022].

[327] W. Press, B. Flannery, S. Teukolsky, and W. Vetterling, *Numerical Recipes in FORTRAN 77: Volume 1, Volume 1 of Fortran Numerical Recipes: The Art of Scientific Computing.* No. v. 2 in Numerical Recipes in FORTRAN: The Art of Scientific Computing, Cambridge University Press, 1992.

[328] M. Richardson and J. V. Lambers, “Recurrence relations for orthogonal polynomials for pdes in polar and cylindrical geometries,” *SpringerPlus*, vol. 5, p. 1567, Sep 2016.

[329] V. G. Nedorezov, S. G. Rykovanov, and A. B. Savel’ev, “Nuclear photonics: results and prospects,” *Physics-Uspekhi*, vol. 64, pp. 1214–1237, dec 2021.

[330] G. Mourou, B. Brocklesby, T. Tajima, and J. Limpert, “The future is fibre accelerators,” *Nature Photonics*, vol. 7, pp. 258–261, Mar. 2013.

[331] K. M. Spohr, M. Shaw, W. Galster, K. W. D. Ledingham, L. Robson, J. M. Yang, P. McKenna, T. McCanny, J. J. Melone, K.-U. Amthor, F. Ewald, B. Liesfeld, H. Schwoerer, and R. Sauerbrey, “Study of photo-proton reactions driven by bremsstrahlung radiation of high-intensity laser generated electrons,” *New Journal of Physics*, vol. 10, p. 043037, apr 2008.

[332] K. W. D. Ledingham, J. Magill, P. McKenna, J. Yang, J. Galy, R. Schenkel, J. Rebizant, T. McCanny, S. Shimizu, L. Robson, R. P. Singhal, M. S. Wei, S. P. D. Mangles, P. Nilson, K. Krushelnick, R. J. Clarke, and P. A. Norreys, “Laser-driven photo-transmutation of 129i—a long-lived nuclear waste product,” *Journal of Physics D: Applied Physics*, vol. 36, pp. L79–L82, sep 2003.

[333] B. Hall and B. Hall, *Lie Groups, Lie Algebras, and Representations: An Elementary Introduction.* Graduate Texts in Mathematics, Springer, 2003.

[334] J. Sakurai, *Advanced Quantum Mechanics.* A-W series in advanced physics, Addison-Wesley Publishing Company, 1967.

[335] C. Cohen-Tannoudji, J. Dupont-Roc, and G. Grynberg, *Photons and Atoms: Introduction to Quantum Electrodynamics.* Wiley, 1989.

[336] W. Greiner, *Relativistic Quantum Mechanics: Wave Equations.* Springer Berlin Heidelberg, 2012.

[337] M. Peskin and D. Schroeder, *An Introduction to Quantum Field Theory.* Advanced book classics, Avalon Publishing, 1995.

[338] M. Schwartz, *Quantum Field Theory and the Standard Model.* Quantum Field Theory and the Standard Model, Cambridge University Press, 2014.

[339] J. D. Brown, “Singular lagrangians and the dirac–bergmann algorithm in classical mechanics,” *American Journal of Physics*, vol. 91, no. 3, pp. 214–224, 2023.

[340] N. Bourbaki, *Lie Groups and Lie Algebras: Chapters 1-3.* Bourbaki, Nicolas: Elements of mathematics, Springer-Verlag, 1989.

[341] N. Bourbaki, *Lie Groups and Lie Algebras: Chapters 4-6.* No. pts. 4-6 in Elements de mathematique [series], Springer Berlin Heidelberg, 2008.

[342] N. Bourbaki, *Lie Groups and Lie Algebras: Chapters 7-9.* No. pts. 7-9 in Elements of mathematics, Springer Berlin Heidelberg, 2004.

[343] J. Elliott and P. Dawber, *Symmetry in Physics.* No. v. 1 in Symmetry in Physics, Macmillan, 1979.

[344] C. Moreno-Pulido and J. S. Peracaula, "Running vacuum in quantum field theory in curved spacetime: renormalizing ρ_{vac} without $\sim m^4$ terms," *The European Physical Journal C*, vol. 80, Aug. 2020.

[345] F. Englert and R. Brout, "Broken symmetry and the mass of gauge vector mesons," *Phys. Rev. Lett.*, vol. 13, pp. 321–323, Aug 1964.

[346] P. W. Higgs, "Broken symmetries and the masses of gauge bosons," *Phys. Rev. Lett.*, vol. 13, pp. 508–509, Oct 1964.

[347] G. S. Guralnik, C. R. Hagen, and T. W. B. Kibble, "Global conservation laws and massless particles," *Phys. Rev. Lett.*, vol. 13, pp. 585–587, Nov 1964.

[348] V. Rubakov and S. Wilson, *Classical Theory of Gauge Fields.* Princeton University Press, 2009.

[349] D. Croon, T. E. Gonzalo, L. Graf, N. Košnik, and G. White, "Gut physics in the era of the lhc," *Frontiers in Physics*, vol. 7, 2019.

[350] M. Gubinelli, F. Hiroshima, and J. Lőrinczi, "Ultraviolet renormalization of the nelson hamiltonian through functional integration," *Journal of Functional Analysis*, vol. 267, no. 9, pp. 3125–3153, 2014.

[351] A. Jaffe, "Stochastic quantization, reflection positivity, and quantum fields," *Journal of Statistical Physics*, vol. 161, pp. 1–15, July 2015.

[352] D. Manzano, "A short introduction to the lindblad master equation," *AIP Advances*, vol. 10, no. 2, p. 025106, 2020.

[353] Y. L. Lin and O. C. O. Dahlsten, "Necessity of negative wigner function for tunneling," *Phys. Rev. A*, vol. 102, p. 062210, Dec 2020.

APPENDIX

A. ATOMIC UNITS

We use two systems of units throughout the work: SI and atomic units. The system of atomic units is defined by setting the numerical values of the following physical constants

$$\hbar = e = m_e = \frac{1}{4\pi\varepsilon_0} = k_{\mathrm{B}} = 1\,. \tag{A.1}$$

There are two additional observations:

- The values of other physical constants are also determined by the definition. One of them is the speed of light in vacuum, its numerical value in atomic units is $c_{\mathrm{a.u.}} = 1/\alpha_0$, where α_0 is the fine-structure constant.

  The gravitational constant can be also computed in atomic units as

  $$G_{\mathrm{a.u.}} = \frac{G_{\mathrm{SI}} m_e^2}{\alpha_0 \hbar c} \approx 2.4 \times 10^{-43}\,.$$

  Since the electric constant together with electron charge and mass are set to one, it provides a direct comparison of gravitational and electric force acting on an electron.[1]
- Last, base SI units contain also candela. To define luminous intensity, one needs also one constant – luminous efficacy – and the luminosity function. Since we are not usually use human eye for direct measurements of light parameters in quantum mechanics, we may let it undefined without any consequences.

---

[1] In fact, the force comes from the Newton and Coulomb laws. We may do an estimation by considering a valence electron in xenon. One of frequent isotopes is ^{131}Xe. The gravitational force is then $F_G \approx G_{\mathrm{a.u.}} 131 \mu_m / r$, while electric force in a neutral atom is $F_e = 1/r$. Their ratio then still gives $F_G/F_e \approx 4.3 \times 10^{-38}$ that totally justifies the neglect of gravitation in atomic physics.

B. FEW NOTES ON DESCRIBING ELECTROMAGNETIC PULSES

The purpose of this appendix is to review the way to describe the electric field and also recalls the physical meaning of various quantities related to the electromagnetic pulses. Section B.1 introduces the complex notation of the field, Section B.2 provides the details about the quantities related with an electromagnetic pulse, which is considered as a form of energy carried through space. Section B.3 defines and uses a Gaussian beam and pulse to illustrate these quantities, the remaining sections provide further notes on photons and angular momenta of the field.

B.1 Complex notation for the field

The pattern of complex number is suitable for the linearity of Maxwell's equations together with the wave behaviour of their solutions. Frequently, complex notation is then very advantageous for the field; many effects, for example interferences, just naturally emerge. There are two possibilities, either $\mathcal{E} = \mathsf{Re}\,\mathscr{E}_1$ or $\mathcal{E} = \mathscr{E}_2 + \mathsf{c.c.}$. However, there are still some points, where a care is needed:

- Quantities beyond linearity–as the intensity–need a specification, since $\mathscr{E}_2 = \mathscr{E}_1/2$. It must be specified which form is used to find a proper scaling to intensity and other quantities.
- We reduce the ambiguity of the sign caused by $\cos(\omega t - kz) = \cos(-(\omega t - kz))$, it proposes $\mathcal{E}_1 = \mathrm{e}^{\mathbf{i}(\omega t - kz)}$ or $\mathcal{E}_1 = \mathrm{e}^{-\mathbf{i}(\omega t - kz)}$. The latter is consistent with the convention of the Fourier transform, that has been set by the choice of the momentum operator in quantum mechanics.
    - Further physical insight may be then obtained. Let us take an arbitrary field written in this form, $\mathscr{E}_1 = \mathrm{e}^{-\mathbf{i}\phi(t,z)}$. We can then obtain local wavenumber using the "momentum operator" $k(z')\mathscr{E}_1 = -\mathbf{i}\,\partial_z\big|_{z=z'}\,\mathscr{E}_1 = -\frac{\partial\phi(t,z')}{\partial z}\mathscr{E}_1$. A similar approach may be done in the time domain. This allow us to define two quantities: *instantaneous frequency* and *local wavelength*:

$$\omega(t) = \frac{\partial\phi}{\partial t}\,, \qquad \lambda(z) = \frac{2\pi}{k(z)} = 2\pi\left(\frac{\partial\phi}{\partial z}\right)^{-1}\,, \tag{B.1}$$

respectively.[1]

---

[1] The same sign of the derivatives is given by the respective Fourier and inverse Fourier transform.

  - The formal description of monochromatic light with a fundamental frequency ω_0 propagating in the direction $\boldsymbol{k}_0$ is given by $\mathcal{E}(\omega, \boldsymbol{k}) = \delta(\omega - \omega_0)\delta(\boldsymbol{k} - \boldsymbol{k}_0)/(4\pi^2)$ in the conjugate domain. The magnitude of $\boldsymbol{k}_0$ comes from the vacuum dispersion relation.

- It provides a direct way to obtain the local phase of electromagnetic field. Let us take $\mathcal{E}(t, \boldsymbol{r}) = \mathsf{Re}\left(\exp(-\mathbf{i}(\omega_0 t - k_0 z - \phi(t, \boldsymbol{r})))\right)$

$$\phi(t, \boldsymbol{r}) = \operatorname{Arg}\left(\mathcal{E}_1(t, \boldsymbol{r})\right) . \tag{B.2}$$

  A convenient way to obtain $\mathcal{E}_1$ is

$$\mathscr{E}_1(t, \boldsymbol{r}) = \mathscr{F}_\omega^{-1}\left[\theta(\omega)\mathscr{F}_t\left[\mathcal{E}(t, \boldsymbol{r})\right](\omega)\right](t) . \tag{B.3}$$

We took a scalar field in these considerations. A general field $\boldsymbol{\mathcal{E}}(t, \boldsymbol{r})$ may be rewritten with only one shared amplitude A and phase ϕ as $A(t, \boldsymbol{r})\mathrm{e}^{-\mathbf{i}\phi(t,\boldsymbol{r})}\boldsymbol{e}(t, \boldsymbol{r})$, where $\boldsymbol{e} = \boldsymbol{\mathcal{E}}/\left\|\boldsymbol{\mathcal{E}}\right\|$ is the local direction of the field. ϕ is the so-called *Eikonal*, see Chapter 7 of [320], and it defines the equations of the *Ray optics*. The curvature of a ray there is $\bigtriangledown_\perp \phi$.

Although the discussion is rather technical, a physical insight emerge not only for the ray optics, but as well for quantum mechanics where the de Broglie's wave links the "local" momentum of a particle with the phase of the wavefunction the same way as for the electric field.

B.2 Energetic picture of electromagnetic pulses

In this appendix we provide the link between the energy and other quantities characterising laser pulses. It will be illustrated on a Gaussian pulse propagating in a Gaussian beam.

It is useful to picture a pulse as energy and momentum carried by an electromagnetic field in the direction of propagation. This abstract definition is useful as it allows easy transition for both classical ($\boldsymbol{A}$-, $\boldsymbol{B}$- and $\boldsymbol{\mathcal{E}}$-field) and quantum description of fields (photons). Let us then start with a part of the energy-momentum tensor (also Maxwell stress tensor) $T^{0\mu} = (w, \boldsymbol{S}/c)$, where $w = \varepsilon_0 \mathcal{E}^2$ is the energy density and the Poynting vector $\boldsymbol{S} = wc\boldsymbol{k}/\left\|\boldsymbol{k}\right\|$ gives the energy flux together with the direction of the propagation given by the wavevector $\boldsymbol{k}$. The total energy contained in the field is then $E = \int_{\mathbb{R}^3} w \,\mathrm{d}^3 x$. Let us consider a pulse carrying the energy in the z-axis direction.[2] We use this axis to define cylindrical coordinates (ρ, φ, z). It is useful to introduce some quantities that provide insight in the physics in a plane perpendicular to the propagation at a given z.[3] We

---

[2] Precisely speaking, it does not necessary mean that this is the direction of the wavevector in any point. But since total momentum is a constant of motion, we can uniquely define it by $\boldsymbol{e}_z = \boldsymbol{P}/\left\|\boldsymbol{P}\right\|$, where $\boldsymbol{P} = \int_{\mathbb{R}} \boldsymbol{S}(t)\,\mathrm{d}^3 x$ at arbitrary time t.

[3] We do not write thus z explicitly in the following formulae since it is fixed.

start with the *instantaneous irradiance* $E_e(\rho, \varphi, t) = \boldsymbol{S}(\rho, \varphi, t) \cdot \boldsymbol{e}_z$, its unit is $\frac{\mathsf{ENERGY}}{\mathsf{TIME \cdot LENGTH^2}}$ and it gives energy flux through the plane.[4] The total energy flowing through a given point is called *instantaneous intensity*, $I(\rho, \varphi, t) = \|\boldsymbol{S}(\rho, \varphi, t)\|$ with the same unit $\frac{\mathsf{ENERGY}}{\mathsf{TIME \cdot LENGTH^2}}$. We consider further that the direction of propagation deviates slightly from the propagation axis (paraxial approximation), in this case $E_e \approx I$. We can now introduce two integral quantities

$$P(t) = \int I(\rho, \varphi, t)\, \mathrm{d}S\,, \qquad\qquad F(\rho, \varphi) = \int I(\rho, \varphi, t)\, \mathrm{d}t\,. \tag{B.4}$$

P is the *instantaneous power* given as $\frac{\mathsf{ENERGY}}{\mathsf{TIME}}$ and F *fluence* as $\frac{\mathsf{ENERGY}}{\mathsf{LENGTH^2}}$. The total energy E can be then integrated from both of them. We called I and P as instantaneous because the nature of the field is that there is usually a fast-oscillating part and carrier envelope with slow evolution compared to these fast oscillations. It allows to average over the fast oscillations and obtain *intensity* $\langle I \rangle_{T_0}$ and *power* $\langle P \rangle_{T_0}$, where T_0 is the period of the fast oscillations.[5] These quantities still depend on time, but only through the envelope. The averaging gives $\langle I(t) \rangle_{T_0} = I(t)/2$ and $\langle P(t) \rangle_{T_0} = P(t)/2$. These two quantities are in most cases used instead of the instantaneous values. One of the reasons is that the phase of the fast oscillations is not controlled in experiments. The averages are necessary for mathematical clarity. However, physical literature usually omits them, and we do the same if there is no special need.

All these quantities have a clear meaning since $E < +\infty$. However, a monochromatic plane wave is a useful frequent model of an electromagnetic wave even though the total energy diverges in that case. Fluence and power also diverge for the plane wave, but they are still sometimes defined as "renormalising" them by saying, respectively, *per unit of time* or *per unit area.* These are also well defined since the distribution is homogeneous in time and space. It is useful for physical models based on monochromatic and/or plane waves that needs only a local field.

B.2.1 Spectral domain

I and P provide an insight into the distribution of the energy in time. A complementary analysis in the spectral domain is useful as well. We then define *the spectrum* $S(\rho, \varphi, \omega) = \left|\mathscr{F}_t\left[\mathcal{E}(\rho, \varphi, t)\right](\omega)\right|^2$, which is basically the intensity in the spectral domain. Second, there is *the spectral power* $\bar{S}(\omega) =$

---

[4] For different boundaries that the plane, $\boldsymbol{e}_z$ is replaced by the proper normal vector.

[5] We do not use term *average intensity* or *average power* since we may use them for the average quantities from the viewpoint of the envelope. Once the duration τ of the envelope is defined, we may define them as $\langle I \rangle_\tau$ and $\langle P \rangle_\tau$, respectively.

$\frac{\mathrm{d}E}{\mathrm{d}\omega}$, which is related to the total energy by[6]

$$E = \int_{\mathbb{R}} \bar{S}(\omega)\,\mathrm{d}\omega\,. \tag{B.5}$$

Finally, we may be interested in a combined analysis in both frequency and time domain. We basically answer the question: "When does a given frequency occur?" The tool answering this question is the so-called *Gabor transform* [192] (see Appendix E of [126] for its illustrations).

B.2.2 Coupling with matter

Up to this point, we did not mention the influence of the matter that affects the field propagation. Since there is interchange of energy, only total energy is conserved $E_{\mathrm{tot}} = E_{\mathrm{f}}(t) + E_{\mathrm{m}}(t)$, while the energy of the field, E_{f}, and that of matter, E_{m}, are not independently.[7] It is useful to change our consideration from the whole space at a given time t to the energy $E_{\mathrm{f}}(z)$ passed through the plane in the given z as we already done. It means that we just add the variable z to all the quantities defined above, which helps us to analyse the processes in the underlying medium. In summary, $E_{\mathrm{f}}(z)$ is not generally conserved and the difference $E_{\mathrm{f}}(z_2) - E_{\mathrm{f}}(z_1)$ tells us the amount of energy absorbed (or emitted) between the planes in z_1 and z_2.[8]

B.3 Example: Gaussian beam

Now, we use a vacuum Gaussian beam with Gaussian time profile as an example of the previously defined quantities. The full field in the whole space is given by

$$\mathcal{E}(\rho, z, t) = \mathcal{E}_0 \frac{w_0}{w(z)} \mathrm{e}^{-\left(\frac{\rho}{w(z)}\right)^2} \mathrm{e}^{-2\ln(2)\left(\frac{t-\frac{z}{v_g}}{\tau_{\mathrm{FWHM}}}\right)^2} \cos\left(\omega_0 t - k_0 z - \frac{k_0 \rho^2}{2R(z)} + \phi_G(z) + \varphi_0\right) , \tag{B.6}$$

where $w(z) = w_0\sqrt{1 + (z/z_R)^2}$, $R(z) = z + z_R^2/z$, $\phi_G(z) = \arctan(z/z_R)$, and $z_R = k_0 w_0^2/2$. In vacuum $v_g = c$. Note that $(\omega_0 t - k_0 z) = \omega_0\,(t - z/c)$. If we take the pulse propagating in vacuum, it gives exactly the retarded time and the phase $\omega_0\,(t - z/c) = \omega_0 t'$.

The defining parameters are

---

[6] Due to the parity of $S(\omega)$ and $\bar{S}(\omega)$ in ω, one can consider only $\omega > 0$. A care in scaling is needed to ensure the normalisation $E = \int \bar{S}\,\mathrm{d}\omega$.

[7] Note that the coupling is not a trivial theoretical problem, as for example the momentum of the light coupled with matter had been unclear throughout the 20th century before a detailed investigation was done in [321].

[8] We then have the energy balance for the matter: $E_{\mathrm{m}}^{(z_1,z_2)}(t \to -\infty) - E_{\mathrm{m}}^{(z_1,z_2)}(t \to +\infty) = E_{\mathrm{f}}(z_2) - E_{\mathrm{f}}(z_1)$. This difference says the amount of energy deposed in the part of the space $\{(z, y, z) \in \mathbb{R}^3 | z_1 \le z \le z_2\}$. This energy has to be understood really in a thermodynamic sense since it may be any from kinetic, potential, internal, thermal, etc. parts. Moreover, we suppose that the planes act as a perfect thermodynamic insulator and only the E-M field carries the energy.

- w_0: the waist at focus, i.e. the radius where the electric field and the intensity reach, respectively, $\mathcal{E}_0/\mathrm{e}$ and I_0/e^2;
- τ_{FWHM}: the FWHM of the envelope in intensity.
- $\mathcal{E}_0$: the peak electric field amplitude at focus.
- λ: the vacuum wavelength related to the frequency $\omega_0 = 2\pi c/\lambda = k_0 c$.
- φ_0: the *carrier envelope phase (CEP)*: the offset of the fundamental phase at the peak of the pulse with respect to the "cosine" pulse defined by $\varphi_0 = 0$ in (B.6).

We now review and calculate the above-mentioned quantities. First, the intensity is

$$\langle I(t)\rangle_{T_0} = \frac{c\varepsilon_0\mathcal{E}_0^2}{2}\mathrm{e}^{-2\left(\frac{\rho}{w_0}\right)^2}\mathrm{e}^{-4\ln(2)\left(\frac{t}{\tau_{\mathrm{FWHM}}}\right)^2} = I_0\mathrm{e}^{-2\left(\frac{\rho}{w_0}\right)^2}\mathrm{e}^{-4\ln(2)\left(\frac{t}{\tau_{\mathrm{FWHM}}}\right)^2}. \tag{B.7}$$

The fluence and power are, respectively,[9]

$$F(\rho) = \sqrt{\frac{\pi}{\ln(2)}}\frac{c\varepsilon_0}{4}\mathcal{E}_0^2\tau_{\mathrm{FWHM}}\mathrm{e}^{-2\left(\frac{\rho}{w_0}\right)^2} = F_0\mathrm{e}^{-2\left(\frac{\rho}{w_0}\right)^2}, \tag{B.9a}$$

$$\langle P(t)\rangle_{T_0} = \frac{\pi}{4}c\varepsilon_0 w_0^2\mathcal{E}_0^2\mathrm{e}^{-4\ln(2)\left(\frac{t}{\tau_{\mathrm{FWHM}}}\right)^2} = P_0\mathrm{e}^{-4\ln(2)\left(\frac{t}{\tau_{\mathrm{FWHM}}}\right)^2}. \tag{B.9b}$$

The last step is the total energy

$$E \approx c\varepsilon_0\sqrt{\frac{\pi^3}{2^6\ln(2)}}\tau_{\mathrm{FWHM}}w_0^2\mathcal{E}_0^2 \qquad \Leftrightarrow \qquad \mathcal{E}_0 \approx \left(\frac{1}{\sqrt{c\varepsilon_0}}\sqrt[4]{\frac{2^6\ln(2)}{\pi^3}}\right)\left(\frac{1}{w_0}\sqrt{\frac{E}{\tau_{\mathrm{FWHM}}}}\right). \tag{B.10}$$

The energy is proportional to the section of the beam and the duration of the pulse as expected.

Finally we can link all the peak values with the peak intensity

$$I_0 = \frac{c\varepsilon_0}{2}\mathcal{E}_0^2 = \sqrt{\frac{2^4\ln(2)}{\pi^3}}\frac{E}{w_0^2\tau_{\mathrm{FWHM}}} = \sqrt{\frac{\ln(2)}{\pi}}\frac{2F_0}{\tau_{\mathrm{FWHM}}} = \frac{2}{\pi}\frac{P_0}{w_0^2}; \tag{B.11}$$

---

[9] We used the following two integrals:

$$\int_{-\infty}^{+\infty}\mathrm{e}^{-\alpha x^2}\cos^2(\beta x+\gamma)\,\mathrm{d}x = \frac{\sqrt{\pi}\left(1+\mathrm{e}^{-\frac{\beta^2}{\alpha}}\cos(2\gamma)\right)}{2\sqrt{\alpha}}, \qquad \int_0^{+\infty}x\mathrm{e}^{-\alpha x^2}\,\mathrm{d}x = \frac{1}{2\alpha}. \tag{B.8}$$

We neglect the term $\mathrm{e}^{-\frac{\beta^2}{\alpha}}\cos(2\gamma)$ since α represents envelope varying slowly compared to the fast frequency β.

$\cos^2$-*envelope*

The model we introduced in (B.6) describes both Gaussian beam (the spatial shape) and Gaussian pulse (the profile in time). Here, we explicitly compute analogical quantities in the case the envelope in time is replaced by the $\cos^2$-shape (using only one half-cycle). This shape is sometimes more convenient in the description as it has a finite support and some manipulations with the field may be easier at it contains only goniometric functions (e.g. the integrations in (2.14)).

Let us consider a pulse having a time profile

$$\mathcal{E}(t) = \mathcal{E}_0 \cos^2(\omega_c t) \cos(\omega_0 t + \varphi_0)\,, \qquad I(t) = \frac{c\varepsilon_0 \mathcal{E}_0^2}{2} \cos^4(\omega_c t)\,. \tag{B.12}$$

The characteristics of this pulse are

$$\tau_{\mathrm{FWHM}} = \frac{2}{\omega_c} \arccos\left(\frac{1}{\sqrt[4]{2}}\right) \approx \frac{1.14372}{\omega_c}\,, \tag{B.13}$$

$$F = \frac{3\pi}{8\omega_c}\,, \tag{B.14}$$

$$\int_0^t \cos^4(\omega_c t')\,\mathrm{d}t' = \frac{12\omega_c t + 8\sin(2\omega_c t) + \sin(4\omega_c t)}{32\omega_c}\,, \tag{B.15}$$

$$\tau_{\mathrm{rms}} = \sqrt{\frac{2\pi^2 - 15}{24}}\,\frac{1}{\omega_c} \approx \frac{0.44437}{\omega_c}\,. \tag{B.16}$$

The correspondence between a Gaussian envelope $\exp(-(t/t_0^{(G)})^2)$ and $\cos^2$-pulse preserving $\mathcal{E}_0$ and τ_{rms} is $\omega_c = \sqrt{\frac{2\pi^2-15}{12}}\frac{1}{t_0^{(G)}} \approx \frac{0.628438}{t_0^{(G)}}$.

Radial distribution of energy

Here, we provide a perspective of the power/energy distribution with the radial coordinate. Let us consider the total energy computed from the fluence

$$E = F_0 \int \mathrm{e}^{-2\left(\frac{\rho}{w_0}\right)^2} \rho\,\mathrm{d}\rho\,\mathrm{d}\varphi = 2\pi F_0 \int \rho\,\mathrm{e}^{-2\left(\frac{\rho}{w_0}\right)^2}\,\mathrm{d}\rho\,. \tag{B.17}$$

The differential of the energy is proportional to $\rho\mathrm{e}^{-2\left(\frac{\rho}{w_0}\right)^2}$. It reaches its maximum at $\rho_m = \frac{w_0}{2}$. It means that the greatest contribution to the energy comes from the first half of the beam radius. Next we can compute the radius, $\rho_{E_{0.5}}$, for which the half of the total energy is deposed:

$$\int_0^{\rho_{E_{0.5}}} \rho\mathrm{e}^{-2\left(\frac{\rho}{w_0}\right)^2}\,\mathrm{d}\rho = \frac{1}{2}\int_0^{+\infty} \rho\mathrm{e}^{-2\left(\frac{\rho}{w_0}\right)^2}\,\mathrm{d}\rho. \tag{B.18}$$

It gives $\rho_{E_{0.5}} = \sqrt{\frac{\ln(2)}{2}} w_0 \approx 0.6 w_0$. The introduced radii, ρ_m and $\rho_{E_{0.5}}$, emphasise the role of the off-axis contributions and possibly limits the accuracy of on-axis studies. However, as non-linear processes follows the local intensity and not the total deposed energy, the role of the near-axis region is amplified. (See also the non-linear scaling by q_{eff} in (2.19).)

B.4 Photons

One of main inspiration of the quantum theory is the quantisation of light (which explained the electric photo-effect [322]). The proposed quantisation assigns the energy $\hbar\omega$ to one photon with the frequency ω. The total number of photons of a monochromatic field with an energy E is then simply $N = E/\hbar\omega$. However, the model of a monochromatic field is unrealistic: its fluence $F(\rho,\varphi) = \int_{-\infty}^{+\infty} \mathcal{E}_0(\rho,\varphi)\cos^2(\omega t)\,\mathrm{d}t$ diverges for any non-zero amplitude $\mathcal{E}_0$. A proper physical quantity then emerges, it is the *spectral density of photons* $\mathcal{N}(\omega) = 2S(\omega)/\hbar$, $\omega > 0$. If the pulse is nearly monochromatic (a narrow peak in the spectrum), the number of photons of the given frequency is then $N_{\omega_0} = \int_{\text{peak}} \mathcal{N}(\omega)\,\mathrm{d}\omega$. Since the total energy may be computed in any domain,[10] the total number of photons in a pulse with a well-defined fundamental frequency is $N = E/\hbar\omega$. However, the formula for N_{ω_0} is more general and may be used, e.g., for harmonics.

The photons are natural to the $(\omega, \boldsymbol{k})$-domain. Although this domain is mathematically fully equivalent to $(t, \boldsymbol{r})$, it frequently tear physicists. The reason are the questions: "Where?" and "When?". These questions are completely (Dirac-δ-)local in $(t, \boldsymbol{r})$, thus completely delocalised in $(\omega, \boldsymbol{k})$. If consider a *sharply* defined photon $\delta(\omega - \omega_0)\delta(\boldsymbol{k} - \boldsymbol{k}_0)$, $\omega_0 = c\,\|\boldsymbol{k}_0\|$; we just simply cannot think when a given photon was created or where it is. Meaningful answer are re-established, if we 1) consider narrow (but not pointy) distributions, 2) give our thanks to the Gabor analysis.

Having in mind the previous discussion, we can construct an artificial *single photon* propagating along a ray defined by the z-axis:

$$\mathcal{E}_{\omega_0,k_0}(t,\boldsymbol{r}) = \mathcal{E}_0 \chi_{\left[0,\frac{2\pi}{\omega_0}\right]}\left(t - \frac{z}{c}\right)\sin\left(\omega_0 t - k_0 z\right)\delta(x)\delta(y)\,, \qquad \mathcal{E}_0 = \sqrt{\frac{\hbar}{\pi c \varepsilon_0}}\omega_0\,. \tag{B.19}$$

The factor ω_0 favours the description by the vector potential because its amplitude $A_0 = \sqrt{\hbar/(\pi c\varepsilon_0)}$ thus preserves the energy of a given field.[11] Although we provided an understandable example, the single-photon state is defined only by its total energy assuming only the possibility to define

---

[10] Mathematically, it is linked with the Parseval's theorem.

[11] $\boldsymbol{A}$ is then much better to quantify the field. For example, the cutoff of the harmonics (1.1) naturally scales with $A = \mathcal{E}/\omega$. The Plasma physics also favours the vector potential in some cases, see for example [323]. This is natural since it adds with (four-)momentum (as seen in (2.1) or in (I.1), where the four-momentum is linked with $\not{p} = \mathbf{i}\not{\partial}$) and it thus characterises one of fundamental physical quantities. Moreover, it also fulfil Lorentz invariance compared to the pseudovectors $\boldsymbol{\mathcal{E}}$ and $\boldsymbol{B}$. A drawback of $\boldsymbol{A}$ is its non-uniqueness due to gauge freedom.

a fundamental frequency. For example, we can construct an arbitrary Gaussian beam with the Gaussian time profile satisfying $E = \omega_0 \hbar$. We see that this requirement is quite loose.

All the above are large simplifications, the real nature – at least closer to the contemporary understanding of physics – are quantised photons (see Appendix I). One of the first attempts to describe it is the so-called second quantisation based on the expansion $|\psi_{\text{field}}\rangle = \int f(\boldsymbol{k})\,|\boldsymbol{k}\rangle$, where $|\boldsymbol{k}\rangle = a^\dagger(\boldsymbol{k})\,|0\rangle$ is a state with sharply defined momentum of field. $a^\dagger(\boldsymbol{k})$ is then the creation operator of the given mode of the field. This is a useful description in quantum optics. However, the Fock space is frequently built from the single-particle Hilbert spaces $\mathscr{H}_1 = L^2(\mathbb{R}^3, \mathrm{d}^3x)$. This is fundamentally wrong because the Lebesgue measure d^3x violates Lorentz invariance. The solution is to use a similar quantisation procedure, but with a Lorentz-invariant measure; the base space is then $\mathscr{H}_1 = L^2\,(\text{Minkowski manifold}, \mathrm{d}\boldsymbol{p}/2E_{\boldsymbol{p}})$.

B.5 Angular momentum: polarisation and helical beams

We started the discussion about the general pulse as a carrier of energy, it is not the only quantity carried through the space. An electromagnetic field can carry angular momentum as well. There are two possible forms of the angular momentum in a pulse: *spin angular momentum* and *orbital angular momentum.*

The spin angular momentum can be considered as an intrinsic property of photons, and it is the so-called polarisation of light. A fully circularly polarised light consists of photons each with the same spin angular momentum $L_{\hat{\boldsymbol{k}}} = \pm\hbar$, where $\hat{\boldsymbol{k}}$ is the direction of propagation. Linearly polarised field is given as a superposition $(|\boldsymbol{k}, \hbar\rangle + \mathrm{e}^{\mathrm{i}\varphi}\,|\boldsymbol{k}, -\hbar\rangle)/\sqrt{2}$, where φ then defines the polarisation axis. Arbitrary polarisation state (even unpolarised) is described by using density-matrix formalism on the photonic states.

The orbital angular momentum is a macroscopic property of a beam, it is given by the spatially shaped wavefront. The eigenmodes are given by the Laguerre-Gaussian distribution [324, 325].

C. STARK SHIFT & NON-DIPOLE CASE IN INVARIANT IONISATION DYNAMICS

In this appendix, we expand the discussion of energy measurements from 3.2.1 and go beyond the dipole approximation, where we prove that spectrum of the Hamiltonian (3.14) is not stabilised once the dipole approximation is not used. Next, we add some physical interpretations. We use the perturbative expansion of interaction in the Hamiltonian to explicitly find the couplings leading to energy shifts. We also provide the physical meaning of the related physics, which complements the discussion from Section 3.2.3.

We start with the physics motivated by the Stark shift in the stabilised energy spectrum. The Hamiltonian at a fixed time in the velocity gauge within the dipole approximation is $H_A = (\boldsymbol{p} - A\boldsymbol{e}_z)^2/2 + V_C$. If we forgot the time dependence, this is, in fact, gauge-equivalent to a field-free case. We can explain the difference that A deforms the momentum space by a linear shift. We employ the usual form of the field-free Hamiltonian $H_0 = \boldsymbol{p}^2/2 + V_C$. Using (3.15), we have $|\tilde{\psi}\rangle = \mathrm{e}^{-\mathbf{i}Az}|\psi\rangle$, where $H_A|\tilde{\psi}\rangle = E|\tilde{\psi}\rangle$ and $H_0|\psi\rangle = E|\psi\rangle$. We now perform an experiment and try to measure the energy of $|\tilde{\psi}\rangle$ by H_0. Using

$$H_0 \circ f(\boldsymbol{x}) = f(\boldsymbol{x}) \circ H_0 + [H_0, f(\boldsymbol{x})] = f(\boldsymbol{x}) \circ H_0 - \mathbf{i}(\bigtriangledown f(\boldsymbol{x})) \cdot \boldsymbol{p} - \left(\frac{\triangle f(\boldsymbol{x})}{2}\right), \tag{C.1}$$

we obtain for the lowest energy state E:

$$\begin{aligned} E_{H_0,|\tilde{\psi}\rangle} = \left\langle \tilde{\psi} \,\middle|\, H_0 \,\middle|\, \tilde{\psi} \right\rangle = \left\langle \psi \,\middle|\, \mathrm{e}^{\mathbf{i}Az} H_0 \mathrm{e}^{-\mathbf{i}Az} \,\middle|\, \psi \right\rangle = \left\langle \psi \,\middle|\, \mathrm{e}^{\mathbf{i}Az} \left(\mathrm{e}^{-\mathbf{i}Az} H_0 + \left[H_0, \mathrm{e}^{-\mathbf{i}Az}\right]\right) \,\middle|\, \psi \right\rangle = \\ = \langle \psi \,|\, H_0 \,|\, \psi \rangle + A \langle \psi \,|\, -\mathbf{i}\partial_z \,|\, \psi \rangle - \frac{A^2}{2} \langle \psi \,|\, \psi \rangle = E_0 - \frac{A^2}{2}\,. \end{aligned} \tag{C.2}$$

This corresponds exactly to the quadratic Stark shift that is expected. However, we mismatched the state with its parent Hamiltonian. We can explain it by the following consideration; most of the measurements of quantum-mechanical systems rely on transitions between states. If we do so by a pump-probe experiment, the gauges of pump and probe need to be consistent. Accepting H_0 as an energy measure of $|\tilde{\psi}\rangle$, we find that the energy shift is deposed in the kinetic part – the oscillatory part of the wavefunction. It fully agrees with the analysis of the spectrum stabilisation and the construction of L_I.

Next, we now have a clearer meaning of the *abrupt turn-off of the field.* As H_A is gauge-equivalent to the field-free Hamiltonian, the abrupt change means only a stop in the time evolution of $A(t)$. However, there is not imposed any discontinuity in the Hamiltonian (there may be discontinuity in the electric field $\mathcal{E}$).

Finally, we recall the relation (3.20): $\langle\psi_V|P(H_V;E)|\psi_V\rangle = \langle\psi_L|P(H_0;E)|\psi_L\rangle$. As the identity is decomposed within as

$$I = P(H;E \geq 0) + P(H;E \in \{\text{bound states}\})\,, \tag{C.3}$$

we get the probability of ionisation by projecting onto the bound states of H_0 from the length gauge. This may be explained as a surprising result: An ostensible definition based on the length gauge is linked with the invariant construction that is expressed in the velocity gauge.

C.1 Beyond dipole approximation

We now discuss a perturbative extension of a non-dipole case. First, we specify the incident field as a monochromatic wave

$$\boldsymbol{A} = (\epsilon\cos(\omega_0(t-\alpha_0 z)),0,0)\,, \tag{C.4}$$

which thus propagates in the z-direction and is polarised along x. It is convenient to use a different coordinate notation in this example, the quantisation axis related to the spin number is along the propagation direction. Physics is, of course, independent on this choice.[1] Corrections of the spatial dependence induced by the field are linked with the orders of the expansion in z, we have

$$A = \underbrace{\epsilon\cos(\omega_0 t)}_{A_0} + \underbrace{\epsilon\omega_0\alpha_0 z\sin(\omega_0 t)}_{A_1} - \underbrace{\frac{\epsilon\omega_0^2\alpha_0^2 z^2}{2}\cos(\omega_0 t)}_{A_2} + \cdots\,. \tag{C.5}$$

We can now expand the Hamiltonian

$$H \approx \frac{(\boldsymbol{p}+\boldsymbol{A}_0(t))^2}{2} + V_C + A_1 p_x + A_0 A_1 + A_0 A_2 + A_2 p_x + A_1^2\,, \tag{C.6}$$

$$A_1 p_x = \epsilon\omega_0\alpha_0 z\sin(\omega_0 t)p_x\,,$$

$$A_0 A_1 = \epsilon^2\omega_0\alpha_0 z\cos(\omega_0 t)\sin(\omega_0 t)\,,$$

---

[1] In the dipole case, it was suitable to identify the direction of the field $\boldsymbol{A}$ with the usual axis for the quantisation of the momentum: L_z. Once we have two exceptional directions (of the field $\boldsymbol{A}$ and the Poynting vector), it turns out that the calculation is simpler by identifying the quantisation axis with the direction of the propagation.

$$
\begin{aligned}
A_0 A_2 &= -\frac{\epsilon^2 \omega_0^2 \alpha_0^2 z^2}{2} \cos^2(\omega_0 t)\,, \\
A_2 p_x &= -\frac{\epsilon \omega_0^2 \alpha_0^2 z^2}{2} \cos(\omega_0 t) p_x\,, \\
A_1^2 &= \frac{\epsilon^2 \omega_0^2 \alpha_0^2 z^2}{2} \sin^2(\omega_0 t)\,.
\end{aligned}
$$

$\left((\boldsymbol{p} + \boldsymbol{A}_0(t))^2 /2 + V_C\right)$ is the Hamiltonian in the dipole approximation. We have kept the corrections up to the second order in the vector potential amplitude, ϵ, and in the fine-structure constant, α_0. We can now inspect how the energy levels are affected. Let us take the lowest order correction in the both parameters, $A_1 p_x$. The ground state is not affected in the first order as it is highly symmetric. Some higher-order corrections are of the same order, and they would have to be taken into account in equal footing. We then move to a higher energetic state and show that the first degenerated energy state is affected. Let us compute $\langle 211; \mathrm{d} | z p_x | 210; \mathrm{d} \rangle$, where $|nlm; \mathrm{d}\rangle = \mathrm{e}^{-\mathbf{i} x A} |nlm\rangle$ is the dressed state in the field. We first recall some expressions in the spherical coordinates,

$$
\langle r, \varphi, \theta | 21m \rangle = \frac{1}{2\sqrt{6}} Y_1^m(\varphi, \theta)\, r \mathrm{e}^{-\frac{r}{2}}\,, \tag{C.7a}
$$

$$
z = r\cos\theta\,, \tag{C.7b}
$$

$$
p_x = -\mathbf{i}\left(\cos\varphi \sin\theta \partial_r - \frac{\sin\varphi}{r\sin\theta}\partial_\varphi + \frac{\cos\theta\cos\varphi}{r}\partial_\theta\right)\,, \tag{C.7c}
$$

$$
Y_1^0(\varphi, \theta) = \frac{1}{2}\sqrt{\frac{3}{\pi}}\cos\theta\,. \tag{C.7d}
$$

First, we show that the dressing of the state does not contribute in the first-order

$$
\begin{aligned}
\langle 211; \mathrm{d} | z p_x | 210; \mathrm{d} \rangle = -\mathbf{i} \left\langle 211 \,\middle|\, \mathrm{e}^{\mathbf{i}\epsilon x \cos(\omega_0(t-\alpha_0 z))} z \partial_x \mathrm{e}^{-\mathbf{i}\epsilon x \cos(\omega_0(t-\alpha_0 z))} \,\middle|\, 210 \right\rangle = \\
= \langle 211 | z p_x | 210 \rangle + \epsilon \cos(\omega_0 t) \langle 211 | z | 210 \rangle + \mathcal{O}(\epsilon\alpha_0)\,.
\end{aligned} \tag{C.8}
$$

Because $\langle 211 | z | 210 \rangle = 0$ from the selection rules of the usual Stark effect, the demonstration that the dressing does not play a role is done. To proceed the calculation of the energy shift, we insert (C.7) and perform trivial derivatives, the matrix element of the interest reads then

$$
\begin{aligned}
\langle 211 | z\partial_x | 210 \rangle = \frac{1}{24}\Bigg(\int_0^{+\infty} r^4 \left(1 - \frac{r}{2}\right) \mathrm{e}^{-r} \mathrm{d}r \int_\Omega \left(Y_1^1\right)^* (\varphi, \theta) \cos\theta \sin\theta \cos\varphi Y_1^0(\varphi, \theta)\, \mathrm{d}\Omega \\
- \frac{1}{2}\sqrt{\frac{3}{\pi}} \int_0^{+\infty} r^4 \mathrm{e}^{-r} \mathrm{d}r \int_\Omega \left(Y_1^1\right)^* (\varphi, \theta) \cos^2\theta \cos\varphi \sin\theta \mathrm{d}\Omega \Bigg) = \frac{\sqrt{2}}{4}\,.
\end{aligned} \tag{C.9}
$$

It proves that there is an energy shift from the first excited state. It follows from the fact that only nilpotent matrices have all eigenvalues 0. The matrix of the perturbation theory of a degenerate state is Hermitian. As the only nilpotent Hermitian matrix is zero matrix, there is always a non-zero eigenvalue of a non-zero Hermitian matrix. Hence, at least one eigenvalue is non-zero in our case because we explicitly computed the matrix element $\langle 211|zp_x|210\rangle = -\mathbf{i}\sqrt{2}/4$.

It is interesting to consider some physical explanation of the computed coupling due to the product zp_x. p_x is in the direction of the vector potential (so is the electric field accelerating the electron), and z is the direction of the Poynting vector, which coincides the direction where the magnetic force induced by (C.4) acts. This coupling is linked with the transition between the magnetic numbers $m = 0$ and $m = 1$. We should note that a quantitative analysis of the corrections is more subtle. We neglected the spin in all our calculations. As it is also a subject of magnetic effects, it should be included in such a study, but it is beyond the scope of this work.

Another aspect is in the whole pre-factor: $\epsilon\omega_0\alpha_0 \sin(\omega_0 t)$. It is time-dependent perturbation and the stationary perturbation theory assumes the adiabaticity of the system. The scope of this study was to inspect the spectral properties of the Hamiltonian, that turned out to be trivial in the dipole case, where the spectrum was stabilised. We shown that even from a stationary viewpoint, the spectral properties are non-trivial in the non-dipole case.

D. DIFFRACTION INTEGRALS (FRAUNHOFER, FRESNEL AND OTHERS)

In this appendix we discus in detail the approximations related with the diffractive integrals together with their physical interpretations. Next, we introduce the diffraction integral of the optical system containing a pinhole in Section D.1.

The approximations of the diffraction integral as the Fraunhofer and Fresnel diffraction rises from the approximation

$$\mathrm{e}^{\mathbf{i}k(\omega)\|\boldsymbol{r}-\tilde{\boldsymbol{r}}\|} \approx \left(\mathrm{e}^{\mathbf{i}k(\omega)D}\mathrm{e}^{-\mathbf{i}k(\omega)\frac{\rho^2}{2D}}\right)\mathrm{e}^{-\mathbf{i}k(\omega)\frac{\tilde{\rho}^2}{2D}}\mathrm{e}^{-\mathbf{i}k(\omega)\frac{\rho\tilde{\rho}\cos\theta}{D}}\,, \tag{D.1}$$

$D = \tilde{z} - z$. The term in the parentheses acts as a phase-pre-factor and is not interesting as a global phase in t-domain. We now recall the zones used for the description of the radiation. There are called as *far-field* and *near-field*. The near-field is further subdivided to *radiative (Fresnel)* and *non-radiative (reactive) zones*, see Section 9.1 of [118]. The approximation (D.1) is shared for both the radiative and far-field regions. The last term, $\mathrm{e}^{-\mathbf{i}k(\omega)\rho\tilde{\rho}\cos\theta/D}$, leads to J_0. The unresolved term is finally $\mathrm{e}^{-\mathbf{i}k(\omega)\tilde{\rho}^2/(2D)}$.

We recall the meaning of the involved quantities. As $k(\omega) = 2\pi/\lambda$, it characterises the wavelength. D is the distance of the source from the screen and $\tilde{\rho}$ is the dimension of the source, we can use it as the radius of an aperture. We present two ways to insight the quantity. First is purely mathematical and imposes the conditions where the exponential can be neglected:

$$\frac{\pi\tilde{\rho}^2}{\lambda D} \ll 1\,. \tag{D.2}$$

The second description is provides a geometrical insight and it is based on the Huygens' principle. Let us consider a circular aperture with the diameter $\tilde{\rho}$ and an on-axis point placed at the distance D from the aperture. Using the picture of rays, we try to sum two rays radiating from the edge of the aperture and from the center. We would like to neglect the difference of the optical paths from these two sources compared to the wavelength. Since these points form a right-angled triangle, we can easily write the condition:

$$\sqrt{D^2+\tilde{\rho}^2}-D = D\left(\sqrt{1+\left(\frac{\tilde{\rho}}{D}\right)^2}-1\right) \approx \frac{\tilde{\rho}^2}{2D} \ll \lambda\,. \tag{D.3}$$

Up to numerical factors within one order of magnitude, these conditions are equivalent: $\tilde{\rho}^2/(\lambda D) = d_{\mathrm{F}} \ll 1$; d_{F} is the *Fresnel number*. Satisfying the condition, we have Fraunhofer diffraction in the far-field region. Otherwise, we include $\mathrm{e}^{-\mathbf{i}k(\omega)\tilde{\rho}^2/(2D)}$ and obtain the Fresnel diffraction in the radiative zone of the near-field region. It is still not valid in the reactive zone due to (D.1).

D.1 Composed optical system

Here, we present the model of the composed optical system we use to model the field passed through the pinhole in Section 5.2.6

We compose two diffraction integrals (5.16) that gives

$$\mathcal{E}(z_{\mathrm{jet}};z,\rho,\omega) \propto \int\limits_{T_2}\int\limits_{T_1} \frac{\mathrm{e}^{\mathbf{i}\frac{k(\omega)}{2}\left(\frac{\rho_2^2}{D_2}+\frac{\rho_1^2}{D_1}\right)}}{D_1 D_2} J_0\left(\frac{k(\omega)\rho\rho_2}{D_2}\right) J_0\left(\frac{k(\omega)\rho_2\rho_1}{D_1}\right) d\left(\rho_1,\omega\right)\rho_2\rho_1\,\mathrm{d}\rho_2\mathrm{d}\rho_1\,, \tag{D.4}$$

where $D_1 = z_{\mathrm{p}} - z_{\mathrm{jet}}$, $D_2 = z - z_{\mathrm{p}}$. We keep the same ordering of the variables to follow the experimental campaign, z_{jet} is the position of the movable target, z_{p} and ρ_{p} are the position and radius of the pinhole, respectively. We first integrate in ρ_2 over the aperture $T_2 = [0,\rho_{\mathrm{p}}]$. Since $J_0\left(k(\omega)\rho_2\rho_1/D_1\right)$ acts as a source, we can use an analytic expression for the diffraction on a circular aperture derived from the integral[1]

$$\int_0^a xJ_0(bx)J_0(cx)\,\mathrm{d}x = a\frac{bJ_1(ab)J_0(ac)-cJ_0(ab)J_1(ac)}{b^2-c^2}\,. \tag{D.5}$$

The analytic integration may be used if we neglect $\mathrm{e}^{-\mathbf{i}k(\omega)\rho_2^2/(2D_2)}$. This leads to the final expression of the diffraction integral of the composed optical system:

$$\mathcal{E}(z_{\mathrm{jet}};z,\rho,\omega) \propto \int\limits_{T_1} \frac{\rho_{\mathrm{p}}}{k(\omega)}\mathrm{e}^{\mathbf{i}\frac{k(\omega)\rho_1^2}{2D_1}}\mathcal{J}(\rho,\rho_1,\omega)d\left(\rho_1,\omega\right)\rho_1\mathrm{d}\rho_1\,, \tag{D.6a}$$

$$\mathcal{J}(\rho,\rho_1,\omega) = \frac{\left(\rho D_1 J_1\left(\frac{k(\omega)\rho\rho_{\mathrm{p}}}{D_2}\right)J_0\left(\frac{k(\omega)\rho_{\mathrm{p}}\rho_1}{D_1}\right) - \rho_1 D_2 J_0\left(\frac{k(\omega)\rho\rho_{\mathrm{p}}}{D_2}\right)J_1\left(\frac{k(\omega)\rho_{\mathrm{p}}\rho_1}{D_1}\right)\right)}{(D_1\rho)^2-(D_2\rho_1)^2}\,. \tag{D.6b}$$

---

[1] If $b = c$, then $\int_0^a x\left(J_0(bx)\right)^2\,\mathrm{d}x = a^2\left(\left(J_0(ab)\right)^2+\left(J_1(ab)\right)^2\right)/2$.

D.1.1 Meaning of the Hankel transform

Here, we provide some additional physical explanation of the Hankel transform (5.16); it applies also for a composed system as (D.6). Let us consider the on-axis field, $\rho = 0$; Bessel function thus does not contribute at since there is only $J_0(0) = 1$.

In the Fraunhofer diffraction, this field is only the average of the sources over the radiating plane. Fresnel diffraction aligns the phases according to the optical-path differences.

E. COMPUTATIONAL COST, CONVERGENCE

We present some details about the numerical parameters and the computational cost of the multi-scale model. We refer to the use case in Section 6.3.6. The goal is thus to simulate the passage of an 800nm-laser pulse trough a 15mm-long medium filled with krypton. There are some typical parameters of the numerical experiment. The pressure of the gas is in the range $p \in [5, 50]$ mbar. The peak entry intensity is in the range $I_0 \in [0.7, 1.6] \times 10^{14}$ W/cm^2. The further parameters of the pulse are its radius at the entry of the medium, $w(z_{\mathrm{entry}}) = 100\mu$m and its duration $\tau = 35$ fs (defined by the FWHM in the intensity). The goal is then to obtain the XUV harmonic spectra in the far-field region using the pipe of the codes: *CUPRAD*, *1D-TDSE*, *Hankel transform*.

E.1 CUPRAD

The first step is the computation of the fields using CUPRAD. The field is represented on a discretised grid in the radial coordinate, ρ, and time/frequency, t/ω.[1] The discretisation in our experiment is $N_t = 2048$ and $N_\rho = 1024$. The computational box spans $4w(z_{\mathrm{entry}}) \times 12\tilde{\tau}$.[2] The discretisation in z is chosen automatically by the adaptive-step-size control, a typical spacing is in the order of 10 μm.

The code has been executed in parallel using 32 threads of 2.6 GHz processors [326]. A typical run is in the order of dozens of minutes. This make the code favourable for a multi-dimensional scans in the input parameters, allowing hundreds of simulations being executed.

E.2 1D-TDSE & Hankel transform

This is the computationally most expensive part of the code. The 1D-TDSE and the Hankel transform are linked by the means that the convergence of the Hankel transform drives the number of 1D-TDSE's to be executed.

We start with a single 1D-TDSE. The only additional parameter defining the physics is the soft-Coulomb potential in (7.23). We use $a = 1.3677$ corresponding to $I_P \approx 0.514$ a.u.. The parameters

---

[1] As explained, CUPRAD performs FFT at each step and represents the field in both domains during its execution.

[2] The window is defined using 1/e-metric in the amplitude of the electric field. The value corresponding to τ is $\tilde{\tau} \approx 30$ fs.

of a single run are $N_x = 16 \times 10^3$, $\Delta x = 0.4$ a.u. for the spatial grid. The discretisation in time uses $\Delta t = 0.25$ a.u.. The grid in time is then refined from the one defined in CUPRAD. The electric field $\mathcal{E}$ is smoothly interpolated using zero-padding in the ω-domain.

Using the same architecture as for CUPRAD, one run of TDSE takes about 20 minutes. The code is not internally parallelised; the parallelisation is made by running many TDSE solvers for various macroscopic points, e.g., different electric fields as inputs. The number of points is determined by the resolution needed for the Hankel transform computation.

The next step is the consecutive Hankel transforms computed by (9.3). We have been interested to compute it only for the spectral range H14-H22; according to the temporal resolution in TDSE, it reads ~ 500 points. The resolution in ρ_{screen} uses 300 points for $\rho_{\text{screen}} \in [0, 15]$ mm. The total amount of integrations is then 150×10^3. The key parameter is then the integration box. We have used $\Delta\rho_{\text{int}} \approx 4$ μm, $\Delta z_{\text{int}} \approx 10$ μm, using ~ 50 points in ρ_{int} and 1500 in z_{int}. The radial dimension than covers the region of interest according to Fig. 6.14 even for defocused beams. The resulting integration has taken several hours using multi-threading with 28 threads of the same architecture as above.

Obviously, the resolution for the final Hankel transform is the most critical parameter as it defines the number of TDSE executed. From that viewpoint, the computational time consumed by CUPRAD and Hankel transform is minor compared that of the TDSE. We then study this in detail. We have been considering possible optimisations of the integration in z. Our metric was to consider the phase of XUV source term $\widehat{\partial_t j_Q}$ in the spectral range of interest. This phase is constant in the co-moving frame for a plane wave without any spatial profile. Complementary to checking the convergence of the computation, we also studied the evolution of this phase in the co-moving frame. According to these analyses, $\Delta z_{\text{int}} \approx 10$ μm appears to be close to this limit for fast evolution in the fast-evolving region at the beginning of the gas medium, Fig. 6.14.

In conclusion, we have arrived to compute $\sim 100 \times 10^3$ of TDSE. Considering the time needed for a single TDSE, the computation cost of one simulation is then $\sim 10 \times 10^3$ CPU hours.

F. TRANSVERSAL PHASE PROFILE OF HARMONICS IN FSPA

In this appendix, we show that only the first order expansion, i.e. (2.19), of the dipole phase φ is included in the model of Gaussian optics and higher contributions included in (2.18) go beyond the Gaussian optics.

We prove that the first-order expansion is exhaustive within the assumption of Gaussian optics. Let use recall α from (2.19) that is assigned to the linear coefficient in the expansion. Let us fix the harmonic order and study only the expansion in intensity around a given I_0. The full expansion is:

$$\varphi(I) = \varphi(I_0) + \frac{\partial \varphi(I_0)}{\partial I}(I - I_0) + \frac{1}{2}\frac{\partial^2 \varphi(I_0)}{\partial I^2}(I - I_0)^2 + \cdots . \tag{F.1}$$

In our approach, we fix z and expand the intensity in the radial coordinate, ρ, of the beam $I(z,\rho) = I_0 \mathrm{e}^{-(\rho/w(z))^2}$. We take the mth term of the expansion,

$$\frac{I_0^m}{m!}\frac{\partial^m \varphi(I_0)}{\partial I^m}\left(\sum_{n=1}^{+\infty}\frac{(-1)^n}{n!}\left(\frac{\rho}{w(z)}\right)^{2n}\right)^m = \left(\frac{\rho}{w(z)}\right)^{2m}\frac{I_0^m}{m!}\frac{\partial^m \varphi(I_0)}{\partial I^m}\left(\sum_{n=1}^{+\infty}\frac{(-1)^n}{n!}\left(\frac{\rho}{w(z)}\right)^{2n-2}\right)^m , \tag{F.2}$$

we see that the leading power of the mth term is $2m$. It proves that only $m = 1$ contributes to the quadratic phase, and all higher orders are automatically beyond the Gaussian optics.

G. ORTHOGONAL POLYNOMIALS

In this appendix, we recall some basic properties of orthogonal polynomials and their construction.

Orthogonal polynomials are important functions applied in various fields because they can be used to construct orthogonal bases of $L^p(]a,b[\,,w(x)\mathrm{d}x)$-spaces. It leads to their wide use in quantum mechanics and also in numerics. We provide only a list of polynomials we are using, detailed information can be consulted in, e.g., the monograph [241]. They are special (or limit) cases of the *Jacobi polynomials* orthogonal w.r.t. the weight $w(x;a,b)=(1-x)^a(1+x)^b$ on the interval $]-1,1[$. See the references for their relations, there is specially a general recursive relation for all these polynomials ([241], Eq. (4.2.9)) that provides a straightforward way to evaluate numerically their values.

G.1 Legendre polynomials

The *Legendre polynomials*, P_n, are obtained from the Jacobi polynomials putting $a=b=0$. They satisfy a recursive relation

$$P_0(x)=1\,,\qquad P_1(x)=x\,,\qquad P_k(x)=\frac{(2k-1)xP_{k-1}(x)-(k-1)P_{k-2}(x)}{k}\,. \tag{G.1}$$

It may be useful to observe that they preserve the parity of polynomials, i.e. they are also a proper basis to describe odd and even functions. Their derivative is given by

$$P_k'(x)=\frac{k(xP_k(x)-P_{k-1}(x))}{x^2-1}\,. \tag{G.2}$$

G.2 Associated Legendre polynomials

Based on the Legendre polynomials, one defines the so-called *associated Legendre polynomials*,

$$P_{lm}(x)=\left(1-x^2\right)^{\frac{m}{2}}\frac{\mathrm{d}^m}{\mathrm{d}x^m}P_l(x)\,,\qquad \text{for } x\in[-1,1] \text{ and non-negative values of } m, \tag{G.3a}$$

the definition for negative values of m follows from

$$P_{l(-m)}(x) = (-1)^m \frac{(l-m)!}{(l+m)!} P_{lm}(x)\,. \tag{G.3b}$$

G.3 Generalised Laguerre polynomials

The *Generalised Laguerre polynomials* are the Jacobi polynomials transformed to the interval $[0, A]$ and extended by $A \to +\infty$. They satisfy a recursive relation

$$L_0^\alpha(x) = 1\,, \quad L_1^\alpha(x) = 1 + \alpha - x\,, \quad L_k^\alpha(x) = \frac{(2k + \alpha - 1 - x)L_{k-1}^\alpha(x) - (k + \alpha - 1)L_{k-2}^\alpha(x)}{k}\,. \tag{G.4}$$

Their derivative is given by (the relation (8.971) of [273]),

$$\frac{\mathrm{d}}{\mathrm{d}x} L_k^\alpha(x) = -L_{k-1}^{\alpha+1}(x) = \frac{kL_k^\alpha(x) - (n + \alpha)L_{k-1}^\alpha(x)}{x}\,. \tag{G.5}$$

The generalised Laguerre polynomials satisfies

$$\int_0^{+\infty} x^\alpha \mathrm{e}^{-x} L_n^\alpha(x) L_m^\alpha(x)\,\mathrm{d}x = \frac{\Gamma(n + \alpha + 1)}{n!}\delta_{mn} \tag{G.6}$$

that means they form an orthogonal set of polynomials on the interval $]0, +\infty[$ with the weight $x^\alpha \mathrm{e}^{-x}$.

G.4 Hermite polynomials

A substitution $x = y^2$ in (G.6) gives a new set of orthogonal polynomials w.r.t. the weight $w(y) = |y|^\gamma \mathrm{e}^{-y^2}$ on the interval $]-\infty, \infty[$. Only odd polynomials are defined by the substitution, the resting even polynomials can be added multiplying the odd ones by y for:

$$H_{2n}^\gamma(y) \propto L_n^{\frac{\gamma-1}{2}}(y^2)\,, \tag{G.7a}$$

$$H_{2n+1}^\gamma(y) \propto y L_n^{\frac{\gamma+1}{2}}(y^2) \tag{G.7b}$$

(the definition is unique up to normalisation).[1] A special case of these polynomials are so-called *Hermite polynomials* obtained by $\gamma = 0$.

---

[1] If one defines $\tilde{H}_n = (-1)^n H_n^0$, their norm is $\frac{\lfloor \frac{n}{2} \rfloor!}{\sqrt{\sqrt{\pi} n! 2^n}}$ that is closer to 1 than the usual definition and it may thus have better numerical performance. The *standard* convention of Hermite polynomials normalises them to $\sqrt{\pi} 2^n n!$, with the same signature as introduced by us.

Another definition suitable from the computational viewpoint [327] are polynomials defined by

$$\tilde{H}_{-1} = 0\,, \qquad \tilde{H}_0 = \frac{1}{\sqrt[4]{\pi}}\,, \qquad \tilde{H}_k = x\sqrt{\frac{2}{k}}\tilde{H}_{k-1} - \sqrt{\frac{k-1}{k}}\tilde{H}_{k-2}\,. \tag{G.8}$$

All three proposed forms are related by:

$$\tilde{H}_n = \frac{(-1)^n 2^{\frac{n}{2}} \lfloor \frac{n}{2} \rfloor !}{\sqrt{\sqrt{\pi} n!}} H_n^0 = \frac{1}{\sqrt{\sqrt{\pi} 2^n n!}} H_n\,, \tag{G.9}$$

H_n is a Hermite polynomial with *standard* normalisation including the sign. A convenient form for numerics is $\tilde{H}_n$ because $\left\|\tilde{H}_n\right\| = 1$.

G.5 Remarks

According to our knowledge, orthogonal polynomials are not treated in much detail considering boundary conditions that arises naturally solving differential equations. One might be interested in such a polynomials [328].

H. DISCRETE FOURIER TRANSFORM

In this appendix, we introduce our notation of the discrete Fourier transform, we also recall the link and conversion factors between the discrete Fourier transform and Fourier transform.

The DFT is defined by

$$X_k = \sum_{i=0}^{N-1} x_i \mathrm{e}^{-\frac{2\pi \mathbf{i}}{N} ik}\,, \qquad\qquad x_k = \frac{1}{N}\sum_{i=0}^{N-1} X_i \mathrm{e}^{\frac{2\pi \mathbf{i}}{N} ik}\,. \tag{H.1}$$

The coefficients in the expansion satisfy similar properties as the Fourier transform described in Appendix A.2 of [126] if one of the sequences is real (only proper index reordering has to be taken into account).

H.1 Relation with the Fourier transform & conventions

The DFT can be used to approximate the Fourier transform. One needs to be little careful with the conventions. Since this work is about physical applications, and we have defined conventions consistently with QM, where the Schrödinger equation is not a subject of a discussion, there is not much choice. Let us start with a real signal f limited in time placed in the interval $[0, T]$ and sampled in N equidistant points, $f_j := f(j\Delta t)$, $0 \leq j \leq N-1$. The Fourier transform can be approximated by

$$\tilde{f}(\omega) = \frac{1}{\sqrt{2\pi}}\int_{-\infty}^{\infty} f(t)\mathrm{e}^{\mathbf{i}t\omega}\,\mathrm{d}t = \frac{1}{\sqrt{2\pi}}\int_{0}^{T} f(t)\mathrm{e}^{\mathbf{i}t\omega}\,\mathrm{d}t \approx \frac{1}{\sqrt{2\pi}}\sum_{j=0}^{N-1} f_j \mathrm{e}^{\mathbf{i}j\Delta t\omega}\Delta t\,. \tag{H.2}$$

The result is evaluated in special points, as defined by $\tilde{f}_k = \tilde{f}(k\Delta\omega)$, $\Delta\omega = \frac{2\pi}{N\Delta t}$, it gives

$$\tilde{f}_k \approx \frac{\Delta t}{\sqrt{2\pi}}\left(\sum_{j=0}^{N-1} f_j \mathrm{e}^{-\frac{2\pi\mathbf{i}}{N}jk}\right)^* = \frac{\Delta t}{\sqrt{2\pi}} F_k^*\,, \tag{H.3}$$

where F_k corresponds to the definition (H.1). This equality provides a consistent link between the Fourier transform and DFT for real signals.

Let us note that we pre-assumed the original signal with a finite support. The formal definition of DFT makes periodic continuation of the function in a contrast with the assumption. The above description is motivated to make a straightforward link with the wide-used FFTW3 [281] algorithm and the conventions used therein.

Last, the integral is approximated by a simple rectangle rule. There are two advantages in relying on this simple rule: 1) There is a simple exact transform doing the inverse (there is no intrinsic error of the method assuming exact computer arithmetic), 2) As the abbreviation FFT suggests, its implementations are fast, and the accuracy may be reached by finer sampling.

I. ON DERIVATION OF FIELD AND QUANTUM EQUATIONS OF MOTION (MAXWELL, DIRAC, PAULI, SCHRÖDINGER) FROM STANDARD MODEL AND THEIR COUPLING

The purpose of this appendix is to conceptualise our work and to provide a strictly theoretical view from the top. To expand this statement in this context, there are three main motivations: I) The coupling of quantum mechanics with the field theory is not self-consistent as introduced at the end of Section 1.4. The internal symmetries of these theories differ: Galilean for quantum mechanics and Lorentzian for the classical field theory. We answer here how to derive both of them as a special case of a unified theory. A useful spin-off of this consideration is a consistent introduction of relativistic corrections mentioned in Section 2.1. II) We discussed in detail the invariant formulation of the ionisation in Chapter 3. We obviously reached a limit in theory as we were able to make a conclusion only within the dipole approximation and the extension beyond that point was problematic. One of the culprits is that we treated the field as an *external* quantity; the energy was considered for the electron only, and there was no coupled energy of the field. This appendix shows a consistent way to overcome this problem by considering dynamically all the terms: the electron, the field and their interaction term. The reached limit also shows that a fully consistent way of thinking is always to consider the full system of the particles coupled with the field and not only some of its subsystems. III) We encounter the gauge treatment at several places of this thesis (e.g. the treatment of the ionisation in Chapter 3 or their suitable choice in the numerical treatment in Section 7.3.2). In this appendix, we recall also a general role of the gauges. The gauge theories may be taken just as a tool to describe the field. However, their role in today geometrised physics [105] is much more important. The field theories are actually only *consequences* of the gauge theories. To illustrate this, we go beyond the $U(1)$-electromagnetism.

To conclude the motivation, this physics is far beyond the scope of HHG today, it is a question if this will change in future. For example, there were sketched some ideas to apply the nuclear photonics to transmute isotopes in the nuclear waste [329, 330, 331, 332]. As the transmutations of atoms is the subject of the weak and strong interaction, this may be eventually framework needed for this task. However, it is necessary to add that these ideas are still far away from applications, and it is a question if our technology would ever be able to use subatomic scales. In any case, some of today trends in HHG go in the direction of studying the symmetries related with chirality and additions of angular momenta. Form this viewpoint, the interplay of more group of symmetries related to the weak and strong interaction would produce wonderfully beautiful physics.

The starting point for this appendix is to resolve the inconsistency of the symmetries. To join the used theories together – the Maxwell's equation and quantum mechanics –, we need to go to the quantum field theory (QFT). It is also a clear way to include relativistic correction of the theory and estimate their contribution. Here, we present only a minimalistic recapitulation of the subject. There is a list of monographs for a comprehensive picture [333, 334, 335, 336, 337, 338].

The organisation is the following, first we introduce the Lagrangian and the underlying mathematical structures with their physical interpretation. The general equations of motion (Section I.5) are then applied to derive the quantum-mechanical equations of motion (Dirac and Schrödinger) in Section I.6 and Maxwell's equations in Section I.7. Finally, we present the limiting procedure leading to the non-relativistic quantum physics in Section I.8.

I.1 Lagrangian

The starting point of all the physics of the interest is the Lagrangian of the Standard Model (SM). It reads[1,2]

$$\begin{aligned}\mathscr{L} = & \underbrace{-\frac{1}{4}F_{\mu\nu}F^{\mu\nu} - \frac{1}{2}W^a_{\mu\nu}W^{\mu\nu}_a - \frac{1}{2}G^a_{\mu\nu}G^{\mu\nu}_a}_{\text{kinetic terms of fields}} + \underbrace{\sum_{\psi\in\{q,l\}} \overline{\psi}\left(\mathbf{i}\not{\partial} - \frac{g'Y_{\mathrm{W}}}{2}\not{A} - \frac{g_w}{2}\boldsymbol{\tau}\cdot\not{\boldsymbol{W}}\right)\psi}_{\text{electroweak sector}} \\ & + \underbrace{\sum_q \overline{q}\left(\mathbf{i}\not{\partial} - g_s\boldsymbol{T}\cdot\not{\boldsymbol{G}}\right)q}_{\text{quantum chromodynamics}} + \mathscr{L}_{\text{mass}} + \underbrace{\cdots}_{\text{beyond SM}} .\end{aligned} \tag{I.1}$$

The chosen form of the Lagrangian keeps the ingredients we would like to point out. The Standard Model is a theory with $U(1)\times SU(2)\times SU(3)$ symmetry formulated in the Minkowski space. This statement itself determines most of the physics up to free parameters of the model, i.e. of the physics as we understand it today. We will go briefly through all the terms in the next section and discuss their physical meaning after. Before we do so, there is an insertion on the mathematical structures acting in (I.1).

---

[1] Just few remarks to the notation, the Einstein summation is used for all up-down indices, it is both for Minkowski-space indexing (μ, ν,...) and also for the structure index a. Further in this appendix, we also use decompose the relativistic index in a given reference frame: its 0th component for time and the resting 3 components for spatial indices denoted by i, j, ... There is also the Dirac slash notation $\not{\Xi} = \gamma^\mu \Xi_\mu$ corresponding to a representation of the γ-matrices in a given Lorentz frame. $\overline{\psi}$ is closely related to $\psi^\dagger$ by $\overline{\psi} = \psi^\dagger\gamma^0$.

[2] The Lagrangian formulation is more convenient in QFT due to its Lorentz invariance and a natural description by path integration (see Sections 3.1 and 6.1.2 of [338]). The correspondence of Lagrangian and Hamiltonian formulation may become subtle when the Legendre transform is singular [339].

I.2 Brief summary of Lie group properties

We would make a short summary of the important parts on Lie groups. The goal is to extract the key properties based on manifolds, matrix algebra and elementary group theory, without a need of studying in precise detail. Consequently, we do not stick to full rigorousness and refer to specialised literature [333, 340, 341, 342].

Lie groups are geometrical structures combining properties of manifolds and groups. Let us take a simple example of 2×2 matrices with the determinant equal to one. We can parametrise them as

$$G = \left\{ \begin{pmatrix} x_{11} & x_{12} \\ x_{21} & x_{22} \end{pmatrix} \middle| \det \begin{pmatrix} x_{11} & x_{12} \\ x_{21} & x_{22} \end{pmatrix} = x_{11}x_{22} - x_{12}x_{21} = 1 \right\} \subset T^4 \,. \tag{I.2}$$

The last equation shows that it is a 3-dimensional hypersurface in a 4-dimensional space. The number field $T \in \{\mathbb{R}, \mathbb{C}\}$ denotes that the manifolds may be both real or complex. We see that the identity matrix belongs to G, as well as any matrix products of two matrices from G; finally, every matrix from G is invertible and the inverse is within G. Consequently, G is both group and manifold as required. Closely connected structures are Lie algebras, $\mathfrak{g}$ can be identified with the tangent space of G at any point (the algebraical structure is independent on the choice). $\mathfrak{g}$ is thus a simple linear space with the dimensionality of G with an additional structure of commutation relations between basis vectors, these relations are inherited from the group structure of G by the following procedure: Let us take two vectors $X, Y \in \mathfrak{g}$, i.e. taken from the tangent space at $A \in G$. X and Y are then direction vectors of two integral curves $A+tX$ and $A+sY$ contained in G. We then do infinitesimal consecutive steps along these curves: $C = A + \varepsilon X + \varepsilon Y$ and $C' = A + \varepsilon Y + \varepsilon X$. As going along such curves is not generally a commutative operation on a curved manifold, C and C' may differ. The direction of their difference defines exactly the commutator $[X, Y]$, i.e. $[X, Y] = C - C'$. The structure of the commutators uniquely defines the Lie algebra, and the generators of the algebra are then exactly the structures describing the fields $F_{\mu\nu}$, $W^a_{\mu\nu}$ and $G^a_{\mu\nu}$.

There is also a converse relation and a group may be reconstructed by the so-called exponential mapping (in fact, only its connected part, see the referred literature for details) from its Lie algebra. As the group is generated only using a basis of the algebra, base vectors of $\mathfrak{g}$ are called generators. Regarding the groups involved in the Standard Model, the Lie algebras $\mathfrak{su}(n)$ are given as traceless $n \times n$ matrices. A non-trivial commutative structure occurs for $\mathfrak{su}(2)$,[3] which can be represented

---

[3] This is the reason we have explicitly mentioned also the other groups than $U(1)$, which lacks the internal commutation structure. Consequently, a part of the physics originating from the gauge theories is no present in electromagnetism. The explicit mention of the other groups than helps to grasp the underlying mechanism, which then provide $U(1)$ only as a simplified case. We mention the consequences for the field equations in Section I.7.

by the Pauli matrices

$$\boldsymbol{\sigma} = \left(\begin{pmatrix} 0 & 1 \\ 1 & 0 \end{pmatrix}, \begin{pmatrix} 0 & -\mathbf{i} \\ \mathbf{i} & 0 \end{pmatrix}, \begin{pmatrix} 1 & 0 \\ 0 & -1 \end{pmatrix} \right) . \tag{I.3}$$

There is needed another step in the application of the symmetry groups: the natural dimensionality of the defining representation of the respective group does not provide enough room. It means that the groups are not used directly, but their representation is required. It turns out that the study of the irreducible representation of the respective groups allows for *derive* the structure of elementary particles, see Chapter 11 of [343]. These particles are then the building bricks of ψ and q in (I.1).

To conclude the discussion of the underlying geometrical structures, we recall that the theory is realised within the special relativity. The associated group is the Lorentz group $O(1,3)$, and the theory is invariant under the Lorentz transformations defined by he generators of $\mathfrak{o}(1,3)$. The practical realisation relies on the γ-matrices, which are included in the description of the fields $\not\Xi = \gamma_\mu \Xi^\mu$. The γ-matrices then provide the underlying geometry of the Minkowsky space in the SM.

This part of the model is also related with one of its limits: a consistent coupling with the general relativity. Practically, we may consider the theory described by (I.1) living on a curved manifold driven by the Einstein's equation. Roughly speaking, this would lead to the replacement of the partial derivatives by the corresponding covariant derivatives. However, the problem is the interlink the two natures of the equations of motion. Despite several attempts (see for instance Chapters 15 and 22 of [338] and [344]), it is still not satisfactory resolved.

I.3 Ingredients of the Standard Model

Here we provide a basic overview of the interpretation of the elementary objects: fields $F_{\mu\nu}$, $W^a_{\mu\nu}$ and $G^a_{\mu\nu}$, and particles ψ. The first ingredient is the *tensor fields* $\Xi^a_{\mu\nu}$, which are retrieved from *gauge fields*, Ξ^a_μ, by $\Xi^a_{\mu\nu} = \partial_\mu \Xi^a_\nu - \partial_\nu \Xi^a_\mu + g \xi^a{}_{bc} \Xi^b_\mu \Xi^c_\nu$, the summation coefficients $\xi^a{}_{bc}$ are the *structure constants*; we use $F^{\mu\nu}$ and A^μ (Maxwell stress tensor and vector potential, respectively) to emphasise the electromagnetic field by its standard notation at this point. Thus the tensor fields are just useful composed objects representing the fundamental gauge fields Ξ^a_μ, which defines the tensors uniquely.

As each gauge field correspond to one vector representation of a given symmetry group, a-indexed components of the field Ξ^a_μ enumerate the generators of the group. These generators are denoted by $\boldsymbol{\tau} = (\tau_1, \tau_2, \tau_3)$ for W^a_μ (generators of the $SU(2)$ group) and analogically by $\boldsymbol{T}$ for G^a_μ (generators of $SU(3)$).[4] The dot product $\boldsymbol{\tau} \cdot \boldsymbol{W}_\mu = \tau_a W^a_\mu$ is then clearly defined. The generators

---

[4] Since the symmetry of $F^{\mu\nu}$ is $U(1)$, its generator is only 1.

also define structure constants as commutators, $[\tau_a, \tau_b] = \mathbf{i} t_{ab}{}^{c}\tau_c$.[5]

Next part are wavefunctions or spinors denoted as ψ (eventually q and l, see the following section). One or more of their components are assigned to elementary particles. The interaction with the fields is provided by the actions of $\not{A}$, $\not{\boldsymbol{W}}$ and $\not{\boldsymbol{G}}$, which include also the representation of γ-matrices. As a result, all their components are functions on the Minkowski timespace, i.e. functions of x^{μ}.

To summarise the representation of fields and particles: fields correspond to the tensor fields $\Xi^{a}_{\mu\nu}$ and particles to the vectors ψ and q from (I.1). We extend the interpretation in the following paragraph.

I.4 Interpretation of the Standard Model

Having introduced all the objects, we can assign the physical meaning to them. The gauge fields mediate the interaction between sensitive elementary particles. The field of our interest is A^{μ} and its quantisation leads to photons. The next field from the electroweak sector, W^{a}_{μ} representing $SU(2)$, correspond to so-called $W^{\pm}$- and Z^{0}-*bosons*. The last field is G^{a}_{μ} representing $SU(3)$, and the force carriers are called *gluons*.

The second part of the model is elementary particles described by ψ: quarks, q, and leptons, l.[6] These are electrons, muons, standard quarks – forming protons and neutrons –, but also neutrinos and others.

Last, we inspect the structure of $\mathscr{L}$. *The kinetic terms* describe kinetic energy of the gauge fields. *The electroweak sector* describes the *electric interaction* that is the driving force for the formation of atoms, molecules. This is of high interest since it basically covers all the chemistry, electro engineering and most of today human technology. Next part is the *weak interaction* that drives the dynamics of atomic nuclei composed from protons and neutrons. The *quantum chromodynamics* is responsible for the formation of compound particles–hadrons. Hadrons may be composed from two quarks (mesons) or three quarks (baryons including protons and neutrons). As both nuclear fission and fusion involves atomic nuclei formation and also transmutations of protons and neutrons, they are a subject of the both preceding mechanisms. Next part, $\mathscr{L}_{\text{mass}}$, is the *Higgs mechanism* [345, 346, 347] responsible for the mass of particles, see Chapter 6 of [348] for its explanation within the terms of classical fields. The last part *beyond SM* denotes that the contemporary model of particle physics is not complete, for example neutrino masses may be included there.

---

[5] The up-down position of the indices a, b and c is just for aesthetics of summations, i.e. $t_{ab}{}^{c} = t^{a}{}_{bc} = t_{abc} = \cdots$.

[6] To be precise, there is required a further steps in QFT. The particle wavefunctions ψ are interpreted in the terms of the classical fields. There are then a subject of the same quantisation procedure as, for example, the photons as quanta of the electromagnetic field. This allows for finding corresponding creation and annihilation, which are used in the construction of the Fock space including an arbitrary number of particles. This shift of the paradigm was one of the most important steps in the construction of the modern QFT.

Another discussed extension is to enlarge the group structure $U(1) \times SU(2) \times SU(3)$, which may is a subgroup of $SU(5)$ providing a larger physical playground [349].

In summary, we have identified the structure of elementary of particles ψ and their mutual interaction provided by the fields $F_{\mu\nu}$, $W^{a}_{\mu\nu}$ and $G^{a}_{\mu\nu}$ via their respective contractions to $\slashed{A}$, $\slashed{\boldsymbol{W}}$ and $\slashed{\boldsymbol{G}}$. The Lagrangian (I.1) provides all their mutual relations. The nature of these links is encoded in the mathematical structure of the groups discussed in Sections I.2 and I.3.

I.5 Euler-Lagrange equations of motion

Any Lagrangian itself encodes the dynamics of the fields or particles that are its variables. The Hamilton variational principle for a field Θ allows to find the Euler-Lagrange equations of motion,

$$\partial_\mu \left(\frac{\delta \mathscr{L}}{\delta \partial_\mu \Theta} \right) - \left(\frac{\delta \mathscr{L}}{\delta \Theta} \right) = 0\,. \tag{I.4}$$

Θ may be both gauge fields, as a vector potential A^μ, or elementary-particles wavefunctions ψ. The dynamics of the full system arises from the set of coupled equations retrieved by the Hamilton principle applied to all dynamical variables of interest.

I.6 Dirac, Pauli & Schrödinger equation

Although all elementary particles are included, we use only a Dirac 4-components bispinor $\Xi = \overline{\psi} = \psi^\dagger \gamma^0 = (\psi^*_+, -\psi^*_-)$ which is assigned to a single electron. The reason is that we intend to derive the relevant equations for our work; however, the same procedure may be applied to other variables. Next, we omit all the interactions except the electromagnetism, $\slashed{A}$, and use the mass as a parameter, $\mathscr{L}_{\text{mass}} = m\overline{\psi}\psi$. Collecting all the terms, we have

$$\mathscr{L}_{\text{Dirac}} = \overline{\psi} \left(\mathbf{i}\slashed{\partial} - \frac{g' Y_{\text{W}}}{2} \slashed{A} - m \right) \psi\,. \tag{I.5}$$

The Euler-Lagrange equation is directly the Dirac equation $(\mathbf{i}\slashed{\partial} - \slashed{A} - m)\,\psi = 0$. The choice of units allows to set the numerical value of the charge $g' Y_{\text{W}}/2 = 1$.

As we have the Dirac equation, we can go down by performing the non-relativistic limit and obtain the Pauli equation. The Dirac equation may be written explicitly as

$$\begin{pmatrix} \hbar \mathbf{i} \partial_{ct} - eA_0 - mc & \boldsymbol{\sigma} \cdot (\mathbf{i}\hbar \bigtriangledown - e\boldsymbol{A}) \\ -\boldsymbol{\sigma} \cdot (\mathbf{i}\hbar \bigtriangledown - e\boldsymbol{A}) & -\hbar \mathbf{i} \partial_{ct} + eA_0 - mc \end{pmatrix} \psi = 0\,, \tag{I.6}$$

where we recovered the physical units, $\partial_{ct} = \partial_t / c$. The equation is then decomposed into the two doublets of the bispinor coupled by the off-diagonal terms. The goal is to perform the non-relativistic limit by the expansion in $1/c$. We see that the mass term is always a leading term for the both doublets. It can be taken out of one equation using a new bispinor defined as

$$\begin{pmatrix} \psi_+ \\ \psi_- \end{pmatrix} = \mathrm{e}^{\mathbf{i}\frac{mc^2}{\hbar}t}\psi\,, \tag{I.7}$$

with the two doublets $\psi_\pm$.[7] The equations (I.6) are then recast:

$$(\mathbf{i}\hbar\partial_t - e\phi)\psi_+ + c\boldsymbol{\sigma}\cdot(\mathbf{i}\hbar\,\triangledown - e\boldsymbol{A})\psi_- = 0\,, \tag{I.8a}$$

$$\left(-\frac{\mathbf{i}\hbar}{c^2}\partial_t + \frac{e\phi}{c^2} - 2m\right)\psi_- - \frac{1}{c}\boldsymbol{\sigma}\cdot(\mathbf{i}\hbar\,\triangledown - e\boldsymbol{A})\psi_+ = 0\,, \tag{I.8b}$$

we used $A^\mu = (\phi/c, \boldsymbol{A})$ to introduce the scalar potential to keep consistently $(1/c)$-terms. Neglecting $(1/c^2)$-terms, the second equation gives

$$\psi_- \approx -\frac{1}{2mc}\boldsymbol{\sigma}\cdot(\mathbf{i}\hbar\,\triangledown - e\boldsymbol{A})\psi_+\,. \tag{I.9}$$

Inserting it in the first equation, we obtain the Pauli equation

$$\mathbf{i}\hbar\frac{\partial\psi_+}{\partial t} = \left(\frac{1}{2m}\left(\boldsymbol{\sigma}\cdot(\mathbf{i}\hbar\,\triangledown - e\boldsymbol{A})\right)^2 + e\phi\right)\psi_+\,. \tag{I.10}$$

The Schrödinger equation is a further approximation given by the neglect of the spin-interaction giving the mutual coupling of the components of ψ_+, mathematically it means $(\boldsymbol{\sigma}\cdot(\mathbf{i}\hbar\,\triangledown - e\boldsymbol{A}))^2 \approx (\mathbf{i}\hbar\,\triangledown - e\boldsymbol{A})^2$. It may seem as a crude approximation at first glance, but the "kinetic" term of the Pauli equation is expanded as $(\boldsymbol{\sigma}\cdot(\mathbf{i}\hbar\,\triangledown - e\boldsymbol{A}))^2 = (\boldsymbol{p} - e\boldsymbol{A})^2 + e\hbar\boldsymbol{\sigma}\cdot\boldsymbol{B}$, where $\boldsymbol{B} = \mathrm{rot}\,\boldsymbol{A}$ is the magnetic field, the effects of which can be neglected in certain cases.

This procedure has led to the non-relativistic theory. There is still one point to discuss, the neglect of $A_0/c = \phi/c^2$. This is valid for non-relativistic strengths of the scalar potential. If these potentials are strong enough – for example electrons in inner shells of atomic nuclei with many protons –, it may not be satisfied. Non-relativistic theory may be used for the electron even in this case, there is machinery called the Foldy-Wouthuysen transformation, that takes into account higher-order relativistic corrections in the Pauli equation. Since there has been no approximation in the vector potential $\boldsymbol{A}$, Pauli or Schrödinger equation may give satisfactory results for the interaction of charged particles with relativistic $\boldsymbol{A}$, eventually with further corrections for relativistic ϕ, up to the case when the particle itself reaches a relativistic velocity.

---

[7] For the sake of clarity, we keep denoting the spinors $\psi_\pm$ hereafter even there is the additional phase factor.

So far, we considered a particle interacting only with fields directly. The full theory with all the elementary particles and their mutual couplings is too complicated for a direct calculation in most cases we meet in everyday life. A way to great simplification is to take into account part of the physics by an averaged model clustering elementary particles into composed particles or even larger units.

For example, we can fairly take a nucleus of an atom as a massive charged center seen by electrons forming an atom. The effect of the nucleus is then given only by the Coulomb potential, which also includes the photonic interaction as a classical field. The only thing to resolve is the origin of the Coulomb potential from QFT. Indeed, this is possible. It is a non-trivial problem, but it can be approached by computing the compound state of a charged particle and photonic field, see Eq. (D.12) of [335].

Once models of nuclei as Coulomb wells are available, larger compounds as molecules, crystal structures and other are constructed. A simplification in this process that deserves to be mentioned is the decoupling of nuclei and electrons that is the so-called Born-Oppenheimer approximation. This is exploited even further as a part of strongly bounded electrons can be taken as a charged continuum as well (see for example the Hartree-Fock method [264]). Continuing in this concept, we can describe complex materials as solids or crystals by complex potentials acting on the less-bounded parts of a physical system – usually electrons in valence or conduction bands. The crystals are modelled by periodic boundaries. Finally, all the classical states of matter are constructed from the fundamental origin.

I.7 Maxwell's equations

Next, we derive the Maxwell's equations. The kinetic term contributes in the equations of motion by

$$-\frac{1}{4}\frac{\delta F_{\iota\lambda}F^{\iota\lambda}}{\delta A_{\mu,\nu}} = F^{\mu\nu} \qquad \Rightarrow \qquad \partial_\mu\left(\frac{\delta \mathscr{L}}{\delta A_{\mu,\nu}}\right) = F^{\mu\nu}{}_{,\mu}\,. \tag{I.11}$$

Complementary equations are the Bianchi identities that emerge purely from the geometrical structure,

$$F_{\mu\nu,\lambda} + F_{\nu\lambda,\mu} + F_{\lambda\mu,\nu} = 0\,. \tag{I.12}$$

This part of the equations remain unchanged even with a presented source. In summary, equations $F^{\mu\nu}{}_{,\mu} = 0$ and (I.12) are the Maxwell's sourceless equation.

The derived equations are linear in the fields A_μ, and a non-linearity comes from the interaction with particles as we proceed to derive. This property is specific for the Abelian $U(1)$-theory of the electromagnetism. The covariant derivatives of the fields in non-Abelian theories are $D_\mu \Xi_{\lambda\iota} = \partial_\mu \Xi_{\lambda\iota} + [\Xi_\mu, \Xi_{\lambda\iota}]$, the commutator of the gauge field with the tensor field provides second-power terms even in the theory without an interaction with other particles. This self-interaction occurs in the case of a non-Abelian field, namely Z-, W-bosonic and gluonic fields arising from $\boldsymbol{W}_\mu$ and $\boldsymbol{G}_\mu$.

I.7.1 Source term

We would expect a classical limit $\mathscr{L}_{\text{interaction, classical}} = j^\mu A_\mu$. The interaction part of the full Lagrangian is $\mathscr{L}_{\text{Dirac}}$. The Euler-Lagrange equation leads to

$$\frac{\delta \mathscr{L}_{\text{Dirac}}}{\delta A_\mu} = \overline{\psi}\gamma^\mu \psi \,. \tag{I.13}$$

$j^\mu = \overline{\psi}\gamma^\mu\psi$ is a good candidate for the corresponding source as it is exactly a Noether current. We thus need only show that the non-relativistic limit leads to the right result.

The 0th component is straightforward, we need only ψ_+ as it is the non-relativistic spinor; $P_{\psi_+} j^0 = P_{\psi_+}\psi^\dagger(\gamma^0)^2\psi = \psi_+^\dagger\psi_+$, where we used the idempotence of γ^0, and P_{ψ_+} takes the first two components from a four-component vector. $\psi_+^\dagger\psi_+$ is then directly the desired density. We use the non-relativistic limit (I.9) from the Dirac equation to retrieve the resting components,

$$\begin{aligned} P_{\psi_+} j^i = P_{\psi_+}\overline{\psi}\gamma^i\psi = \psi_+^\dagger\sigma^i\psi_- \approx \psi_+^\dagger\sigma^i(\boldsymbol{\sigma}\cdot(\boldsymbol{p}-\boldsymbol{A}))\psi_+ = \\ = \psi_+^\dagger\left(\sigma^i\right)^2(\boldsymbol{p}-\boldsymbol{A})\psi_+ + \mathbf{i}\psi_+^\dagger\sum_{j=1,\, j\neq i}^{3}\varepsilon_{ijk}\sigma^k(\boldsymbol{p}-\boldsymbol{A}))\psi_+ \,. \end{aligned} \tag{I.14}$$

The non-relativistic limit is is then

$$P_{\psi_+}\boldsymbol{j} = \psi_+^\dagger(\boldsymbol{p}-\boldsymbol{A})\psi_+ + \boldsymbol{j}^{(\text{spin})} \,, \tag{I.15}$$

it is in the form of the Gordon decomposition, where $\boldsymbol{j}^{(\text{spin})}$ corresponds to the current induced by the gradient of the spin density. Finally, we recovered the expression from the non-relativistic quantum mechanics.

I.7.2 Maxwell's equations with the source term, classical limit, macroscopic form

If we put together the previous results, we have the Maxwell's equations[8]

$$F^{\nu\mu}{}_{,\mu} = \mu_0 j^\nu \tag{I.16}$$

---

[8] We use explicitly the vacuum permeability μ_0 to recall the form in dimensional units.

and (I.12). These equations are the equations for the electric, $\boldsymbol{\mathcal{E}}$, and magnetic, $\boldsymbol{B}$, field since they are related to the electromagnetic tensor

$$F^{00} = 0\,, \qquad F^{0i} = -\frac{\mathcal{E}_i}{c}\,, \qquad F^{i0} = -F^{0i}\,, \qquad F^{ij} = \varepsilon_{ijk}B_k\,, \tag{I.17}$$

where we have directly the components of the electric, $\boldsymbol{\mathcal{E}}$, and magnetic, $\boldsymbol{B}$, field. By writing down the partial derivatives explicitly or by expanding $F^{\mu\nu}$, one may easily retrieve many known forms of the Maxwell's equations.

Next, we see the correspondence with the electromagnetism induced by non-quantum charge distribution. Neglecting spin in (I.15) and simplifying notation in the terms of non-relativistic quantum mechanics, we have $\boldsymbol{j} = \psi^*(\boldsymbol{p} - \boldsymbol{A})\psi$. As $\boldsymbol{v} = \boldsymbol{p} - \boldsymbol{A}$, it suggests the link with the classical expression $\boldsymbol{j}_{\text{classical}} = \rho\boldsymbol{v} \sim |\psi|^2\boldsymbol{v}$. A correct approach is to average the quantum current. Such averaging can be seen also as a path from microscopic quantum physics to macroscopic description:

$$\boldsymbol{j}(\boldsymbol{x}_{\text{macro}}) = \int\limits_{V(\boldsymbol{x}_{\text{macro}})} f\psi^*(\boldsymbol{p} - \boldsymbol{A})\psi\,\mathrm{d}V\,. \tag{I.18}$$

The integration is performed over a microscopic volume $V(\boldsymbol{x}_{\text{macro}})$, f is a test function ensuring the correct normalisation with a smooth treatment of boundaries $\partial V(\boldsymbol{x}_{\text{macro}})$.

The averaging procedure is treated in great detail in [125]. It can be seen as a dynamical counterpart of the discussion in the last paragraph of Section I.6. This averaging procedure allows to simplify the calculations with two additional fields $\boldsymbol{D}$ and $\boldsymbol{H}$ that requires a split of charges and currents into *free* and *bound* summands. The responses of the bound parts are contained within $\boldsymbol{D}$ and $\boldsymbol{H}$, so there is no need to solve the dynamics in the microscopic scale. The details of the split are a part of the approximating procedure using the averaging.

I.8 Quantum to classical

To conclude the grounding of the derivation of the physical description based on (I.1), we retrieve a non-quantum non-relativistic theory. A popular shorthand could be saying that it is obtained from the Standard Model by the limits $c \to +\infty$ and $\hbar \to 0$. Indeed, the path to the non-relativistic theory was straightforwardly analytical considering a *perturbative* expansion in $1/c$. However, the second transition requires a different approach: the reason is that the playgrounds of quantum mechanics and a non-quantum theory are different. The states are given by vectors from Hilbert spaces or points in a phase-space, respectively. We recall two possible ways to perform the non-quantum limit. We illustrate these approaches on an already simplified system described equivalently by a Hamiltonian, $H(\boldsymbol{x}, \boldsymbol{p}) = \boldsymbol{p}^2/(2m) + V(\boldsymbol{x})$, or Lagrangian, $L(\boldsymbol{x}, \dot{\boldsymbol{x}}) = m\dot{\boldsymbol{x}}^2/2 - V(\boldsymbol{x})$:

- The Ehrenfest theorem states that the expectation values of the position and momentum operators evolves similarly to the classical Hamilton equations of motion:[9] $\mathrm{d}\langle \boldsymbol{x}\rangle/\mathrm{d}t = \langle \boldsymbol{p}\rangle$, $\mathrm{d}\langle \boldsymbol{p}\rangle/\mathrm{d}t = -\langle \triangledown V(\boldsymbol{x})\rangle$. Generally, $\langle \triangledown V(\boldsymbol{x})\rangle \neq \triangledown V(\langle \boldsymbol{x}\rangle)$; the difference in this expression may be seen as quantum corrections.
- The Feynman path integral provides an expression for the solution of the Schrödinger equation

$$\psi(\boldsymbol{x},t) = \int\limits_{\substack{\boldsymbol{\xi}(t_0)=\boldsymbol{y},\\ \boldsymbol{\xi}(t)=\boldsymbol{x}}} \mathrm{e}^{\frac{\mathrm{i}}{\hbar}\int L(\boldsymbol{\xi}(\tau),\dot{\boldsymbol{\xi}}(\tau))\,\mathrm{d}\tau}\psi(\boldsymbol{y},t_0)\,\mathscr{D}\boldsymbol{\xi}\,, \tag{I.19}$$

  $\mathscr{D}\boldsymbol{\xi}$ is a measure over all possible trajectories given as a limit: $\mathscr{D}\boldsymbol{\xi} = \lim_{n\to+\infty}\Pi_{i=1}^{n}\mathrm{d}\boldsymbol{\xi}_i$, where $\boldsymbol{\xi}_i$ are all the possible intermediate points the particle may travel through.[10] The interesting point is the action $\mathcal{S} = \int L(\boldsymbol{\xi}(\tau),\dot{\boldsymbol{\xi}}(\tau))$, its stationary points are are prescribed by the classical Euler-Lagrange equation of motion. The weight factor $1/\hbar$ puts an infinite contribution to the classical path if $\hbar \to 0$.

I.9 Conclusion

Finally, we have introduced a consistent approach of coupling the Galilean and Lorentzian symmetries and linked it with the physics we use. The resolution is that the non-relativistic limit (I.9) is performed in a reference frame, where the velocities of the particles are non-relativistic. The laboratory frame fulfils this condition in HHG.

The second use of this appendix is in the invariant study of the ionisation. There was reached the limit of the coupling from the energetic viewpoint. The reason is that the field was taken as *external*, thus unaffected by the evolution of the particles. The solution is to include the fields consistently by $F^{\mu\nu}F_{\mu\nu}$ and the interaction term $j_\mu A^\mu$.

Finally, we have introduced framework which may be used to extend theory to different kinds of interaction than electromagnetic. It still seems as a difficult question to estimate if we master the sub-atomic physics to a sufficient state that we will need to treat the dynamics of the Z- and W-bosonic or gluonic fields within the atomic nuclei for our future technology.

---

[9] The average of an operator A is $\langle A\rangle = \langle\psi|A|\psi\rangle$.

[10] It should be noted that a correct definition of the measure $\mathscr{D}$ is non-trivial (see Section 2-4 of [32]). Today formulation arises from stochastic approaches (for example [350, 351] and references therein).

J. MODELLING MATTER FOR LASER PROPAGATION

This appendix explains the hierarchy to derive the source term related with the ionisation, which is included in the non-linear optics.

The model of the interaction of a gaseous medium with a laser pulse may be done on different levels of complexity. This appendix is a brief review of possible physical pictures using top-down approach. The advantage of such a description is that physical approximations and neglects becomes obvious in consecutive steps. Here, we always consider a classical field coupled with matter – the field is modelled by Maxwell's equations in any case.

1. Starting with a general formulation, we use a quantum-statistical description. It means an n-body density matrix ρ to describe a state. For the simplicity of formulation, we stay within a subspace of the Fock space with a fixed number of particles. The evolution of the density matrix is driven (in the Schrödinger picture) by the *Von Neumann equation*:

   $$\frac{\partial \rho(t)}{\partial t} = -\frac{\mathbf{i}}{\hbar}\left[H(t), \rho(t)\right] \, , \tag{J.1}$$

   where H is the Hamiltonian of the system. This Hamiltonian principally includes all the mutual interactions of various particles and the effects of the coupled external field as well, see Lindblad master equation [352]. The exact solution of this equation is absolutely out of any bounds for practical numerical calculation. However, it is a good starting point for simplifications.

2. In the first step, we move from quantum statistics to classical statistics using the Wigner distribution.[1] A state of the system is classically described by a phase-space distribution

---

[1] The Wigner distribution does not satisfy non-negativity. This is sometimes a subject of discussions about its interpretation, Chapter 15 of [124]. We do not intend to precisely analyse this topic, but we can recall some ideas. 1) There are still some constraints about f, so it cannot be arbitrary negative in large regions. There also holds the fundamental normalisation $\int f \prod_{i=1}^{n} \mathrm{d}^3 x_i \mathrm{d}^3 p_i = 1$. 2) Let us mention one classical example: quantum tunnelling. This process also violates locally the energy conservation and more energy than classically available is used to "climb over the barrier". This can be seen as the energy is "borrowed" from adjacent regions of the phase space. Such a picture is supported by studies of the Wigner distribution in the tunnelling regime [353].

function f. A way to link this with ρ is to use the n-body Wigner distribution defined by

$$f(\boldsymbol{x}_1,\ldots,\boldsymbol{x}_n,\boldsymbol{p}_1,\ldots,\boldsymbol{p}_n,t) = \langle \boldsymbol{p}_1,\ldots,\boldsymbol{p}_n \,|\, \rho(t) \,|\, \boldsymbol{x}_1,\ldots,\boldsymbol{x}_n \rangle \, \langle \boldsymbol{p}_1,\ldots,\boldsymbol{p}_n \,|\, \boldsymbol{x}_1,\ldots,\boldsymbol{x}_n \rangle \; . \tag{J.2}$$

The Von Neumann equation then limits to the *Liouville equation* that governs the classical evolution of the density

$$\frac{\partial f}{\partial t} = \sum_{i=1}^{n} \left(\bigtriangledown_{\boldsymbol{x}_i} H \cdot \bigtriangledown_{\boldsymbol{p}_i} f - \bigtriangledown_{\boldsymbol{p}_i} H \cdot \bigtriangledown_{\boldsymbol{x}_i} f \right) \; . \tag{J.3}$$

What is the physics lost by this approximation? Basically, we have lost the quantum nature of the interaction. It means quantum entanglement of the particles, but also HHG, for example, as well as this is a quantum-mechanical process. However, we should have in mind, that this still follows only the logic of the derivation: the collective contribution of all the electrons within the medium. The interaction on the microscopic level of a single atom may be still covered by the Macroscopic Maxwell's equations.

3. Although f is a statistical quantity, it still gives the probability distribution for each particle, it means that f lives on very large space, which is still beyond all practical computational tools. A next possible step is to reduce the number of variables and use a true continuum in the description. The idea is to create a sequence of distributions with reduced number of variables. As the particles are of the same kind, it would lead to continuum of this kind. This procedure is the so-called BBGKY hierarchy.[2] It defines the sequence:

$$f_s(\boldsymbol{x}_1,\ldots,\boldsymbol{x}_s,\boldsymbol{p}_1,\ldots,\boldsymbol{p}_s,t) = \int \prod_{i=s+1}^{n} \mathrm{d}^3 x_i \mathrm{d}^3 p_i \; f(\boldsymbol{x}_1,\ldots,\boldsymbol{x}_n,\boldsymbol{p}_1,\ldots,\boldsymbol{p}_n,t) \, . \tag{J.4}$$

The first and last terms of the chain are, respectively, $f_1 = f_1(\boldsymbol{x}_1,\boldsymbol{p}_1,t)$ and $f_n = f$. The important hierarchical structure derived from (J.4) links only two consecutive distributions:

$$\frac{\partial f_s}{\partial t} + \mathcal{L}_s f_s = \Phi_s[f_{s+1}] \, . \tag{J.5}$$

$\mathcal{L}_s$ is a linear differential operator and Φ_s is a functional, both may depend on $\boldsymbol{x}_i$, $\boldsymbol{p}_i$, $i = 1,\ldots,s$. The functional Φ_s contains an integration, so the number of variables is correct. The distribution of interest is f_1. The lowest equation in the chain is

$$\frac{\partial f_1}{\partial t} + \left(\frac{\boldsymbol{p}}{m} \cdot \bigtriangledown_{\boldsymbol{x}} \right) f_1 + \left(\boldsymbol{F} \cdot \bigtriangledown_{\boldsymbol{p}} \right) f_1 = \Phi_1[f_2] \, , \tag{J.6}$$

---

[2] Bogoliubov-Born-Green-Kirkwood-Yvon hierarchy.

where $\boldsymbol{p}$ and $\boldsymbol{F}$ are the local momentum and force,[3] respectively. We have identified $\boldsymbol{x} = \boldsymbol{x}_1$ and $\boldsymbol{p} = \boldsymbol{p}_1$ as they are the only variables of f_1. This is already almost the *Boltzmann equation* driving the continuum, the difference is the source $\Phi_1[f_2]$. A way to break the chain is to approximate it without the need of knowing f_2. The source $\Phi_1[f_2]$ represents the changes induced by the two-particle distribution. In other words, we may see it as the effect of collisions. The resolution is then to replace $\Phi_1[f_2]$ by the so-called *collision integral* $\mathscr{S}$, that is obtained by modelling two-particle collisions. There are various approaches originating from this model as, for example, *Vlasov equation* for a collisionless medium.

Again, we review the effects lost by this approximation. We arrived to truly continuous description, containing up to two-particle collisions by $\mathscr{S}$. The missing part may be then the interaction of more than 2 particles. Next, all the parts of the medium are then given by the local density only. In the detailed sense, this state is not unique. A possible viewpoint is a local grand canonical ensemble in the thermodynamic sense. This becomes indistinguishable within this theory. However, a lot of these things are still fairly modelled: collective effects of more particles may be included by Debye screening; instabilities allows a completely distinct evolution of various points. The instabilities grow from random fluctuations, which can be seen as different states within the grand canonical ensemble. In summary, this formulation opens the way for practical calculation (e.g. particle-in-cell codes). It then becomes a notorious starting equation for modelling plasma.

4. A further simplification is useful for both the insight in the physics and a simpler numerical procedures. It is obtained by a further reduction of the momentum space in the Boltzmann equation. The kinetic equations of the continuum are found by computing the moments of the Boltzmann equation, the 0th and 1st moments are related to the density and flow velocity

$$\varrho(\boldsymbol{x},t) = \int f_1(\boldsymbol{x},\boldsymbol{p},t)\,\mathrm{d}^3p\,, \qquad \boldsymbol{u}(\boldsymbol{x},t) = \frac{\int \frac{\boldsymbol{p}}{m} f_1(\boldsymbol{x},\boldsymbol{p},t)\,\mathrm{d}^3p}{\int f_1(\boldsymbol{x},\boldsymbol{p},t)\,\mathrm{d}^3p}\,, \tag{J.7}$$

respectively. The related moments are

$$\frac{\partial\varrho}{\partial t} + \triangledown(\varrho\boldsymbol{u}) = \underbrace{\int \mathscr{S}\,\mathrm{d}^3p + \int (\triangledown_{\boldsymbol{p}}\boldsymbol{F})\,f_1\,\mathrm{d}^3p}_{S}\,, \tag{J.8a}$$

$$\frac{\partial(\varrho\boldsymbol{u})}{\partial t} + \triangledown\boldsymbol{T} = \boldsymbol{\mathcal{F}} + \int \boldsymbol{p}\mathscr{S}\,\mathrm{d}^3p\,, \tag{J.8b}$$

we use $\triangledown = \triangledown_{\boldsymbol{x}}$ as $\boldsymbol{x}$ is an explicit variable of the equations for the continuum, while $\boldsymbol{p}$ is

---

[3] The force in the Hamiltonian contracted to single particle is $\boldsymbol{F} = -\triangledown_{\boldsymbol{x}} H$. However, the force there comes also from the other particles integrated by the BBGKY hierarchy. We do not precise details here as it is beyond the purpose of this appendix.

contracted by the integration. The derivation is straightforward using only the integration by parts in $\bigtriangledown_{\boldsymbol{p}} f_1$-terms and boundedness of f_1 given by $\lim_{\|\boldsymbol{p}\|\to+\infty} f_1 = 0$.

The 0th moment, (J.8a), is the continuity equation. S gives the sources and sinks. If we consider electronic fluid, as is of the main interest of this work, its created or absorbed, respectively, by ionisation or recombination. The ionisation may be due to avalanche – electron-atomic collisions – ionisation or photoionisation by the electromagnetic field. The sink is due to recombinations. The rightmost term vanishes for $\boldsymbol{p}$-divergence-free forces, which includes the Lorentz force.

The 1st moment, (J.8b), is the Euler equation of motion for the fluid. The driving force is $\boldsymbol{\mathcal{F}} = \int \boldsymbol{F} f_1 \,\mathrm{d}^3p + \int \boldsymbol{p} \left(\bigtriangledown_{\boldsymbol{p}} \boldsymbol{F}\right) f_1 \,\mathrm{d}^3p$. Again, it is simplified for $\boldsymbol{p}$-independent forces – and also the Lorentz force – to just force density $\boldsymbol{\mathcal{F}} = \varrho \boldsymbol{F}$. The collision term including $\mathscr{S}$ may change the amount of the fluid either by sourcing or sinking with a given momentum distribution. The last interesting quantity is the tensor $\boldsymbol{\mathcal{T}} = \int \left(\boldsymbol{p} \otimes \boldsymbol{p}\right) f_1 \,\mathrm{d}^3p$. Its diagonal terms are related to the kinetic energy-density $\epsilon = \left(\int \|\boldsymbol{p}\|^2 f_1 \,\mathrm{d}^3p\right)/m$. The off-diagonal terms relate to fluxes of the momentum (e.g. $\mathcal{T}_{12} = \int p_1 p_2 f_1 \,\mathrm{d}^3p$ describes the flux of the x-component of to momentum in the y-direction). Principally, this would require a higher moment of the Boltzmann equation; which would contain another higher-order quantity as heat-flow: $\boldsymbol{q}(\boldsymbol{x}, t) = \left(\int \boldsymbol{p} \,\|\boldsymbol{p}/m\|^2 f_1 \,\mathrm{d}^3p\right)/(m\varrho(\boldsymbol{x}, t))$.

A way to stop the need of equations for higher-moments is to truncate the chain by an empiric law. There is no universal recipe. The beauty of the equation is in the universality: They may be used to model phenomena from cosmical scales as formation of stars, stellar winds, supernovae – passing macroscopic and laboratory scales –, inertial fusion, tokamaks – down to the microscopic world –, the free electrons due to the optical ionisation as of the interest of this thesis. Some closure examples are the state equation of a polytropic gas; Fourier's law of heat conduction or instantaneous thermalisation.

Let us show a possible simplification for a microscopic volume of a gas ionised by an ultrashort laser impulse. Assuming instantaneous thermalisation – no transport of higher moments –, the dynamics of free electrons is given by

$$\frac{\partial \varrho_e}{\partial t} + \bigtriangledown(\varrho_e \boldsymbol{u}_e) = S\,, \tag{J.9a}$$

$$\frac{\partial \boldsymbol{u}_e}{\partial t} + \left(\boldsymbol{u}_e \cdot \bigtriangledown\right) \boldsymbol{u}_e = -\frac{e}{m_e}\left(\boldsymbol{\mathcal{E}} + \boldsymbol{u}_e \times \boldsymbol{B}\right) - \nu_e \boldsymbol{u}_e - S\frac{\boldsymbol{u}_e}{\varrho_e}\,. \tag{J.9b}$$

ϱ_e and $\boldsymbol{u}_e$ are the electronic density and average velocity, respectively. The RHS terms are: 1) The source S is due to ionisation from collisions, but also photoionisation by the optical field. It is an external mechanism within the description. 2) The Lorentz force,

$\boldsymbol{F}_L = -e\left(\boldsymbol{\mathcal{E}} + \boldsymbol{u}_e \times \boldsymbol{B}\right)$. 3) The collisions generally originating from collision integrals. The presented model, $\nu_e \boldsymbol{u}_e$, simplifies this quantity down to a single parameter: the collision frequency ν_e.

5. The final simplification is the *Drude model*. It comes from the equation (J.9b) for $\boldsymbol{u}_e$, the parameter of collisions is $\nu_e = 1/\tau_e$. The collision frequency is seen in the terms of the kinetic theory of gases; τ_e is the average time between the collisions of electrons with neutrals and ions. The kinetic equation for a single electron is

$$m_e \ddot{\boldsymbol{x}} = \boldsymbol{F}_L - \nu_e \dot{\boldsymbol{x}} \,. \tag{J.10}$$

The form of the collisions is simply a linear drag force. It is then an easy-to-understand explanation.

The main goal of this top-down derivation throughout the physical theories was to describe a collective motion of electrons. We have lost HHG and other effects of non-linear optics quite early in the procedure. We then may put this into context even in this description. A way to obtain these effects is to break the collectivity early after the first step, the decomposition of the space would give:

2*. We omit the interaction between the particles; moreover, we assume each particle to be given by a pure state, so there are no off-diagonal terms in the density matrix ρ. Summarising these ideas mathematically:

$$\rho_{ij} = 0\,, \qquad \rho_{ii} = \left|\psi_i\right\rangle \left\langle\psi_i\right| \;; \qquad H = \bigotimes_{i=1}^{n} H_i \,. \tag{J.11}$$

The Von Neumann equation reduces into single-particle subspaces

$$\mathbf{i}\hbar \frac{\partial \left|\psi_i\right\rangle \left\langle\psi_i\right|}{\partial t} = H_i \left|\psi_i\right\rangle \left\langle\psi_i\right| - \left|\psi_i\right\rangle \left\langle\psi_i\right| H_i \,, \tag{J.12}$$

which can be transformed into the *Schrödinger equation*. The index i relates to the particle, it implies that the H_i describes the microscopic volume of the interest placed in the macroscopic position $\boldsymbol{x}_i$.

In conclusion, we have provided a systematic derivation scheme to describe a macroscopic physical system from a fundamental quantum-mechanical statistical approach. It would be possible to follow the scheme analogously in a relativistic case, which we have not used for simplicity. The choice of a correct description always relies on the complexity of the problem and the need of various effects to be included as commented in the derivation.